HALOGEN DIFFUSION IN SILICIC MELT AND IMPLICATIONS FOR MAGMATIC PROCESSES

Dissertation

zur Erlangung des Akademischen Grades
"Doktor der Naturwissenschaften"
im Promotionsfach Geologie/Paläontologie

am Fachbereich für Chemie, Pharmazie, Geographie und Geowissenschaften
der Johannes Gutenberg-Universität, Mainz

Yves Feisel

geb. in Frankenberg (Eder)

Mainz, August 2022

1. Gutachter: **Prof. Dr. Jonathan M. Castro (JGU Mainz)**

2. Gutachter: **Prof. Dr. Donald B. Dingwell (LMU München)**

Tag der mündlichen Prüfung: 08.03.2023

Abstract

Dissolved magmatic volatiles control many substantial physico-chemical properties of silicate melt which is why they are of profound importance to the nature and style of volcanic eruptions. Even though the halogens account only for a small fraction of the typical volcanic volatile budget, they exhibit characteristics that stand out among the volatiles and may affect fundamental melt properties and — once released from the volcano — impact the environment and atmosphere. Moreover, their properties in silicate melts bear the potential to utilize halogen degassing behavior to characterize magmatic processes at shallow crustal levels. To support the development of a detailed understanding of halogen behavior in silicate melts, this thesis presents experimental results of halogen (F, Cl, Br, I) diffusion experiments in silica-rich natural melts under both dry and hydrous conditions. The diffusion couple technique was applied with a range of different experimental setups at temperatures characteristic of natural magmatic systems (750–1200 °C) and pressures of 0.1 and 160 MPa. Experimental samples were evaluated using a variety of analytical methods.

The experiments reveal that halogen diffusion in silicic melt follows Arrhenian behavior and is strongly dependent on the melt structure. In anhydrous silicic melt, halogen diffusivity is inversely correlated with the ionic radius of the diffusing species, spanning a range of diffusivities of 3–4 orders of magnitude among F, Cl, Br, and I. Upon the addition of 1.5 wt.% of H_2O to the melt, the diffusivity of all halogens increases significantly due to the depolymerizing effect of water. The increase is most pronounced for the largest halogen iodine and is subsequently less for the smaller halogens, leading to a narrower diffusive range of only 1–2 orders of magnitude and, consequently, merely a weak correlation of diffusivity and ionic radius compared to the anhydrous case. This behavior is interpreted to represent a gradual decrease of the influence of ionic porosity on the diffusion-rate, making the process of bond-breaking more relevant as a diffusion-rate-limiting mechanism with increasing water content.

In a related experimental study, the effects of F and Cl on the phase equilibria of a near-liquidus hydrous trachyte melt was investigated by employing a novel disequilibrium approach which involved diffusion couple experiments at temperatures of 925–990 °C and 100 MPa. The results demonstrate a pronounced decrease of the melt's liquidus temperature by ~50 °C, which is induced by the diffusion of F and Cl into a formerly halogen-depleted clinopyroxene-bearing melt. These observations suggest that the liquidus decrease is a consequence of clinopyroxene dissolution by increased solubility of its main cationic components (Fe, Mg, Ca) due to their complexation with F and Cl. These findings illustrate that even low fluctuations in halogen concentration can strongly influence the physical properties of the melt, e.g., by shifting a melt's liquidus temperature due to pre- or syn-eruptive volcanic degassing.

The findings of this thesis provide a significant addition to the understanding of magmatic halogen behavior and include the first ever diffusion data of iodine in silicate melt. Moreover, the results may be applied in future studies to characterize magmatic processes at depth, such as bubble growth or magma ascent, and may ultimately help to identify volcanic unrest of silicic volcanoes.

Zusammenfassung

In Magma gelöste flüchtige Stoffe (Volatile) haben tiefgreifenden Einfluss auf die Art und den Verlauf vulkanischer Eruptionen, da sie zahlreiche physikalisch-chemische Eigenschaften des Magmas substanziell mitbestimmen. Die Elementgruppe der Halogene macht zwar nur einen kleinen Teil typischer vulkanischer Volatile aus, dennoch haben sie einzigartige Eigenschaften, die das fundamentale Verhalten einer Schmelze verändern und — nach vulkanischer Freisetzung — auch die Umwelt und Atmosphäre signifikant beeinflussen können. Darüber hinaus haben ihre speziellen Eigenschaften in Silikatschmelzen das Potenzial das Entgasungsverhalten von Halogenen zu nutzen, um magmatische Prozesse in der oberen Kruste zu charakterisieren. Zur Entwicklung eines besseren Verständnisses des Halogenverhaltens in Magma präsentiert diese Dissertation umfangreiche Ergebnisse von Experimenten zur Bestimmung der Halogen-Diffusivität (F, Cl, Br, I) in silikatreichen natürlichen Schmelzen, sowohl unter wasserfreien als auch wasserhaltigen Bedingungen. *Diffusion-Couple*-Experimente wurden anhand verschiedener Versuchsaufbauten bei magmatischen Temperaturen (750–1200 °C) und Drücken von 0.1 und 160 MPa durchgeführt und mit diversen analytischen Methoden ausgewertet.

Die Experimente verdeutlichen, dass Halogendiffusion in silikatreicher Schmelze dem Arrhenius‘schen Verhalten folgt und stark von der Schmelzstruktur abhängt. In wasserfreier Schmelze ist die Diffusivität in etwa umgekehrt proportional zu dem Ionenradius der diffundierenden Spezies und umfasst einen Bereich von drei bis vier Größenordnungen zwischen F, Cl, Br und I. Durch Zugabe von 1.5 Gew.-% H_2O zur Schmelze steigt die Diffusivität aller Halogene durch die depolymerisierende Wirkung des Wassers deutlich an. Dieser Effekt ist für das größte Halogen Jod am stärksten und nimmt für die kleineren Halogene sukzessive ab. Dies führt zu einem geringeren Diffusionsbereich von nur ein bis zwei Größenordnungen und folglich nur zu einer schwachen Korrelation von Diffusivität und Ionenradius. Dieses Verhalten ergibt sich daraus, dass der Einfluss der ionischen Porosität auf die Diffusionsrate bei zunehmendem Wassergehalt graduell abnimmt, wodurch die Diffusionsgeschwindigkeit zunehmend durch den Prozess des „Herauslösens“ der Halogene aus ihren ionisch koordinierten Verbindungen limitiert wird.

In weiterführenden Untersuchungen wurde außerdem die Wirkung von F und Cl auf die Kristallisation einer wasserhaltigen Trachytschmelze bei Temperaturen nahe des Liquidus experimentell untersucht. Bei Temperaturen von 925–990 °C und einem Druck von 100 MPa wurde dafür ein neuartiger Ansatz angewendet, der auf dem chemischen Ungleichgewicht von *Diffusion-Couple*-Experimenten basiert. Die Ergebnisse zeigen eine Abnahme der Liquidustemperatur um ~50 °C, die durch die Anreicherung von F und Cl in einer klinopyroxen-haltigen Schmelze verursacht wird. Diese Beobachtungen deuten darauf hin, dass Klinopyroxen durch die erhöhte Löslichkeit seiner kationischen Komponenten (Fe, Mg, Ca) aufgrund ihrer Komplexierung mit F und Cl aufgelöst und dadurch die Liquidustemperatur

verringert wird. Diese Ergebnisse zeigen, dass bereits geringe Schwankungen der Halogenkonzentration die physikalischen Eigenschaften einer Schmelze stark beeinflussen können, z.B. durch Veränderung der Liquidustemperatur durch vulkanische Entgasung vor oder während einer Eruption.

Die Ergebnisse dieser Dissertation liefern einen bedeutenden Beitrag zum Verständnis des Verhaltens von Halogenen in vulkanischen Schmelzen und beinhalten darüber hinaus den ersten konsistenten Datensatz zur Diffusion von Jod bei magmatischen Temperaturen. Des Weiteren können die Ergebnisse in zukünftigen Studien zur Charakterisierung magmatischer Prozesse in der Erdkruste eingesetzt werden — z.B. für die Untersuchung des Wachstums von Gasblasen in einer Schmelze — und können damit potentiell dazu beitragen, vulkanische Aktivität frühzeitig zu erkennen.

Preamble

Parts of the content of this thesis have already been published or are currently under review for publication in a peer-reviewed scientific journal. References relevant for this thesis are listed below:

Feisel, Y., Castro, J.M., and Dingwell, D.B., 2019. Diffusion of F and Cl in dry rhyodacitic melt. *American Mineralogist*, 104, 1689 – 1699, doi: 10.2138/am-2019-7095

Feisel, Y., Castro, J.M., Helo, C., and Dingwell, D.B., 2022. The effect of halogens (F, Cl) on the near-liquidus crystallinity of a hydrous trachyte melt. *American Mineralogist*, 107, 1007 – 1017, doi: 10.2138/am-2022-8120

Feisel, Y., Castro, J.M., Helo, C., Bouvier, A.-S., Ludwig, T., and Dingwell, D.B., (*in review*). Diffusion of Halogens (F, Cl, Br, I) in silicic melts. *Under review* at *Geochimica et Cosmochimica Acta.*

The following additional studies were published during enrolment but are not directly associated with the subject of this thesis:

Hughes, E.C., Mazot, A., Kilgour, G., Asher, C., Michelini, M., Britten, K., Chardot, L., **Feisel, Y.**, and Werner, C., 2019. Understanding Degassing Pathways Along the 1886 Tarawera (New Zealand) Volcanic Fissure by Combining Soil and Lake CO_2 Fluxes. *Frontiers in Earth Science*, 7, 264, doi: 10.3389/feart.2019.00264

Castro, J.M., Keller, F., **Feisel, Y.**, Lanari, P., Helo, C., Mueller, S.P., Schipper, C.I., and Thomas, C., 2020. Lightning-induced weathering of Cascadian volcanic peaks. *Earth and Planetary Science Letters*, 552, 116595, doi: 10.1016/j.epsl.2020.116595

Cáceres, F., Scheu, B., Colombier, M., Hess, K.-U., **Feisel, Y.**, Ruthensteiner, B., and Dingwell, D.B., 2022. The roles of microlites and phenocrysts during degassing of silicic magma. *Earth and Planetary Science Letters*, 577, 117264, doi: 10.1016/j.epsl.2021.117264

Castro, J.M., and **Feisel, Y.**, 2022. Eruption of ultralow-viscosity basanite magma at Cumbre Vieja, La Palma, Canary Islands. *Nature Communications*, 13, 3174, doi: 10.1038/s41467-022-30905-4

Table of contents

List of tables

List of figures

Chapter 1
Introduction

Volcanic eruptions are a major force of nature and have been modifying the surface of our planet ever since the formation of the earth. They are not only one of the greatest natural threats to the human population and infrastructure but may also impact the atmosphere and environment on a local to global scale (Cashman and Sparks, 2013). The profound importance of volcanoes was recently demonstrated by impactful eruptions, such as the 2021 basanite eruption of Cumbre Vieja, La Palma (e.g., Castro and Feisel, 2022; Pankhurst et al., 2022), which caused severe destruction of local infrastructure and agriculture, or the 2022 eruption of Hunga Tonga-Hunga Ha'apai (e.g., Yuen et al., 2022) which sent ash into the stratosphere and initiated a Tsunami in the pacific ocean, causing several fatalities. Due to the potentially devastating impacts of volcanic eruptions, volcanoes have been and still are studied extensively to better understand and ultimately forecast their behavior based on scientific observations, such as for example seismicity, geochemical analyses or eruption history.

1.1 The role of volatiles during volcanic eruptions

Various styles of volcanic eruptions exist, ranging from the effusion of highly fluid lava flows, over the emplacement of lava domes or highly viscous obsidian lava flows, to highly hazardous explosive eruptions (e.g., Cashman and Sparks, 2013). These processes may last for weeks to months, or may be very short-lived. Even though magma viscosity is one of the main controlling factors for the style of volcanic eruptions, examples of highly explosive basaltic eruptions (e.g., Cole 1970) or effusion of highly viscous obsidian lava (e.g., Parejas et al., 2012; Castro et al., 2016) prove that there are other important factors to take into account. A crucial role in all volcanic and magmatic processes is played by the gas species dissolved in magmas. These gas species are referred to as magmatic volatiles due to their tendency to exsolve from the melt across a range of crustal pressures. Volatiles are essential constituents of natural melts and their presence has significant effects on magma properties, such as rheology, density, phase equilibria or bubble content. These properties define how magma moves through the crust; hence, volatiles are another major controlling factor for the style of volcanic eruptions (e.g., Gonnermann and Manga 2007). Typically, volatiles are exsolved during magma ascent at crustal pressures, causing growth of bubbles and by this modification of the melt composition and silicate phase equilibria. Bubble growth in turn accelerates magma ascent and decompression by increasing its buoyancy or magma chamber overpressure ultimately facilitating volcanic eruptions (e.g., Ochs and Lange 1999; Cashman and Sparks 2013). However, the growth of bubbles is a complex process that is affected by many melt parameters. The rates of bubble nucleation and growth depend highly on the

degree of volatile supersaturation and the availability of nucleation sites, as for example the presence of microlite crystals (e.g., Cáceres et al., 2022). The study of volatiles and their complex interplay with other melt parameters is therefore fundamental to understanding volcanic eruptions.

The volatiles dissolved in magmas are typically dominated by H_2O and CO_2, followed by sulfur species (SO_2^{2-}, SO_3) (Edmonds and Wallace, 2017). Even though halogens are usually less abundant, F and Cl can still reach weight percent levels in magmas and Br and I may occur in concentrations up to several 100s of ppm (Aiuppa et al., 2009). The solubility of all volatiles in a given melt composition is mainly controlled by pressure, which — in a volcanic scenario — translates to the depth of the magma in the crust (e.g., Papale et al., 2006). The lower solubility of CO_2 causes it to saturate and exsolve at greater depths compared to H_2O which typically dominates the vapor phase of magma at lower crustal levels (e.g., Edmonds and Wallace 2017). The halogens are typically released at shallower depths (Spilliaert et al., 2006) and may even be retained in the melt during the eruption, being slowly released from a post-eruptive lava flow (Schipper et al., 2019). The monitoring of volatile degassing at volcanic centers therefore bears the potential to help characterize volcanic processes at depth. Before halogens are exsolved from the melt, they may exert strong effects on magma properties which is discussed in detail in the following paragraphs.

1.2 Halogens in magmatic processes

The elemental group of the Halogens comprise the elements of the 17th group of the periodic table. The stable elements include fluorine (F), chlorine (Cl), bromine (Br) and iodine (I). A fifth halogen, astatine (At), is radioactive and highly unstable with a half-life of up to only ~8 h. Therefore, At is not considered any further in the scope of this thesis. The halogens are chemically characterized by one missing electron in their outer p shell. This results in high electronegativity and thus high reactivity which among the halogens decreases with increasing ionic radius (F > Cl > Br > I). Therefore, they are reactive with all metals and most nonmetal elements of the periodic table (e.g., Aiuppa et al., 2009).

The high abundance and low melt solubility of H_2O and CO_2 make them the main drivers for volcanic eruptions (Cashman, 2004). However, the halogens can still affect many fundamental magma properties such as viscosity (e.g., Dingwell and Hess 1998; Zimova and Webb 2007; Baasner et al., 2013b) or phase equilibria (e.g., Filiberto and Treiman 2009; Feisel et al., 2022). Moreover, halogen gases released from volcanoes have been shown to have strong effects on the environment (e.g., Cronin et al., 2003; Flueck and Smith-Flueck 2013) and the atmosphere, for example through the release of reactive Br-species which have the potential to destroy stratospheric ozone (e.g., Bobrowski et al., 2003; von Glasow et al., 2009).

The following characterization represents an overview of the significant halogen properties in the volcanological context of this thesis and is therefore not complete. Thus, for thorough reviews of the role and behavior of halogens in magmatic and volcanogenic processes the reader is referred to the study of Aiuppa et al. (2009), and the in-depth reviews of Dolejš and Zajacz (2018) and Webster et al. (2018). Important halogen properties are also presented in the context of each of the studies associated with this thesis in their respective chapters (4, 5 and 6).

1.2.1 Fluorine

Natural abundances of F span a range from several ppms up to ~7 wt%, of which high concentrations are typically associated with evolved rhyolitic melts. Abundances in basaltic melts are commonly not more than 1000s of ppms (e.g., Aiuppa et al., 2009). Due to its ionic radius being similar to that of oxygen, F is known to substitute for hydroxyl and bridging oxygens in silicate melts and phases (e.g., Mysen and Virgo 1985; Dolejš and Zajacz 2018 and references therein) and was shown to strongly influence phase equilibria, for example by reducing olivine stability relative to pyroxene or stabilizing F-bearing minerals such as amphibole or phlogopite (e.g., Foley et al., 1986a, 1986b; Johnson and Fegley 2003; Dolejš and Baker 2007b, 2007a; Filiberto et al., 2012). Early studies demonstrated that F is similarly effective in reducing melt viscosities as H_2O and that the effects of the two may be additive or even more effective when combined, compared to their individual effects (Dingwell et al., 1985; Dingwell, 1987; Dingwell and Hess, 1998). These observations were further characterized, for example, by showing that F's viscosity reducing effects strongly depend on the melt composition (Giordano et al., 2004; Giordano et al., 2008; Baasner et al., 2013a, 2013b). Along with early studies on the effect of F on liquidus temperatures (Manning, 1981), Filiberto et al. (2012) demonstrated that the addition of F to a basaltic melt significantly decreased the melt's liquidus and at the same time caused crystallization of Fe-rich olivine, suggesting preferred complexing of F with MgO in the melt. Similarly, chapter 6 of this thesis demonstrates the even stronger liquidus-depressing effect of the addition of F (and Cl) to a trachyte melt (Feisel et al., 2022).

F was shown to be highly soluble in silicate melt (e.g., Carroll and Webster 1994; Dolejš and Baker 2007) and F dissolution is much less pressure dependent than that of H_2O, which typically leads to late F degassing of an ascending melt and relatively high F abundances at shallow crustal levels or in lava flows and domes (e.g., Schipper et al., 2019). F solubility typically correlates with increasing peralkalinity (molar [Na+K+Ca] / [Al] > 1) or increasing abundance of network modifying cations such as Ca and Mg (e.g., Foley et al., 1986; Mysen et al., 2004; Brey et al., 2009). For peraluminous melts, F solubility increases with increasing excess network-modifying Al (e.g., Mysen and Virgo 1985). Spectroscopic studies on the behavior of F in different simplified and natural melts show that F

coordinates with Al, Na and Ca and may form Si-F and Al-F bonds (e.g., Zeng and Stebbins 2000; Mysen et al., 2004; Karpukhina et al., 2007).

1.2.2 Chlorine

Natural chlorine concentrations in silicate melts are generally lower than those of F, typically being less than 1000 ppm in basalt (Webster et al., 2018). However, especially in high-silica peralkaline magmas, Cl may reach higher concentrations of up to 1.2 wt.% (Aiuppa et al., 2009), also seen in some few cases of basalts (e.g., Coombs et al., 2004). At these high concentrations, Cl may exert significant effects on melt properties such as viscosity or phase equilibria. Most studies report a decrease of the solidus temperature by Cl enrichment (e.g., Wyllie and Tuttle 1964). Recent studies on the effects of Cl on liquidus relations in basaltic melts revealed a significant composition-dependent depression of the isobaric liquidus, defined by a shift of olivine or pyroxene crystallization temperatures and pressures (Filiberto and Treiman, 2009; Filiberto et al., 2014; Farcy et al., 2016). The same authors also showed the influence of Cl on the olivine/liquid and pigeonite/liquid exchange partition coefficients ($K_D^{Fe/Mg}$). Significant depression of liquidus temperatures were also demonstrated for trachyte melt during a study conducted in the scope of this thesis (chapter 6; Feisel et al., 2022). Bell and Webster (2015) demonstrated the profound effect of Cl on the $Fe^{3+}/\sum Fe$ ratio, for example, leading to increased magnetite solubility with increasing Cl concentration. The influence of Cl on viscosity is less understood and generally smaller than that of F. The available studies indicate both, increased and decreased melt viscosity upon the addition of Cl, depending strongly on the melt composition and temperature (e.g., Hirayama and Camp 1969; Dingwell and Hess 1998; Baasner et al., 2013a, 2013b; Webb et al. 2014). For example, Zimova and Webb (2006) demonstrated that Cl addition generally increased the viscosities of peralkaline but decreased those of peraluminous melts, which is opposite to what Zimova and Webb (2007) found by adding both, F and Cl to the same melts. The larger ionic radius of Cl prevents it from substituting for hydroxyl groups in silicate systems and restricts its position to interstitial or network modifier sites (Dolejš and Zajacz, 2018). Therefore, Cl dissolution is strongly dependent on melt composition and has been shown to be particularly correlated with the availability of network-modifying cations such as, for example, Fe, Mg, Ca, or Na and also with F contents (e.g., Thomas and Wood 2021). Evidence for this behavior was found by spectroscopy-based analyses indicating preferred complexing of Cl with Mg, Fe, and Ca (Zimova and Webb, 2006; Evans et al., 2008; Webb et al., 2014). In general, Cl dissolution increases with increasing temperature, however, the influence of pressure on dissolution is complex and varies with the fluid phase assemblage (e.g., Botcharnikov et al., 2015; Webster et al., 2015).

1.2.3 Bromine and iodine

Bromine and iodine abundances in natural silicate melts are by far lower than F and Cl for corresponding volcanic environments. Concentrations range from less than one up to few 100's of ppms in matrix glass and melt inclusions (e.g., Bureau and Métrich 2003) while Br concentrations are typically an order of magnitude higher than those of I (Aiuppa et al., 2009; Webster et al., 2018). Moreover, Bureau et al. (2000) showed that the fluid-melt partition coefficients of Cl, Br and I increase linearly with increasing ionic radius ($D_{Cl} < D_{Br} < D_I$) at 900 °C and 200 MPa. Studies of Bureau and colleagues indicate a general trend of increasing Br dissolution in melts of decreasing SiO_2 content, however, the influence of other variables such as pressure, temperature and compositional parameters is complex and still poorly understood (Bureau et al., 2000; Bureau and Métrich, 2003; Bureau et al., 2010). One of the few studies on I properties in silicate melt was carried out by Musselwhite and Drake (2000) who investigated I solubility in a synthetic basalt.

1.3 Theoretical background of diffusion

Diffusion describes the random motion of atomic-scale particles in various media such as minerals, glasses, melts, gases or fluids and is directly correlated with temperature (Zhang, 2010). Even though diffusion is typically considered to take place due to the presence of concentration gradients of the diffusing particles, thermally activated particle motion is naturally always occurring if $T > T_0$, even in a medium which is already equilibrated with respect to the diffusing components. Diffusion processes are generally subdivided into three main categories: 1) self diffusion, 2) tracer diffusion, and 3) chemical diffusion, which are all briefly discussed in the following paragraphs. This discussion of the fundamentals of diffusion represents a brief overview of the topic, focusing on the processes relevant for the scope of this thesis. For a thorough review of the fundamental theory of diffusion, the reader is referred to the review of Zhang (2010).

1.3.1 Types of diffusion

Self diffusion describes the random movement of particles in a medium without an elemental chemical gradient. It can be detected by measuring different stable isotopes of the diffusant. As this type of diffusion happens in absence of a chemical potential it is considered to be constant for the given systems. Even though slightly different diffusivities among different isotopes of the same element may cause some diffusive fractionation, the process is negligible for quantifying self diffusion (typically <<1 % difference; e.g., Zhang, 2010; Fortin et al., 2017). An example of a geologically relevant process is the self diffusion of oxygen in silicate melts which is closely related to anhydrous melt viscosity (Shimizu and Kushiro, 1984; Dingwell, 1990; Zhang and Ni, 2010). This topic is discussed in chapters 4 and 5 in the light of defining a lower limit of halogen diffusion in anhydrous silicate melt.

In the case of *tracer diffusion*, low concentrations of an easily detectable element — i.e., the tracer — are introduced into a diffusion medium without affecting its bulk composition. A radioactive isotope is often used as tracer as it can be detected without having to introduce a chemical gradient. The absence of a chemical potential implies that tracer diffusion is independent of the tracer concentration, similar to the case of self diffusion and this is true for most species; however, a notable exception is H_2O. Tracer diffusion can also be considered self diffusion in the case when a radioactive tracer is introduced into a medium that contains stable isotopes of the tracer material.

During *chemical diffusion*, a chemical potential gradient of the diffusing component is present in the diffusion medium. The gradient may be present for either major or minor components. Definitions of chemical diffusion include different processes such as trace element diffusion (e.g., Baker, 1989), binary diffusion (e.g., Fe-Mg exchange in olivine), multispecies diffusion (e.g., diffusion of water in the form of either H_2O_m or OH^-), multicomponent diffusion (simultaneous diffusion of several components) and effective binary diffusion (Zhang, 2010). The majority of natural melts are indeed multicomponent systems involving three or more diffusing components. However, due to the mathematical complexity of multicomponent diffusion, the process is often simplified and treated as effective binary diffusion (EBD; Cooper, 1968). In the case of EBD, diffusion is treated as if there were only two components: the diffusant which can vary independently and the diffusion medium (e.g., multicomponent silicate melt) treated as one combined component. This case is also applied for characterizing halogen diffusion in this thesis.

1.3.2 Mathematical approaches to describing diffusion

The principle equation describing how the concentration relates to space and time by virtue of one-dimensional diffusion is given by Fick's second law:

$$\frac{\partial C}{\partial t} = D \frac{\partial^2 C}{\partial x^2} \tag{1.1}$$

Where D is the diffusion coefficient and is independent of C and x, which denote the concentration and space dimension, respectively. Using equation 1.1, diffusion is typically considered to occur in an isotropic medium, but may also occur in an anisotropic medium along a principal axis. However, in the scope of this thesis, diffusion is always considered to occur in an isotropic medium (silicate melt).

Geologically relevant diffusion processes that are commonly investigated to derive diffusion coefficients for chemical diffusion of one component in a diffusion medium include for example sorption or desorption and the diffusion couple or triple. Even though several other geologically relevant processes exist (e.g., crystal dissolution, crystal homogenization), the following paragraphs will focus

on sorption and diffusion couple processes as these are typically applied in the form of experiments to derive volatile diffusion parameters.

Sorption or desorption of solids, gases or fluids to or from a mineral or glass are processes often encountered in nature. During sorption or desorption, the concentration of the diffusant outside the diffusion medium will not deplete or enrich during diffusion — it is considered an infinite source or sink. The concentration in the diffusion medium is considered semi-infinite, hence, the concentration at the far end stays constant over the time of diffusion. The concentration profile produced by the sorption or desorption process can be described by the following equation (Crank, 1975; Zhang, 2010):

$$C(x,t) = C_s + (C_i - C_s)\,\mathrm{erf}\left(\frac{x}{\sqrt{4\,D\,t}}\right) \tag{1.2}$$

Where C is the concentration at distance x from the surface of the medium after time t. C_s describes the surface concentration at the boundary to the medium and C_i is the initial concentration in the medium. The term *erf* describes the error function. The diffusion coefficient D can be obtained from fitting the equation to measured concentration profiles. An ideal diffusion profile calculated by equation 1.2 for different times is illustrated in figure 1.1a. A natural example of a sorption process is the uptake of atmospheric H_2O into initially anhydrous glassy fulgurites which was investigated to calculate the time of fulgurite formation based on known H_2O diffusion coefficients (Castro et al., 2020). Sorption experiments are also often applied to obtain effective binary diffusivities of volatile components in melts and are used in several studies discussed in this thesis (e.g., Dingwell and Scarfe, 1985; Yoshimura, 2018).

The diffusive growth of bubbles in a magma can be viewed as a desorption problem in which the volatile concentration in the magma is depleted by loss of volatiles to the bubble, leaving a diffusion profile in the melt around the bubble (e.g., Watson, 2017). However, in nature, bubbles typically rise within the magma after formation and during growth. The relative movement through the magma enhances mass transport due to advection into the bubbles compared to that induced by diffusion alone. Therefore, in elaborate mathematical bubble growth models, the convective component must be included to achieve realistic results and these models are typically referred to as convective bubble growth (e.g., Zhang and Xu, 2008; Zhang, 2010). During convective bubble growth, the diffusion domain around the bubble (boundary layer) is affected and deformed by motion relative to the surroundings. This may result in a narrow boundary layer on the leading and a wider boundary layer on the trailing side, which is typically simplified by using an average boundary layer thickness in mathematical models (e.g., Zhang and Xu, 2003). For further discussions of mathematical solutions to convective bubble growth, the reader is referred to the studies of Zhang and Xu (2003) and Zhang and Xu (2008). These solutions have been

widely applied in various studies of bubble growth and diffusive fractionation (e.g., Fortin et al., 2017; Watson, 2017).

The diffusion couple is often employed in experimental studies to determine effective binary diffusion of various components in minerals or melts. Assuming the halves of the diffusion couple are isotropic and semi-infinite with respect to the diffusant concentration, the one-dimensional concentration profile caused by the diffusion process can be described using the following equation:

$$C(x,t) = \frac{C_{high} + C_{low}}{2} + \frac{C_{high} - C_{low}}{2} \operatorname{erf}\left(\frac{x - x_0}{\sqrt{4\,D\,t}}\right) \tag{1.3}$$

Here, C is the resulting concentration at distance x after time t. C_{high} and C_{low} denote the high and low endmember concentrations, respectively. The term x_0 describes the position of the diffusion interface, i.e., the interface of the different diffusion couple halves. Initially x_0 is usually unknown and is determined during fitting. However, the value does not have much meaning but is allowed to vary to optimize the fitting. The diffusion coefficient D is also determined by fitting of equation 1.3 to concentration vs. distance data obtained from diffusion processes. The diffusion triple is based on the same concept as the diffusion couple but uses three different media stacked together, basically making two diffusion couples in one package. An idealized diffusion couple profile calculated for different times (t1<t2<t3) using equation 1.3 is shown in Figure 1.1b. Diffusion couples are an idealized model of a binary diffusion problem and processes like convection make them rare in nature. However, diffusion between two differently composed layers of a crystal or between two layers of melt may be viewed as a diffusion couple problem. Most of the halogen diffusion studies discussed in this thesis derive diffusivity values from basic diffusion couple experiments, as was also the case for the experimental studies of chapters 4, 5 and 6. Even though multiple halogen atoms were present during the experimental runs of these studies, the diffusion processes were considered as effective binary diffusion to simplify the mathematical data evaluation (Zhang, 2010). Consequently, equation 1.3 was used to derive diffusion coefficients of all experimentally obtained diffusion profiles in this thesis and is therefore introduced again in each individually published or submitted chapter.

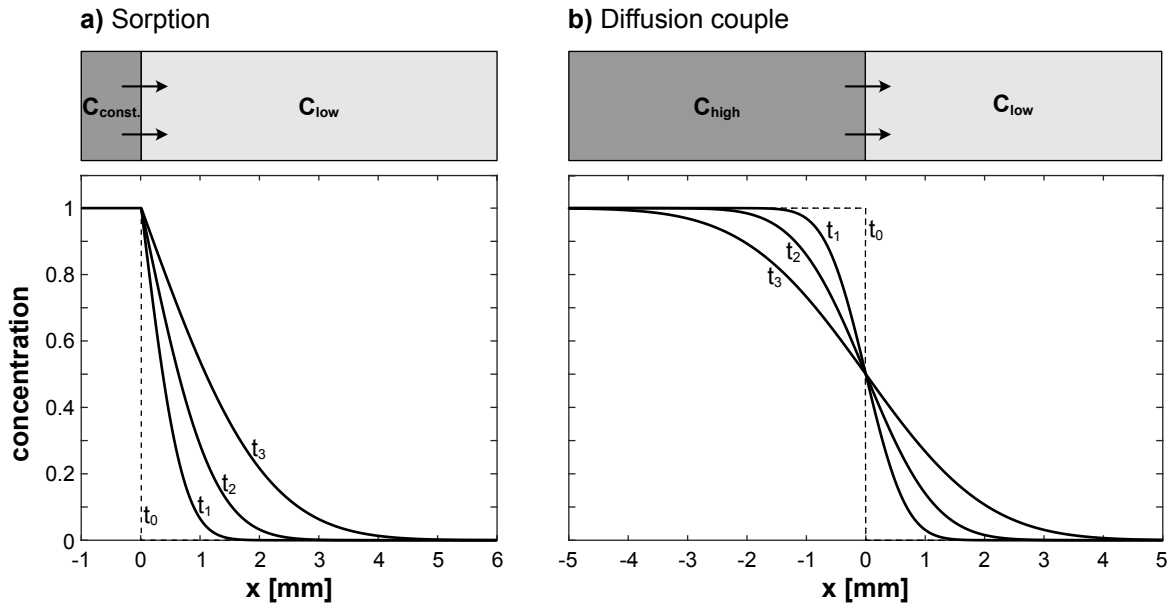

Figure 1.1: Ideal diffusion profiles calculated using equation 1.2 for **a)** sorption, and equation 1.3 for **b)** the diffusion couple. During sorption the concentration outside of the diffusion medium (negative x-values) is constant. In the diffusion couple case, C_{high} is progressively depleted during diffusion. The profiles were calculated for a typical magmatic F diffusion coefficient (in dry melt at ~1000 °C) of 5x10-12 m^2 sec^{-1}. The dashed line labelled t_0 represents the initial concentration profile, mimicking the shape of a step function at the diffusion interface. t_1 = 6 h, t_2 = 24 h, t_3 = 72h

The cases of diffusion described above are typically valid for constant diffusivity at the given conditions (e.g., composition, temperature, pressure). However, it has to be noted that diffusivity may be variable along a diffusion profile. This can be the case when the major element composition of the diffusion medium changes significantly along the diffusion direction, though this case would not represent effective binary diffusion. Another possibility is that the diffusivity of a component is dependent on its own concentration in the medium. A prominent example is the diffusivity of H_2O in silicate melt which is positively correlated with H_2O concentration, typically leading to unsymmetric diffusion profiles. Therefore, empirical H_2O diffusion equations are commonly derived experimentally for certain melt compositions (e.g., Zhang and Stolper, 1991; Behrens et al., 2004; Behrens and Zhang, 2009). The case of concentration dependent diffusion is included for completeness; however, as halogen diffusion was shown to be concentration independent (Baker and Balcone-Boissard, 2009), it will not be discussed any further in the scope of this thesis.

1.4 Halogen diffusion in silicate melts – current state of knowledge

Chemical diffusion is an important transport mechanisms in silicate melts and diffusion rates have effects on many volcanological processes such crystal growth or the composition of melt inclusions and bubbles (e.g., Baker et al., 2005; Watson, 2017). However, diffusion of volatiles in silicate melt is slow which limits the spatial extent to which it can operate (e.g., Zhang and Ni 2010). Many processes that

are important for the eruptive behavior of volcanoes operate on local scales but have nonetheless effects on the whole magma body. The growth of bubbles for example is controlled by many processes such as decompression of the ascending magma and diffusion of volatiles from the melt into the bubbles (e.g., Sparks et al., 1994; Gonnermann and Manga, 2007). If bubbles grow fast, diffusive transport of volatiles into the bubbles is limited by the volatile's respective diffusive properties and may lead to an enrichment of slower diffusing species in the melt and their depletion in the gas bubble — a process called diffusive fractionation. Halogens typically diffuse at much slower speeds compared to the main bubble forming volatiles H_2O and CO_2. This means halogens are not contributing to the growth of bubbles while still affecting the composition, which is why they are referred to as "passive volatiles" in the context of bubble growth (Watson, 2017). Diffusive fractionation among the different halogens may be an important process occurring during degassing of volcanic centers (e.g., Baker and Balcone-Boissard 2009).

Due to the increasing interest in halogen behavior during magmatic processes, also their chemical diffusion characteristics have been increasingly studied in recent years. All studies presenting experimentally determined halogen diffusion data in silicate melts demonstrate that halogen diffusion is concentration independent and displays Arrhenian behavior, which can be described by the Arrhenius equation:

$$D = D_0 \, e^{-\frac{E_A}{R\,T}} \tag{1.4}$$

where D is the diffusion coefficient ($m^2\ s^{-1}$) at temperature T (K). E_A denotes the activation energy (J mol^{-1}) and represents the slope in an Arrhenius diagram, and D_0 is the pre-exponential factor ($m^2 s^{-1}$). R is the universal gas constant (8.3143 J mol^{-1} K^{-1}). Even though numerous studies are available on the diffusivity of F and Cl, only few exist on the diffusion behavior of Br and to date no study on iodine diffusion in silicate melt is available. All studies that investigated halogen diffusion in silicate melts until the submission of this thesis are presented below (except the studies published in the scope of this thesis). Figures 1.2–1.4 show the respective Arrhenius relations of F, Cl and Br, illustrating the diffusion characteristics determined in these studies.

1.4.1 Fluorine

Dingwell and Scarfe (1984, 1985) were the first to experimentally investigate F diffusion in geologically relevant melts. They performed high temperature experiments at 1 atm using simplified melts and showed that F diffusion is fastest in jadeitic and slowest in albitic melts. In another set of experiments they employed the diffusion couple technique on the jadeitic melt under pressurized conditions of 1.0–1.5 GPa and found ~1 order of magnitude higher diffusivities compared to the previous case. They

attributed this discrepancy to a possible weak pressure dependence, systematic differences due to the different experimental approach or to a slight water enrichment at pressurized conditions.

Fluorine diffusion was also investigated by Gabitov et al. (2005) who dissolved fluorite crystals in haplogranitic melt containing 1–3.5 wt.% H_2O at 900–1000 °C and 100 MPa. They demonstrated enhanced diffusivity of F compared to the findings of Dingwell and Scarfe (1984, 1985) which is explained by the presence of water in the employed melt. As Gabitov et al. (2005) studied F and Ca diffusion simultaneously, there were significant major element gradients present in their diffusion experiments (0–8 wt.% Ca). The diffusion of F is therefore not considered to represent effective binary diffusion. Consequently, the data of Gabitov et al. (2005) were not included in the F diffusion overview (Fig. 1.2)

Alletti et al. (2007) performed diffusion couple experiments using basaltic melt over the temperature range 1250–1450 °C and found D_F values in the range of 10^{-11} to 10^{-10} m^2s^{-1} which is comparable to the case of jadeitic melt. Addition of water increased D_F by a factor of ~2. Experiments at different pressures did not reveal a significant pressure dependence of F diffusion.

Balcone-Boissard et al. (2009) also employed the diffusion couple technique to investigate halogen diffusion in two different phonolitic melts. They showed that anhydrous K-rich phonolite comprises slightly lower F diffusivities and higher activation energies than anhydrous Na-rich phonolite. Values of D_F were on the order of 10^{-10} m^2s^{-1} for both melt compositions. The addition of up to 5 wt.% of H_2O weakly increased F diffusivities and resulted in similar diffusivities in both melts.

Another phonolitic melt composition was investigated by Böhm and Schmidt (2013) who employed the diffusion couple technique in the temperature range 800–1200 °C and for both anhydrous and hydrous (2.1 and 2.4 wt.% H_2O) melt compositions. The diffusivities determined in their study are on the same order of magnitude like those of Balcone-Boissard et al. (2009) but display lower activation energies. They attribute this discrepancy to slightly different experimental approaches and compositional differences. A weak pressure dependence is also described as a feasible explanation.

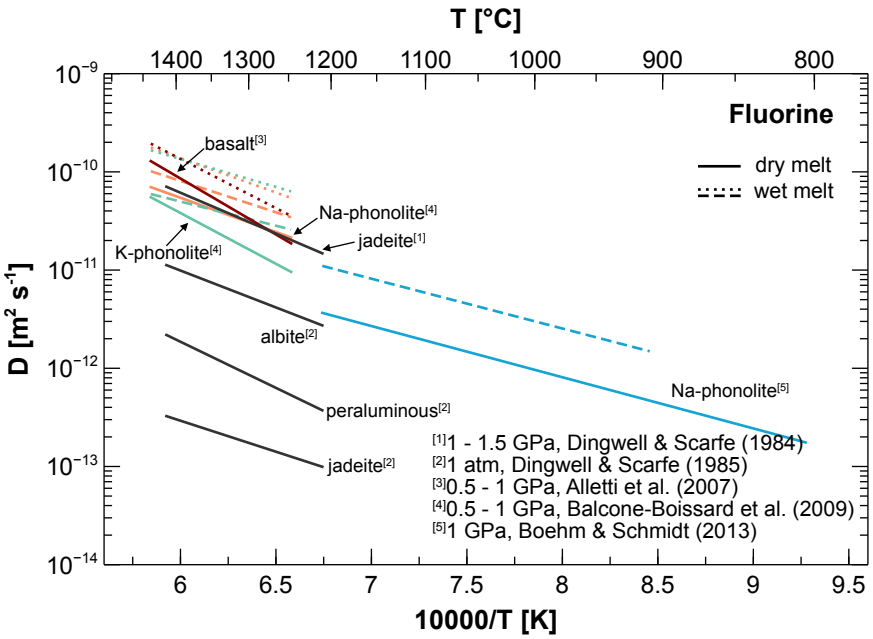

Figure 1.2: Compilation of the results of all F diffusion studies published until the submission of this thesis. A mismatch between the published Arrhenius parameters and the experimental diffusivities of dry K- and Na-Phonolite (Balcone-Boissard et al., 2009) was recognized during data plotting. Therefore, the respective Arrhenius parameters were re-calculated based on the published diffusivities at the experimental temperatures and these results were used for this diagram.

1.4.2 Chlorine

Chlorine diffusion was first investigated by Watson and Bender (1980) who studied tracer diffusion in a simplified anhydrous silicate melt composition over the temperature range 1100–1300 °C. They determined an activation energy of ~207 kJ mol^{-1} and D_0 of $3.4x10^{-4}$ m^2s^{-1}. In further studies Watson (1991) investigated natural rhyolitic and dacitic melt and determined diffusivities on the order of 10^{-12} to 10^{-11} m^2s^{-1} over the temperature range 850–1100 °C.

Bai and Koster van Groos (1994) studied Cl diffusion in haplogranitic melt and a natural obsidian by reacting spheres of the starting material with either pure NaCl or NaCl-fluid. They determined diffusivities over the temperature range 650–1400 °C and found that the addition of H_2O significantly increased diffusion. In contrast to the findings of Watson and Bender (1980) they observed a weak pressure dependence of Cl diffusion.

The study of Alletti et al. (2007) also investigated Cl diffusion in the same basaltic melt. They found that D_{Cl} was only slightly lower than D_F at lower temperatures due to its higher activation energy. Values of E_A were generally larger than those determined for granitic compositions by Bai and Koster van Groos (1994) but similar to those determined for haplobasaltic melt (Watson and Bender, 1980). The addition of water to the melt increased D_{Cl} by a factor of ~2.

The two phonolitic melt compositions studied by Balcone-Boissard et al. (2009) were also investigated for Cl diffusion applying the same conditions like those used for F. Cl diffusivities in the different melt compositions were very similar to each other and both exhibited an increase upon the addition of water. Indeed, the increase in diffusivity was stronger than that previously observed for F.

Böhm and Schmidt (2013) also studied Cl diffusion in the phonolitic melt and found that Cl diffuses slower in anhydrous melt compared to F, showing similar activation energies to those determined by Balcone-Boissard et al. (2009). While Cl diffusion is enhanced by almost one order of magnitude due to the addition of 2.4 wt.% water, the diffusivity of F is only weakly increased.

Fortin et al. (2017) studied the diffusion of two Cl isotopes (^{35}Cl and ^{37}Cl) in dacite melt over the temperature range 1200–1350 °C. For these temperatures they found diffusivities on the order of 10^{-12} m^2s^{-1} and determined an activation energy of ~155 kJ mol^{-1}, which is somewhat lower than those determined for phonolitic melt compositions. A weak mass effect during the diffusion of both isotopes was determined and is reported to favor ^{35}Cl over ^{37}Cl by a factor of $^{37}Cl/^{35}Cl \sim 0.995$.

Yoshimura (2018) investigated Cl diffusion by reacting rhyolitic obsidian with various chlorine sources. Diffusivities were relatively low due to the low temperatures investigated (650–950 °C), however, fitted activation energies were similar to previous studies on mafic compositions (135–202 kJ mol^{-1}). The addition of up to 1.2 wt.% water enhanced diffusivity of Cl by up to two orders of magnitude.

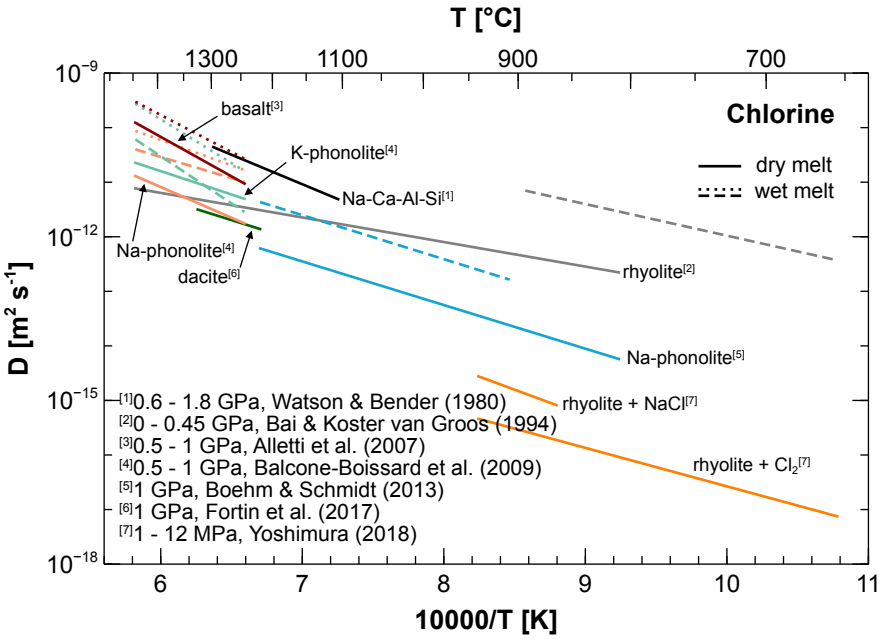

Figure 1.3: Compilation of the results of all Cl diffusion studies published until submission of this thesis.

1.4.3 Bromine and iodine

The study of Alletti et al. (2007) was the first to also investigate Br diffusion in a geologically relevant melt composition. Br diffusion was found to yield slightly lower diffusivities than F and Cl in anhydrous basalt with D_{Br} on the order of $1x10^{-11}$ m^2 sec^{-1} at 1250–1450 °C.

Balcone-Boissard et al. (2020) expanded on their 2009 study and investigated Br diffusion in the same phonolitic melt compositions over the temperature range 1250–1450 °C and at hydrous (~2.7 wt.% H_2O) and anhydrous conditions. They found Br diffusion to be dependent on the dominant alkali in the melt and showed that diffusivity is only weakly enhanced by the addition of H_2O. Overall, Br diffusivities were only slightly lower than those of Cl.

Until the submission of this thesis no iodine diffusion data in silicate melt — except those acquired during the PhD project — was available from the literature.

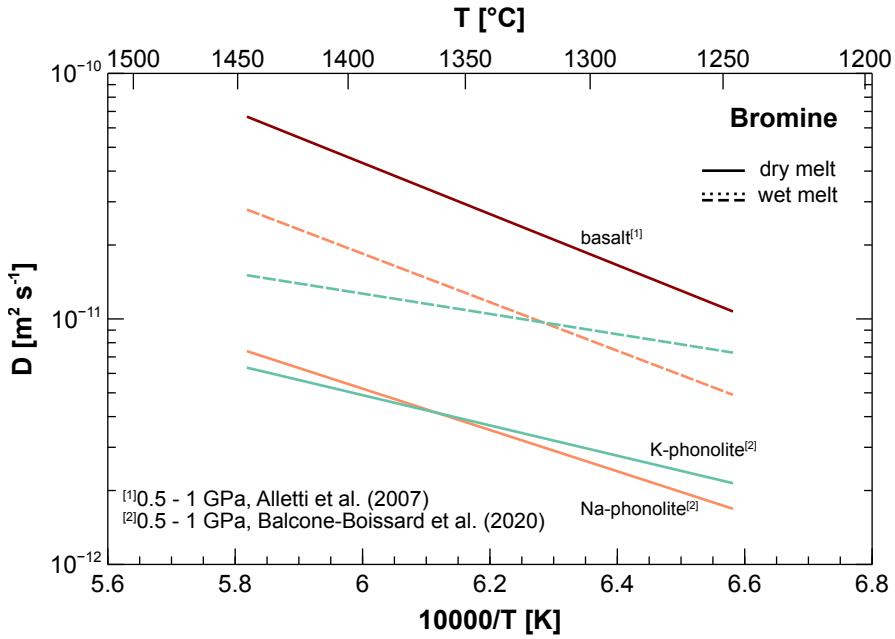

Figure 1.4: Compilation of the results of the only two Br diffusion studies available in the literature.

1.5 Thesis outline

This thesis aims to expand the knowledge of halogen diffusion and to provide a consistent and complete characterization of the diffusivity of all halogens including F, Cl, Br and I in evolved natural silicate melts. In doing so, this thesis fills a significant gap in the magmatic halogen diffusion database. Additionally, it includes results showing how the diffusion of halogens can have effects on physical melt properties such as crystallinity and by this, may affect volcanic processes at shallow crustal levels.

Chapter 2 describes the methodology used for the experimental studies presented herein, including sample synthesis and the different experimental approaches.

Chapter 3 introduces the different analytical techniques that were used to characterize the experimental products of the different studies.

Chapter 4 of this thesis is published as Feisel et al. (2019) and presents results of F and Cl diffusion in anhydrous rhyodacitic melt over a temperature range of 750–950 °C and at atmospheric pressures. It is shown that F and Cl diffusion is slower in the silicic melt compared to intermediate or basaltic melts and that diffusivity in this melt is inversely correlated with the ionic radius of the diffusing halogen.

Chapter 5 presents experimental results of halogen diffusion of all halogens in anhydrous and hydrous trachytic melt. It is shown that halogen diffusion in anhydrous trachyte melt is highly dependent on the ionic radius of the halogens, which implies that the diffusion mechanism relies strongly on the structure of the melt. The addition of water increases diffusivity of all halogens, however, the increase is most pronounced for large ionic radii. This study highly expands the findings of chapter 4 and is a significant addition to the halogen diffusion database. This study was submitted for publication with *Geochimica et Cosmochimica Acta* and is currently under review (August 2022).

Chapter 6 demonstrates the strong influence of the halogens F and Cl on the liquidus temperature of a hydrous trachyte melt and is published as Feisel et al. (2022). The study illustrates how the diffusion of F and Cl into a halogen depleted melt leads to dissolution of formerly formed clinopyroxene spherulites by complexation of F and Cl with the main elements of clinopyroxene, Fe, Mg and Ca. In doing so, the presence of halogens depresses the liquidus temperature of the melt, which has implication for several volcanic processes.

Chapter 7 concludes the main results and findings of this thesis and describes their implications in the context of magmatic processes. Furthermore, this chapter provides an outlook for future scientific questions that arose from the results of this thesis.

1.6 Author contributions

Chapter 4: Diffusion of F and Cl in dry rhyodacitic melt. – *Feisel, Y, Castro, J.M., Dingwell, D.B. (2019):* YF developed the experimental approach and conducted the experiments. He carried out all sample preparation and analyses, processed and interpreted the data and wrote the manuscript. JMC and DBD both contributed to the development of the experimental approach, helped with data interpretation and reviewed and edited the manuscript. DBD acquired project funding.

Chapter 5: Diffusion of halogens (F, Cl, Br, I) in silicic melt. – *Feisel, Y., Castro, J.M., Helo, C., Bouvier, A.-S., Ludwig, T., Dingwell, D.B. (under review):* YF developed the experimental approaches, conducted all experiments, carried out sample preparation and EMPA analyses, processed and interpreted the data and wrote the manuscript. JMC and CH both contributed to the experimental methodology, helped with the conduction of experiments and were involved in data interpretation. ASB and TL carried out SIMS analyses and helped with data interpretation. DBD helped with data interpretation and provided project funding. All authors reviewed and edited the manuscript.

Chapter 6: The effect of halogens (F, Cl) on the near-liquidus crystallinity of a hydrous trachyte melt. – *Feisel, Y., Castro, J.M., Helo, C., Dingwell, D.B. (2022):* YF developed the experimental methods, conducted the experiments, carried out sample preparation and analyses, interpretated the data and wrote the manuscript. JMC contributed to the experimental methodology and helped with FTIR analyses and data interpretation. CH contributed to the experimental methodology and helped with Raman analyses and data interpretation. DBD helped with data interpretation and provided project funding. All authors reviewed and edited the manuscript.

1.7 Software

The thesis was created using *Microsoft Word for Mac* (ver. 16.62). Diagrams were prepared using either *Matlab 2017a* or *Veuzs* (ver. 3.3.1). Figures were created with *Affinity Designer* (ver. 1.10.5) or *Adobe Illustrator CS6*. Other software used is mentioned in the respective chapters.

Chapter 2
Experimental Methods

2.1 Starting glass synthesis

2.1.1 Pre-synthesis

To assure homogeneity of the starting materials, which is a requirement for successful diffusion couple experiments, samples of natural volcanic rocks were synthesized and homogenized at high temperature to produce crystal and bubble free glasses to be used for experiments. Two different natural samples of rhyodacitic to rhyolitic composition were used to synthesize starting material. The first batch of sample material was synthesized from rhyodacitic pumice of the Hekla H3 eruption (e.g., Thordarson and Larsen 2007; Weber and Castro 2017). This material was used for the studies of Feisel et al. (2019) and Feisel et al. (*under review*) (chapters 4 and 5, respectively). The second batch was synthesized from a large piece of obsidian lava from the 2011–2012 Cordón Caulle eruption, of the Puyehue-Cordón Caulle volcanic complex, Chile (e.g., Singer et al., 2008; Parejas et al., 2012; Castro et al., 2013, 2016). The major element composition of this sample is very similar to that of the Hekla sample (rhyodacitic-rhyolitic) which was one of the reasons why it was chosen. Additionally, both samples were chosen due to the good knowledge of the petrological and compositional properties based on several studies from the volcanology group in Mainz (Castro et al., 2013; Weber and Castro, 2017) and thus the availability of large amounts of well characterized sample material ensured that several homogeneous synthesis batches could be made.

As the synthesis approach was generally similar for all the different batches, the procedure explained in the following paragraphs is considered representative for all samples. The sample synthesis of the Hekla and Cordón Caulle glasses was carried out in the laboratories of the Earth Science department of the LMU, Munich. In a first step the respective hand samples were crushed with a mortar or a jaw breaker to achieve pieces of sizes < 1.5 cm. These were successively molten in a Pt-crucible (ca. 250 ml) at temperatures up to 1400 °C using a *Nabertherm* muffle furnace. The melting involved adding few pieces (~1–2 spoons) of material every 15–30 minutes after making sure all material in the crucible was completely molten and initially formed bubbles were mostly degassed (Fig. 2.1a & b). This way it was possible to fill the crucible almost completely to produce as large of a batch as possible. The samples were pre-synthesized by this procedure within the course of about half a day.

The next pre-synthesis step for all the samples involved stirring of the melt at high temperatures (1450–1550 °C) using a platinum-rhodium (Pt-Rd) rod attached to a rheometer. This procedure was employed in order to intensify the degassing process of the melt and ensure thorough mixing and homogenization. The rod was centered and inserted as deep into the melt as possible without touching the bottom of the crucible. Stirring was done by the axial rotation of the rod. The rotation speeds were set to values between 10 and 40 rpm (rotations per minute) and adjusted according to the viscosity and the torque that the melt exerted on the rod. As the rheometers used were not calibrated quantitively with the stirring setup used, only the torque reading was monitored. The reading changed over time as a reaction to the change in melt viscosity due to dissolution of volatiles and the formation and loss of bubbles. Typically, the torque decreased during the first hour of the stirring process and slowly increased afterwards until reaching a steady plateau, i.e., reaching a state where the torque did not change significantly over several hours. This was interpreted to represent the bulk loss of volatiles. The melt was constantly stirred and left in the furnace for durations of 2–7 days depending on the torque behavior.

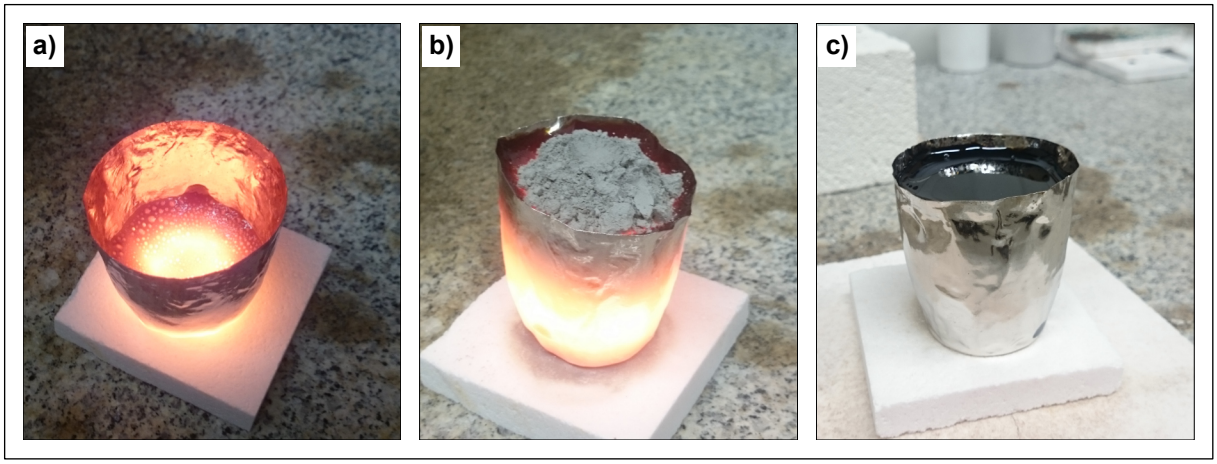

Figure 2.1: Examples of the successive melting and homogenization of volcanic samples in the laboratories of LMU, Munich. **a)** The first molten batch of Córdon Caulle material. The degassing of the melt is apparent in the open bubbles preserved in the fast cooling crust on the melt surface. **b)** Successive filling of the crucible with powdered obsidian lava. **c)** Cooled and homogenized glass made from Hekla tephra after high-temperature stirring for several days.

The early decrease in torque was attributed to the formation of bubbles with capillary numbers of $Ca > 1$, where Ca is a measure of the ratio between the surface tension of a bubble and the viscous stresses that act to deform it (Stein and Spera, 1992).

$$Ca = \frac{\mu G a}{\gamma} \tag{2.1}$$

The surface tension is represented by γ while μ is the viscosity of the suspending fluid. G is the shear rate and a the undeformed bubble radius. In the case of $Ca > 1$, the shear stresses overcome the surface

tension of the bubble and deform it in the direction of shear. For high values of *Ca* the viscosity of the bubble-melt suspension can be lowered due to the *shear thinning* effect of elongated bubbles (Manga et al., 1998). In the case of low capillary numbers, the surface tension of the bubbles is large enough to preserve their spherical shape which may contribute great shear stress to the suspension, further depending on the bubble volume fraction (Φ). In the synthesis experiments of this thesis, the observed initial torque decrease was likely caused by a large volume fraction of bubbles that were elongated during stirring, which resulted in high-*Ca shear thinning* behavior of the bubble-melt suspension. In the course of the synthesis, bubbles ascended to the melt surface and progressively left the melt which is likely to have caused the observed progressive torque (~viscosity) increase.

At the end of the synthesis, the rod was slowly pulled out of the melt and the crucible was removed from the furnace to be left for cooling at room temperature (Fig. 2.1c). The cooled glass was successively removed from the crucible by (1) using a large diamond drill bit to weaken the coherence of the glass in the crucible and (2) using a softhead hammer to lightly tap the crucible walls to promote pieces of glass to come lose which could then be removed carefully using a small flat-head screwdriver. Afterwards, the recovered glass was ground to fine powder (<< 1 mm) and the crucible was cleaned in hydrofluoric acid (HF).

2.1.2 Synthesis of halogen and sodium enriched glasses

The ground powders were each split in half to make one halogen-bearing and one halogen-depleted glass of each starting composition. The enriched mixtures were prepared by adding halogen-bearing sodium-salts (NaF, NaCl, NaBr, NaI) so that each halogen would account for 1 wt.% in the resulting glass, assuming no losses during the synthesis process. For the halogen-depleted batch Na_2CO_3 was added to account for and balance the Na-enrichment in the halogen-bearing glass, due to the use of Na-salts as dopants, in order to achieve two glasses of the same major element composition except the difference in halogen content. Synthesis of the different doped glasses was carried out similar to the pre-synthesis step. The homogeneously mixed powders were successively added to a Pt crucible, which was placed in a high-T furnace. After the powder batches melted and the melt settled, the crucible was recovered and filled before being put back into the furnace again (e.g., Fig. 2.1b). This procedure was repeated until the crucible was almost completely full or the powder mixture was depleted. All melts were again stirred for 2-6 days, at temperatures between 1350 and 1550 °C. The temperature and duration used for the stirring was adjusted according to torque-measurements and the appearance of the melt. However, it was expected that some of the added halogens would degas during the synthesis. Therefore, the synthesis times were tried to be kept short with the halogen-doped mixtures. At the end, each crucible was taken out of the furnace and left cooling at room temperature.

Cylinders with an outer diameter of ~4.5mm were drilled out of the synthesized glasses while still being in the crucible. In a next step, the cylinders were cut to discs with a thickness of 2–2.5 mm using a diamond wire saw. The obtained discs were polished on one side using polishing solutions of 9, 3, and 1 µm grain-size to ensure proper contact between the diffusion couple halves during the experiment. The polished glass discs were used for anhydrous diffusion couple experiments under atmospheric pressure (chapters 4 and 5). In the case of the synthesized Cordón Caulle glasses (CC1 – halogen enriched; CC2 – halogen depleted), the glass fragments that were left after drilling were recovered from the crucible and powdered to be later used for water bearing diffusion couple experiments (chapter 5).

Detailed major element compositions of the synthesized Hekla and Córdon Caulle glasses are reported in chapters 4, 5 and 6. Figure 2.2 illustrates the starting glass compositions and their natural precursors cast as a TAS diagram.

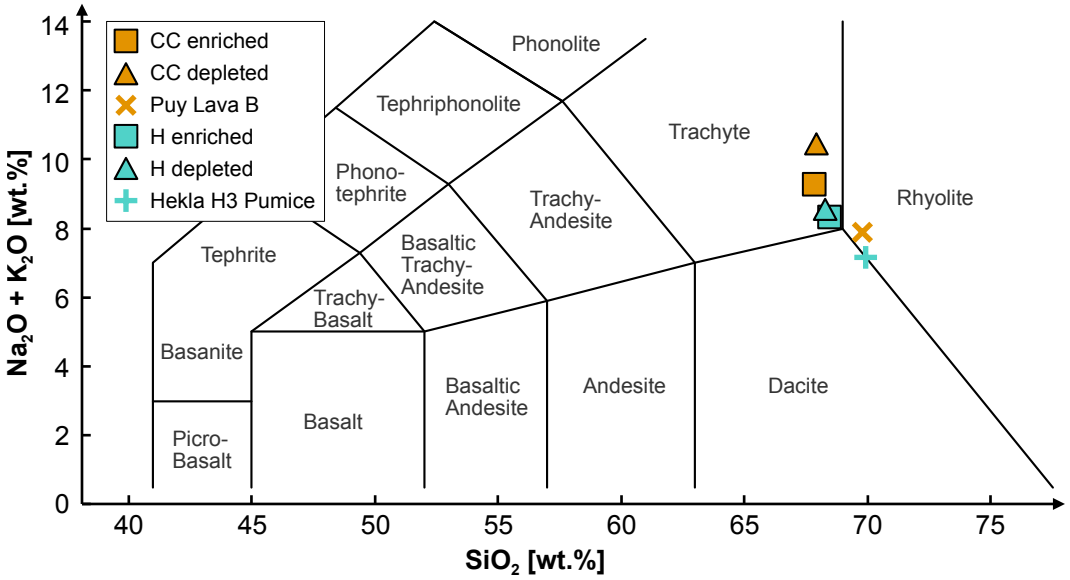

Figure 2.2: TAS diagram of the major element composition of the synthesized glasses and their natural precursors. "CC" refers to Córdon Caulle and "H" refers to Hekla. Compositions of samples "Puy Lava B" and "Hekla H3 Pumice" from Castro et al., (2013) and Weber and Castro (2017), respectively.

2.2 Hot Isostatic Press (HIP) synthesis

In an attempt to produce large homogeneous batches of water-bearing glass for diffusion couple experiments under hydrated conditions, powders of the synthesized Cordón Caulle samples CC1 and CC2 were used. The batches were prepared and synthesized at the Rock Physics and Mechanics Laboratory of the ETH Zürich, Switzerland. For the preparation of each synthesis, a metal tube (inner diameter ~3.2cm) was welded shut on one side and its inside was fitted with molybdenum foil in order

to avoid Fe contamination during the synthesis. The canister was progressively filled, using 10–25 g of sample powder per step, which was pressed into the canister using a hydraulic press applying a pressure of ~30 tons in order to minimize the amount of air being trapped and to allow for as much material as possible to be filled into the canister. After each step of pressing, an equivalent amount of 3.6 wt.% H_2O was added to the canister using a precision syringe and immediately topped with a new weighed batch of powder to avoid water loss. Once the canister was full, it was closed using molybdenum foil and a metal lid which was pressed into the canister and welded shut.

All prepared canisters were loaded into a Hot Isostatic Press (HIP). The target temperature and pressure conditions of 1050 °C and 140 MPa were reached over a period of ~70 and 45 minutes, respectively. The temperature was kept constant for about 5.5 hours before the synthesis was quenched by switching off the power of the heating elements and letting the sample chamber cool down to 250°C over a period of ~45 minutes. The pressure was kept constant over the time of cooling until the temperature was at a constant 250 °C for 90 minutes. At the end of the synthesis both, temperature and pressure were decreased to 25°C and 1 atm over the course of ~30 minutes.

The two samples were recovered by opening the canisters using a metal saw and cutting the exposed glass with a rock saw to obtain different sized pieces of glass still mantled by parts of the metal tube. The glass contained many cracks and some pieces fell off upon recovery. However, most of the glass cylinder stayed in shape. The outer 1–2 mm of the glass, which were in contact with the metal tube were almost black and appeared very clear and glassy. The area towards the center instead was light grey and opaque with less cracks. Electron microprobe analysis (chapter 3) revealed the presence of microlites with a size of <2 μm in the center parts of samples (Fig. 2.3). The crystals were too small to be characterized by conventional microprobe analysis. Compositional maps were acquired on crystal-rich parts which revealed that the microlites are mainly enriched in Fe and Ca and slightly enriched in Mg, compared to the glass composition (Fig. 2.3). Based on the results of the semi-quantitative compositional maps, the microlite crystals were suspected to be clinopyroxene. However, due to the inhomogeneity and high microlite content, the glasses produced by HIP synthesis were not used for the diffusion couple experiments. Instead, cylinders with a diameter of ~4.5 mm were drilled from areas with homogeneous crystal content about half-way between the center and the rim of the HIP canister, and these cylinders were cut into discs of 3 mm thickness using a diamond wire saw. The obtained samples were used for the study of Cáceres et al. (*in prep.*) who experimentally investigated the influence of microlites on bubble nucleation in hydrated silicic melt, by performing heating experiments in an optical dilatometer furnace at atmospheric pressure (e.g., Cáceres et al., 2020; Cáceres et al., 2022).

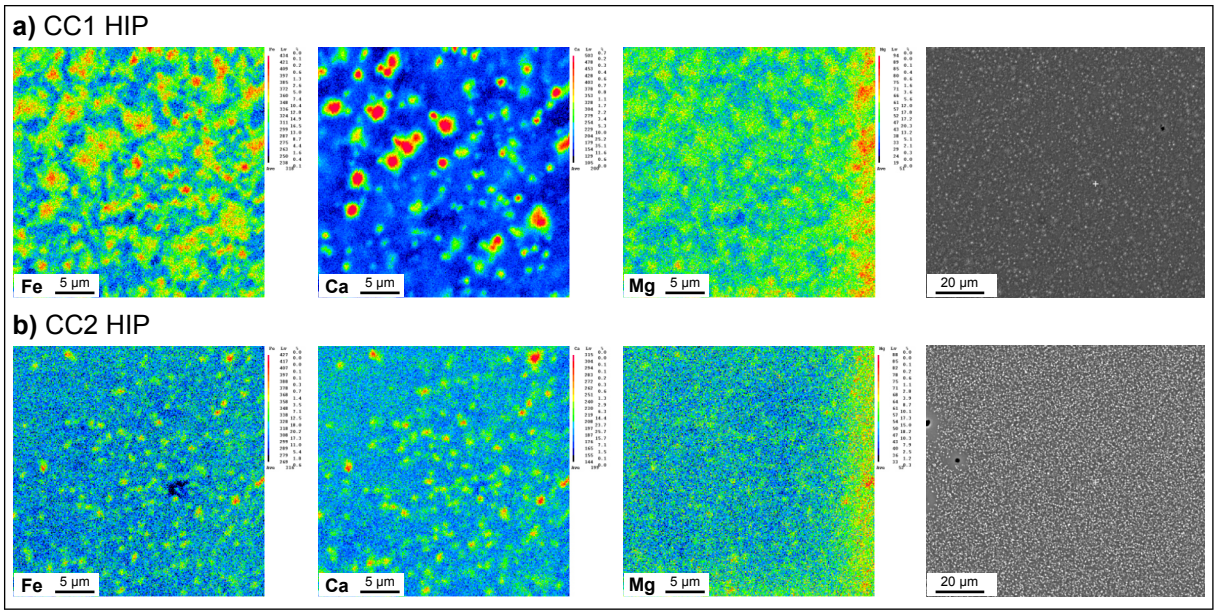

Figure 2.3: Compositional maps and backscattered images of HIP samples. **a)** halogen-bearing sample CC1_HIP **b)** halogen-depleted sample CC2_HIP. Concentrations not calibrated. Cold colors refer to low and warm colors refer to high concentrations (blue–green–yellow–red). Backscattered images do not represent the areas of map acquisition.

2.3 Diffusion couple preparation

2.3.1 Diffusion couple capsule preparation

Diffusion couple capsules were constructed from Pt-tube with a wall thickness of 0.2 mm. Tube with an inner diameter of 4.6 mm was used for dry experiments (glass discs) and tube with an inner diameter of 3.6 mm was used for the wet experiments (glass powders). Tubes with a length of 5–15 mm, depending on the experimental setup, were cut using a pipe cutter. Lids were prepared from 0.2 mm Pt-sheets. Pt-plates with a diameter of 5 or 6 mm were punched out of a strip of Pt-sheet using a custom-made tool. Before cutting the Pt tubes and sheets into shape, the parts were heated to glow red for ~1 s using a blowtorch to soften the material for easier machining. The plates were then pressed into a bowl shape employing another custom-made tool and used to close one end of the tube. In particular, the lid was put on one open end of the tube and pressed into the tube using a light hammer and a flat piece of metal. Afterwards, the edges of the lid and tube were filed flush and welded shut using an arc welder. To ensure cylindrical inner geometry of the capsule, the lid was tamped down from the inside of the capsule by inserting a tight-fitting rod and applying a pressure of 500–1000 kg using a hydraulic press and a guiding tool.

2.3.2 Buffer capsule preparation

The TZM rapid quench assembly (2.4.3) does not provide a simple way to control the oxygen fugacity during an experiment, as is possible with the filler rod technique used with the cold seal pressure vessel

setup (2.4.2). Therefore, the experiment must be buffered internally for controlled redox conditions by the use of a buffer capsule inside the experimental capsule. For the buffer capsules Pt-tube with an outer diameter of 2.2 mm and a wall thickness of 0.1 mm was cut in pieces of ~4 mm length. One side of the tube was pressed flat using pliers, filed flush and welded shut. The capsule was filled with some Ni-powder and a drop of de-ionized water or $Mg(OH)_2$. Also a mixture of Ni and $Ni(OH)_2$ was used for some capsules. Capsules were closed on the open side by pressing it flat, filing flush and welding it shut so that the final capsule would have a pillow-shaped geometry.

Buffer capsules were used for several reconnaissance experiments with the TZM assembly (2.4.3). However, for the diffusion experiments published and discussed in this thesis (chapter 5), buffer capsules were not used. The oxygen fugacity was instead moderated by the addition of ~0.3 MPa of CH_4 to the pressure line and the Ni-rich environment of the TZM assembly and the *Inconel* sample rod. This method is a well-established alternative to the capsule technique (e.g., Sisson and Grove, 1993; Hammer et al., 2002; Larsen, 2006; Alex and Zajacz, 2020).

2.3.3 Diffusion couples for dry experiments

The procedure of diffusion couple preparation described in the following paragraph was likewise carried out for both synthesized starting glass compositions. Capsules with an inner diameter of 4.6 mm and a length of 5–6 mm were used. The capsules were each loaded with a halogen-bearing and halogen-depleted glass disc, with the discs touching at the polished surface to avoid entrapment of air and aid the sintering process during the experiment. Most capsules were loaded with the halogen-enriched glass disc in the bottom and the depleted disc at the top, which was found to be the most stable configuration that minimized the risk of melt convection in the diffusion couple. The capsule was closed using a second lid which was gently pressed into the capsule, filed flush and welded shut like described in 2.3.1. However, the capsule was not tamped again after the second lid was attached, in order not to break the glass discs inside the capsule.

2.3.4 Diffusion couples for hydrous experiments

Diffusion couples for wet experiments were prepared using a smaller capsule diameter (4 / 3.6 mm). For diffusion experiments carried out with the TZM rapid quench assembly (2.4.3) capsules with a length of 10–14 mm were prepared as described in 2.3.1 and filled with powder of the dry starting glasses according to the following procedure. The capsule was first weighed empty and then filled about half-way of the total height using CC1 (halogen enriched) powder. The powder was gently tamped by hand during filling using a tight-fitting rod to minimize the amount of entrapped air and to consolidate the powder in the capsule. Afterwards, the capsule was weighed with the powder and an equivalent amount of ~1.5–3.5 wt.% of de-ionized H_2O was added using a micro-syringe. The halogen-depleted powder

CC2 was immediately added and slightly tamped on top of the CC1 + H_2O mixture to avoid water loss. The capsule was weighed again and another ~1.5–3.5 wt.% of de-ionized H_2O were added before the capsule was closed by carefully pressing a Pt-lid into the capsule, filing it flush and welding it shut. Afterwards, the capsules were tamped into a cylindrical shape by applying a pressure of ~750 kg to the capsule using an hydraulic press with a specialized tool.

The capsules were first weighed and then heated to ~120 °C for 30–50 seconds using a heating plate. After the heating, they were weighed again and the process was repeated at least 4 times to ensure the capsule would not lose weight (i.e., loss of water-vapor from the capsule) to confirm closed system conditions. Capsules with significant weight-loss were discarded. The preparation of capsules for crystallinity experiments (chapter 6) using the cold-seal pressure vessel setup was similar to the process described above but a capsule geometry with an inner diameter of 4.6 mm and a length of 6–8 mm was used.

2.4 Diffusion experiments

All experiments described in this section were carried out in the Volcanology laboratories of the Johannes Gutenberg-University, Mainz.

2.4.1 Anhydrous diffusion couples, 1 atm

The setup for diffusion experiments using anhydrous glass consisted of a *Thermoconcept* 1100 °C vertical tube furnace and a sample holder made of a heat-resistant alumina tube which is closed on one side. The diffusion couple capsule was placed at the bottom of the sample holder in an upright position. In addition to the internal thermocouple of the furnace, a K-type thermocouple was inserted into the sample holder touching the capsule to provide reliable temperature readings during each experiment. After the target furnace temperature was reached and stabilized, the experiment was started by inserting the sample holder into the furnace chamber through a tight-fitting opening at the top of the furnace and closing the top opening of the tube with insulation material. This way the diffusion couple was placed in the center of the furnace chamber within seconds. Heating times typically ranged between 3 to 5 minutes, based on observation of the second thermocouple. Upon quench, the sample holder was removed from the furnace through the same opening and let cool at room temperature, leaving the assembly in an upright position. This procedure was applied for the experiments presented in chapter 4 and some of the experiments presented in chapter 5. The procedures are described in more detail in the respective chapters.

2.4.2 Water-bearing diffusion experiments — cold-seal pressure vessel

Experiments with hydrated melt were carried out at pressurized conditions to avoid water degassing and bubble formation at high temperature. Therefore, Ni–Co–alloy (*Rene-41* and *Waspaloy*) cold-seal pressure vessels (autoclaves) consisting of a ~260 mm long cylinder with a diameter of 38 mm and a 6.35 mm (1/4 inch) bore in the center (Fig. 2.4) were used for experiments up to temperatures of 1000 °C and pressures up to 100 MPa. Autoclaves were closed and connected to the H_2O pressure line using a high-pressure fitting before being loaded into vertical or horizontal tube furnaces (*Thermoconcept*). Before starting an experiment, the autoclaves were first pressurized to the target pressure, which was controlled by a rotary vein pump and read by an analog Heise gauge and separate digital readout connected to a pressure transducer. Additionally, to compensate for pressure fluctuations during heating or quenching, the pressure line was connected to a ~5 l reservoir which could be closed off for pressure leakage testing. After the autoclave equilibrated at the target pressure, the experiment was started by turning on the furnace heating elements. Upon heating to the target temperature, which typically took between 40–70 minutes, the pressure was constantly monitored and fluctuations were adjusted for to keep the pressure constant. The temperature was monitored by the internal thermocouple of the furnace and an external K-type thermocouple, which was inserted into a bore at the end of the autoclave, providing the closest possible position to the capsule (Fig. 2.4).

For the experiments conducted in the scope of this thesis, the free space below the capsule in the autoclave was filled with a pure nickel metal filler-rod (Matthews et al., 2003). The slow oxidation of Ni during the experiment adjusted the oxygen fugacity close to NNO+1 (e.g., Schmidt and Behrens 2008; Castro et al., 2013). Additionally, the rod served to prevent convection of H_2O and to position the capsule in the top part of the autoclave when mounted vertically.

Shortly before quenching an experiment, the pressure was increased by about 0.3 MPa to account for pressure loss during cooling. The hot vessel was first air-cooled using compressed air until it stopped glowing and the pressure approximately decreased back to the run pressure (~60–90 s). Afterwards, the vessel was dropped into a water bath resulting in a fast quench time of about 3–4 minutes in total.

This experimental setup was mainly used for the experiments presented in chapter 6 of this thesis.

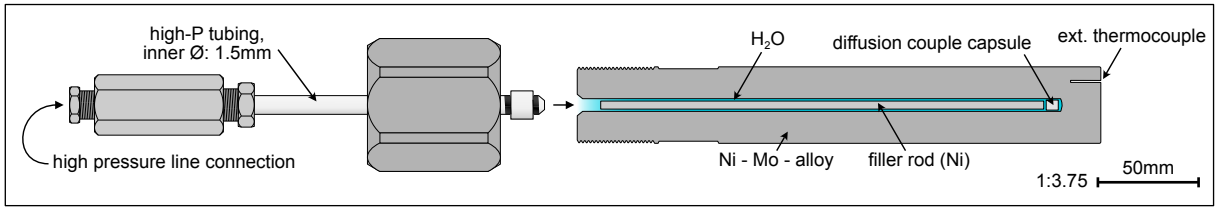

Figure 2.4: Schematic illustration of a cold seal pressure vessel made from Ni–Mo–alloy used for hydrated diffusion couple experiments.

2.4.3 Water-bearing diffusion experiments — TZM rapid quench assembly

The TZM (Tungsten Zirconium Molybdenum) rapid quench assembly, which is fitted to a *Deltech* DV-29-VT vertical tube furnace, allows running experiments at higher temperature and pressure conditions than the *Rene-41* or *Waspaloy* cold-seal pressure vessel setup. The TZM cold-seal assembly is connected to a stainless steel high-pressure tube network that transmits Ar gas as a pressure medium (Fig. 2.5). During the first experiments, water loss from the capsule was observed and was mitigated in later experiments by introducing ca. 0.3 MPa of CH_4 to the pressure system before pressurizing with Ar (e.g., Sisson and Grove, 1993; Szramek et al., 2006; Shea and Hammer, 2013).

The assembly consists of an inner autoclave made of TZM (~30 mm outer diameter, ~6.5 mm inner diameter) and an outer sheath made of *Inconel* (~50 mm diameter, 5 mm wall thickness). Both, the autoclave and the sheath are attached to a water cooled base at the bottom, which in turn couples these two pieces to the lower vessel that accommodates the travel in the internal sample holder; this is described in more detail below. The sheath is mounted over the inner autoclave leaving ~5 mm space between the two. During an experiment, this space is constantly purged with Ar using a pressure of 0.6–1 bar and adjusting an Ar flow rate of ~ 50 cm^3 min^{-1} (Fig. 2.5a). The purging is necessary to provide a non-reactive atmosphere for the inner pressurized autoclave. The inner autoclave is tightened against a stainless steel cylinder via a doubly coned and sealed beryllium-bronze cylinder ("football"-shape) between the two. On the bottom of the water-cooled coupling base, a second, lower vessel made of stainless steel is attached, and pressed against the coupling "football"-cylinder from the bottom side. This stainless steel cylinder is in turn connected to the pressure line with a high pressure fitting. The sample capsule is introduced with a sample rod that consists of a small cup to hold the capsule and a long rod made of Inconel with a magnet at the bottom end. The magnet allows for the control of the position of the sample capsule from outside using a neodymium ring-magnet that slides over the lower steel cylinder. The position of the magnet can be secured from outside by aluminum rings which can be clamped to the lower steel cylinder (Fig. 2.5b). During an experiment, the upper part of the assembly is introduced into the tube furnace (TZM autoclave and sheath; "hot zone" in Figure 2.5a); the water-cooled base remains outside the furnace and the opening between the base and the furnace is covered with high temperature insulation. In order to keep the base at moderate temperatures and to provide a cool environment for the rapid quench process, the base is constantly flushed with cold tap water (~15 l min^{-1}). Experiment pressure is generated by a *High Pressure Equipment* (HIP) GB-60 gas booster device operated with compressed air and employing Ar gas a pressurizing medium. Before the start of an experiment, the autoclave is brought up to the target pressure and temperature with the sample still in the water-cooled zone of the assembly. When the target *P-T* conditions are reached and equilibrated, the capsule is — within seconds — slid vertically into the hot zone of the TZM autoclave by upward movement of the sample holder using the outer ring-magnet. Quenching is done the opposite way by

downward movement of the magnet which brings the capsule back into the water-cooled zone. By doing so, an almost immediate quench can be achieved. During the experiments, temperature is monitored using the internal thermocouple of the furnace and an external K-type thermocouple which is inserted from the top of the furnace and into a small bore in the sheath of the assembly and touching the top of the autoclave. This way, the thermocouple is in the closest possible position to the experimental capsule. The pressure was monitored with a factory-calibrated Bourdon-tube gauge and a pressure transducer attached to an *Omega* digital process meter.

During the start and quench of the TZM experiments conducted in the scope of this thesis, significant short-lived pressure fluctuations were observed. Upon insertion of the sample, the pressure typically decreased by up to 20 MPa within the first ~10 s and increased by about 10 MPa in the following ~60 s. The opposite process was observed upon quench: after an initial increase of ~20 MPa, the pressure decreased by another 10 MPa within one minute. These processes were interpreted to occur due to the displacement and concomitant cooling of a large amount of the hot gas from the autoclave to the cooler parts of the pressure system, caused by the insertion of the sample rod. The rod is cold relative to the hot atmosphere in the autoclave and upon heating causes the pressure to increase again slowly. Upon quench, the processes occurred in a reverse manner. These pressure fluctuations were accounted for in each experiment by slightly over-pressurizing the autoclave before the start of the experiment and making subsequent adjustments of the pressure to the target values. The pressure increase during quench additionally ensured that bubbles could not form. As halogen diffusivity was shown to be mostly insensitive to pressure variations (e.g., Baker and Balcone-Boissard, 2009), these short-lived pressure fluctuations are considered insignificant for the results of the diffusion experiments.

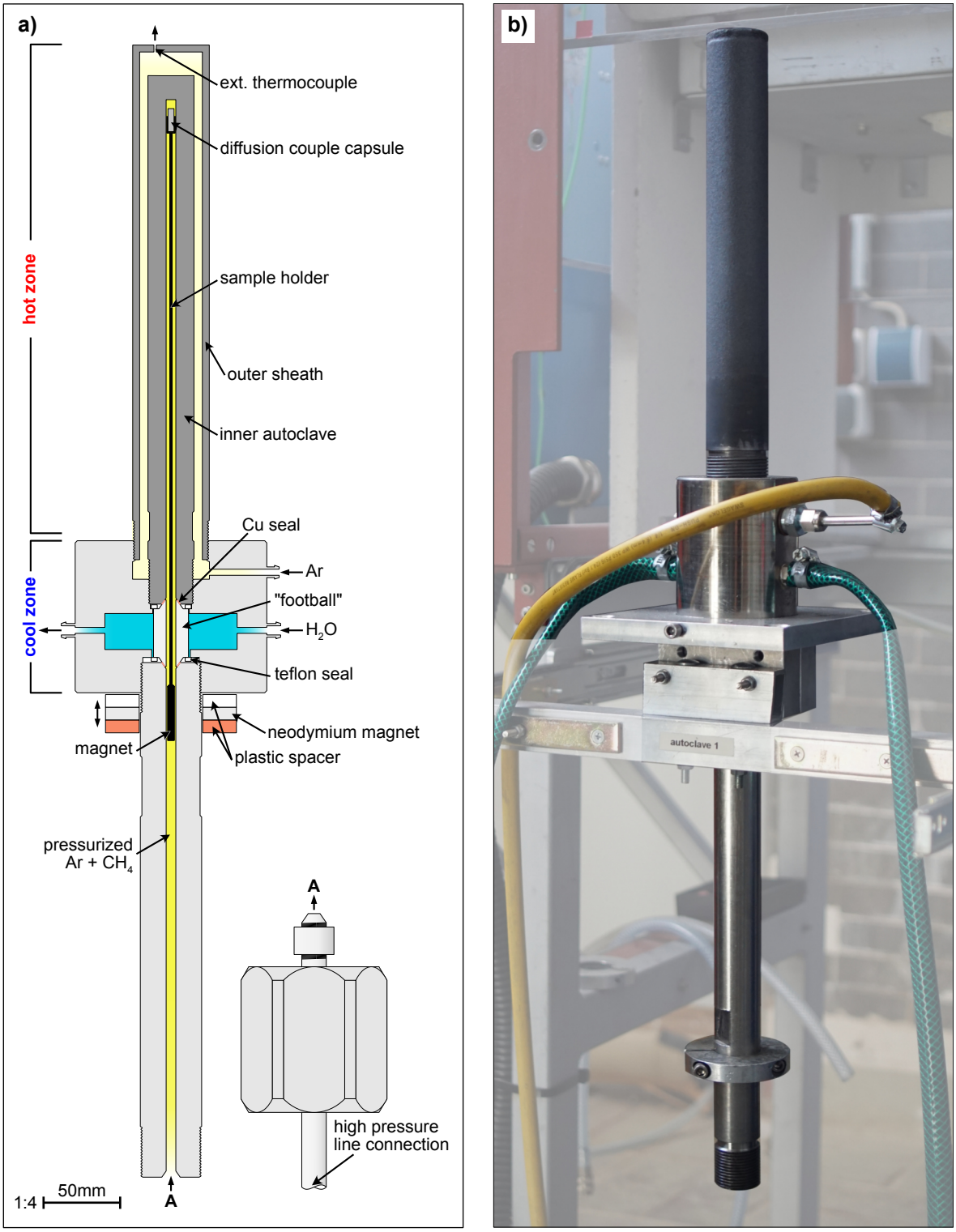

Figure 2.5: Schematic sketch and photograph of the TZM rapid quench cold-seal assembly. **a)** Illustrative sketch showing the main parts and functions of the assembly. **b)** Photograph of the autoclave assembly mounted in the assembly-holder. The holder allows to slide the whole assembly underneath the tube furnace. The top parts (sheath and inner autoclave) are introduced into the hot zone of the furnace. The yellow hose connects purging Ar gas which constantly flows up through the sheath, leaving it at the top opening where the external thermocouple is introduced. The green hoses connect the tap water for cooling of the middle part by purging it with H_2O (~15 l min^{-1}) during an experiment.

Chapter 3
Analytical Methods

3.1 Electron Microprobe Analysis (EMPA)

Electron Microprobe Analysis is one of the most common analytical techniques in geological sciences and is used to quantitively determine the chemical composition of materials on the micrometer scale. It allows for analyses of a wide range of elements from Be to U at major and minor concentrations down to ~100 ppm or lower in some cases (e.g., Cherniak et al., 2010). It is sometimes also referred to as EPMA – electron probe microanalysis. During EMPA analyses, materials are bombarded with a focused electron beam, which may cause inner-shell ionization of the hit atom, producing a secondary electron and leaving an inner-shell vacancy. Due to the instability of the excited atom, an electron from an outer-shell will fall into the vacancy which causes the release of an X-ray photon (or an Auger electron). The emitted X-rays have a characteristic wavelength dependent on the released energy which in turn is unique to the excited element. These characteristic X-rays can be detected using either Energy Dispersive Spectrometers (EDS) or Wavelength Dispersive Spectrometers (WDS) of which the latter is typically used for quantitative analyses. The WDS analyzers consist of different diffraction crystals, which disperse X-rays and allow to select and detect specific characteristic wavelengths based on Bragg diffraction. The diffraction follows Bragg's law which relates a multiple n of the wavelength λ to the distance between adjacent lattice planes d of the diffracting crystal (e.g., Goldstein et al., 2017):

$$n\,\lambda = 2\,d\sin(\theta) \tag{3.1}$$

Where θ is the angle of the incident X-ray beam on the diffraction crystal. At a certain angle θ the beams reflected at different lattice planes will be in phase and cause an X-ray intensity maximum which can be detected. Typically, the first order reflection (n = 1) is the strongest and is usually used in electron probe analysis (Cherniak et al., 2010).

Upon the bombardment of the sample, most incident electrons undergo inelastic collisions which leads to the loss of energy and subsequent emittance of secondary electrons and characteristic X-rays. However, a small fraction of the incident electrons undergo sufficient scattering events to completely reverse their initial travelling direction and leave the specimen without losing significant energy (Goldstein et al., 2018). These electrons are referred to as backscattered electrons (BSE). Both, the secondary and backscattered electrons are commonly used for imaging purposes. However, the backscattered electron yield correlates with the size of the atom, i.e., with the atomic number. This means that the higher the atomic number of the bombarded atom, the more electrons are reflected back

from the specimen, which results in higher BSE intensities of sample material containing atoms of higher atomic numbers. This property of backscattered electrons is commonly used for sample imaging as minerals or glasses containing heavy elements (such as Fe, Mg etc.) typically are represented by lighter colors (e.g., magnetite, pyroxene) compared to lighter elements such as Si, Na, etc (e.g., quartz, plagioclase). This imaging method was routinely used for sample characterization in this thesis.

During EMPA analyses, samples are analyzed almost non-destructively with spot sizes down to <1 µm, which allows for a very high spatial resolution. The small beam spot size is particularly important for analyzing diffusion profiles, as it allows the investigation of the measured concentration data in high geometric resolution. Other advantages of this technique for the scope of this thesis are the easy availability of the device at the JGU Mainz, the relatively straightforward sample preparation (polish and graphite coating) and the short measuring time per spot compared to other techniques (e.g., SIMS 3.2), allowing for the collection of numerous data points yielding lower statistical errors. For further information on the principles of electron microprobe analysis, the reader is referred to Goldstein et al. (2018). A thorough review of the application of EMPA to diffusion studies is provided by Cherniak et al. (2010).

Major element, F, and Cl concentrations of the synthesized sample materials, as well as the experimental diffusion couple glasses, were measured using a *JEOL JXA 8200* electron microprobe at the Institute of Geoscience of the Johannes Gutenberg-University, Mainz. Typically, the microprobe was run using an acceleration voltage of 15kV, a beam current of 12nA and a probe diameter of 5–10 µm, depending on the desired spatial resolution. A range of reference materials were used for calibration and were analyzed during each analytical session to ensure data reliability (e.g., natural obsidian, VG-2, VG-A99). During each session, BSE images of all samples were acquired in varying magnifications for documentation purposes and were used to define the position of concentration profiles to be measured with the microprobe. Diffusion couples were usually analyzed by placing line scans across the sample parallel to the diffusion direction, i.e., perpendicular to the coupling interface. The step width was chosen to be small (5–25µm; depending on the sample) close to the interface and larger (50–250 µm) at the ends of the profiles in the respective half-spaces, to achieve a good spatial resolution of the diffusion profiles by still covering the whole concentration range.

The EMPA was additionally used to acquire semi-quantitative compositional maps of several different experimental samples. For example, glasses synthesized by the HIP method (2.2) were analyzed by compositional mapping to identify the chemical composition of microlites that were too small for conventional EMPA analysis. This technique was also used to characterize experimental products of chapters 4 and 6. The EMPA also served to map the craters in the samples that were produced by SIMS analysis (3.2) in order to reference the measured SIMS data geometrically for diffusion profile

investigation. Electron microprobe analysis was the main technique used for all the different studies associated with this thesis. The detailed procedures, including EMPA settings, reference materials etc., that were used for each analytical objective are described in the respective studies (chapters 4, 5 and 6).

3.2 Secondary Ion Mass Spectrometry (SIMS)

Secondary Ion Mass Spectrometry is a powerful microanalytical tool that utilizes a focused ion beam (e.g., $^{133}Cs^-$, $^{16}O^-$) to eject ("sputter") secondary particles from the upper 10s of nanometers of the sample specimen. Of these secondary particles, elemental and molecular ions are accelerated by a high voltage and magnified to form a secondary ion beam which can be analyzed by a mass spectrometer, through separation of the ions by their mass-to-charge ratio (e.g., Ihinger et al., 1994; Cherniak et al., 2010). The separated ions can then be detected by Faraday-cups (FC) or electron-multiplier (EM) detectors. The SIMS method is particularly well suited for the investigation of trace elements and isotopes but can in principle be used to measure all elements of the periodic table, except the noble gasses. Similar to the electron beam of the EMPA, the primary ion beam can be focused to the size of few micrometers to allow for *in situ* analyses. The SIMS has proven to be useful in the context of diffusion studies as it can be used for horizontal line scans with a lateral resolution of up to ~10 µm but also for depth profiling by continuous sputtering over a small raster, reaching a depth resolution of up to 20 nm (e.g., Cherniak et al., 2010). The main advantage in using the SIMS in the context of this thesis is the ability to analyze even trace concentrations of Br and I, along with H (and therefore water content) which are not covered by the EMPA analysis. However, due to the long measuring times compared to electron microprobe analyses and the high costs associated with running a SIMS, only the most promising experimental samples were preselected and just one concentration profile could be measured on each of the samples.

In the course of this study, SIMS analyses were carried out at two different facilities: Samples based on the synthesized Hekla (HX) and some of the synthesized Cordón Caulle composition (CCX) were measured under supervision of Dr. Anne-Sophie Bouvier at the SIMS laboratory of the University of Lausanne, Switzerland (*SwissSIMS*; October 2018 and January 2019). Other CCX samples and water-bearing experiments (CCX-H) were analyzed under supervision of Dr. Thomas Ludwig at the SIMS laboratory of the University of Heidelberg, Germany (Heidelberg Ion Probe *HIP*; May 2021 and April 2022). In all cases a *Cameca IMS 1280-HR* ion probe was used (Fig. 3.1a & b). Samples were analyzed by setting up line scans across the diffusion couples similar to the procedure used for the EMPA. Spot-sizes of 4–20 µm were used. For samples with relatively short diffusion profiles, individual analysis points were arranged in a zig-zag pattern close to the interface to allow for a small step width without overlapping of the individual points (Fig. 3.1c).

At the two SIMS facilities, different analytical approaches were chosen for halogen concentration measurements. Due to the lack of a well characterized reference material, the measurements carried out

at the *SwissSIMS* relied on the homogeneously constant Si content in the experimental glasses. For analyses of ^{19}F and ^{35}Cl the more abundant Si-isotope ^{28}Si was simultaneously measured as a reference. Br and I concentrations in the diffusion couples are generally lower compared to F and Cl. Therefore, the less abundant Si-isotope ^{30}Si was used as a reference for $^{79/81}Br$ and ^{127}I. Points acquired at the high halogen concentration side of the diffusion couple were used as reference halogens–Si ratios and were repeatedly acquired every 5–6 points to ensure system stability and reliability of the subsequently acquired data. This way, no absolute concentrations but the ratios of the halogens over Si were measured and used for diffusion profile investigation. Analyses carried out at the *Heidelberg Ion Probe* were calibrated using different reference materials by calibrating the ratio of each halogen over ^{28}Si with the known halogen–Si ratio of reference glass JV1 (Pichavant, 1987) and internal standards.

The water bearing experiments of the CCX-H series were additionally analyzed for H_2O concentration using a *Cameca IMS 3f* ion probe at the *Heidelberg Ion Probe* facility. Concentration profiles of ~20 points per sample were analyzed along the profiles previously analyzed for halogen content. Details of the analytical conditions of the different ion probe sessions are provided in the supplementary information of chapter 5.

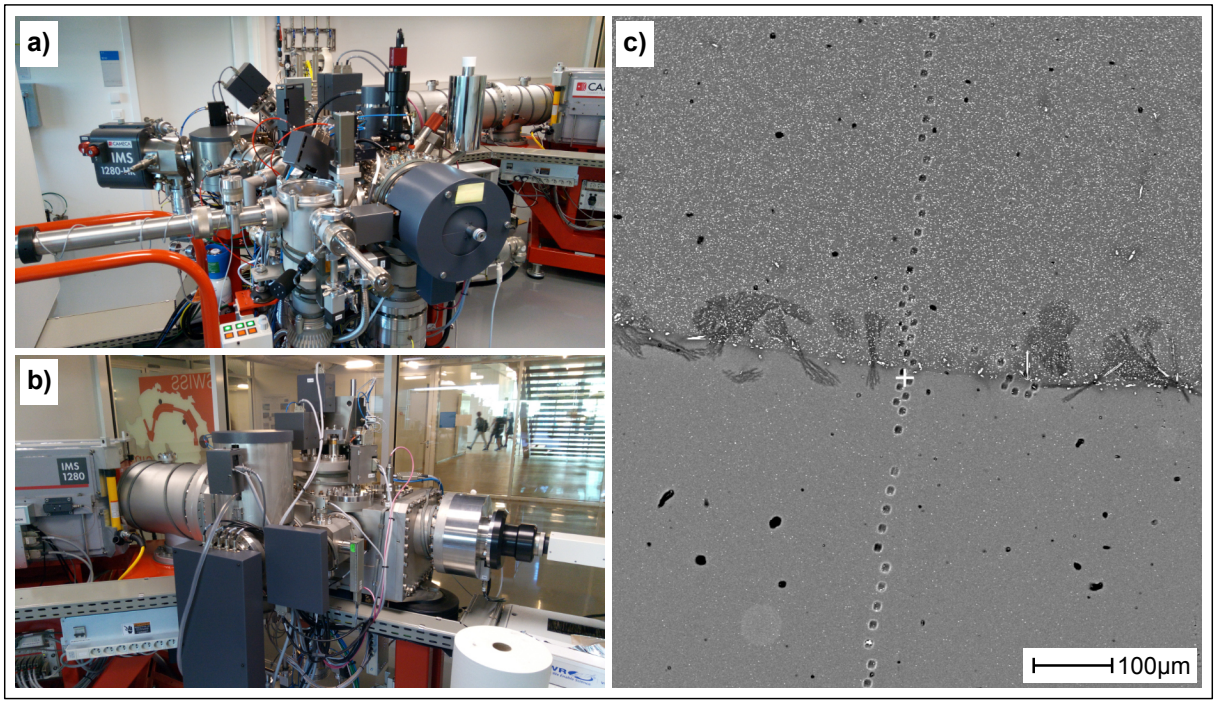

Figure 3.1: Secondary Ion Mass Spectrometer and BSE image of a SIMS analyzed sample. **a)** + **b)** *Cameca* IMS 1280-HR at the University of Lausanne. **a)** Sample chamber and primary ion source with parts of the electromagnetic focusing system and magnet in the background. **b)** Collector for counting secondary ions including monocollection and multicollection systems. **c)** Backscattered image of a diffusion couple sample (HX 8) after analysis with the SIMS. Image acquired on the EMPA at the University of Mainz.

3.3 Raman spectroscopy

Raman spectroscopy is a common method in Geoscience and is typically employed to identify mineral phases, amorphous materials such as silicate glasses, volatiles in glasses and fluid inclusions (e.g., Neuville et al., 2014; Helo et al., 2020). Here, the method was primarily used to identify microcrystalline phases in water-enriched silicic glasses. The technique is based upon the interaction of photons of monochromatic light in the visible spectral range (laser) with the molecular vibrations of the sample material which induces a shift in the wavelengths of the scattered photons. This means that photons which underwent the process of Raman scattering have a different energy to the incident photons. The shift in energy (or wavelength) can be detected by a spectrometer and corresponds to the vibrational frequency of the vibrational source (different atoms or molecules in the sample material). Moreover, the relative intensities of Raman peaks provide semi-quantitative information of the composition of the material. Raman spectra typically present Raman intensities vs. the vibrational frequency (in wavenumbers). Generally, high wavenumbers relate to lighter vibrational atoms, e.g., 4500 cm^{-1} corresponds to the H_2 molecule. Acquired spectra are typically compared to spectra of well characterized known materials (e.g., RRUFF database; Lafuente et al., 2015) to identify the unknown sample. The successful application of Raman spectroscopy for the identification of silicate phases therefore relies heavily on the availability of well characterized sample spectra provided via databases.

Advantages of Raman spectroscopy over other techniques include that it is truly non-destructive and provides a high spatial resolution by using small spot sizes of typically 1–3 µm. The small spot sizes in turn result in very small analyzed sample volumes compared to Fourier-Transform Infrared Spectroscopy (FTIR; 3.4). Sections need to be polished on one side only which makes sample preparation straightforward. A significant disadvantage is, however, that quantitative analyses are complex and need elaborate calibrations.

Raman spectroscopy was used to identify microcrystalline silicate phases present in water-enriched diffusion experiments which were ultimately used to study the influence of halogens on the phase equilibria of a melt (chapter 6). All analyses were carried out at the University of Mainz, using a *Horiba-Yvon* Labram-HR Raman microscope with a focal length of 800 mm. A green diode-pumped 200mW laser (λ = 532 nm) was used as the excitation source. As the analyzed crystals were relatively small (<2 µm), the recorded spectra contained background signal of the vibrational response of the glass matrix. Therefore, crystal-bearing spectra were corrected by recording and subtracting pure glass spectra from the crystal-bearing spectra. More details on the Raman methodology used in the scope of this study is provided in chapter 6.

3.4 FTIR spectroscopy

Fourier-Transform Infrared (FTIR) spectroscopy is a common method in Geoscience and is used to quantitively analyze chemical species and molecules in solids, liquids or gases (e.g., Cherniak et al., 2010). Similar to Raman spectroscopy, FTIR analyses utilize the vibrational modes of the analyzed species which absorb incident light and produce spectra characteristic of the analyzed material. For excitation of the atoms and molecules of the sample material, electromagnetic radiation of the IR spectrum ($\lambda \sim 0.75$–100 μm) is used, which has a longer wavelength than visible light ($\lambda \sim 400$–750 nm). For spectral analysis, the beam coming from the sample is introduced into a Michelson interferometer. The beam passes through a beam splitter and parts of the beam oscillate between mirrors while interfering with the incoming beam. This way, an interference pattern of the complete IR spectral range is produced which is transformed to a spectrum by Fourier transformation. Because the beam usually travels through air (i.e., through gas molecules), sample-free background spectra have to be acquired routinely for sample spectra correction.

FTIR spectra typically show the absorbance (*A;* dimensionless) of the specimen over the IR frequency range, expressed as wavenumbers (cm^{-1}). The *Beer–Lambert Law* states that the absorbance A is proportional to the molar concentration c (mol l^{-1}) of the absorber species, the path distance of the light through the sample l (cm), and the molar absorptivity of the sample ϵ (L mol^{-1} cm^{-1}), which is a pre-determined constant for the material of interest.

$$A = \epsilon\, l\, c \tag{3.2}$$

Generally in Geoscience and also in the scope of this study, a modified form of equation 3.2 is used to derive mass fractions from the absorbance spectra (e.g., von Aulock et al., 2014):

$$w = \frac{A\, M}{\epsilon\, l\, \rho} \tag{3.3}$$

Where M is the molar mass of the absorber (g mol^{-1}), ρ is the density of the sample (kg m^{-3}) and w is the weight fraction of the absorber in the sample. For quantitative measurements, ϵ, l, ρ and M need to be known in advance to calculate the weight fraction w based on the height of characteristic absorbance peaks in the IR spectrum. In transmission FTIR spectroscopy, the path length l is given by the thickness of the wafer. When working with silicate glasses or minerals, the density ρ of the sample can often be estimated by applying melt density models to a known bulk chemistry (e.g., Ochs and Lange, 1999; Iacovino and Till, 2019). The molar absorption coefficient ϵ relates to the chemistry of the sample and should ideally be determined for every sample material. However, calibrated absorption coefficients of samples of similar chemical composition and structure may be available in the literature. These are

typically sufficient to calculate accurate mass fractions in common melt compositions (e.g., Stolper, 1982; Ihinger et al., 1994; Di Matteo et al., 2004).

FTIR samples are typically prepared either as powders which are mixed and pressed with KBr, or as polished glass or crystal wafers. KBr-powder spectra are commonly used for bulk qualitative analyses, or for very fine powders (e.g., ash), but where spatially resolved quantitative data is needed wafers have to be prepared. FTIR wafer preparation is more elaborate than for EMPA or Raman analyses because the wafers have to be polished from both sides ("doubly-polished") and need to have a certain ideally uniform thickness of only 10s to 100s of micrometers which makes handling samples during post-preparation difficult. The right thickness needs to be estimated in advance, based on the expected volatile content, the absorbance band of interest, sample opacity, crystal content, and other factors that may affect the resulting absorbance measurements. Sample preparation is the most time-consuming part of FTIR analysis but it is also the most important step to produce successful measurements. For a thorough guide on modern FTIR sample preparation methods the reader is referred to the review of von Aulock et al. (2014).

The main advantages of FTIR analysis are the ability to deliver precise quantitative data with a relatively simple, nearly cost-free instrumentation at short measuring times, especially compared to methods such as SIMS (3.2). The spatial resolution can be as high as 3 μm on conventional apparatuses, to 1 μm in Synchrotron-source instruments, and analyses cover the whole IR spectral region. A major advantage of FTIR over Raman is the ability to deliver precise quantitative data, even though the spatial resolution may be better with Raman spectroscopy (Cherniak et al., 2010). The main disadvantage, however, is the complex and time-consuming sample preparation necessary to achieve good results. Additionally, for the determination of precise quantitative data, appropriate extinction coefficients for the studied sample material are not always available and may need to be derived from calibrations using other techniques first.

FTIR analysis was used to quantitatively determine the water contents of samples used in the study of chapter 6. Three select samples were analyzed at the University of Mainz, using a LN_2 cooled *Thermo-Nicolet* 6700 FTIR spectrometer coupled to a *Continuum* microscope. The samples were analyzed in transmission mode, covering the mid-IR and near-IR regions using a KBr beamsplitter and a MCT/A detector. Each spectrum was acquired using a resolution of 4 cm^{-1} and 256 scans and sample-free background spectra were collected every 20 min. The bulk water content was calculated with equation 3.3 and based on the height of the two absorbance peaks at 4500 cm^{-1} (OH) and 5200 cm^{-1} (H_2O) relative to a linear background. The details of the employed FTIR methodology are further described in chapter 6. The FTIR technique was also used for determining the bulk H_2O content in the samples of the study of Cáceres et al., (2022).

Chapter 4

Diffusion of F and Cl in dry rhyodacitic melt[1]

Abstract

Chemical diffusion of F and Cl has been experimentally determined in a rhyodacitic melt obtained from remelting a sample of Hekla pumice (Iceland). Diffusion couple experiments were conducted in a vertical tube furnace over a temperature range of 750–950 °C and in air for durations of 1 to 35 days. Concentration profiles of F and Cl were obtained for the quenched samples using an electron microprobe. Fluorine and chlorine exhibit Arrhenian behavior over the range of temperature investigated here. The pre-exponential factors of F and Cl are $D_0(F) = 4.3x10^{-4}$ *and* $D_0(Cl) = 1.6x10^{-5}$ m^2/s. *Fluorine diffusion coefficients vary in the order of* $1x10^{-15}$ *to* $1x10^{-13}$ m^2/s, *whereas Cl diffusivity is up to two orders of magnitude slower. The activation energies for F and Cl diffusivities are equal within error at 223 ± 31 and 229 ± 52 kJ/mol, respectively. The difference in diffusivity between F and Cl is particularly pronounced in the melt of our study, compared to results obtained for other magmatic melt compositions. This means that the potential for diffusive fractionation exists and may occur especially under conditions of magma ascent and bubble growth, as this would favor partitioning of the relatively fast-diffusing halogens into growing bubbles, due to* H_2O *exsolution. A dependence of diffusivity on atomic radius observed here is enhanced over that observed in more basic, less viscous melts, indicating that diffusive fractionation is more likely to be pronounced in more silicic, more viscous systems. A proper parameterization and modeling of diffusive fractionation of halogens in actively degassing volcanic systems thus holds the potential of serving as a tool for quantifying the processes responsible for volcanic unrest.*

Keywords: Halogens (F, Cl), diffusion, silicate melt, diffusion couple, experimental volcanology

---

[1] This chapter is published as Feisel, Y., Castro, J.M., and Dingwell, D.B. (2019) *American Mineralogist*, 104, 1689 – 1699, doi: 10.2138/am-2019-7095

4.1 Introduction

Volatiles are an important constituent of melts and play a significant role in igneous processes. The chemical composition of the volatile phase crucial for the style of volcanic eruptions depends on parameters such as solubility, partitioning, and diffusion of the different species, which in turn are controlled by compositional parameters (e.g., initial volatile content, magma composition) and ambient conditions (e.g., pressure, temperature). While the dominant components of volcanic volatiles are water (H_2O), carbon dioxide (CO_2), and sulfur-species, halogens (F, Cl, Br, I) can be highly concentrated in silicic melts (e.g., tin and topaz rhyolite, Carroll and Webster, 1994; Webster and Duffield, 1994) and are a significant component of volcanic gases (Symonds et al., 1994; Aiuppa et al., 2009; Webster et al., 2018) venting from active silicic volcanic centers. Halogens affect magma viscosity and diffusivities (Dingwell et al., 1985; Dingwell and Hess, 1998; Baasner et al., 2013a) as well as phase equilibria (Manning, 1981) and directly influence the stability of hydrous minerals and halogen-bearing phases in igneous rocks (e.g., micas, fluorite, topaz; Webster et al., 2018). Schipper et al. (2017) showed that the degassing of F and Cl into isolated pores of slowly cooling magma could cause silica redistribution and the formation of vapor-phase cristobalite. Halogen degassing is also essential for the formation of ore deposits in active volcanic systems and can have a major impact on Earth's climate and environment including potential destruction of ozone in the stratosphere (Aiuppa et al., 2001; Bobrowski et al., 2003; Bobrowski et al., 2007; von Glasow et al., 2009; Boichu et al., 2011; Surl et al., 2015; Roberts, 2018). The escape of F and Cl from ascending magma has been argued to occur at relatively shallow depths (Spilliaert et al., 2006). Thus, their study in volcanic gas emissions can help identify and characterize pre- or syn-eruptive volcanic degassing and might augment volcano monitoring.

The potential for widely varying diffusivities between the halogens may mean that diffusive fractionation between the halogens may provide further insights into the timing of magma ascent and volatile exsolution (Alletti et al., 2007). Halogens are also increasingly routinely measured in volcanic plumes.

Despite investigations to date, our knowledge of halogen solubility and diffusivity in silicate melts is far from complete. Rhyolitic volcanoes are commonly known to be the most explosive and hazardous and typically comprise melts with the highest F concentrations (e.g., Aiuppa et al., 2009). Yet, halogen diffusivity data are scant for such systems. Instead, most studies describing volatile behavior in silicate melts have concentrated on H_2O, CO_2, and S. Previous studies on F and Cl diffusion are available for simplified model systems such as albite, jadeite, or Na-aluminosilicate (Dingwell and Scarfe, 1984; Dingwell and Scarfe, 1985, only for F), basaltic (Alletti et al., 2007), and phonolitic melts (Balcone-Boissard et al., 2009; Böhm and Schmidt, 2013). Only a few studies exist on more evolved dacitic to rhyolitic melt compositions (Bai and Koster van Groos, 1994; Fortin et al., 2017; Yoshimura, 2018),

and those have concentrated solely on Cl diffusion. Furthermore, most previous studies have been conducted at higher experimental temperatures than those relevant for natural systems.

While some authors report a pressure dependence of the diffusion coefficients (e.g., 1.0–1.5 GPa; Dingwell and Scarfe, 1984; Bai and Koster van Groos, 1994) most recent studies have found only minor pressure effects (e.g., 0.5–1.0 GPa; Alletti et al., 2007; Balcone-Boissard et al., 2009). The addition of H_2O is reported to enhance diffusivities up to an order of magnitude (Baker and Balcone-Boissard, 2009; Böhm and Schmidt, 2013). For a complete compilation of all studies on halogen-diffusion in silicate melts until 2010, see reviews by Baker and Balcone-Boissard (2009) and Zhang et al. (2010) and for a recent comprehensive review about halogens in volcanic systems of mafic to intermediate compositions see Webster et al. (2018).

In this study we apply the diffusion couple technique on remelted, mechanically homogenized glasses synthesized from natural pumice of the Hekla H3 eruption, one of Hekla's most recent Plinian silicic eruptions (2879 BP; 2.2 km^3 DRE; e.g., Sverrisdottir, 2007; Thordarson and Larsen, 2007; Weber and Castro, 2017). We determine the chemical diffusion of F and Cl in melts of rhyodacitic composition over a temperature range relevant for these magmatic systems to improve and expand our understanding of volatile transport in magmatic systems. Even though diffusion is not the only mechanism responsible for volatile transport in melts, it is one of the fundamental processes necessary to understand and model volcanic degassing.

4.2 Experimental and Analytical Technique

The initial sample synthesis was carried out in the laboratories of the Earth Science department of the LMU Munich. Experimental starting glasses were synthesized from natural rhyodacitic pumice of the Hekla H3 eruption (Table 4.1). The pumice was synthesized in a 1 atm high-*T* furnace at 1400–1550 °C for 2–7 days to produce volatile-depleted glass (Table 4.1). During the synthesis, the melt was slowly stirred using a platinum-rod attached to a viscometer to improve devolatilization and ensure homogeneity of the whole batch. In addition, the viscosity of the glass was monitored and the synthesis was continued until the viscosity reached a steady state, i.e., the viscosity did not change any more over a timescale of several hours, which we interpreted to reflect the bulk loss of volatiles. After the first synthesis, the batch was split and crushed. One half was doped with halogen-bearing Na-salts (NaF, NaCl, NaBr, and NaI) so that each halogen would account for 1 wt.% of the whole batch after doping. Bromine and iodine, even though present in the melt, are the subject of another study in progress. However, it has to be taken into account that all halogen species are diffusing in our experiments and that this might have an effect on the results. The other, halogen-depleted half of the batch was in turn doped with a certain amount of Na_2CO_3 to account for the sodium enrichment in the halogen-bearing glass. After thorough mixing, each half was then re-homogenized by high-*T* stirring at the same

conditions as in the first synthesizing step for 4–7 days. It is noted that, even though the samples were synthesized at high temperatures for several days, the halogen-depleted sample still contained a few hundreds of parts per millions of halogens (Table 4.1). However, the diffusion of halogens nevertheless occurred under a significant chemical potential gradient between the two diffusion couple halves. The small amount of halogens in the depleted half is therefore not expected to have an effect on the resulting diffusivities. After synthesis, cylinders with a diameter of 4.6 mm were drilled out of the glass within the Pt crucible and cut into small disks with a thickness of ~2 mm using a diamond wire saw. The disks were polished on one side to ensure proper contact between the two diffusion couple halves during the experiment. The final major-element compositions of the two different anhydrous starting glasses are presented in Table 4.1. Sodium enrichment in the experimental glasses compared to the original H3 pumice is attributed to the addition of halogens by Na-halogenides in the enriched and the addition of sodium carbonate in the depleted glass.

The capsules for each diffusion couple were constructed from 5 mm Pt tube with a wall thickness of 0.2 mm. The bottom of the capsule was closed with a Pt lid that was pressed onto and welded to the tube using an arc-welder. Afterward the bottom of the capsule was tamped down to ensure cylindrical geometry. The halogen-doped glass disks were loaded into the bottom part of the capsules and the halogen-depleted disks on top of them with both disks touching at the polished surfaces (Fig. 4.1a). Each capsule was closed by welding a second lid to the top of the capsule to ensure closed system conditions (Fig. 4.1b).

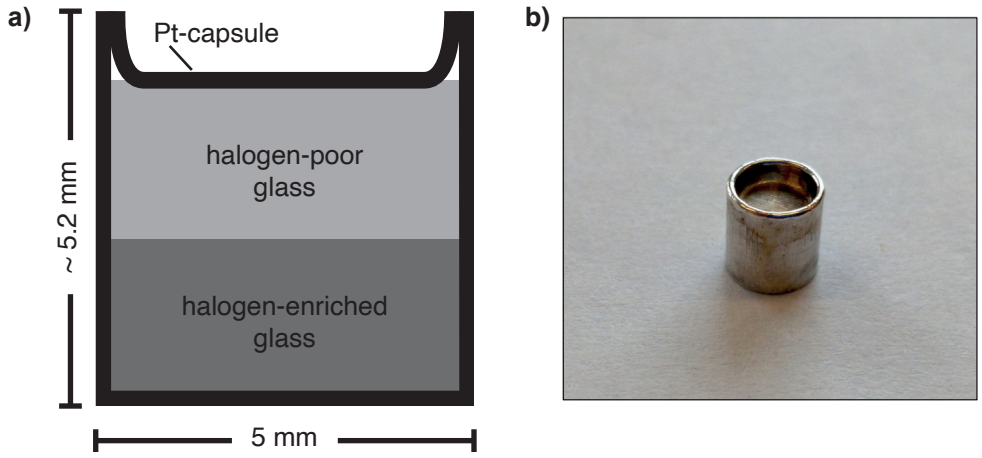

Figure 4.1: Capsule geometry used for diffusion couple experiments. **a)** Schematic section through an experimental capsule. **b)** Finished capsule before the experiment.

The diffusion experiments were conducted in the laboratories of the University of Mainz. For each experiment, one diffusion couple was first weighed and then loaded into an alumina tube that is closed on one side. The tube was inserted vertically into a small opening on the top of the vertical tube furnace

that was preheated to the target temperature. All experiments were carried out at atmospheric pressure. The capsule was placed upright on the closed bottom of the tube and located in the hot spot of the furnace chamber. The temperature was monitored during the entire run using the internal furnace thermocouple and an additional K-type thermocouple that was in direct contact with the diffusion couple capsule. Temperatures are estimated to be accurate to ±2 °C based on the accuracy of the thermocouple device. The experimental duration ranged from one to 35 days depending on the temperature investigated (Table 4.2). The time needed for the capsule to heat to the target temperature ranged between 3 and 5 min. The samples were quenched by sliding the alumina tube out of the furnace and letting it cool in air to room temperature, leaving the assembly in an upright position. Typical cooling times to a temperature of 200 °C were in the range of 3 to 4 min. After each experiment the samples were weighed again to confirm closed system conditions during the experiment. To investigate a possible pressure effect on halogen diffusion one experiment (HX2b) was conducted at 900 °C and 100 MPa in a cold-seal pressure vessel within a horizontal tube furnace. For this experiment Ag-Pd was used as capsule material. Even though heating and quenching times were longer due to the more complex setup, the related error is considered small compared to the long relative experimental durations.

After quenching each capsule was embedded in epoxy, cut open parallel to the diffusion direction, and polished for electron microprobe analysis (EPMA). All analyses were performed with an electron microprobe of the type *JEOL* JXA 8200 in the Department of Geoscience of the University of Mainz. F and Cl concentrations were measured simultaneously along with most major elements. An acceleration voltage of 15 kV, a beam current of 12 nA, and a probe diameter of 5 mm were used for all quantitative analyses. For F and Cl dwell times of 120 and 30 s were used, respectively. The detection limits for F and Cl were both 60 ppm (1s). Standards used for calibration are SrF_2 (F), tugtupite (Cl), VG-2 (Ca, Mg), VG-A99 (Fe, Si), MnTi (Mn, Ti), and orthoclase (Al, K). VG-2, VG-A99, and a natural obsidian standard were analyzed repeatedly during each analytical session. The data were corrected with the ZAF method. The profiles were acquired with a step-size of 20 µm on the ends of the profile and smaller step-sizes of 10 and 5 µm for analyses closer to the diffusion interface. This way it was possible to achieve a high spatial resolution of data necessary to resolve slow diffusion but also cover a large range of diffusion widths while keeping analysis time low. Additionally, one qualitative 2D compositional map of F, Cl, and some major elements (Si, Al, Na, Ca, Fe, Ti) was acquired for sample HX8 using a pixel-size of 3 x 3 mm, an acceleration voltage of 15 kV and a beam current of 100 nA. Dwell times were 200 ms for each element.

Table 4.1: Chemical composition of Hekla H3 pumice and the resulting synthesized glasses. Synthesized compositions include corrections for Na-loss. Major elements are normalized to 100 wt.%.

	H3 pumice[a]	Enriched glass	1 S.D.	Depleted glass	1 S.D.
wt.%	whole rock	*n* = 15		*n* = 14	
SiO_2	69.93	68.47	0.35	68.26	0.31
TiO_2	0.34	0.46	0.02	0.46	0.02
Al_2O_3	14.72	14.70	0.12	14.57	0.08
FeO	4.83	4.60	0.29	4.76	0.06
MgO	0.13	0.46	0.02	0.44	0.02
MnO	0.14	0.13	0.02	0.15	0.02
CaO	2.66	2.85	0.07	2.82	0.05
Na_2O	4.85	6.24	0.12	6.35	0.07
K_2O	2.33	2.10	0.03	2.20	0.03
P_2O_5	0.05	-	-	-	-
F	[a]	0.53	0.02	0.04	0.03
Cl	[a]	0.26	0.01	0.02	0.02
Total	99.1	101.35	0.33	100.07	0.43

Note: Synthesized compositions include corrections for Na loss. Major elements are normalized to 100 wt.%.

[a] data from Weber and Castro (2017) obtained by XRF. Significant F (1800 ppm) and Cl (500 ppm) concentrations are reported for matrix glass analyses (EPMA) of the H3 pumice.

4.3 Results

4.3.1 F and Cl diffusion coefficients

Diffusion coefficients for each experimental temperature were derived from the diffusion profiles acquired by EPMA. In each sample both F and Cl were analyzed. Typical examples of diffusion profiles are presented in Figure 4.2. For each sample, two profiles with distances ranging from 100–700 mm (except only one profile for HX9) were analyzed and processed to confirm homogeneity. Additional backscattered electron images of all samples and a compositional map of sample HX8 (950 °C) further confirmed the homogeneity of the major elements and the concentration gradient of F and Cl along the diffusion interface produced by this experimental setup (Figure 4.3). The semi-quantitative compositional map was acquired with a size of 500 x 350 pixels and a spot size of 3 μm. Even though no quantification has been done to the raw data, the map still shows the sharp difference in initial halogen contents of the two diffusion couple halves, in addition to the relative homogeneity of major element composition across the charges. Concentrations of Si, Al, Fe, and Ti are very homogeneous in the investigated area. Ca concentration is mostly homogeneous but is enhanced at some points close to the diffusion interface, likely due to the growth of apatite microlites. Na concentration is homogeneous in most parts but is increased in small irregular patches close to the diffusion interface. These Na-rich areas also correspond to low-concentration zones of F and Cl. Profile 2 of HX8 was acquired crossing one of those low-concentration patches. Despite these microscale heterogeneities, the compositional map allowed us to select appropriate traverse positions and discard the data points acquired in one of these patches to calculate the diffusion coefficients just from the unaffected data. The compositional map along with backscattered electron images additionally confirmed that no convection occurred in our high-viscosity rhyodacitic diffusion couples. This agrees well with previous studies that demonstrated that even in low-viscosity basaltic melts no convection influenced the experiments (Alletti et al., 2007; Balcone-Boissard et al., 2009). Even though a slight downward bend of the interface was observed in sample HX8 (950 °C, Figure 4.3a) there is no effect on the resulting diffusion coefficients calculated from linear profiles. A compilation of all analyzed diffusion profiles and the complete compositional map can be found in the Supplemental Material[2].

[2] Deposit item AM-19-117095, Supplemental Material. Deposit items are free to all readers and found on the MSA website, via the specific issue's Table of Contents (go to http://www.minsocam.org/MSA/AmMin/TOC/2019/Nov2019_data/ Nov2019_data.html).

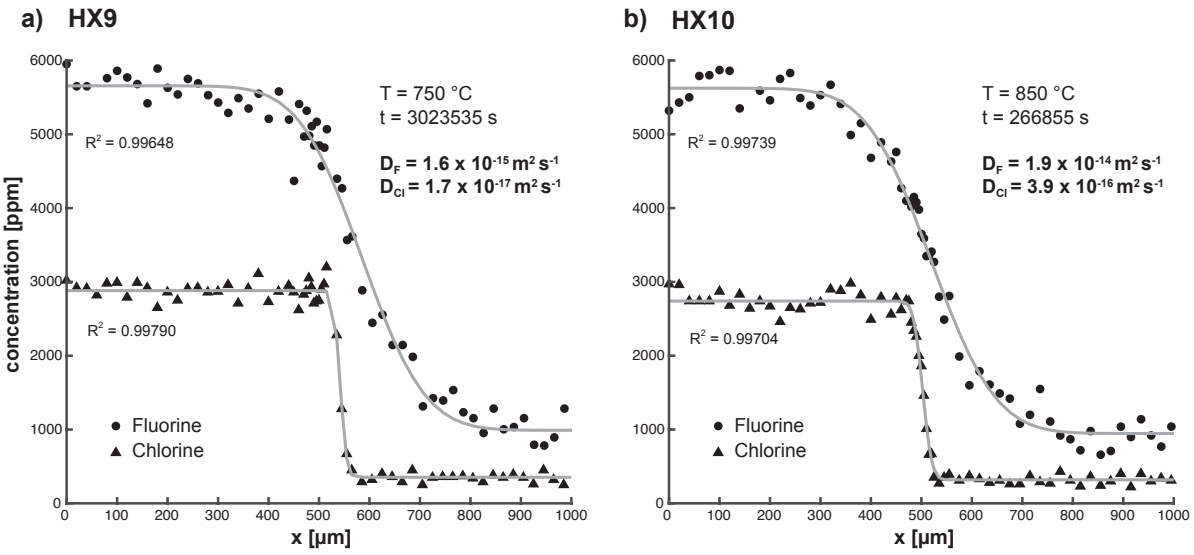

Figure 4.2: Representative concentration–distance diagrams of F and Cl obtained by electron microprobe analysis. Also shown are the corresponding fits of equation 4.1 and the respective diffusion coefficients as determined by fitting. **a)** Sample HX9 (750 °C/~35 days). **b)** Sample HX10 profile 1 (850 °C/~3 days).

Most concentration profiles show a relatively smooth transition between the enriched and the depleted halves of the sample, which is especially true for the higher temperature runs (e.g., Fig. 4.2b). Diffusion lengths, i.e., the length over which significant departure from the original concentration occurred, are up to 850 mm for F and 150 mm for Cl in the high-*T* experiments. Experiments run at lower temperatures developed only short diffusion profiles (several tens of micrometers), especially those of Cl. Profiles of Cl concentration in sample HX6 (750 °C) were particularly short with only a few points falling in the transition zone between enriched and depleted end-members. Samples HX3 (850 °C) and HX4 (800 °C) had lower maximum concentrations than all other experiments, supposedly due to our use of a piece of glass that was positioned close to the surface of the stirred sample. Therefore, three additional experiments were performed at the lowest temperatures (750, 800, and 850 °C) running for longer experimental duration to improve the diffusion width and thus data quality. However, as diffusivity has previously been shown to be concentration-independent (e.g., Dingwell and Scarfe, 1984; Bai and Koster van Groos, 1994; Baker and Balcone-Boissard, 2009; Zhang et al., 2010) we included the data of HX3 and HX4 in the results.

The diffusion coefficients for each profile and each species were calculated by fitting the concentration data to the concentration-independent equation for constant one-dimensional diffusivity between two semi-infinite media in a cartesian coordinate system (Crank 1975):

$$C(x,t) = \frac{C_{high} + C_{low}}{2} + \frac{C_{high} - C_{low}}{2} \operatorname{erf}\left(\frac{x - x_0}{\sqrt{4\,D\,t}}\right) \quad (4.1)$$

where $C(x,t)$ is the concentration (ppm) at distance x (m) after the experimental time t (s). C_{low} (ppm) and C_{high} (ppm) are the concentrations of the respective halogen-poor and halogen-enriched starting glasses. Parameter x_0 describes the position of the diffusion interface between the two individual media and D (m^2/s) is the diffusion coefficient. The term *erf* defines the error function.

Parameters D, x_0, C_{low}, and C_{high} were determined by fitting equation 4.1 to the respective data. Analyses with totals below 97 wt.% or F and Cl values below 2 times the detection limit (120 ppm, 2s) were discarded. Fitting was carried out using the nonlinear least-squares method implemented in a *Matlab*-based computer program. The program is easy to use, offers control over all important parameters and provides the user with information about the goodness of fit (e.g., R^2, plot of residuals, etc.) and confidence intervals calculated from the fit. Additionally, the user can fix C_{low} and C_{high} when necessary, e.g., when the profile obtained by EMPA is too short to cover the end-member concentrations of the starting glasses, but information about the highest and lowest concentrations is available from another profile analyzed in the same sample. The results obtained by using this program were validated by cross-checking some results with commercially available curve-fitting software (*CurveExpertPro*). Before fitting the data were filtered for outliers. All calculated diffusion coefficients are compiled in Table 4.2 together with the experimental conditions.

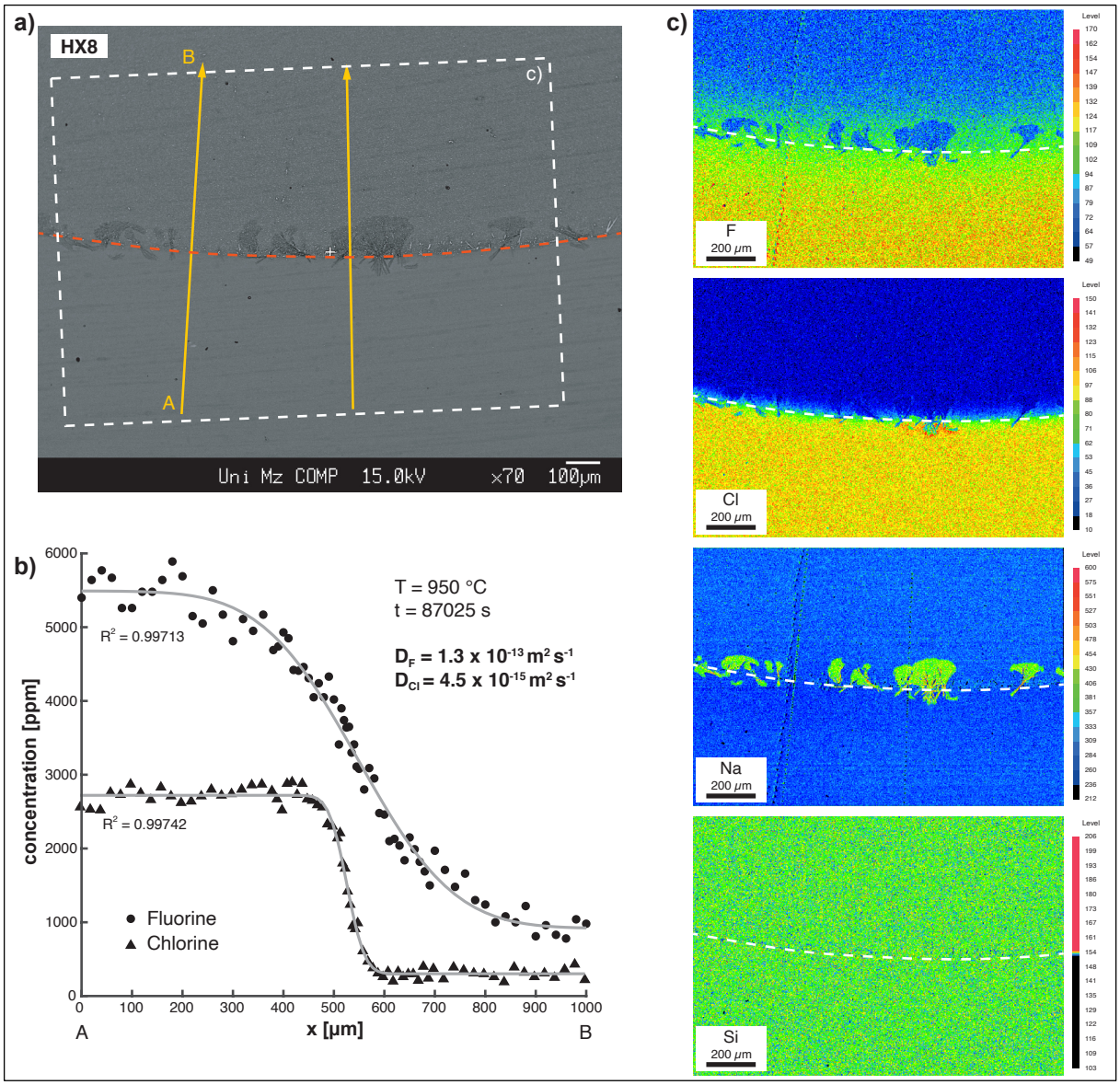

Figure 4.3: Results of point- and map-analysis of sample HX8 (950 °C). **a)** Backscattered electron image showing the slightly bent diffusion interface and irregular lower density patches (darker). Yellow lines show the position of two profiles acquired with point-analysis. **b)** Diffusion concentrations determined for F and Cl along the left profile in a), from A to B. **c)** Compositional maps of F, Cl, Na, and Si. Maps of F and Cl show a clear concentration gradient parallel to the diffusion interface. Note the high homogeneity of Si and Na apart from irregular patches of Na enrichment. Please see text for further discussion.

Table 4.2: Conditions and results of all experiments.

Sample	*T* [°C]	Time [s]	profile #	D_F	±[a]	C_{max}	C_{min}	D_{Cl}	±[a]	C_{max}	C_{min}
HX6	750	851880	1	1.6E-15	3.8E-16	5428	944	5.2E-17	7.8E-17	2647	292
			2	2.1E-15	5.7E-15	5473	988	7.5E-17	4.0E-17	2710	320
HX9	750	3023535	1	1.6E-15	4.3E-16	5657	996	1.7E-17	8.4E-18	2881	353
HX4	800	359334	1	2.6E-15	9.1E-16	3355	548	4.6E-17	3.5E-17	1083	189
			2	3.2E-15	1.3E-15	3409	498	8.6E-17	1.3E-16	1057	188
HX7	800	587235	1	6.6E-15	1.6E-16	5549	758	4.9E-17	1.4E-17	2732	257
			2	1.1E-14	1.9E-15	5580	671	1.6E-16	4.2E-17	2714	291
HX3	850	171502	1	1.6E-14	5.0E-15	3829	1045	3.9E-16	2.0E-16	1534	326
			2	1.9E-14	5.9E-15	3928	1014	4.5E-16	2.4E-16	1471	319
HX10	850	266855	1	1.9E-14	4.4E-15	5624	947	3.9E-16	1.2E-16	2740	318
			2	2.0E-14	5.1E-15	5482	970	7.4E-16	4.0E-16	2733	315
HX5	900	154560	1[b]	4.7E-14	6.7E-15	5186	501	1.0E-15	2.0E-16	2762	222
			2	4.6E-14	8.9E-15	5186	501	8.7E-16	1.9E-16	2758	196
HX8	950	87025	1	1.3E-13	2.5E-14	5491	917	4.5E-15	1.1E-15	2721	302
			2	1.1E-13	1.4E-14	5304	993	1.5E-15	6.7E-16	2715	294
HX2b[c]	900	83400	1	4.7E-14	9.3E-15	5507	832	1.4E-15	4.8E-16	2726	310
			2	3.4E-14	9.2E-15	5320	859	1.3E-15	4.0E-16	2747	311

[a] 95 % confidence interval calculated from the fit.

[b] C_{max} and C_{min} of F fixed from profile 2.

[c] Experiment run at 100 MPa.

4.3.2 Temperature dependence of F and Cl diffusion

Diffusion coefficients of both F and Cl increase with increasing temperature (Fig. 4.4, Table 4.2). The calculated diffusion coefficients for F range from 1.6 x 10^{-15} m^2/s (750 °C) to 1.3 x 10^{-13} m^2/s (950 °C). Those for Cl are up to 2 orders of magnitude smaller and range from 1.7 x 10^{-17} m^2/s (750 °C) to 4.5 x 10^{-15} m^2/s (950 °C). Diffusion profiles acquired in a single sample may yield slightly different diffusion coefficients (F: <0.2 log units; Cl: <0.5 log units, both except HX7) that partly accounts for the variability in diffusivities, cast in terms of an uncertainty value. However, the results for one sample are in general within the same order of magnitude. Experiment HX2b that was run at an elevated pressure of 100 MPa and 900 °C yielded diffusion coefficients of F and Cl comparable to those obtained at atmospheric pressure and the same temperature (Table 4.2). We therefore conclude that pressure does not play a significant role in modifying F and Cl diffusion in rhyodacitic melt over a *P-T* range relevant for volcanic processes. This agrees well with the findings of other recent studies (Baker and Balcone-Boissard, 2009; Zhang et al., 2010; Böhm and Schmidt, 2013).

As shown in previous studies, F and Cl diffusion in silicate melts follow Arrhenian behavior described by the following equation:

$$D = D_0 \, e^{-\frac{E_A}{\mathrm{R}\,T}} \tag{4.2}$$

where D is the diffusion coefficient ($m^2\,s^{-1}$), D_0 is the pre-exponential factor ($m^2\,s^{-1}$), E_A is the activation energy (J mol^{-1}), R is the universal gas constant (8.3145 J mol^{-1} K^{-1}), and T is the temperature (K). To determine the constants D_0 and E_A necessary to describe diffusion behavior of the individual species, the diffusion coefficients calculated with equation 4.1 are plotted in an Arrhenius diagram of log(D) vs. 10000/T (K) (Fig. 4.4) and the data are fitted to the linear equation:

$$\log(D) = -\frac{E_A}{\ln(10)\,\mathrm{R}\,T} + \log\,(D_0) \tag{4.3}$$

E_A correlates with the slope of the line in the Arrhenius diagram, and D_0 represents the intercept at 10000/T = 0. From our experiments we calculated pre-exponential factors of D_0 = 4.3 x 10^{-4} for F and D_0 = 1.6 x 10^{-5} for Cl. The activation energies of F and Cl are similar [E_A(F) = 223.7 ± 31 kJ mol^{-1}; E_A(Cl) = 229.1 ± 52 kJ mol^{-1}] as can be seen from the slopes of the trendlines. The uncertainty values of the activation energies represent the 95% confidence interval calculated during fitting.

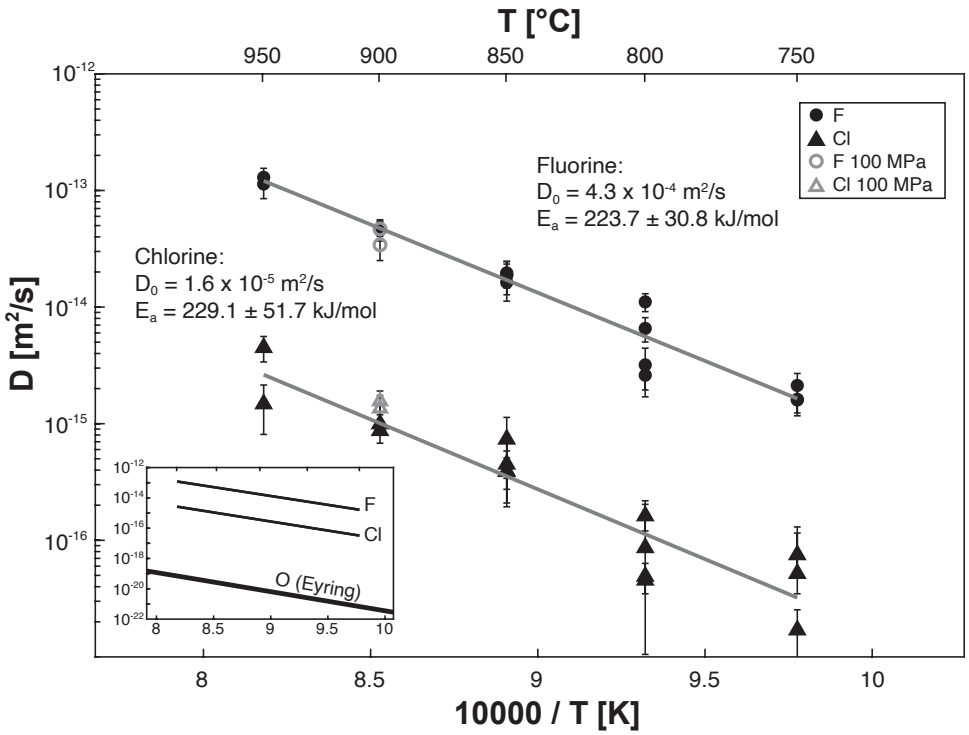

Figure 4.4: Diffusion coefficients for F and Cl determined in this study plotted on an Arrhenius diagram. Solid symbols represent experiments at 1 atm while open gray symbols represent pressurized conditions (100 MPa). Results from the 100 MPa series have not been used for fitting. The inlet shows the position of the Arrhenius laws of F and Cl relative to the calculated self-diffusion of oxygen. See text for further explanation. Error bars correspond to the 95 % confidence interval calculated from fitting of the diffusion coefficients. Errors in x-direction are within the symbol size.

4.3.3 Experimental and analytical uncertainties

The errors given for the diffusion coefficients (Table 4.2) were calculated during the fitting process and represent the 95% confidence intervals based on the fitted data points only. However, other sources of uncertainty that may have affected the final Arrhenius parameters include heating and quenching times, spot distance, accuracy of temperature measurements and homogeneity of the glass. After the experiments, few microlites (<1 vol%) were present in some samples. In particular, some apatite crystals up to 30 mm length crystallized close to the interface mainly in the halogen- depleted sample. However, because we selected analysis traverses so as to avoid these microlites, we did not observe anomalous F and Cl concentrations. In some samples, small patches of F-depletion and Na-enrichment developed close to the interface (Fig. 4.3). However, those patches are recognizable from the backscattered images and were either avoided for diffusion profile acquisition or corrected for during data reduction.

Due to the long experimental durations used (minimum 1 day), the short heating and quenching times with a maximum of 5 min are considered to have minor effects only. For example, for sample HX8 that had the shortest experimental duration of 87025 s (~1 day) the diffusion coefficients for F and Cl would

change by only ±0.01 x 10^{-13} or 0.02 x 10^{-15}, respectively, (both <1%), for experimental durations varying ±5 min. These values are well within the calculated 95% confidence intervals. For longer experimental durations the error induced by 5 min of heating and quenching would be even smaller. For example an error of 2 h on the experimental duration of sample HX9 (750 °C; ~35 days) would change the resulting diffusion coefficients for F and Cl by less than 1%. As is shown in the results section, the diffusivities of F and Cl are exceedingly slow, which precludes the development of a significant concentration profile at the relatively short time scales of heating and quenching (max. 10 min total). Even at the highest temperature investigated, well-defined profiles of 500 µm needed one day to develop. Therefore, zero-time experiments have not been carried out. To assess the error introduced by a non-perfect angle between the analyzed profile and the diffusion interface we used the same samples (HX8 and HX9) and calculated the diffusion coefficients for the case that the profile was not perfectly perpendicular to the diffusion interface but tilted by up to 10 °. In this case the actual distance between each spot with regard to the diffusion interface would only be ~98% of the target distance, which results in a diffusion coefficient that is smaller by less than 4% for F and Cl in both samples. The combination of both effects discussed above (5 min longer experimental duration and diffusion profile tilted by 10 ° to the diffusion direction) would result in F and Cl diffusion coefficients both being less than 5% smaller compared to the apparent value. This is still well within the limits of the 95% confidence interval calculated from the fit of the concentration profile and is therefore covered by the given error bars. The accuracy of the measured temperature during the experimental run may have an effect on the calculation of the Arrhenian diffusion law. However, the accuracy of the thermocouple device is at least ±5 °C and the thermocouple was in direct contact with the capsule during the whole run. Therefore, we consider the effect of possible temperature deviations to be negligible compared to the relatively large 95% confidence intervals of the activation energies (Fig. 4.4).

4.4 Discussion

4.4.1 Influence of temperature

Our experiments confirm that the diffusion of both F and Cl are strongly positively correlated with temperature and follow Arrhenian behavior (Fig. 4.4). The temperature dependences of both elements, represented by their activation energies, are similar and suggest the same diffusion mechanism. However, in the temperature range investigated F diffusion is always faster than Cl diffusion, which is also true for the theoretical case of very low or very high temperatures due to the similar activation energies. The experimental temperatures were chosen according to typical natural magma storage conditions of rhyodacitic systems (e.g., Weber and Castro, 2017). Using the model of Giordano et al. (2008) a glass transition temperature (T_G) of 687 °C for the depleted half and 692 °C for the enriched half of the diffusion couple was calculated. We consider no significant diffusion to happen below T_G,

which is supported by the fact that diffusion at 750 °C was already so slow it took weeks to develop proper diffusion profiles. Furthermore, at these low temperatures the halves of the diffusion couple did not weld together perfectly over the whole interface, so at lower temperatures the conditions necessary for a diffusion couple would not have been given. However, diffusion at lower temperatures could still take place and could be significant in scenarios of very slow magma ascent rates (e.g., Boudon et al., 2015), or during post-eruptive lava-flow degassing (e.g., Schipper et al., 2015; Schipper et al., 2019) rather than explosive eruptions.

4.4.2 F and Cl diffusion in different melt compositions

Figure 4.5 illustrates the results of all published studies on F and Cl diffusion in silicate melts (Watson and Bender, 1980; Dingwell and Scarfe, 1984; Dingwell and Scarfe, 1985; Bai and Koster van Groos, 1994; Alletti et al., 2007; Balcone-Boissard et al., 2009; Böhm and Schmidt, 2013; Fortin et al., 2017; Yoshimura, 2018). Only the results of anhydrous experiments are shown for better comparability to our study. In general, diffusion coefficients in different silicate melt compositions vary by three orders of magnitude for both F and Cl. Melts of basaltic composition yield the highest diffusivities compared to studies on other compositions such as phonolite, dacite or rhyolite. Dingwell and Scarfe (1984, 1985) were the first to study the diffusion of F in different synthetic silicate melt compositions. Their results for jadeite melt are comparable to those of Alletti et al. (2007) who investigated melts of natural basaltic composition and also studied Cl diffusion. Phonolitic compositions in general yield slower diffusion coefficients for F and Cl with the exception of potassic phonolite from the Laacher See eruption that yields F diffusivities similar to those of basalt (Balcone-Boissard et al., 2009). Böhm and Schmidt (2013) also studied a natural phonolitic composition but at lower temperatures that are potentially more significant to natural systems. They found intermediate diffusivities for F but lower diffusivities for Cl compared to other phonolitic compositions. Watson and Bender (1980) studied tracer diffusion of Cl in a synthetic melt composition and found results similar to basaltic compositions of Alletti et al. (2007).

When our data are extrapolated to the temperature range that has been used by many previous studies (~1200–1450 °C), F diffusivity plots close to, yet below that in basalt, jadeite or Na-phonolite, having a very similar activation energy as this determined for dry basalt (Fig. 4.5a). For Cl, even when the data are extrapolated to high temperatures, diffusivity in our samples is still about one order of magnitude slower than in Na-phonolite and dacite, and even slower compared to other melts (Fig. 4.5b).

Studies investigating a similar, silicic melt composition are those of Bai and Koster van Groos (1994), Fortin et al. (2017), and Yoshimura (2018). Bai and Koster van Groos (1994) studied Cl diffusion in granitic and haplogranitic melts using different approaches of which the “high-temperature series” is the most similar approach to our study. This set of experiments was run with haplogranitic melt at atmospheric pressure and under dry conditions in a temperature range from 850–1400 °C. They found

a pre-exponential factor of D_0 = 3.16 x 10^{-9} and a relatively low activation energy of E_A = 86.2 kJ mol^{-1}. By contrast, our study presents an almost three times larger activation energy and 5 orders of magnitude larger pre-exponential factor resulting in significantly slower diffusivities than those suggested by Bai and Koster van Groos (1994). This discrepancy is most likely a result of the simplified melt compositions and experimental approaches. Bai and Koster van Groos (1994) equilibrated haplogranitic melt with molten NaCl instead of using a diffusion couple. This way not only diffusion but also partitioning from the molten NaCl into the melt may influence the results. Yoshimura (2018) used three different experimental setups based on the absorption of Cl to a piece of natural obsidian. The source of Cl was either Cl_2, Cl_2 + H_2O, or molten NaCl. At 750 and 950 °C and under mostly dry conditions he found D_{Cl} = 2.0 x 10^{-17} m^2/s and D_{Cl} = 3.1 x 10^{-16} to 3.3 x 10^{-15} m^2/s, respectively. The lower temperature results (~750–800 °C) are based on molten Cl_2 as Cl source and agree well with our findings at the same temperatures. However, at higher temperatures (>800 °C) this experimental series yields slower diffusion than our experiments. Instead, the higher value of his 950 °C results, based on molten NaCl as Cl source, are similar to our results. It is likely that the results of both of these studies are affected by other mechanisms than pure diffusion, such as solubility and depolymerization of the melt due to Na-infiltration (Yoshimura, 2018), of which the latter would result in increased diffusivity. In addition to Na-infiltration, the simplified haplogranitic melt composition used by Bai and Koster van Groos (1994) has likely caused increased diffusivity as a result of the availability of more vacancies within the melt structure compared to a natural melt. The application of their results to natural systems and a direct comparison to our study is therefore difficult. The general results of Fortin et al. (2017) who studied diffusive fractionation of Cl-isotopes in a dacitic melt are comparable to those obtained in our experiments, even though their data were collected at higher temperatures. The enhanced diffusivity in the dacite melt may be explained by the lower content of SiO_2 in addition to the higher amount of network modifying cations (e.g., Fe, Mg) compared to the rhyodacitic composition investigated in this study.

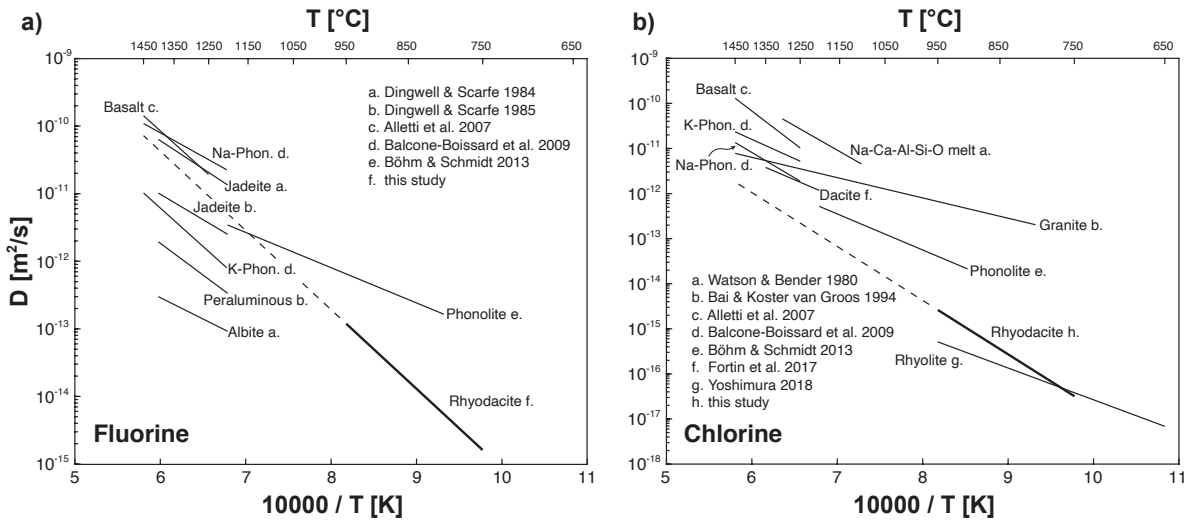

Figure 4.5: Overview of Arrhenian diffusion for different melt compositions determined in this and other studies. **a)** Fluorine, **b)** chlorine. Results of experiments using dry compositions are shown only. Bold lines represent data obtained in this study and dashed lines show the same data extrapolated to higher temperatures. Note the different y-axis scaling between the diagrams.

4.4.3 Effects of melt structure on diffusion

It has been shown in the past that diffusion is highly dependent on the composition of the medium and on its structure (e.g., Jambon and Semet, 1978; Margaritz and Hofmann, 1978; Lowry et al., 1982; Henderson et al., 1985). Typical natural melt compositions comprise a wide range of chemical compositions and vary greatly in their structure, which is determined by various parameters such as the amount of SiO_2, network modifying cations, volatiles, and the resulting degree of polymerization, defined by parameters such as NBO/T, i.e., the ratio of non-bridging oxygen atoms over tetrahedally coordinated ions (Mysen, 1988). The classic interpretation that diffusion in silicate melts depends strongly on the radius of the diffusing element has been shown to be true mainly for noble gases and monovalent cations (Henderson et al., 1985; Lux, 1987; Alletti et al., 2007). This strong correlation of diffusivity and atomic radius was interpreted to indicate the movement of these elements through vacancies in the melt structure (Henderson et al., 1985). For divalent and trivalent cations this correlation does not apply; instead the diffusivities of those elements seem to be mostly independent of their respective ionic radius. Rather, Henderson et al. (1985) propose diffusion of divalent and trivalent elements is dominantly controlled by exchange mechanisms that preserve local charge balance and is therefore mainly dependent on the proportion of network modifying cations. Fig. 4.6a illustrates the correlation of atomic radius and diffusivity of the most recent studies on halogen diffusion. The data shown represents diffusivities at 1250 °C. As our study and that of Böhm and Schmidt (2013) only provide data up to lower temperatures, diffusion coefficients have been scaled to 1250 °C using equation (4.2). Data of Alletti et al. (2007) follow a behavior similar to di- and trivalent elements for F, Cl, and Br in natural basaltic melt, observing almost no correlation between the diffusion coefficient and the

atomic radius of the diffusant. Therefore, they interpret the diffusion of halogens in basaltic melt to be dominated by exchange mechanisms. Our data instead show consistently slower diffusion of Cl that has a larger radius than F. Other recent experimental data, which was mostly obtained from phonolitic compositions also shows a correlation between the diffusivity and the atomic radius, even though very variable and not as strong as observed in our experiments. The correlation of the variable diffusivity between F and Cl and their atomic radius in more evolved melts suggests that the degree of polymerization does have an influence on diffusion and the diffusion mechanism. For a better estimate of the degree of polymerization of the different melts, we calculated NBO/T and the network modifier parameter (SM) for the melts discussed. For NBO/T we followed the method of Mysen (1988) and split FeO_{tot} equally (wt.%) between Fe_2O_3 and FeO (Giordano et al., 2008). SM was calculated after Giordano and Dingwell (2003) as the molar oxide sum of network modifiers: $SM = \Sigma(Na_2O + K_2O + CaO + MgO + MnO + FeO_{tot}/2)$ [mol%]. The highest SM value (~32) and the highest NBO/T ratio (0.5) corresponds to the basaltic melt of the study of Alletti et al. (2007), which comprises the fastest diffusion and almost no correlation between the atomic radius and the diffusion coefficient. In contrast, the rhyodacitic melt used in our study has the lowest NBO/T ratio (0.04) and the lowest SM (~12) among previous studies and yielded generally slow diffusion with diffusion coefficients of F and Cl differing by up to two orders of magnitude. The phonolitic melts (Balcone-Boissard et al., 2009; Böhm and Schmidt, 2013) that yield intermediate diffusivities range between NBO/T = 0.08–0.09 with SM ~18–20. However, the K-phonolite series shows only weak correlation between diffusivity and atomic radius similar to the basaltic melt. Figure 4.6b shows the correlation between parameter SM and the diffusion coefficient of this and other recent studies. From the diagram, it can be seen that diffusivities of F and Cl are expected to be similar at higher SM but deviate significantly with decreasing SM.

In basaltic melts where the proportion of network modifying cations (i.e., SM) is sufficiently high and polymerization is relatively low, diffusion is likely dominated by the charge balancing exchange of ions. As this mechanism mainly depends on the charge of the diffusant, the atomic radius has no significant influence on the diffusion behavior. In more highly polymerized melts with lower SM, ion-exchange is less efficient and diffusion along vacancies in the melt structure becomes more important. However, among elements of the same charge, this mechanism is likely most efficient for those with a small atomic radius, which potentially explains the observed differences in diffusivity between F and Cl in our and other studies. Even though the correlation between *D*, the proportion of network modifying cations and atomic radius becomes clear with these results there is still the need to investigate the diffusion behavior of other halogens (Br and I) and more intermediate silicate melts to validate and refine this hypothesis.

In addition to the obtained diffusion data, the viscosity of the sample material was measured by micro-penetration at three different temperatures (690, 720, and 750 °C). The viscosities were used to calculate the Eyring diffusivity of oxygen in our melt using the following equation (Glasstone et al., 1941):

$$D = \frac{k_B T}{\lambda \eta} \tag{4.4}$$

Where k_B is the Boltzmann constant (J K^{-1}), T is temperature (K), h is the viscosity (Pa s), and l is the effective jump distance of the diffusant (m), in this case, oxygen (2.8 Å, Shimizu and Kushiro, 1984). The obtained diffusion coefficients were in turn fitted to the Arrhenius equation to extrapolate the Eyring diffusivity to higher temperatures, relevant for our experiments. The calculated diffusivity of oxygen plotted in an Arrhenius diagram has a similar slope (i.e., activation energy) as F and Cl but is located more than 4 orders of magnitude below Cl diffusivity (Fig. 4.4 inset). With this high contrast in diffusivity, the Si-O bonds in the melt appear to behave as if in fixed structural sites relative to the diffusing F- and Cl-ions (Dingwell, 1990; Dingwell and Webb, 1990), so their diffusion is not affected by self-diffusion of the silicate structure over the relevant timescales. At higher Eyring mobilities, i.e., lower viscosities, the jump frequency of Si-O bonds would approach the jump frequency of the investigated diffusant and by this the observed diffusivity of F and Cl would likely be increased, as each Si-O jump would allow the diffusing ion to jump to another site as well. Even though the Eyring equation does not predict oxygen diffusivity perfectly (e.g., Liang et al., 1996), it still gives a good approximation of the structurally defined lower limit of transport rates in the melt.

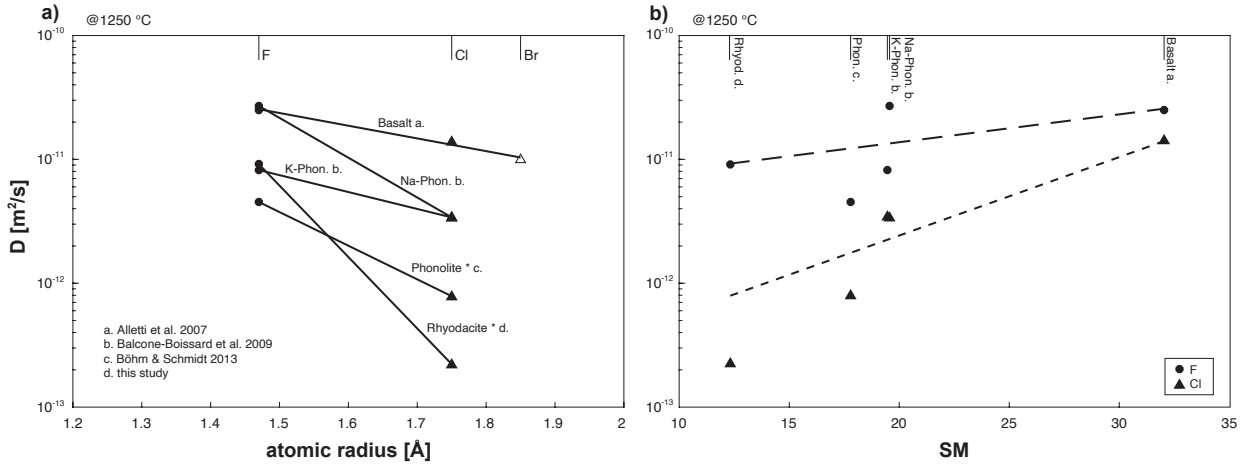

Figure 4.6: Diagrams showing the correlation of diffusivity with the atomic radius and the sum of the network modifying cations of this and other recent studies. **a)** Atomic radius vs. *D*. *D* of basalt and Na-phonolite show only weak correlation with the atomic radius, while diffusion in rhyodacite is strongly correlated. Lines marked with "*" are calculated from equation 4.2. **b)** Diffusivity of F and Cl as a function of the proportion of network modifying cations in the host melt, represented by the parameter SM (= $\Sigma Na_2O + K_2O + CaO + MgO + MnO + FeO_{tot}/2$ [mol%]). Dashed lines indicate a simplified exponential fit of the form $y = ae^{bx}$ for each set of data points. As they both represent the same SM value, Na- and K-phonolite together have been accounted for as one datapoint with averaged *D*. All diffusivities presented are for anhydrous conditions at 1250 °C. See text for further discussion.

4.4.4 Potential for diffusive fractionation

The diffusivities presented in this study are based upon experiments utilizing dry melt. The main driving force for the growth of bubbles in a natural magma, is however, the exsolution of H_2O and CO_2, neither of which is present in our experimental melt. The following discussion of diffusive fractionation is therefore hypothetical, and based on the assumption that the ratio of diffusivities between F and Cl is equal in dry and wet rhyodacitic melt, which has been shown to be largely the case for other silicic melt compositions by previous studies (e.g., Baker and Balcone-Boissard, 2009).

As shown previously, diffusivities of F and Cl differ by up to 2 orders of magnitude. This variation is likely to produce fractionated volatile compositions during bubble growth, with the faster diffusing F being enriched in the volatile phase compared to the slower diffusing Cl. Recent studies showed that even with only small differences in diffusivity, fractionation can be significant (e.g., Fortin et al., 2017) but is highly dependent on the ratio of the bubble growth rate (R) and the diffusivity (D) [(R/D) Watson, 2017], and of course assuming the same vapor-melt partition coefficient (K) for both diffusants. Watson (2017) discussed this relationship on the basis of different isotopes of the same volatile element, which have the same vapor-melt partition coefficient but small differences in diffusivity and showed that purely diffusive fractionation in bubbles up to 10 mm is most pronounced at R/D values $<10^4$ m^{-1}. However, while the same principles generally apply for other diffusing volatile elements such as F and Cl, the vapor-melt partition coefficient cannot be assumed to be identical for both of these elements and thus could greatly influence the exact relative behavior of F and Cl during bubble growth and degassing. In particular, F is known to behave paradoxically in silicate melts, in that it exhibits high solubility in silicic melts (Carroll and Webster, 1994) and usually prefers partitioning into melt rather than aqueous fluid (e.g., Lowenstern et al., 2012). However, F degassing during volcanic eruptions is commonly measured, e.g., in volcanic plumes and fumaroles, and preferred partitioning into the vapor phase has been determined experimentally in basaltic compositions (Baker and Alletti, 2012). F partitioning may also be influenced by late-stage crystallization of magma, the so-called “second boiling” process. For example, Schipper et al. (2019) showed based on glass inclusion analysis that only 2 wt.% of F and 7 wt.% of Cl were degassed during the 2011–2012 Cordón Caulle eruption’s explosive phase, but the bulk of these halogens were later degassed during lava flow emplacement and coincident syn-eruptive laccolith intrusion (Castro et al., 2016). Schipper et al. (2019) postulate that late-stage crystallization of the lava and laccolith played a key role in driving otherwise soluble F out of the melt and into degassing pathways. In summary, the lack of accurate, composition-specific data on the partitioning behavior of F hinders precise modeling of diffusive fractionation of F and Cl during bubble growth. Future experimental efforts could profitably focus on constraining F partitioning in various melt compositions and under a range of different degassing regimes (e.g., open vs. closed system).

We speculate that diffusive fractionation will be most important when magma ascent rates are slow enough to favor significant transport of F and Cl to growing bubbles, which in turn depends on the characteristic spacing of bubbles within the melt, as determined by bubble number density and size distribution (Gonnermann and Manga, 2007). We therefore propose that diffusive halogen fractionation may be most significant during scenarios of slow mass effusion such as lava dome forming eruptions or the slow cooling of lava flows or shallow intrusions (Castro et al., 2016; Schipper et al., 2019).

4.5 Implications

Diffusion of F and Cl in dry rhyodacitic melt was characterized experimentally using the diffusion couple technique. Even though the temperature dependence of the two is very similar, there is a large difference in diffusivity over the temperature range investigated, which suggests that diffusive fractionation with an increasing F/Cl ratio is a possible outcome of magma degassing under conditions of relatively slow ascent and bubble growth, as would be expected during lava dome formation. Diffusion of F and Cl was shown to be generally slower in our rhyodacitic melt compared to basaltic or other simplified silicate melts. We interpret this to be related to the higher degree of polymerization in the rhyodacite melt. This is supported by the fact that the correlation between the atomic radius of the diffusing component and its diffusivity is more pronounced in more silicic, more viscous melts. We propose that concentrations of F and Cl in volcanic gases, when monitored, could help identify volcanic unrest. However, for a comprehensive understanding of diffusive fractionation during degassing, knowledge of halogen fluid/melt partition coefficients in a range of melt compositions are still needed, in addition to other parameters such as bubble nucleation and growth rates under diverse magma ascent scenarios. With these important factors in hand, we anticipate future modeling-based studies on diffusive fractionation processes at volcanoes (e.g., Watson, 2017).

4.6 Acknowledgements

We thank B. Scheu, U. Küppers, and K.-U. Hess for their assistance during sample preparation and N. Groschopf and S. Buhre for their assistance with electron microprobe analyses. B. Watson, H. Balcone-Boissard, and one anonymous reviewer are thanked for their insightful comments that helped to improve this paper.

4.7 Funding

This research is part of the Ph.D. thesis of Y. Feisel and is supported a fellowship of the Gutenberg Research College of the Johannes Gutenberg-University of Mainz to D.B. Dingwell. Additional support was provided by the VAMOS research center of the Johannes Gutenberg-University.

Supplementary Material

Supplementary Figures (Fig. S1 and S2) can be found and downloaded online from *American Mineralogist*:

Deposit item AM-19-117095, Supplemental Material. Deposit items are free to all readers and found on the MSA website, via the specific issue's Table of Contents (go to http://www.minsocam.org/MSA/AmMin/TOC/2019/Nov2019_data/Nov2019_data.html).

Chapter 5

Diffusion of halogens (F, Cl, Br, I) in silicic melt[3]

Abstract

Chemical diffusion of the halogens F, Cl, Br, and I in silica-rich natural melts was experimentally investigated by the diffusion couple technique. Experiments were conducted under anhydrous conditions at atmospheric pressure and hydrous conditions (~1.5 wt.% H_2O) at 160 MPa, over a temperature range of 750–1000 °C and 1000–1200 °C, respectively. Quenched trachytic melt samples were analyzed using an electron microprobe (EMPA) and secondary ion mass spectrometry (SIMS). All halogens exhibit Arrhenian behavior during diffusion in the investigated melt compositions with F always diffusing fastest. The other halogens show progressively slower diffusion (F > Cl > Br > I) correlated to their ionic radii. In anhydrous melt a diffusivity range of 3–4 orders of magnitude is covered among the halogens with D_F(1000 °C) ~5×10^{-13} m^2s^{-1} and D_I(1000 °C) ~1×10^{-16} m^2s^{-1}. The diffusivities of all halogens increase in hydrous melt yielding for example D_F(1000 °C) ~ 3×10^{-12} m^2s^{-1}. However, the largest increase is observed for the slowest-diffusing halogens, resulting in a narrower overall diffusive range of only 1–2 orders of magnitude with iodine diffusivity yielding D_I(1000 °C) ~9×10^{-15} m^2s^{-1}. Activation energies (E_A) of all halogens consistently range from ~200–290 kJ mol^{-1} in anhydrous melts. In hydrous melt E_A generally decreases, with the highest decrease determined for F (~131 kJ mol^{-1}) and only slight changes for the other halogens (~201–222 kJ mol^{-1}). Our diffusivity data of the anhydrous series exhibit a pronounced correlation of diffusivity with the ionic radii, suggesting that halogen diffusion in highly polymerized melt is closely related to the melt's ionic porosity. The correlation between diffusivity and ionic radius is only weakly observed in the hydrous experiments indicating that the ionic porosity is sufficiently large to weaken the rate-limiting effect of the ionic radius due to the more depolymerized melt structure in the hydrous case. In hydrous experiments, the process of ionic detachment becomes more important as a rate-limiting diffusion mechanism, comparable to the case of diffusion of divalent/trivalent cations or halogen diffusion in basaltic melt. The results of this study provide the first consistent diffusion dataset including all halogens under naturally relevant magmatic conditions and highlight the pronounced compositional effect of both, major element and dissolved H_2O on halogen diffusion. These data emphasize the potential of diffusive fractionation among the halogens,

---

[3] This chapter was submitted by Feisel, Y, Castro, J.M., Helo, C., Bouvier, A.-S., Ludwig, T., and Dingwell, D.B. and is currently *under review* for publication in *Geochimica et Cosmochimica Acta*.

especially in a melt of low water content, which may be applied as a monitoring tool for volcanic unrest on actively degassing volcanoes.

Keywords: halogens (F, Cl, Br, I); diffusion couple; ionic porosity; iodine; silicate melt

5.1 Introduction

Volatiles are among the most influential constituents of natural silicate magmas. They affect various chemical and rheological melt parameters, which in turn have crucial implications for individual volcanic eruption behavior. Typically, volcanic volatiles are dominated by water (H_2O) and carbon dioxide (CO_2), however, sulfur-species (e.g., SO_2) and halogens, mainly F and Cl, can reach significant concentrations (up to few wt.%) in silicic melts and volcanic gases (e.g., Aiuppa et al., 2009; Dolejš and Zajacz, 2018). Halogens are known to exert strong effects on the physico-chemical properties of silicate melts such as melt viscosity or phase equilibria (e.g., Manning, 1981; Mysen and Virgo, 1985; Webster et al., 2018). For example, F is known to reduce the viscosity of silicic melts to a similar degree as added H_2O (Dingwell et al., 1985; Dingwell and Hess, 1998; Zimova and Webb, 2007; Giordano et al., 2008; Baasner et al., 2013a), and can depress the isobaric liquidus temperature in basalt (e.g., Filiberto et al., 2012) and felsic melts (e.g., Dolejš and Baker, 2007a, 2007b). Even though more complex, substantial effects on the liquidus temperature have also been reported for Cl-bearing natural melts of both basaltic (e.g., Filiberto et al., 2014; Farcy et al., 2016) and silicic systems (Feisel et al., 2022). The physico-chemical effects of added Br and I to a melt are, by contrast, far less understood. Concentrations of Br and I are typically lower than those of F and Cl, consistent with an increasing fluid-melt partition coefficient with increasing ionic radius of Cl , Br and I (181, 196 and 220 pm, respectively; Bureau et al., 2000). F (133 pm) instead has an ionic radius very similar to O^{2-} and OH^- (140 and 137 pm; Shannon, 1976) and can therefore easily substitute for these components which promotes its solubility and compatibility in the melt (Balcone-Boissard et al., 2010).

Volcanic halogen degassing can have significant impacts on the environment and Earth's climate, for example by the depletion of stratospheric ozone by Cl and Br (Bobrowski et al., 2003; Bobrowski et al., 2007; von Glasow et al., 2009; Surl et al., 2015; Roberts, 2018). The degassing of F and Cl into isolated pores of slowly cooling magma was shown to cause etching of silica and re-precipitation of vapor-phase cristobalite (e.g., Horwell et al., 2010; Schipper et al., 2020).

Due to the high impacts that halogens can have on volcanological and environmental processes, they have received increasing attention in recent years and are routinely measured in volcanic plumes. Halogen exsolution was shown to occur at relatively shallow depths compared to the release of H_2O or CO_2 (e.g., Spilliaert et al., 2006; Schipper et al., 2019) and may therefore help to characterize volcanic degassing. Due to the large differences in diffusivity between water and the halogens, as well as amongst

halogens themselves, diffusive fractionation is expected to occur during melt inclusion entrapment or bubble and crystal growth (e.g., Alletti et al., 2007). Relative halogen (or halogen ratios) measurements in volcanic gases and plumes could therefore be applied to track diffusive fractionation processes in order to monitor volcanic activity at depth.

Even though halogen diffusion has been investigated since the 1980s our knowledge is still far from complete. It was shown that halogen diffusion is independent of its concentration and follows Arrhenian behavior in silicate melts. A weak pressure-dependence on diffusivities was reported by some authors (e.g., Dingwell and Scarfe, 1984; Bai and Koster van Groos, 1994), however, most recent studies have found only minor pressure effects (e.g., Alletti et al., 2007; Balcone-Boissard et al., 2020). Many studies focused on simplified model systems (Dingwell and Scarfe, 1984; Dingwell and Scarfe, 1985; Bai and Koster van Groos, 1994) and most investigated F and/or Cl only (Balcone-Boissard et al., 2009; Böhm and Schmidt, 2013; Fortin et al., 2017; Yoshimura, 2018; Feisel et al., 2019). To date only two studies include Br diffusion (Alletti et al., 2007; Balcone-Boissard et al., 2020) and, to our knowledge, no study has addressed iodine diffusion.

In this study we applied the diffusion couple technique on three different homogeneous melts synthesized from natural silicic pumice and lava to determine the diffusivity of all halogens (F, Cl, Br, I) over a temperature range relevant to the studied magmatic systems. Concentration profiles of F and Cl were measured by electron microprobe (EMPA) and additional profiles were acquired by secondary ion mass spectrometry (SIMS) covering all halogens. We report data for both anhydrous and hydrous (~1.5 wt.% H_2O) conditions and this is — to our knowledge — the first study to report iodine diffusion data in natural silicate melts. These results highly improve our understanding of magmatic halogen transport mechanisms at crustal conditions and expand the database of halogen diffusion to advance a thorough understanding of volcanic processes.

5.2 Methods

5.2.1 Experimental procedure

Two different starting materials were used in this study comprising glass synthesized from tephra of the Hekla (Iceland) H3 eruption (e.g., Thordarson and Larsen, 2007; Weber and Castro, 2017), and glass synthesized from natural obsidian lava of the 2011 Cordón Caulle eruption, Chile (e.g., Castro et al., 2013, 2016; Schipper et al., 2013, 2019; Alloway et al., 2015). Synthesis and experimental methods utilizing the Hekla material ("HX" series – "Hekla experiments") are described in detail in the study of Feisel et al. (2019). Synthesis of starting glass derived from Cordón Caulle obsidian lava ("CCX" series – "Cordón Caulle experiments") is described in detail in Feisel et al. (2022). The general approach used for both melts is briefly described below.

The initial sample synthesis was carried out in the laboratories of the Earth Science department of the LMU Munich. Natural obsidian was crushed, synthesized and homogenized at high temperature (1400–1550 °C) for ~2 days to produce almost completely volatile-free glass. After the first synthesis, the batch was crushed and split. One half was enriched with halogen-bearing Na-salts (NaF, NaCl, NaBr, NaI) so that each halogen would account for approximately 1 wt.% of the whole batch after mixing. The halogen-depleted split was in turn enriched with a certain amount of Na_2CO_3 to account for the sodium enrichment in the halogen-bearing glass, due to the use of aforementioned Na-salts to add halogens. Each aliquot was again synthesized and homogenized at high T before preparation of ca. 2 mm thick polished glass discs (4.6 mm diameter) and crushed glass powder to be used in anhydrous and hydrous diffusion experiments, respectively.

5.2.2 Anhydrous diffusion experiments

Diffusion couples were constructed using 5 mm platinum tube with a wall thickness of 0.2 mm. The bottom of the capsule was closed with a Pt lid which was pressed onto and welded to the tube using an arc-welder. Afterwards the bottom of the capsule was tamped into a cylindrical shape. One halogen-enriched glass disc was loaded into the bottom of the capsule and a disc of the equivalent halogen-depleted glass was loaded on top of it, resulting in both pieces touching at their polished surfaces. Each capsule was closed by welding a second lid to the top of the capsule, which ensured closed-system conditions. The diffusion experiments were carried out in a vertical tube furnace at atmospheric pressure. Each capsule was first weighed and then loaded into an alumina tube that is closed on the bottom end, making sure the halogen-depleted half was facing upwards. After the furnace equilibrated at the target temperature the alumina tube was inserted vertically into the furnace through a small opening in the top, ensuring that the capsule was sitting upright on the closed bottom of the alumina tube in the hot zone of the furnace. The temperature was monitored by the internal thermocouple and an external K-type thermocouple being in direct contact with the experimental capsule. Additionally, most experiments were monitored using a second external K-type thermocouple interfaced with an Arduino microprocessor to read the temperature remotely and store the *P-T-t* data to a computer. Temperatures are estimated to be accurate to ±2 °C based on the manufacturer's (*Omega*) reported accuracy of the thermocouple device. The experimental durations ranged from ~20 hours to 35 days depending on the temperature investigated. The time needed for the capsule to heat to the target temperature ranged between 3 and 5 minutes. The experiments were quenched by sliding the alumina tube out of the hot furnace and letting it cool in air at room temperature in an upright position. Typical cooling times to a temperature of 200 °C as indicated by the external thermocouple were in the range of 3 to 4 minutes. After each experiment the samples were weighed again to confirm closed-system conditions were maintained during the experiment.

5.2.3 H_2O-bearing diffusion experiments

Hydrous experiments were carried out using CCX starting material only and are denoted by "CCX-H". The capsule preparation followed the procedure described in Feisel et al. (2022) using powdered starting glass and Pt-tube with a diameter of 4 mm and a wall thickness of 0.2 mm as capsule material. After welding the capsule shut on the bottom and tamping into a cylindrical shape using a tight-fitting rod, ground glass powder of the halogen-enriched samples was introduced until the capsule was filled about halfway. During filling the powder was slightly tamped several times to avoid entrapment of air and ensure a flat diffusion interface. The exact amount of added sample powder was weighed using an analytical balance of 5-digit precision and the equivalent amount of 1.5 wt.% H_2O was added to the capsule using a microsyringe. The procedure was repeated using the halogen-depleted powder and again the equivalent amount of 1.5 wt.% H_2O for the top part of the capsule. Finally, the capsule was closed by welding a tight-fitting lid to the open end and tamped into cylindrical shape with a pressure of ~750 kg using a hydraulic press. Before an experiment, the capsules were repeatedly heated to ~120 °C and weighed to confirm no weight loss. Capsules with significant weight loss were discarded.

Experiments were performed in a *Deltech* vertical tube furnace fitted with a gas-pressurized TZM (Tungsten Zirconium Molybdenum) cold-seal pressure vessel assembly. The sample capsule is loaded into the cold-seal assembly which is connected to a stainless-steel high-pressure tubing using Argon gas as a pressure medium. To mitigate water-loss from inside the capsule to the Ar-atmosphere ca. 0.3 MPa of CH_4 was inserted to the pressure system before pressurizing with Ar (e.g., Sisson and Grove, 1993; Szramek et al., 2006; Shea and Hammer, 2013). The cold-seal assembly consists of an inner autoclave made of TZM (~30 mm outer, ~6.5 mm inner diameter) and an outer sheath made of Inconel (~50 mm diameter, 5 mm wall thickness), both attached to a water-cooled base on the bottom. The outer sheath slides over the inner autoclave leaving ~5 mm between the two. This space is constantly purged with Ar during the experiment to provide a non-reactive atmosphere for the inner pressurized autoclave. The inner autoclave is tightened against a steel cylinder via a doubly coned and sealed small Beryllium-bronze cylinder ("football"-shape) between the two. A second, lower vessel made of stainless steel is attached to the bottom of the water-cooled coupling base and is connected to the pressure line on the bottom with a high-pressure fitting. The sample capsule sits in a small cup which in turn is attached to an Inconel rod which is inserted into the bottom of the steel cylinder. A magnet at the bottom of the rod allows for the control of the position of the sample capsule in the assembly from the outside using a neodymium ring-magnet that slides over the lower steel cylinder. The whole assembly including the experimental capsule is inserted into the vertical tube furnace from the bottom before it is brought up to the target temperature and pressure. The pressure is generated by an HIP GB-60 gas booster device operated with compressed air and conveying Ar gas as a pressurizing medium.

During the time of heating, the capsule remains in the water-cooled part of the assembly (rapid-quench coupler) which is outside the furnace and constantly flushed with water (~15 l/min). When the target *P-T* conditions are reached and equilibrated, the experiment is started by upward movement of the sample holder using the outer magnet. In this way, the capsule is — within seconds — brought into the top part of the TZM autoclave, which is in the hot zone of the furnace. Quenching is done the opposite way by sliding the magnet down to bring the capsule back into the water-cooled zone of the assembly, resulting in an almost immediate quench. During the experiments, temperature is monitored using the internal thermocouple of the furnace and an external K-type thermocouple which is inserted into a small bore in the sheath of the TZM assembly and touching the top of the internal autoclave, which is the position closest to the capsule. The pressure is monitored with a factory-calibrated Bourdon-tube gauge and a digital pressure transducer. Considering the small thermal volume of the capsule relative to the massive TZM autoclave we expect no significant thermal gradient within the diffusion couple capsule.

Upon the start of the experiment while inserting the rod with the sample capsule into the hot zone of the autoclave, a pressure drop of up to 20 MPa over ca. 10 s is commonly observed. We interpret this to occur due to the displacement and concomitant cooling of a large amount of the hot gas from the autoclave to the cooler parts of the pressure system during to insertion of the rod. The rod is cold relative to the hot atmosphere in the autoclave and upon heating causes the pressure to increase again slowly by typically about 10 MPa over the duration of ca. 50 s. The opposite process is observed upon quench of the experiment, resulting in an up to 20 MPa overpressure during quench, which decreases to ca. 10 MPa overpressure in about 50 s at the end of an experiment. These processes are accounted for by slight over-pressurization before the start of the experiment. The pressure increase at the end of the experiment also ensures that bubbles do not form during the quench. Additionally, it was shown that halogen diffusion is mostly insensitive to pressure variations (e.g., Baker and Balcone-Boissard, 2009). Therefore, we consider these short-lived pressure fluctuations to be insignificant for the results of the diffusion experiments.

5.3 Analytical methods

Before preparation for further analyses all samples were weighed individually to ensure no weight loss or gain occurred during the experiment. Diffusion couple capsules were embedded in epoxy and cut open along the center of the capsule and parallel to the diffusion direction (i.e., parallel to the cylindrical capsules rotation axis) using a *Buehler* IsoMet precision saw. All samples were polished using a series of diamond embedded disks to an ultimate grain size of 1 µm while taking care that the polished surface remained parallel to the diffusion direction.

5.3.1 Electron microprobe analysis (EMPA)

Major element and halogen concentration analyses of experimental glasses were conducted at the Department of Geoscience of the University of Mainz, and using a *JEOL* JXA8200 electron microprobe. Analyses employed an acceleration voltage of 15 kV, a beam current of 12 nA, and a beam diameter of 10 µm. Dwell times for F and Cl were 120 s and 30 s, respectively, yielding a detection limit of 60 ppm (1 σ). Analysis dwell times of each major element was: Si 25 s, Al 40 s, Na 20 s, K 30 s, Ca 30 s, Fe 60 s, Mg 30 s, Mn 50 s, and Ti 30 s. The device was calibrated before a measurement using the following reference materials: SrF_2 (F), tugtupite (Ca, Na), VG-2 (Ca, Mg), VG-A99 (Fe, Si), MnTi (Mn, Ti), and orthoclase (Al, K). Proper calibration was assessed by analyzing standards VG-2, VG-A99, VG-568 and a natural obsidian standard (~74 wt.% SiO_2) repeatedly during each analytical session. The data was corrected using the ZAF method.

Concentration vs. distance profiles were acquired using line-scans with a fixed step-width of 5–250 µm depending on the sample (i.e., the anticipated diffusive speeds and therefore profile distances) and the position of the analyzed points relative to the diffusion interface. Points in the transition zone between the two diffusion couple halves were analyzed using a smaller step-width while the profile ends were covered by a larger step-width. This way it was possible to achieve a high spatial resolution of data, in turn facilitating good resolution of slow diffusion patterns while covering a large range of diffusion widths and keeping analysis time low. Profiles were acquired along traverses away from the capsule edges to avoid analyzing inhomogeneities that could distort diffusion profile data (e.g., devitrification, Feisel et al., 2019).

5.3.2 Secondary Ion Mass Spectrometry (SIMS)

As the concentration of Br and I in the samples is too low to be analyzed by EMPA, experimental samples were further analyzed on the SIMS. The analyses of all HX samples and of CCX1 and CCX4 were carried out during two analytical sessions in October 2018 and January 2019 at the University of Lausanne, Switzerland. The other samples (CCX3, CCX5 and all CCX-H) were analyzed at Heidelberg University, Germany, in two sessions in May 2021 and April 2022. Both facilities feature a *CAMECA* IMS 1280HR ion microprobe. The analytical parameters for all SIMS analyses (halogens and H_2O) in both labs are summarized in Table S1 of the supplementary material.

Analyses carried out at the University of Lausanne were referenced internally on each sample in an area far outside of the region of diffusion where the constant Si-content was known from EMPA analyses. These data included the less abundant Si-isotope ^{30}Si for calculation of ratios with Br and I which are of low concentration in our samples compared to F and Cl. ^{28}Si and ^{19}F intensities were detected using a Faraday-Cup. The other halogens (^{35}Cl, $^{79/81}Br$, ^{127}I) and ^{30}Si were analyzed using electron multipliers.

The SIMS analyses of halogens in Heidelberg were calibrated using an obsidian glass (JV1, Pichavant, 1987) for F and Cl and the GSE-1G glass for Br and I (Marks et al., 2017a, 2017b; Wiedenbeck, 2017). The accuracy of these analyses is limited by the poor homogeneity of halogens in GSE-1G and the fact that JV1 is not an established reference material with multiple independent determinations of the concentrations. The halogen concentrations determined by SIMS must therefore be interpreted as semi-quantitative with an estimated accuracy of ≤ 50 % (relative error).

For each water-bearing sample (CCX-H), H_2O concentration profiles were acquired next to the halogen profiles using a *CAMECA* IMS3f ion microprobe at Heidelberg University. The H_2O background caused by in-situ contamination was reduced by using a LN_2-cooled metal plate in the sample chamber. The apparent H_2O concentration caused by in-situ contamination was monitored by analyzing San Carlos olivine and was < 0.01 wt.%. H_2O analyses were calibrated using JV1 as reference material. Accuracy is estimated to be < 20 % relative error.

5.4 Results

5.4.1 Chemical composition of starting materials

The major element compositions of the different starting materials as determined by microprobe analyses are compiled in Table 5.1. The synthesized samples reveal a similar composition, both plotting in the field of Trachyte in a TAS diagram, very close to the borders to rhyolite and dacite. However, the CCX melt is slightly enriched in alkalies (Na_2O, K_2O) compared to the HX melt. All samples were analyzed using line scans on the microprobe not only to measure F and Cl gradients but also to validate major element homogeneity over the diffusion couple (Fig. 5.1). Maximum absolute concentrations of F are around 0.5–0.6 wt.% in the HX samples, and about 0.8–1 wt.% in the CCX samples. Cl concentrations are about 0.2–0.3 wt.% in the HX samples and about 0.3–0.4 wt.% in the CCX samples. Absolute Br and I concentrations were only measured for the CCX samples using the SIMS at Heidelberg University. The maximum Br and I concentrations in the halogen-enriched glasses of the CC melts are ~2500 ppm and ~300 ppm, respectively.

5.4.2 Post-experimental diffusion couple textures

During data acquisition, all diffusion couples were assessed for textural homogeneity by means of backscattered electron images. Most samples comprised a clean and straight diffusion interface between two homogeneous glassy areas which were particularly prominent in the anhydrous samples. Some samples and mainly those of the hydrous series contained minor cracks in the glass, which were interpreted to stem from the relatively fast quenching rates (Fig. 5.2a). However, the cracks were not found to influence the acquired diffusion data. Few samples underwent deformation during the experiments caused by bubble formation or the onset of convection. Both phenomena were mostly

recognized in experiments of the water-bearing series in which the melt viscosity was reduced due to the presence of water (e.g., Giordano et al., 2008) which enhanced convection. These effects resulted in distorted diffusion couple geometry, and according samples were discarded from further analysis. Small amounts of oxide phases (<100µm; <<1 vol.%) were recognized in the halogen-bearing parts of some experiments utilizing the CCX melt. These were analyzed qualitatively using EDS which showed they are tungsten-oxides. This was interpreted to stem from a slight contamination of the sample powder caused by using a tungsten-carbide mill for sample preparation. However, these oxides are not thought to affect halogen diffusion in our experiments.

Table 5.1: Major element composition of the synthesized starting glasses as determined by EMPA and SIMS analysis. All values represent units of wt.% unless otherwise stated. All data are corrected for Na-loss during EMPA analysis.

	HX[a]		**CCX**	
	enriched (n = 15)	depleted (n = 14)	enriched (n = 6)	depleted (n = 5)
SiO_2	68.5 (4)	68.3 (3)	67.8 (3)	67.9 (5)
TiO_2	0.46 (2)	0.46 (2)	0.66 (3)	0.67 (2)
Al_2O_3	14.7 (1)	14.57 (8)	14.49 (4)	14.48 (7)
FeO	4.6 (3)	4.76 (6)	3.84 (5)	3.94 (8)
MgO	0.46 (2)	0.44 (2)	0.60 (3)	0.62 (2)
MnO	0.13 (2)	0.15 (2)	0.12 (4)	0.11 (2)
CaO	2.85 (7)	2.82 (5)	2.11 (3)	2.12 (3)
Na_2O	6.2 (2)	6.35 (7)	6.9 (1)	7.8 (1)
K_2O	2.10 (3)	2.20 (3)	2.39 (3)	2.65 (4)
F	0.53 (2)	0.04 (3)	0.96 (2)	0.03 (1)
Cl	0.26 (1)	0.02 (2)	0.4 (1)	0.04 (1)
Br	nd	nd	~ 2500 ppm	~ 1 ppm
I	nd	nd	~ 290 ppm	0
Total	100.52	100.05	99.82	100.35
NBO/T[c]	0.08	0.08	0.09	0.11

[a] Data from Feisel et al. (2019)

[b] Absolute values of Br and I estimated based on SIMS analyses and only available for CCX melts.

[c] NBO/T is calculated after Mysen (1988) and Giordano et al. (2008).

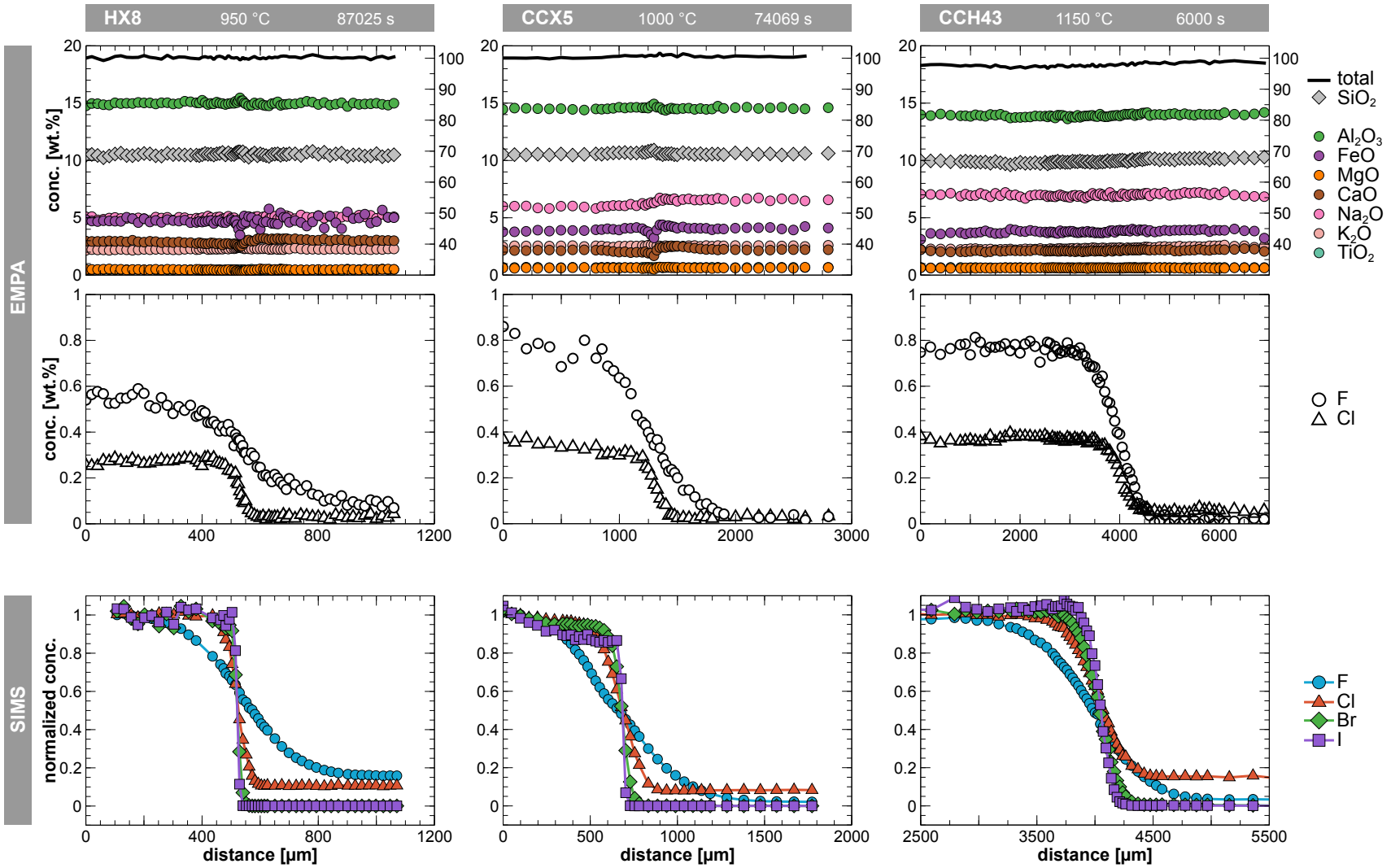

Figure 5.1: Concentration vs. distance diagrams of one sample of each melt composition acquired by EMPA and SIMS analyses. In the upper row, data of SiO_2 and totals refer to the secondary y-axis. EMPA data represents absolute values whereas the SIMS data was normalized to the average of the 4 outermost datapoints of each respective halogen in the enriched diffusion couple half. This way it is possible to visualize all halogens of a sample in one diagram.

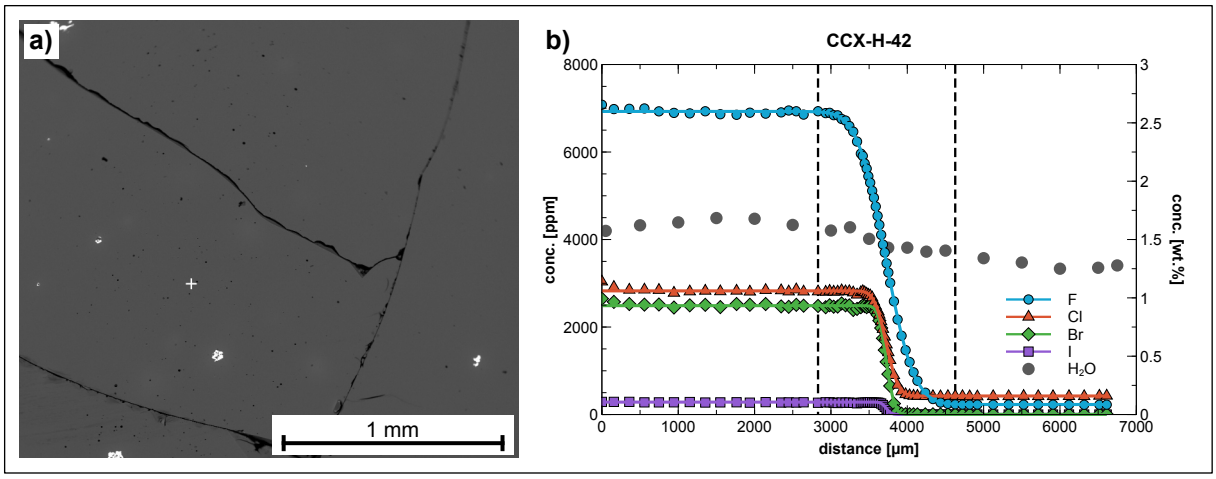

Figure 5.2: Backscattered image and diffusion profiles of sample CCX-H-42. **a)** Backscattered image of the center part of sample CCX-H-42 showing minor cracks likely caused during rapid quench (few seconds). **b)** Concentration vs. distance profiles of F, Cl, Br, I and H_2O as acquired by SIMS. The halogen data are plotted together with their respective fit curves calculated using equation 5.1. Diagrams of the other CCX-H samples are provided in the supplementary material.

5.4.3 Halogen diffusion coefficients

Most concentration profiles comprise a smooth and symmetric transition between the high and low halogen concentration portions of the charge, indicating that no other processes than diffusion (e.g., convection) were involved (Fig. 5.1). Smooth and symmetric profiles are recognized especially for experiments run at high temperatures. Diffusion profiles of Br and I are in general shorter than those of F and Cl. However, all concentration vs. distance profiles presented here yielded good results during fitting and are treated as effective binary diffusion of each halogen element in the melt matrix (e.g., Zhang 2010).

Diffusion coefficients for each acquired concentration vs. distance profile were calculated by fitting the respective data to the equation for constant one-dimensional diffusivity between two semi-infinite media (Crank, 1975):

$$C(x,t) = \frac{C_{low} + C_{high}}{2} + \frac{C_{low} - C_{high}}{2} \operatorname{erf}\left(\frac{x - x_0}{2\sqrt{D\,t}}\right) \quad (5.1)$$

The parameter $C(x,t)$ describes the concentration at distance x (m) after the experimental time t (s). C_{low} (ppm) is the concentration of the halogen-poor, and C_{high} (ppm) the concentration of the halogen-rich half-space. The term *erf* indicates the error function. x_0 (m) describes the position of the diffusion interface and is in this case determined mathematically. The term D ($m^2\ s^{-1}$) is the diffusion coefficient.

Data fitting was performed using the nonlinear least-squares method implemented in a *Matlab* script, specifically programmed for easy use with diffusion profile data. The results obtained by this script were

regularly validated by comparing to the results calculated by the commercially available curve-fitting software *CurveExpertPro*. As equation (5.1) is independent of absolute concentrations it was used with both, concentration data determined by EMPA and SIMS and ratios of halogen- over silica-concentration (e.g., F/Si) as determined by SIMS to calculate diffusion coefficients. All parameters of equation 5.1 except x and t were calculated based on the fitting algorithm. In some cases, parameters C_{low} and C_{high} were set manually to facilitate proper fitting calculations, for example where the analyzed profiles did not cover the whole length of diffusion for that particular profile. Additionally, some profiles suffered from slight distortion, caused, for example, by deformation of the capsule during quench, and resulting in asymmetrical profiles which was mainly prominent in the longest profiles of F diffusion. Where profiles were asymmetrical, each half of the diffusion profile was fitted individually using equation 5.1 and the results were compared to those of the complete profile. Those profiles of which the individually fitted halves yielded different diffusion coefficients larger than 0.6 orders of magnitude were discarded. F diffusion coefficients calculated on profiles where this method was applied are indicated by "*" in Table 5.2. Typical concentration vs. distance profiles of sample CCH-X-42 fitted with equation 5.1 are illustrated in Figure 5.2b. All measured diffusion profiles with their respective fit curves are provided in Figures S1-S4 of the supplementary material.

Anhydrous HX. Of the nine HX experiments presented in Feisel et al. (2019), six samples were analyzed by SIMS for the scope of this study. One concentration vs. distance profile was acquired for each of the samples, covering lengths of ~500–1000 µm. Diffusivities of F and Cl determined here agree well with the results of microprobe analyses indicating that F is generally faster than Cl by up to 2 orders of magnitude in the investigated temperature range. D values are on the order of 10^{-15} to 10^{-13} m^2 s^{-1} for fluorine and 10^{-17} to 10^{-15} m^2 s^{-1} for chlorine, of which the lower and higher values each correspond to temperatures of 750 °C (HX9) and 950 °C (HX8), respectively (Table 5.2). Bromine and iodine diffusivities are generally lower than those of chlorine, with Br consistently being faster than I. D_{Br} ranges from 10^{-18} to 10^{-15} m^2 s^{-1} while D_I values are about half an order of magnitude smaller at the corresponding temperatures, ranging from ca. 10^{-18} to 10^{-16} m^2 s^{-1} (Table 5.2).

Anhydrous CCX. Out of seven anhydrous experiments performed using CCX melt and analyzed by EMPA, three were discarded due to textural features indicating compromised geometry. The remaining four experiments were additionally analyzed by SIMS. Diffusivities of all halogens in samples using the CCX melt are similar to those obtained for the HX melt. However, the difference between F and Cl diffusion is less pronounced in this melt composition compared to HX. Diffusion coefficients of F (D_F) range from ~10^{-14} to 10^{-13} m^2 s^{-1} in the temperature range of 850 °C (CCX3) to 1000 °C (CCX5). Cl diffusion is up to two orders of magnitude slower with ~10^{-17} to 10^{-14} m^2 s^{-1} at these temperatures. For these two halogens, results of EMPA and SIMS analyses agree well within statistical errors (Table 5.2). Diffusion of Br is slower than that of Cl by ~0.5–1.5 orders of magnitude and I is even slower than Br

by ~1 order of magnitude with diffusivities in the range of ~10^{-16}–10^{-14} and ~10^{-16}–10^{-15} m^2 s^{-1}, respectively.

Hydrous CCX-H. All diffusion couple experiments of the hydrous series performed in the TZM assembly were analyzed both by EMPA (F, Cl) and by SIMS (F, Cl, Br, I). In general, diffusivities are higher than those obtained for the anhydrous CCX series with D_F ranging from ~10^{-12} to ~10^{-11} m^2 s^{-1} from 1000–1200 °C. Cl diffusion is 0.5 to 1 orders of magnitude slower than F, and Br and I are even slower. However, diffusivities of Cl, Br and I are all within less than one order of magnitude of each other at the respective experimental temperatures (Table 5.2). This results in a total diffusivity range of only 1–2 orders of magnitude among all halogens which is significantly less than observed for the anhydrous series of CCX melt which spans a range of 3–4 orders of magnitude among all halogens (Table 5.2).

5.4.4 Temperature dependence of halogen diffusion

All diffusion coefficients determined in this study increase with increasing temperature for each of the used melt compositions. As shown in various previous studies, diffusivity follows Arrhenian behavior (e.g., Baker and Balcone-Boissard 2009), which is also confirmed by our data. Plotted in a diagram of log(D) vs. inverse temperature (Fig. 5.3), the data clearly shows this Arrhenian trend and can be described by the following equation:

$$D = D_0 * e^{-\frac{E_A}{R*T}} \tag{5.2}$$

where D is the diffusion coefficient (m^2 s^{-1}), D_0 is the pre-exponential factor, E_A the activation energy (J/mol), R the universal gas constant (8.3145 J mol^{-1} K^{-1}), and T is the temperature (K). The characteristic parameters describing the diffusive behavior of each halogen in a specific melt composition are D_0 and E_A which are mathematically represented by the y-axis intersect and the slope of the trendline in the Arrhenius diagram, respectively. For the calculation of the characteristic Arrhenius parameters, equation 5.2 was linearized to the form

$$\log(D) = -\frac{E_A}{\ln(10) * R * T} + \log(D_0) \tag{5.3}$$

and fitted to all available data (EMPA + SIMS) of each starting material using the nonlinear least-squares method implemented with *Matlab*. Where multiple profiles were measured on one sample and with the same method, the resulting diffusion coefficients were averaged to avoid a weighing effect during the Arrhenius fitting calculations. The results of all fits are illustrated in Figure 5.3 and listed in Table 5.3. Fitted with the data of the two anhydrous series, the results of the HX and CCX starting

materials are similar, yielding activation energies in the range of ~200–290 kJ/mol for all halogens. However, diffusion in HX melt generally comprises slightly higher activation energies than in CCX melt. The similarity is further represented by the parallel fit curves in the Arrhenius diagrams (Fig. 5.3). However, in the HX series it is apparent that F is significantly faster than all other halogens which is represented by a gap of 1.5–2 orders of magnitude between the fit lines of F and Cl, while Cl, Br and I are all within about 1.5 orders of magnitude. In comparison, the data of the CCX series shows more equally spaced Arrhenius fits of the halogens spanning an overall similar range of diffusivities compared to the HX experiments.

The data of the hydrous series shows the same ordering of diffusive speeds, with F being the fastest and I being the slowest, but spanning a narrower range of diffusivities among all halogens. In the Arrhenius diagram this is represented by the more closely spaced fit curves compared to the anhydrous data. Activation energies are similar to the anhydrous series, except for F whose E_A is only 131 kJ/mol in the hydrous case compared to 198–213 kJ/mol in the anhydrous experiments (Table 5.3).

5.4.5 H_2O content in CCX-H experiments

The experimental products of the CCX-H series show a range of 1.5–2 wt.% H_2O (Table 5.2). Most of the hydrous experiments suffered from water loss to some extent, which was indicated by increasing totals towards one end of the diffusion profile recognized in the EMPA results (Fig. 5.1) and confirmed by SIMS analyses (Fig. 5.2b; Fig. S1 of the supplementary material). The use of CH_4 in the pressure medium helped to reduce this issue but did not resolve it completely. Interestingly, water was only lost on the halogen-depleted side of the diffusion couple leading to a weak, mostly linear H_2O-concentration gradient over the length of the diffusion couple. Experiments comprising significant water loss were discarded, however, small losses were considered negligible with regard to diffusivity. This is particularly true considering that the transition between high and low halogen concentration in most cases is relatively narrow, especially relative to the short diffusion lengths of the slower diffusing halogens. Over this narrow range the H_2O concentration can be considered to be constant within error. Due to this issue, we have calculated the average H_2O-concentration over the length of the transition zone of each hydrous diffusion profile and reported it with other relevant data in Table 5.2.

Table 5.2: Conditions and results of all experiments. Experiments of the anhydrous series (HX and CCX) were carried out at P = 1 bar. Hydrous experiments were done at P = 160 MPa. All diffusivities in $m^2\ s^{-1}$.

sample	*T* [° C]	*t* [s]	H_2O [wt.%]	#	D_F	s.d.	D_{Cl}	s.d.	D_{Br}	s.d.	D_I	s.d.
HX9	750	3023535	-	1[a]	1.6×10^{-15}	4.3×10^{-16}	1.7×10^{-17}	8.4×10^{-18}				
				2[b]	1.6×10^{-15}*	3.2×10^{-16}	3.9×10^{-17}	1.1×10^{-17}	3.4×10^{-18}	8.8×10^{-19}	1.8×10^{-18}	7.8×10^{-19}
HX7	800	587235	-	1[a]	6.6×10^{-15}	1.6×10^{-16}	4.9×10^{-17}	1.4×10^{-17}				
				2[a]	1.1×10^{-14}	1.9×10^{-15}	1.6×10^{-16}	4.2×10^{-17}				
				3[b]	1.1×10^{-14}	6.0×10^{-16}	4.0×10^{-16}	6.2×10^{-17}	2.3×10^{-17}	4.7×10^{-18}		
HX3	850	171502	-	1[a]	1.6×10^{-14}	5.0×10^{-15}	3.9×10^{-16}	2.0×10^{-16}				
				2[a]	1.9×10^{-14}	5.9×10^{-15}	4.5×10^{-16}	2.4×10^{-16}				
				3[b]	2.3×10^{-14}*	4.6×10^{-15}	4.3×10^{-16}	9.7×10^{-17}	6.2×10^{-17}	2.9×10^{-17}	4.0×10^{-17}	2.1×10^{-17}
HX10	850	266855	-	1[a]	1.9×10^{-14}	4.4×10^{-15}	3.9×10^{-16}	1.2×10^{-16}				
				2[a]	2.0×10^{-14}	5.1×10^{-15}	7.4×10^{-16}	4.0×10^{-16}				
				3[b]	2.1×10^{-14}*	1.8×10^{-15}	6.2×10^{-16}	7.4×10^{-17}	8.9×10^{-17}	1.6×10^{-17}	2.7×10^{-17}	3.6×10^{-16}
HX5	900	154560	-	1[a]	4.7×10^{-14}	6.7×10^{-15}	1.0×10^{-15}	2.0×10^{-16}				
				2[a]	4.6×10^{-14}	8.9×10^{-15}	8.7×10^{-16}	1.9×10^{-16}				
				3[b]	3.2×10^{-14}*	6.2×10^{-15}	1.0×10^{-15}	1.3×10^{-16}	1.6×10^{-16}	6.5×10^{-17}		
HX8	950	87025	-	1[a]	1.3×10^{-13}	2.5×10^{-14}	4.5×10^{-15}	1.1×10^{-15}				
				2[a]	1.1×10^{-13}	1.4×10^{-14}	1.5×10^{-15}	6.7×10^{-16}				
				3[b]	1.4×10^{-13}	1.6×10^{-14}	5.9×10^{-15}	8.7×10^{-16}	1.3×10^{-15}	2.7×10^{-16}	3.9×10^{-16}	1.9×10^{-16}

[a] Results from EMPA analyses. EMPA data of HX series from Feisel et al. (2019)

[b] Results from SIMS analyses

*Asymmetric profiles were first fitted each half at a time to confirm reliability of the fit of the complete profile (see text for further discussion)

Table 5.2: (continued)

sample	*T* [° C]	*t* [s]	H_2O [wt.%]	#	D_F	s.d.	D_{Cl}	s.d.	D_{Br}	s.d.	D_I	s.d.
CCX3	850	237370	-	1[a]	6.6×10^{-14}*	1.3×10^{-14}	2.4×10^{-15}	9.0×10^{-16}				
				2[b]	3.6×10^{-14}*	1.2×10^{-14}	3.5×10^{-15}	7.1×10^{-16}	4.8×10^{-16}	7.3×10^{-17}		
CCX4	900	170880	-	1[a]	6.3×10^{-14}*	1.2×10^{-14}	1.7×10^{-15}	4.9×10^{-16}				
				2[a]	6.6×10^{-14}*	1.1×10^{-14}	5.7×10^{-15}	1.2×10^{-15}				
				3[b]	5.4×10^{-14}	1.0×10^{-14}	9.7×10^{-15}	1.4×10^{-15}	1.2×10^{-15}	1.2×10^{-16}	1.7×10^{-16}	5.9×10^{-17}
CCX1	950	82770	-	1[a]	1.1×10^{-13}*	1.6×10^{-14}	8.8×10^{-15}	1.3×10^{-15}				
				2[a]	1.2×10^{-13}*	1.9×10^{-14}	7.1×10^{-15}	1.2×10^{-15}				
				3[b]	1.1×10^{-13}*	1.4×10^{-14}	7.7×10^{-15}	7.5×10^{-16}	1.1×10^{-15}	1.3×10^{-16}	2.5×10^{-16}	1.1×10^{-16}
CCX5	1000	74069	-	1[a]	6.9×10^{-13}	6.1×10^{-14}	4.0×10^{-14}	5.9×10^{-15}				
				2[a]	5.0×10^{-13}	4.2×10^{-14}	5.8×10^{-14}	8.2×10^{-15}				
				3[a]	6.4×10^{-13}	1.4×10^{-13}	6.7×10^{-14}	2.3×10^{-14}				
				4[b]	6.7×10^{-13}	7.4×10^{-14}	7.0×10^{-14}	2.6×10^{-14}	1.3×10^{-14}	7.5×10^{-15}		
				5[b]	7.5×10^{-13}	4.4×10^{-14}	7.3×10^{-14}	4.3×10^{-15}	1.2×10^{-14}	1.3×10^{-15}	9.4×10^{-16}	1.3×10^{-16}
CCX-H-38	1000	16380	1.9 (1)	1[a]	3.3×10^{-12}	4.2×10^{-13}	4.3×10^{-13}	1.4×10^{-13}				
				2[b]	3.3×10^{-12}	1.6×10^{-13}	5.4×10^{-13}	3.7×10^{-14}	2.5×10^{-13}	1.6×10^{-14}	9.4×10^{-14}	8.1×10^{-15}
CCX-H-40	1050	10200	1.9 (1)	1[a]	6.2×10^{-12}	9.6×10^{-13}	9.2×10^{-13}	2.2×10^{-13}				
				2[b]	6.6×10^{-12}	2.6×10^{-13}	1.3×10^{-12}	1.4×10^{-13}	5.8×10^{-13}	6.8×10^{-14}	2.3×10^{-13}	2.9×10^{-14}
CCX-H-42	1100	8100	1.5 (1)	1[a]	5.5×10^{-12}	7.7×10^{-13}	7.9×10^{-13}	1.6×10^{-13}				
				2[b]	5.3×10^{-12}	1.3×10^{-13}	9.5×10^{-13}	2.3×10^{-13}	4.2×10^{-13}	3.8×10^{-14}	1.6×10^{-13}	2.4×10^{-14}
CCX-H-43	1150	6000	2.1 (2)	1[a]	1.3×10^{-11}	1.4×10^{-12}	4.2×10^{-12}	6.7×10^{-13}				
				2[b]	1.3×10^{-11}	4.4×10^{-13}	3.6×10^{-12}	2.4×10^{-13}	1.6×10^{-12}	9.3×10^{-14}	6.5×10^{-13}	6.7×10^{-14}
CCX-H-44	1200	4800	2.0 (2)	1[a]	1.9×10^{-11}	2.0×10^{-12}	7.6×10^{-12}	1.3×10^{-12}				
				2[b]	2.0×10^{-11}	1.1×10^{-12}	7.7×10^{-12}	8.5×10^{-13}	3.9×10^{-12}	4.8×10^{-13}	2.1×10^{-12}	4.2×10^{-13}

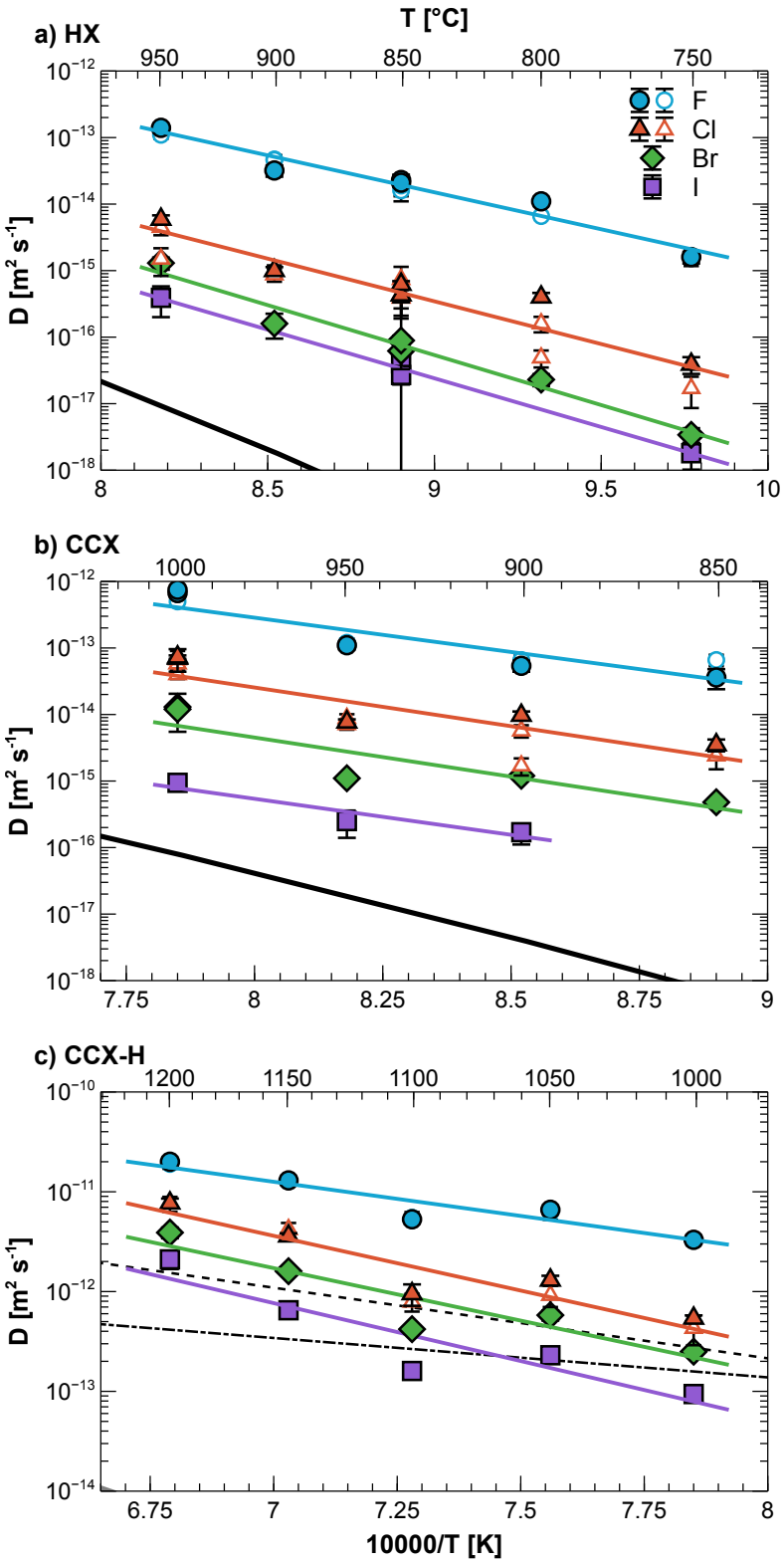

Figure 5.3: Arrhenius diagrams of all investigated melt compositions. Both, the individual diffusion coefficients and the corresponding Arrhenius fits of all halogens are shown. **a)** anhydrous HX melt. **b)** anhydrous CCX melt. **c)** hydrous CCX melt (~1.5 wt.% H_2O). The bold black lines indicate the self-diffusivity of oxygen calculated with the Eyring equation and based on the calculated viscosities of the anhydrous melt compositions (Giordano et al., 2008). The dashed lines in c) indicate calculated oxygen self-diffusion in Rhyolite (dash-dot) and Dacite (dashed) from (Zhang and Ni, 2010). Open symbols represent data based on EMPA analyses.

Table 5.3: Arrhenius parameters of all halogens and oxygen self-diffusion in all investigated melt compositions. D_0 is given in $m^2\ s^{-1}$ and E_A is given in kJ mol^{-1}. Calculation of Eyring diffusivities is described in the text.

	HX			CCX			CCX-H		
	D_0	E_A	+/-	D_0	E_A	+/-	D_0	E_A	+/-
F	1.50×10^{-4}	212.7	28	5.11×10^{-5}	197.5	99.4	7.76×10^{-7}	131.0	38.0
Cl	1.24×10^{-4}	245.8	51	5.10×10^{-5}	222.6	112	1.74×10^{-4}	210.1	67.6
Br	1.78×10^{-3}	287.6	66.5	1.16×10^{-5}	225.2	367.8	3.97×10^{-5}	201.4	153.5
I	3.50×10^{-4}	280.0	63.8	2.51×10^{-7}	207.4	973.2	1.02×10^{-4}	222.2	180.2
O_{Eyring}	6.9×10^{-1}	399.1	26.4	1.43×10^{-1}	375.5	22.0	-	-	-

5.5 Discussion

5.5.1 Halogen diffusion mechanisms

Diffusivity and the mechanism of halogen diffusion are both strongly dependent on the composition and internal structure of the host glass. In the case of aluminosilicate melts a vast range of compositions are present in nature and structural melt parameters such as the degree of polymerization show an accordingly wide range. Arrhenius parameters of halogen diffusion have been determined for a range of different melt compositions and illustrate the strong compositional dependence of halogen diffusion (Watson and Bender, 1980; Dingwell and Scarfe, 1984; Dingwell and Scarfe, 1985; Bai and Koster van Groos, 1994; Alletti et al., 2007; Balcone-Boissard et al., 2009; Böhm and Schmidt, 2013; Fortin et al., 2017; Yoshimura, 2018; Balcone-Boissard et al., 2020). Most of these studies studied F and Cl diffusion and only few have investigated Br diffusion. However, none of the available studies provide I diffusivity data. Hence the present study is the first to our knowledge.

One major compositional parameter defining the behavior of silicate melts is the degree of polymerization, which itself is a function of, for example, the amounts of SiO_2, volatiles or network modifying cations. Typically, the degree of polymerization in a melt is characterized by the parameter of NBO/T, i.e., the ratio of non-bridging oxygen atoms over tetrahedally coordinated ions (Mysen, 1988). The melts of the present study exhibit NBO/T values in the range of ~ 0.08–0.11, calculated using the method of (Mysen, 1988) and splitting FeO_{tot} equally between Fe_2O_3 and FeO (Giordano et al., 2008). The NBO/T values are reported together with the bulk rock chemistry in Table 5.1.

The bond strength of an ionic species dissolved in melt generally increases with the charge of that species (Zhang et al., 2010). Halogens in the combined state (e.g., as a halide) typically have an univalent charge of -1 and are therefore comparably weakly bonded to other atoms, despite being very reactive.

This means that halogens are relatively easily detached from their original site by breakage of the ionic bonds around a previously coordinated halogen ion before moving to a new site (Zhang et al., 2010). Additionally, even though the halogen group elements have the highest electronegativity of all elements in their respective periods, the significant within group variation in this parameter means that the bond strength should also vary accordingly. For example, F, being the most electronegative, should foster the highest bond strength of the halogens. Within this simplified chemical framework the diffusive "jump" can be envisioned to proceed by passing through an aperture formed by neighboring ions. The size and stiffness of the aperture should generally be structurally controlled and relate to the polymerization of the melt, while the detachment rate should be controlled by ionic charge (Zhang et al., 2010). The size and number of the apertures are determined by the ions present in the melt and the resulting "free space" formed which is called the ionic porosity. Naturally, smaller ions such as F diffuse faster, because they can pass through apertures of various sizes and are therefore less sensitive to ionic porosity. Larger ions can only pass large apertures and their diffusion-rate is therefore structurally controlled and, hence, more sensitive to ionic porosity. This is typically the case for noble gases and monovalent ions (e.g., Henderson et al., 1985; Lux, 1987; Alletti et al., 2007) and was also confirmed for halogens by recent studies which showed that diffusion is negatively correlated with the ionic radius of the halogen in low NBO/T melts, i.e., in melts with a high degree of polymerization (Rhyodacite/Trachyte, NBO/T: ~0.08, Feisel et al., 2019; Na- and K-Phonolite, NBO/T: ~0.08, Balcone-Boissard et al., 2020). In melts with higher NBO/T (lower degree of polymerization) halogen diffusion typically comprises only weak correlation with the ionic radius. Alletti et al. (2007) suggested that halogen diffusion in a basaltic melt (NBO/T ~0.5) is mostly independent of "free space" in the melt structure but instead occurs by exchange mechanisms that are predominantly controlled by the preservation of local charge balance, similar to the diffusion of divalent and trivalent cations (Henderson et al., 1985). This means that in this kind of melt movement of halogens is mainly rate-limited by the charge-controlled detachment process.

The present study complements the data of Feisel et al. (2019) by including all new SIMS analyses which also cover Br and I in two different highly polymerized melts (HX: NBO/T ~0.08; CCX: NBO/T ~0.08–0.11). Figure 5.4 illustrates the diffusivity of the halogens in different melt compositions relative to their ionic radii (Shannon, 1976) at 1250 °C. The data of Alletti et al. (2007) are included as a reference of a weakly polymerized melt and the data of studies performed at lower temperatures were calculated based on the published Arrhenius parameters. The results of the present study and especially those of Br and I confirm the strong influence of the ionic radius on diffusivity in polymerized anhydrous melts. The difference between F and Cl is particularly pronounced for most anhydrous studies, yielding a significant negative slope between the two in the diagram (Fig. 5.4). However, the slope between Cl and Br defines a discordance to the trend between F and Cl in most studies. For the anhydrous CCX melt the slope increases from Cl to Br and this trend is continued to I. For the anhydrous HX melt,

however, the slope decreases from Cl to Br and I. This stepwise correlation of ionic radius and diffusivity is recognized for all polymerized melts that were analyzed for Br (and I). We interpret this behavior to show that the ionic porosity of the melt is limited to distinct aperture sizes dictated by the melt structure. The fact that Cl and Br seem to have a similar diffusivity in anhydrous phonolite (Balcone-Boissard et al., 2009) regardless of their different ionic radii suggests that Cl and Br move through similarly sized apertures in this melt. By contrast, in the HX and especially CCX melt, Br cannot move through the same apertures as Cl due to its size, resulting in its lower diffusivity. Likewise, the I ion is too large to pass these aperture sizes and can diffuse only in the vicinity of ions that allow the formation of larger openings between sites. F, being the fastest diffuser among all of the halogens, can move through both small openings and all the larger apertures that are used by Cl, Br, and I in a polymerized anhydrous melt.

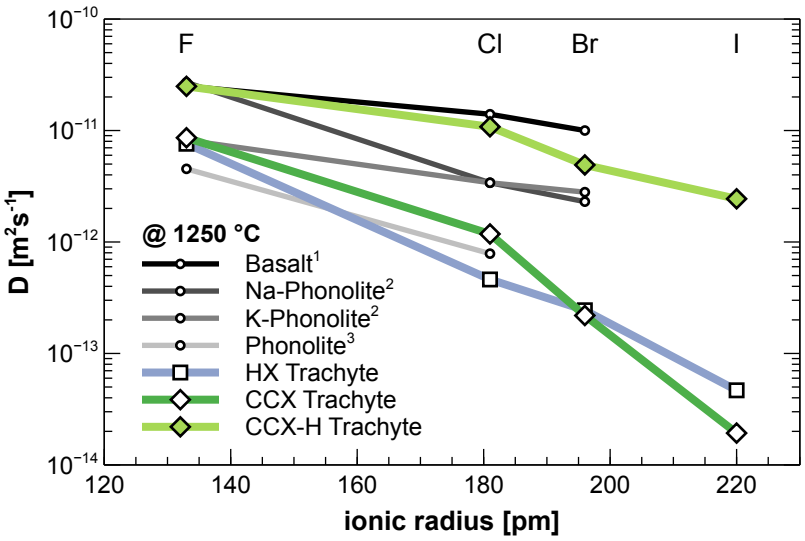

Figure 5.4: Halogen diffusivity at 1250 °C of the melts of this and other published studies plotted relative to the ionic radius of the respective halogen. All data are for anhydrous compositions except the hydrous data of the present study. Diffusivities at 1250 °C were calculated from the respective Arrhenius parameters of each composition and halogen. Data from: [1] Alletti et al., (2007); [2] Balcone-Boissard et al., (2009) and Balcone-Boissard et al., (2020); [3] Böhm and Schmidt, (2013).

5.5.2 The effect of H_2O on diffusion

The hydrous experiments (~1.5 wt.% H_2O) generally yield high diffusivities which span a range of only 1–2 orders of magnitude among the different halogens (Fig. 5.3). This restricted range of diffusivities contrasts those of the anhydrous CCX melt which displays 3–4 orders of magnitude variation. For better comparison to the anhydrous results, the Arrhenius parameters of the anhydrous CCX series were used to calculate hypothetical anhydrous diffusivities in the temperature range of the hydrous experiments and plotted in an Arrhenius diagram together with the hydrous Arrhenius fits (Fig. 5.5). The calculated anhydrous values are consistently lower than the hydrous data. While the difference for F is only ~0.2

log units at high *T* (1200 °C) and ~0.8 log units at low *T* (1000 °C), the difference for the slower diffusing halogens is more pronounced. Cl is ~1 log unit, Br ~0.5–1.5 log units and I ~2 log units faster in hydrous compared to dry melt. These results highlight the strong influence of H_2O on halogen diffusivity in the high silica melts of this study. These findings are in contrast to the those of Balcone-Boissard et al., (2020), who showed that the addition of up to 2.65 wt.% H_2O exerts only minor influence on Br diffusion in phonolitic melts; a fact which further underlines the strong compositional dependence of halogen diffusion.

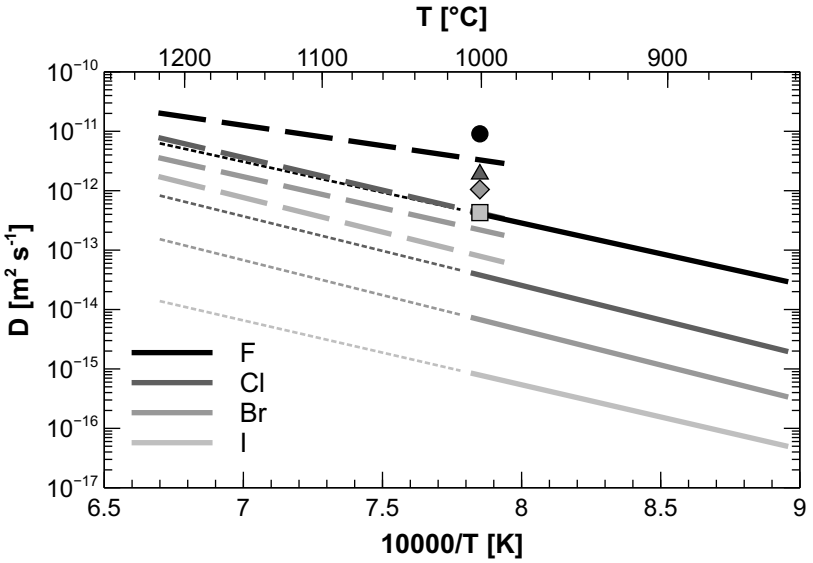

Figure 5.5: Comparative Arrhenius diagram of halogen diffusion in anhydrous and hydrous (1.5 wt.% H_2O) trachytic melt. Solid lines represent diffusion in anhydrous melt and dotted lines indicate extrapolation to higher temperatures. Long-dashed lines represent diffusion in hydrous melt. Solid symbols show preliminary results of halogen diffusion in melt containing 3.5 wt.% H_2O. Note that the diffusivity of all halogens is even more enhanced in the more strongly hydrated melt.

The increase in diffusivity in the melts of this study indicates a change in the diffusion mechanism that is likely caused by the modification of the melt structure due to the addition of H_2O. This effect can also be observed in Figure 5.4, where the strong correlation of diffusivity with the ionic radii observed in the anhydrous melts is highly attenuated for the hydrous case. Indeed, the hydrous data is more similar to those of basalt confirming that water effectively lowers the degree of polymerization of the melt. In doing so, the rate-limiting influence of melt structural apertures is reduced which makes the process of detachment more relevant as a diffusion-rate-limiting factor. Interestingly, the slope between Cl and Br increases in the hydrous melt similar to the behavior in the anhydrous CCX melt. At the relatively low water contents of ~1.5 wt.% used in the present study, the majority of the added H_2O is expected to be dissociated to form hydroxyl (OH^-) in the melt (e.g., Silver et al., 1990; Ihinger et al., 1999). The experimental results indirectly show that hydroxyl effectively depolymerizes the melt and allows for faster halogen diffusion. However, even in the hydrated melt, halogen diffusion is still somewhat

correlated with the ionic radii. This may indicate that for the given added water content (~1.5 wt.%) the melt structure is still polymerized enough to assert some control on the aperture-limited jumping processes, mainly affecting larger ions. We speculate that diffusivities will increase even more and may become more equal among the halogen species with increased water content. Indeed, our own preliminary results using 3.5 wt.% of H_2O added to the same CCX melt and in the same experimental setup (e.g., 1000 °C / 160 MPa) yield still higher diffusivities that span over an even smaller range among all the halogens (Fig. 5.5). This strongly implies that the rate at which a halogen ion jumps into a new site grows as the melt becomes increasingly depolymerized.

Another notable distinction between anhydrous and hydrous melt is the change in the activation energy, E_A, of F diffusion, which is lowered from 198 to 131 kJ mol^{-1}, while the E_A of the other halogens are only weakly affected (Table 5.3). That is, F diffusion becomes less sensitive to temperature in hydrous melts, which is apparent in the comparably shallow slope of the F Arrhenius fit in Figure 5.3c & 5.5. As already concluded from the observation that F diffusion is less strongly enhanced in the hydrous melt, compared to the other halogens, F diffusion appears only weakly sensitive to the melt structure and is more strongly controlled by the detachment process. F is known to substitute for bridging oxygen in Si-O-Si units (e.g., Mysen and Virgo, 1985) and preferably coordinates with Si or Al (e.g., Zeng and Stebbins, 2000; Liu and Nekvasil, 2002) , while Cl and Br prefer to coordinate in larger sites (Cassidy et al., *in press*). Similarly, OH^- typically replaces oxygen bonds of the Si-O network (Mysen et al., 1980). Consequently, the addition of H_2O and the concomitant formation of OH^- in the melt must influence the preferred bonding environment of F in the silicate network. Here, we interpret the change in activation energy of F to reflect that the rate of detachment from its site is enhanced by the replacement of F with OH^-. This way more F is available for diffusion compared to the anhydrous case, which in turn suggests that F diffusion becomes less sensitive to temperature (i.e., lower activation energy) under hydrous conditions. Consequently, we speculate that the introduction of water has a two-fold effect on the halogen diffusion mechanism: 1) The resulting decrease in the degree of polymerization generally promotes halogen diffusivities by increasing the ionic porosity; 2) The strong effect on the activation energy of F is interpreted to be due to OH^- directly affecting the bonding environment of F. Clearly, these explanations are qualitative, and therefore meant to suggest possible microscale chemical processes that might explain our macroscopic observations. Testing these ideas could benefit from appropriate imaging experiments (e.g., Schaller et al., 1992; Zeng and Stebbins, 2000; Mysen et al., 2004) that may isolate the relevant coordination and bonding environments of the halogens, with implications for their bond strengths in natural silicate melt.

5.5.3 Halogen diffusion and viscosity

Oxygen self-diffusion is commonly seen as a solid estimate of the structurally defined lower limit of diffusion rates in silicate melts (Oishi et al., 1975; Shimizu and Kushiro, 1984; Dingwell, 1990; Lesher, 2010; Zhang and Ni, 2010) and appears closely related to anhydrous melt viscosity via the Eyring equation (Glasstone et al., 1941; Dingwell, 1990; Zhang and Ni, 2010). Calculated oxygen self-diffusivity of our anhydrous samples using viscosity data derived from the model of Giordano et al. (2008) are included in Figure 5.3.

Diffusion of all four halogens in the dry melt is at least 1 order of magnitude faster than the calculated oxygen self-diffusion (Fig. 5.3), indicating that the silicate network behaves as in quasi-static structural sites relative to the diffusing halogen ion; therefore, diffusion may only be affected weakly by self-diffusion of the silicate network. Notably, iodine diffusion is the slowest of the halogens and thus closest to the calculated Eyring diffusion. The steeper slope of the Eyring diffusivity compared to the slope of the halogen fits in the Arrhenius diagrams (Fig. 5.3) suggests that with increasing temperature the jump frequency of iodine may approach that of the Si-O bonds in the silicate structure and the network surrounding iodine may no longer be viewed as quasi-static. With increasing temperature, iodine diffusion might therefore be enhanced by the cooperative rearrangement of the local silicate structure as oxygen diffuses.

The activation energy of diffusion, i.e., the slopes of the Arrhenius fits of the other halogens (Fig. 5.3) likewise indicate that all fits will meet the lower limit of oxygen self-diffusion at higher temperatures. Consequently, at sufficiently high temperatures (i.e., sufficiently low viscosity), all halogens will move with the same frequency as the silicate network, hence, diffusion will be the same for all halogens, being determined by the jump frequency of the structural movement of the Si-O bonds, broadly consistent with the conclusions of Dingwell (1990).

The indicated oxygen self-diffusivities in Figure 5.3 are considered to represent the lower limit of possible values as they are based on the halogen-depleted melt compositions. In F bearing melts, like those of the enriched diffusion couple halves, the viscosity can be significantly reduced due to the depolymerizing effect of F (e.g., Dingwell et al., 1985; Giordano et al., 2008), which will in turn yield higher calculated oxygen self-diffusivities. For the melts used in this study, the F-bearing melts yield Eyring diffusivities of up to 1 order of magnitude higher than the F-depleted melts, approaching the derived diffusivities of iodine at the highest of the experimental temperatures. Therefore, during the experiments, the melt structural lower limit of halogen diffusion is expected to change upon diffusion of F. In the resulting F enriched melts, the halogen diffusivities might approach the Si-O jump frequency already at lower temperatures compared to the F-depleted case. Expanding on this idea, we speculate that when F diffusivity and the F-depleted Eyring diffusivity are within ~1 order of magnitude in

Arrhenius space (i.e., at sufficiently high temperatures), diffusion of F into the depleted melt will enhance F diffusivity by decreasing the degree of polymerization. This would in turn result in a concentration dependent F diffusivity comparable to the case of H_2O (e.g., Behrens et al., 2004). However, it is unclear if the Eyring equation is valid for the case of F-enriched polymerized melts.

In case of the hydrous melt, the Eyring equation was shown to be inapplicable as it under-estimates oxygen-diffusion by 3–4 orders of magnitude in rhyolitic melt (Behrens et al., 2007). In this case, oxygen no longer moves solely by self-diffusion but is mainly transported by the diffusion of molecular H_2O in the melt (Behrens et al., 2007; Zhang and Ni, 2010) which shows that the structural limit of diffusion rates in hydrous melt can no longer be described by the self-diffusion of oxygen.

In an attempt to define a lower limit of diffusion rates in the hydrous melt of the present study, calculated oxygen self-diffusivities of rhyolite and dacite (Tables 4 and 5 of Zhang and Ni, (2010)) have been included in Figure 5.3c. However, these predicted self-diffusivities are faster than the experimentally constrained diffusivities of Br and I over a large range of the investigated temperatures. This is interpreted to indicate that in a slightly depolymerized melt of sufficiently large ionic porosity, the jumps of Si-O bonds no longer define the lower limit of transport rates but that the diffusive characteristics may be mostly determined by the ionic charge and radius.

5.6 Conclusions

The diffusion characteristics of four halogens in silicic melts were determined experimentally under anhydrous and hydrous conditions and over a temperature range relevant for magmatic processes (750–1200 °C). The results are consistent in that F is the fastest diffusing halogen and diffusivity decreases with increasing ionic radius indicating that diffusivity is highly dependent on the melt structure and therefore melt composition. Halogen diffusion covers a range of 3–4 orders of magnitude in silica-rich anhydrous melt, but diffusivities increase dramatically when water is added. The diffusivity increase due to the addition of water is most pronounced for the largest of the halogens and thus, the slowest diffusing halogen iodine. The effect of added water is weaker for the smaller halogens, leading to an overall diffusive range of only 1–2 orders of magnitude among all halogens. While the temperature dependence in terms of activation energies of Cl, Br and I diffusion is similar in the dry and wet case (~200–290 kJ/mol), E_A of F is reduced by about 35% in hydrous (~131 kJ/mol) compared to anhydrous melt (~200 kJ/mol). This is interpreted to indicate that F diffusion is more strongly dependent on the ionic detachment during diffusion and is therefore less sensitive to ionic porosity, especially in hydrous melt.

This study represents a significant contribution to the experimental database of halogen diffusion in natural silicate melts, and to our knowledge, is the first to include coherent results on iodine diffusion.

The new data are highly relevant for the better understanding of halogen mobility in magmatic processes. Our results suggest that diffusive fractionation of faster diffusing components such as H_2O and the halogens, could occur during bubble formation in a weakly water-enriched magma during slow magma ascent (e.g., Watson, 2017). Modeling of different magma ascent and bubble growth scenarios using the proposed diffusion parameters may help to characterize possible halogen fractionation trends during volcanic unrest.

5.7 Acknowledgements and funding

We thank N. Groschopf and S. Buhre for their guidance during electron microprobe analyses. T. Häger is thanked for access to the precision diamond wire saw. The help of B. Scheu, U. Kueppers, and K.-U. Hess with pre-synthesis sample preparation at LMU Munich is appreciated. This research was part of the Ph.D. thesis of Y. Feisel at the Johannes Gutenberg-University, Mainz. It was supported by a fellowship of the Gutenberg Research College of the Johannes Gutenberg-University of Mainz to D.B. Dingwell, who also acknowledges the support of ERC2018 ADV Grant 834225 (EAVESDROP).

Supplementary Material

Supplementary Figures S1–S4 and supplementary Table S1 can be found in the Appendix at the end of this thesis (p. 159).

Chapter 6

The effect of halogens (F, Cl) on the near-liquidus crystallinity of a hydrous trachyte melt[4]

Abstract

The effect of F and Cl on the liquidus temperature of a hydrous (~3.5–4 wt.% H_2O) trachytic melt (~66 wt.% SiO_2) at 925 to 990 °C and at 100 MPa has been experimentally investigated. We employed a novel disequilibrium approach involving diffusion couple experiments with the two-diffusion couple end-members differing solely in halogen concentrations. A shift of the liquidus temperature by ~50 °C was observed between a halogen-poor and halogen-enriched melt. Each experiment spanned the entire range of F and Cl concentrations between the two end-member compositions. We determined the halogen concentrations at the transition from crystal-bearing to crystal-free melt. These concentrations correspond to the liquidus halogen concentrations of the melt at each experimental temperature. We demonstrate that there is a limiting halogen concentration (~0.19–0.52 wt.% F; ~0.07–0.24 wt.% Cl), below which the melt crystallizes spherulitic clinopyroxene during heating to the run temperature. At high temperatures, upon diffusion of F and Cl into the halogen-poor melt, those crystals dissolve, leaving behind a dissolution front parallel to the diffusion interface. We propose that the dissolution is a consequence of F and Cl complexing with some of the main cationic components of clinopyroxene (Mg, Fe, Ca), thereby destabilizing this phase. Thus, the experimental dissolution of clinopyroxene is a manifestation of a liquidus depression caused by increased halogen content. Our results show that the liquidus shifts at a rate of ~1575(379) K mol.%$^{-1}$ of F and Cl in the melt, which is a minimum estimate, assuming both halogens equally drive dissolution. This liquidus depression is valid for a range of halogen concentrations (~0.06–0.87 wt.% F; ~0.06–0.36 wt.% Cl) and the experimental temperatures. Our findings illustrate that the degassing of halogens during or prior to an eruption can enhance crystallization in the melt and therefore influence magma physical properties that may ultimately affect eruption style.

Keywords: Halogens; liquidus depression; phase equilibria; diffusion couple; crystal dissolution; Halogens in Planetary Systems

---

[4] This chapter is published as Feisel, Y., Castro, J.M., Helo, C., and Dingwell, D.B. (2022) American Mineralogist, 107, 1007 – 1017, doi: 10.2138/am-2022-8120

6.1 Introduction

Volatile species (H_2O, CO_2, F, Cl, S, etc.) are important constituents of natural silicate melts and play a crucial role in determining melt properties (e.g., viscosity, density) and a magma's phase assemblage (e.g., crystallinity, bubble content). Hence they can ultimately control the style of volcanic eruptions (e.g., Gonnermann and Manga, 2007). Despite their typically moderate concentrations in magmas, compared to other major volatiles such as H_2O or CO_2, F and Cl may reach abundances of hundreds of parts per million up to few wt.% and, thus may exert significant effects on their own (e.g., Aiuppa et al., 2009; Dolejš and Zajacz, 2018). For example, F has long been known to decrease melt viscosity in silica-rich melts in a manner qualitatively similar to that of H_2O (Dingwell et al., 1985; Dingwell and Hess, 1998; Zimova and Webb, 2007; Giordano et al., 2008). By contrast, although the details of the effect of Cl on melt viscosity vary, it has been shown that Cl cannot decrease viscosity with the same efficiency as F and that the effect on viscosity depends on the melt composition (Hirayama and Camp, 1969; Dingwell and Hess, 1998; Zimova and Webb, 2006; Webb et al., 2014). The solubility of Cl in silicate melts has been demonstrated to be roughly an order of magnitude higher in basaltic melts than in rhyolitic compositions and increases with the availability of Mg, Ca, Na, Fe, K, Al, and F in the melt, while decreasing with the concentration of network-forming Si (Carroll and Webster, 1994; Signorelli and Carroll, 2002; Webster and De Vivo, 2002; Chevychelov et al., 2008; Webster et al., 2015; Webster et al., 2018; Thomas and Wood, 2021). These findings are consistent with spectroscopy-based investigations, which indicate a preferred complexing of Cl with Ca, Mg, and Fe (Zimova and Webb, 2006; Evans et al., 2008; Webb et al., 2014; Bell and Webster, 2015). F solubility has also been demonstrated to correlate with the concentration of Ca and Mg where they assume the role of network-modifiers and with increasing peralkalinity [molar (Na+K+Ca)/(Al) > 1; e.g., Koster van Groos and Wyllie, 1968; Foley et al., 1986a, 1986b; Mysen et al., 2004; Brey et al., 2009]. Additionally, F dissolution in silicate melt increases in peraluminous melts with excess network-modifying Al in fourfold coordination (Webster et al., 2018 and references therein). F has been shown to replace bridging O atoms (Schaller et al., 1992; Dolejš and Zajacz, 2018) and form complexes with Ca, Mg, or Na, as well as Al in fourfold or sixfold coordination (e.g., Zeng and Stebbins, 2000; Mysen et al., 2004; Karpukhina et al., 2007).

The effects of halogens on phase equilibria include significant depression of liquidus temperatures by F in both basaltic (Filiberto et al., 2012) and felsic melts (Wyllie and Tuttle, 1961; Koster van Groos and Wyllie, 1969; Manning, 1981; Dolejš and Baker, 2007a, 2007b). Of the studies available for the effect of Cl on phase equilibria, the majority indicate a decrease of the solidus temperature depending on the melt composition and Cl concentration (e.g., Wyllie and Tuttle, 1964; Koster van Groos and Wyllie, 1969). Recent studies on the effects of Cl on liquidus relations in basaltic melts showed a significant Cl-composition-dependent depression of the isobaric liquidus, defined by the first occurrence of olivine or

pyroxene depending on the pressure (Filiberto and Treiman, 2009; Filiberto et al., 2014; Farcy et al., 2016). The addition of Cl to a hydrous rhyodacitic melt was shown to exert a strong influence on the $Fe^{3+}/\Sigma Fe$ ratio, resulting in increased magnetite solubility (Bell and Webster, 2015). While some of the above studies were carried out on simplified model systems (e.g., Wyllie and Tuttle, 1961; Wyllie and Tuttle, 1964; Koster van Groos and Wyllie, 1968; Koster van Groos and Wyllie, 1969; Manning, 1981; Swanson and Fenn, 1992; Dolejš and Baker, 2007a, 2007b; Evans et al., 2008; Clarke et al., 2009), most recent work was done using natural compositions and therefore provide an extensive but not yet complete base of knowledge of the effects of halogens on a broad range of melt compositions (e.g., Webster and De Vivo, 2002; Bell and Simon, 2011; Filiberto et al., 2012; Filiberto et al., 2014; Webb et al., 2014; Bell and Webster, 2015b; Webster et al., 2015; Farcy et al., 2016; Thomas and Wood, 2021). For more comprehensive summaries of the effects of halogens on silicate melt properties, see reviews by Aiuppa et al., (2009), Dolejš and Zajacz, (2018), and Webster et al., (2018).

Here we investigate the effects of fluorine and chlorine on the crystallization behavior of a hydrous trachytic melt. During the investigation of the diffusivity of F and Cl in silicic melts (e.g., Feisel et al., 2019 and *under review*) we have observed the strong effects of the halogen concentration gradient on the phase equilibria in this melt system. Below, we determine the halogen concentrations at the transition from crystal-bearing to crystal-free assemblages of hydrous trachytic melt. We show that very low-F and low-Cl concentrations added to the melt phase (hundreds of parts per million) lead to a first-order effect on the crystallization properties and may therefore influence the state and behavior of these systems during a volcanic eruption or during hot volcanic deposition processes.

6.2 Methods

6.2.1 Experimental procedure

Synthesis of the starting materials was conducted at the LMU Munich. Experimental glasses were synthesized from natural lava of the obsidian flow of the 2011 eruption of Cordón Caulle, Chile (e.g., Castro et al., 2013; Schipper et al., 2013; Alloway et al., 2015; Castro et al., 2016). In a first step ca. 800 g of the powdered lava was melted in a large Pt crucible (~10 × 4 cm) at high temperatures (1450–1500 °C) for ~4 days to drive off all volatiles and to homogenize the melt. During the synthesis, the melt was stirred with a Pt-rod (~3 mm diameter) attached to a rheometer to accelerate homogenization and thereby to outrun volatile loss. After stirring, the crucible was removed from the furnace and placed on insulation to cool to a crystal- and bubble-free glass. The resultant glass was split into two aliquots. These aliquots were then remelted to generate the halogen-bearing and halogen-free (hereafter halogen-poor) glasses. Sample CC1, the halogen-bearing glass, was enriched in NaF + NaCl + NaBr + NaI, by adding powders of the sodium halides to achieve ~1 wt.% of each halogen in the mixture. Sample CC2, the halogen-poor glass, was enriched in Na_2CO_3, to yield an equivalently Na-enriched halogen-depleted composition

(Feisel et al., 2019). During the second synthesis, the melts were again stirred for several days to ensure homogenization before being quenched in air to room temperature.

Diffusion couple experiments were prepared by introducing the ground glass powders made from samples CC1 and CC2 into 5 mm diameter Pt-tubing (6 mm long). Each capsule was closed on one end with a Pt-lid, and then welded shut and tamped with a tight-fitting metal rod to ensure cylindrical inner geometry. Powder of the halogen-bearing glass was then loaded in the bottom half of the capsule and tamped. An equivalent of ~3.5 wt.% H_2O was added to the capsule using a microsyringe. The capsule was then filled with the halogen-poor powder, tamped by hand, and another ~3.5 wt.% H_2O was added. Tamping of the powders after loading them into the capsule ensured a flat diffusion interface oriented perpendicular to the capsule walls (i.e., perpendicular to the diffusion direction). Finally, a tight-fitting lid was welded to the open end of the capsule using a micro-arc welder and tamped into a cylindrical shape with a pressure of ~750 kg. To confirm that the capsules were reliably sealed, they were repeatedly heated to ~120 °C using a heating plate and weighed to confirm no weight loss. Capsules with significant weight loss were discarded. To confirm that the diffusion couple experiments were representative of longer term experiments, approaching equilibrium conditions, two additional capsules were prepared, each containing only one of the starting materials and the equivalent amount of ~3.5 wt% H_2O.

All experiments were conducted at the University of Mainz using horizontal and vertical tube furnaces and Ni-Co-alloy (*Rene-41*) cold-seal pressure vessels. H_2O was used as the pressure medium. To control the oxygen fugacity during an experiment and to prevent convection of H_2O in the vessel, the free space below the sample capsule inside the autoclave was filled with a nickel-metal filler-rod (Matthews et al., 2003). The oxidation of the Ni-rod during the experiment con- trolled the oxygen fugacity in the system close to NNO+1 (e.g., Geschwind and Rutherford, 1995; Schmidt and Behrens, 2008).

For each experiment, the vessel was placed in the furnace and brought to the target pressure (100 MPa) before increasing the temperature. The pressure was monitored with a pressure transducer and a factory-calibrated Bourdon-tube gauge. Upon heating to the target temperature, the pressure was continuously monitored and adjusted to stay at 100 MPa. Heating took between 40 and 70 min to reach the dwell temperature — monitored using a K-type thermocouple being inserted into a bore at the end of the vessel at a point closest to the capsule. The internal thermocouple of the furnace was additionally used to monitor the tem- perature. Due to the small capsule size (~5 × 6 mm) compared to the larger vessel (~39 × 260 mm; ~16 mm wall thickness) and the constant temperature readings of both thermocouples during all runs, we consider the temperature to be constant in the diffusion couple capsule.

To preserve the full gradient of halogen concentrations across the diffusion couple the run time was chosen based on the estimated diffusivities of the halogens, and these times varied from ~1 to ~15 h

depending on the temperature. To evaluate when during the relatively short experimental durations the crystallization and dissolution occurred, a zero-time experiment was conducted whereby the diffusion couple was heated to target temperature (~40 min/950 °C) and then quenched. Two experiments with pure starting materials were performed simultaneously in the same vessel to ensure the same *P-T* history for both. The duration for these experiments was limited to ~30 h to avoid failure of the vessel. Before quenching experiments, the pressure was increased by ~30 bar to account for pressure loss upon cooling. The hot vessel was first air-cooled with compressed air until it stopped glowing, and the pressure approximately decreased back to the run pressure (~60–90 s). The vessel was then dropped into a water bath for the final quench. This complete process lasted 2 to 3 min, so a quenching time of ~4 min is estimated.

6.2.2 Chemical analyses

After the removal of capsules from the vessel, they were dried and weighed to ensure that no weight loss or gain occurred during the experiment. Samples were embedded in epoxy, cut open along the center of the capsule and polished for electron microprobe analysis. Care was taken to ensure that the final sample surface was parallel to the long axis of the capsule, i.e., parallel to the diffusion direction. All major element and halogen analyses were conducted with a *JEOL* JXA 8200 electron microprobe in the Department of Geoscience of the University of Mainz. Major elements were analyzed simultaneously with F and Cl using an acceleration voltage of 15 kV, a beam current of 12 nA, and a beam diameter of 10 µm. Dwell times of 120 and 30 s were used for F and Cl, respectively, and the detection limits for both were 60 ppm (1σ). Dwell times of the major elements were: Si 25 s, Al 40 s, Na 20 s, K 30 s, Ca 30 s, Fe 60 s, Mg 30 s, Mn 50 s, and Ti 30 s. Standards used for calibration are SrF_2 (F), tugtupite (Cl, Na), VG-2 (Ca, Mg), VG-A99 (Fe, Si), MnTi (Mn, Ti), and orthoclase (Al, K). VG-2, VG-A99, VG-568, and a natural obsidian standard were analyzed repeatedly during each analytical session. The ZAF method was used for matrix correction. As the crystal size was generally too small for quantitative EPMA analysis, qualitative EDS maps of a small crystal-bearing area of sample 18X were acquired, being representative of all crystal-bearing samples. The maps included F, Cl, and major elements (Ca, Fe, Mg, Si, Al, Na, K) with a pixel size of 0.5 × 0.5 µm, using an acceleration voltage of 15 kV, beam current of 30 nA, and dwell times of 280 ms for each element.

The transition from crystal-bearing to crystal-free glass was characterized by acquiring halogen concentration profiles perpendicular to the diffusion interface. The F and Cl concentrations at the interface (c_{liq}) were determined by calculating the average of the four points of the concentration profile, which are closest to the crystal interface (2 on each side). In 8 out of a total of 11 diffusion couple samples, an additional line was measured for characterization of c_{liq}. In this additional approach, a line parallel to the crystal-glass interface was first defined on a backscattered image of the sample. Along

this line, 20–25 spots per sample were measured with fixed spacing (~80–100 µm), and from these spots, the average concentrations of F and Cl were calculated.

6.2.3 Spectroscopic analyses

To identify the microcrystalline silicate phases present in the experimental samples Raman spectroscopy was carried out in the laboratories of the Department of Geoscience of the University of Mainz, using a *Horiba-Yvon* Labram-HR Raman microscope with a focal length of 800 mm. A 200 mW diode-pumped solid-state laser with a wavelength of 532 nm was used as the excitation source. The spectra were recorded with a 50× long-distance objective and pinhole size and slit width of 400 and 100 µm, respectively, to ensure optimal confocal conditions. An edge filter was employed to suppress Rayleigh-scattering intensities. Spectra were collected within the interval from 200 to 1100 cm^{-1} as a single spectral window using a grating of 1800 grooves/mm. Due to the small crystal size, recorded spectra usually contained some background signal related to the vibrational response of the glass matrix. Therefore, crystal-free areas in the experimental glasses were measured and compared to crystal-bearing measurements to identify the vibration bands of the crystalline phase. Spectra of crystals were then corrected by subtracting the background and vibrational response of the glass matrix from the crystal-bearing signal.

To confirm homogeneity of H_2O within the experimental capsules, FTIR analyses were carried out on three representative samples (4X, 7X, and 15X), using a *Thermo-Nicolet* 6700 FTIR spectrometer coupled to a *Continuum* microscope at the JGU, Mainz. Doubly polished wafers with a thickness of ~120–220 µm were analyzed in transmission mode, covering the mid-IR and near-IR regions (450–6500 cm^{-1}) using a KBr beamsplitter and a MCT/A detector. Sample-free background spectra were collected every 20 min and each spectrum was acquired using a resolution of 4 cm^{-1} and 256 scans. Two samples (7X and 15X) were analyzed by line scans following the diffusion direction. Sample thickness was measured at a minimum of ≥15 points per sample along the linear measurement traverses with a Mitutoyo precision micrometer. Thicknesses were then linearly interpolated to assign each analyzed spot with a corresponding thickness value. Single doubly polished glass fragments of sample 4X were analyzed by individual spot measurements. Here, the sample thickness was determined by multiple measurements of each fragment. Bulk water content was determined from the height of the two absorbance peaks at 4500 cm^{-1} (OH) and 5200 cm^{-1} (H_2O_m) relative to a linear background below the peaks (e.g., Ihinger et al., 1994; Cherniak et al., 2010) and was calculated with Beer's law using the following extinction coefficients for trachyte: 1.58 L/mol^{-1} and 1.36 L/mol^{-1} (for the bands at 4500 and 5200 cm^{-1}, respectively; Di Matteo et al., 2004). Melt densities between 2446–2453 g/L were calculated using *DensityX* (Iacovino and Till, 2019), which accounts for the average major element composition of the melt (Table 6.1) and the mass of water added to the glass during capsule preparation (Table 6.2).

Due to the presence of abundant crystals in some parts of the analyzed samples (Fig. 6.1), the measured water concentrations had to be corrected for the anhydrous crystal content (e.g., von Aulock et al., 2014), which will "dilute" H_2O values by virtue of their occupying a fraction of the measurement path. Backscattered images of the respective samples were converted to binary images and analyzed for crystal-volume fraction using the software *ImageJ*. The water content in the crystal-bearing part was then corrected by the factor of crystal abundance to achieve the final H_2O values.

6.3 Results

6.3.1 Starting glass compositions

The starting material compositions are provided in Table 6.1 and compared to bulk rock data of Castro et al. (2013). The data are based on the concentration profiles of the experimental samples, measured by EPMA and were calculated from the average concentration of the 10 outermost points of each end of the concentration profiles (i.e., in areas that were unaffected by diffusion and thus retained their pre-experimental major element and halogen concentration). Where profiles of F or Cl did not exhibit a concentration plateau of sufficient length, fewer analysis points were included in the calculation of F and Cl concentrations (min. 3 points). Analyses with totals below 95 wt.% or F and Cl values below three times the detection limit (180 ppm, 3σ) were discarded. Analyses with elevated values of Fe, Mg, and Ca co-occurring at the same spot were interpreted to have been acquired on areas including crystals and were therefore also discarded.

6.3.2 Post-experimental sample textures

All experiments (925–990 °C; 100 MPa; Table 6.2) produced glassy samples with only few small bubbles (Fig. 6.1). In all but two experiments, a single-crystal phase developed. These euhedral crystals range from <1 to a few 10s of μm in size and are of prismatic shape. They are chiefly concentrated in spherulitic clusters, i.e., they form spheroidal aggregates of radially oriented crystals (Fig. 6.1a) commonly associated with the process of devitrification (e.g., Keith and Padden, 1963; Lofgren, 1971). The spherulites are up to 100 μm and they occur exclusively scattered throughout the initially halogen-poor part of the sample. The border of the crystal-bearing zone is well-defined and is approximately parallel to the initial diffusion couple interface.

Table 6.1: Major element composition of synthesized glasses in wt.%. See text for details.

	CC1	CC2	*Puy av.* [b]
F	0.87 (4)	0.06 (3)	-
Cl	0.36 (1)	0.06 (1)	-
SiO_2	65.8 (5)	66.4 (6)	69.9 (1)
TiO_2	0.63 (2)	0.63 (2)	0.70 (3)
Al_2O_3	13.7 (2)	13.9 (3)	14.4 (1)
FeO_{tot}	3.4 (3)	3.5 (3)	4.1 (1)
MnO	0.11 (3)	0.10 (3)	0.11 (1)
MgO	0.58 (5)	0.5 (2)	0.54 (5)
CaO	2.00 (2)	1.8 (4)	2.24 (4)
Na_2O	7.6 (2)	7.7 (3)	5.16 (7)
K_2O	2.37 (5)	2.43 (6)	2.76 (2)
LOI	-	-	0.34 (6)
Total	96.93[a]	97.02[a]	100.25

[a] Totals of CC1 and CC2 are corrected for stoichiometric oxygen, calculated by the EPMA matrix correction process.
[b] XRF data from Castro et al. (2013); composition of the starting material used for synthesis of CC1 and CC2.

The two control experiments, 33X and 34X (both 950 °C), produced sample textures similar to those observed within the spatial end-members of the diffusion couples: the halogen-bearing melt remained mostly crystal free except for a few anhedral crystal nuclei smaller than 1 μm (Fig. 6.1b). The halogen-depleted sample developed spherulitic crystals throughout the whole charge (Fig. 6.1c). In one low-temperature experiment 26X (940 °C), the crystals did not form clusters throughout the entire halogen-poor zone. Instead, there are two textural transitions oriented roughly parallel to the diffusion front, one from glassy to crystal bearing where the crystals are randomly oriented and irregularly scattered, and a second transition from random to spherulitic aggregates (Fig. 6.1d). For the determination of c_{liq} (see "Assessment of c_{liq}: F and Cl concentration at the transition from crystal-free to crystal-bearing glass" section), the transition to clustered crystal-bearing glass was analyzed. The zero-time experiment (7X) developed homogeneously distributed crystals in the halogen-poor half that are smaller in size but more numerous than those produced by the experiments of longer duration, and they show a very sharp transition to crystal-free glass at the initial diffusion interface (Fig. 6.1e).

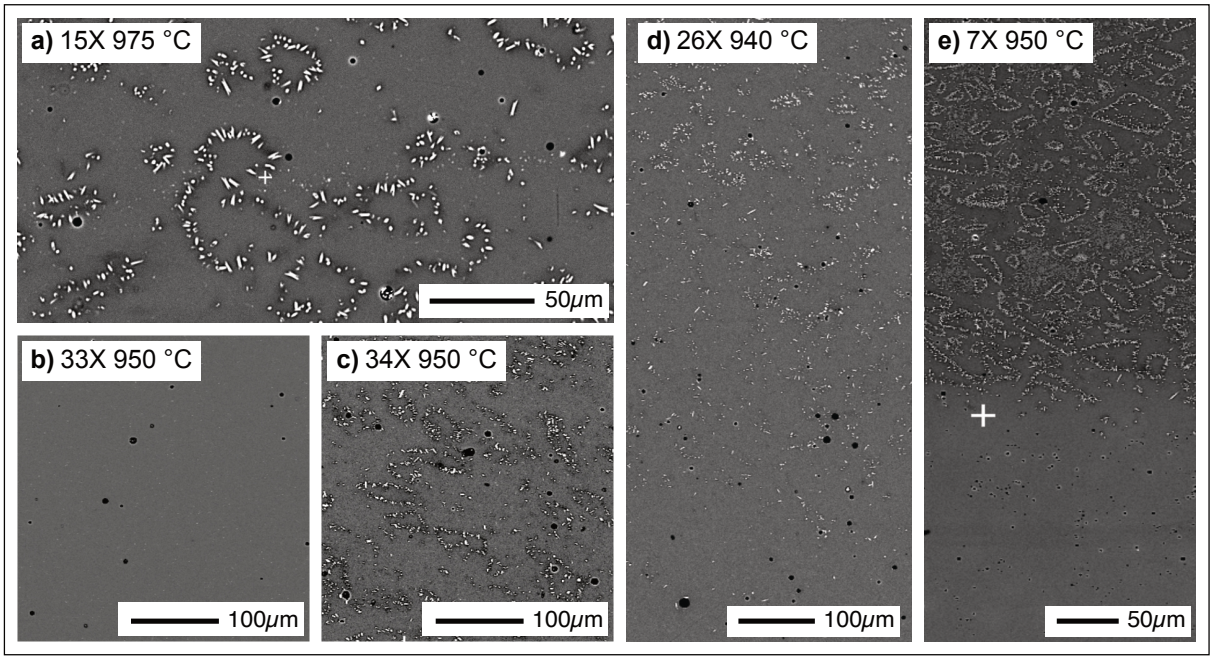

Figure 6.1: Backscattered images of experimental run products. **a)** Detailed view of sample 15X showing the spherulitic aggregation of elongate crystals. **b)** and **c)** The halogen-bearing and halogen-depleted control experiments 33X and 34X (both ~30 h) illustrating the strong contrast in crystallinity. **d)** Sample 26X illustrating the lack of one sharp transition from crystal-free to crystal-bearing glass. **e)** Sample 7X (zero-time) showing uniformly crystalline upper half, corresponding to the initially halogen-poor aliquot.

The halogen-poor melt contains spherulitic crystals up to temperatures of at least 975 °C at 100 MPa and is crystal-free at 990 °C. The halogen-enriched melt remains crystal free down to temperatures of at least 940 °C but contains spherulites at 925 °C. The onset of crystallization in these experiments is interpreted to reflect that the melt was below the liquidus. Considering 940 °C to be the lowest temperature at which halogen-bearing melt is crystal free (26X) and 990 °C to be the lowest temperature at which halogen-depleted melt is crystal free (22X), these results imply a liquidus depression of 50 °C for the highest measured values of c_{liq} (~0.51 wt% F, ~0.24 wt% Cl) in the melt of this study and at the experimental conditions (100 MPa, 3.5–4 wt% H_2O).

Table 6.2: Conditions and results of all experiments (P = 100 MPa).

sample	*T* (°C)	*t* (s)	H_2O[a] (wt.%)	liquidus concentration c_{liq}					
				profile [b]			diss. front [c]		
				F (wt.%)	Cl (wt.%)	F+Cl (mol%)	F (wt.%)	Cl (wt.%)	F+Cl (mol%)
17X	925	92280	3.62	-	-	-	-	-	-
26X	940	53640	3.66	0.52 (4)	0.23 (1)	0.034 (2)	0.51 (3)	0.24 (1)	0.034 (2)
4X	950	15840	3.58	0.48 (3)	0.21 (2)	0.031 (2)	0.44 (3)	0.19 (1)	0.029 (2)
6X	950	37860	3.97	0.41 (1)	0.17 (2)	0.026 (1)	-	-	-
7X	950	0	3.87	0.50 (7)	0.24 (3)	0.033 (5)	-	-	-
18X	960	15960	3.50	0.41 (3)	0.18 (3)	0.027 (2)	0.41 (3)	0.18 (2)	0.026 (2)
23X	960	21180	3.58	0.43 (2)	0.16 (2)	0.027 (2)	0.42 (2)	0.16 (1)	0.027 (2)
25X	968	15780	3.53	0.35 (3)	0.16 (2)	0.023 (2)	0.39 (3)	0.17 (2)	0.025 (2)
15X	975	8520	3.68	0.20 (3)	0.07 (1)	0.012 (2)	0.19 (1)	0.07 (1)	0.012 (1)
24X	975	10320	3.57	0.27 (5)	0.09 (3)	0.017 (3)	0.26 (2)	0.09 (1)	0.016 (1)
22X	990	3960	3.70	-	-	-	-	-	-
33X	950	108660	3.39	-	-	-	-	-	-
34X	950	108660	3.49	-	-	-	-	-	-

[a] H_2O initially added to the capsule; considered maximum value.
[b] calculated from the 4 points of the concentration profile which are closest to the dissolution front.
[c] calculated from profiles measured along the dissolution front.

6.3.3 Glass and crystal chemistry

In the compositional map of sample 18X crystals show enrichment in Ca, Fe, and Mg relative to the melt (Fig. 6.1a–c; Online Materials[5] Fig. S1), suggesting clinopyroxene, as was confirmed by Raman spectroscopy of several grains in sample 24X. The Raman spectra showed two prominent peaks at ~664 and ~1010 cm^{-1} and two smaller peaks at ~327 and ~392 cm^{-1}, respectively (Fig. 6.2d), consistent with the three main vibration regions of clinopyroxene (Lafuente et al., 2015). The 1010 cm^{-1} peak is ascribed to T-O stretching, while the peak at ~664 cm^{-1} is caused by chain bending/stretching modes. The two low-frequency bands in the region 400 cm^{-1} are characteristic of the vibrational response of both M-sites (e.g., Tribaudino et al., 2012). The broad double band between 700 and 800 cm^{-1} is a remnant signal of the glass matrix (e.g., Helo et al., 2020). The slight depletion of Mg and Ca in the glass of CC2 (Table 6.1) agrees well with the presence of clinopyroxene crystals and the corresponding depletion of these elements in the melt.

All concentration profiles exhibit typical diffusion patterns of F and Cl (e.g., Feisel et al., 2019), while the major element concentrations are relatively constant (Fig. 6.3). Some variability along the profile is observed in SiO_2 content, possibly related to the presence of microlites on the crystal-bearing, halogen-poor side and concomitant shift in residual glass composition due to the growth of crystals. Furthermore, scatter of FeO, MgO, and CaO concentrations on the crystal-bearing side of the diffusion couple are likely caused by analytical regions partly containing crystals. This effect is particularly pronounced in the zero-time experiment 7X, which contains abundant small crystals, which could not be avoided during data acquisition. Most analyses yielded totals between 96 and 97 wt.%, which is consistent with the expected H_2O-concentration in the capsule.

FTIR analyses on three representative samples showed mostly homogeneous distribution of H_2O with variation limited to just a few tenths of weight percent. However, due to the lack of appropriate published extinction coefficients for the melt composition used in our study, and the presence of abundant crystals, the absolute values determined by FTIR are considered to be only approximate. For example, in sample 15X a water concentration of 4.2 wt.% was determined for both the crystal- bearing and crystal-absent parts of the sample. However, upon preparation of the sample, only 3.67 wt.% of H_2O was added (Table 6.2). This water content (3.67 wt.%) is considered to be a maximum possible value as a small loss of

[5] Deposit item AM-22-68120, Online Materials. Deposit items are free to all readers and found on the MSA website, via the specific issue's Table of Contents.

(go to http:// www.minsocam.org/MSA/AmMin/TOC/2022/Jun2022_data/Jun2022_data.html).

water during the subsequent preparation of the capsule (tamping, welding, etc.) could have occurred. Water-gain, in contrast, is not likely to have occurred during the experiment and was monitored by weighing the capsule directly before and after the experiment. The overestimation of the water content in sample 15X is, therefore, likely a consequence of the presence of bubbles in parts of the sample and the lack of appropriate extinction coefficients for the melt composition used. Sample 4X has an average water content of 3.4 and 3.5 wt.% in the crystal-bearing and crystal-free parts, respectively. The crystal content of this sample is similar to that of 15X (6% compared to 4%). The zero-time experiment 7X also shows a homogeneous H_2O-profile with 3.7 and 3.9 wt.% in the crystal-free and crystal-bearing parts, respectively. The water content in this sample was corrected considering a crystal content of 15% in the crystal-bearing part. The data of all measured FTIR profiles are provided in Online Materials Figure S2.

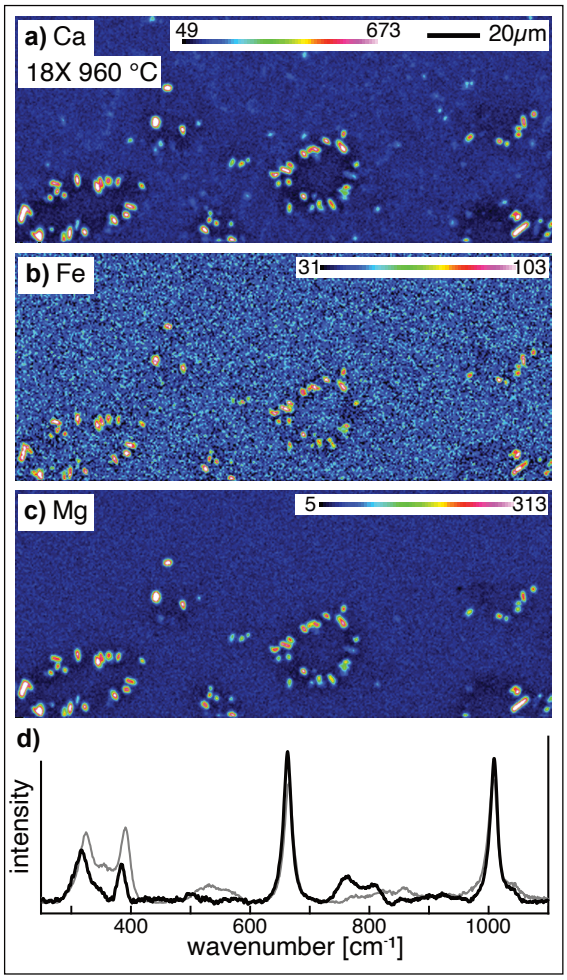

Figure 6.2: Compositional maps and Raman spectra acquired for crystal identification. **a)–c)** Compositional maps of sample 18X. Concentrations of Ca, Fe, and Mg are significantly enriched in the crystal phases. Units of intensity correspond to counts (cts). Maps showing the concentrations of other components in this area are provided in Online Materials Figure S1. **d)** Raman spectrum of a crystal in sample 24X (bold line). Augite reference spectrum (thin gray line) from the Raman data repository (Lafuente et al., 2015). Intensities in arbitrary units.

6.3.4 Assessment of c_{liq}: F and Cl concentration at the transition from crystal-free to crystal-bearing glass

A section of a typical concentration profile is shown in Figure 6.3. In these diagrams, the transition to crystal-bearing glass (dashed orange line) is displaced with respect to the original interface between the diffusion-couple halves (dashed white line). Figure 6.3b shows a backscattered image spatially coincident with the concentration profile geometries of sample 4X. This image shows that the transition from crystal-free melt (bottom) to crystal-bearing melt (top) is indeed quite sharp. Figure 6.3c shows the corresponding homogeneous major ele- ment concentrations. The c_{liq} data of F and Cl are presented in Table 6.2 and illustrated in Figure 6.4. c_{liq} values are in the range of 0.19–0.52 and 0.07–0.24 wt.%, respectively with higher values corresponding to lower experimental temperatures. In Table 6.2, the data labeled "Profile" are based on the diffusion profile approach, and data labeled "Dissolution Front" are based on analyses along the transition interface. Values determined by the two different methods agree well for each sample. All concentration vs. distance diagrams for F, Cl, and all major elements, measured along the diffusion direction and the dissolution front, are provided in Online Materials Figures S3 and S4.

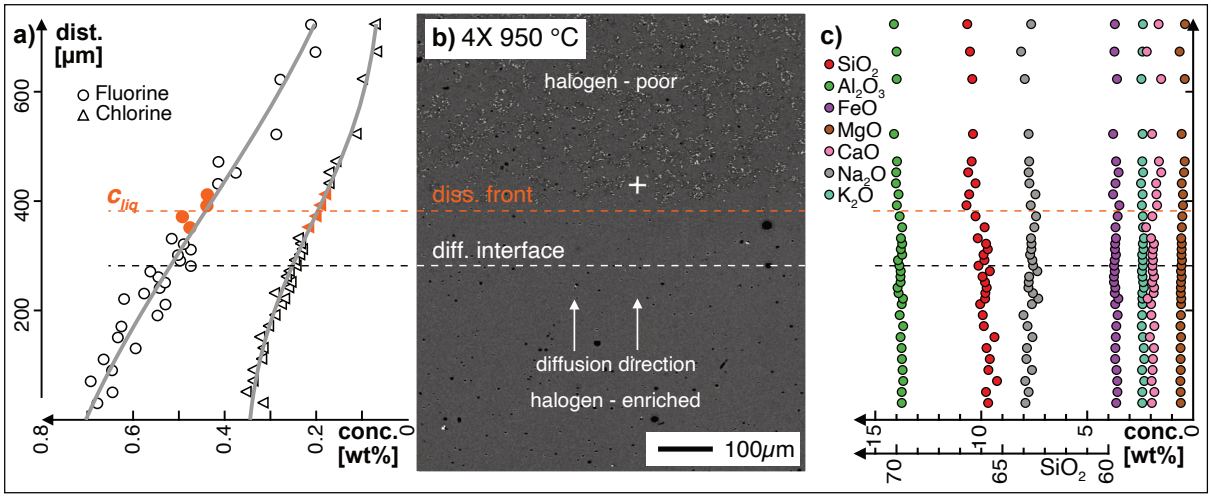

Figure 6.3: Halogen and major element concentration profiles of sample 4X (100 MPa – 950 °C – 15840 s). **a)** Section of a concentration profile of F and Cl. The diagram is scaled to match the backscattered image in **b)** showing an enlargement of the very sample. **c)** Diagram showing the major element concentration of the same section of the profile as in a). SiO_2 concentration is referenced to the secondary y-axis. The white/black dashed lines mark the inferred diffusion interface at the start of the experiment and the orange dashed lines mark the concentration and position at the transition to crystal-bearing melt. Orange data-points are used to calculate the transition concentration c_{liq} for F and Cl, respectively. The grey lines in a) are fits calculated with the equation for diffusion between two semi-infinite half spaces (Crank, 1975).

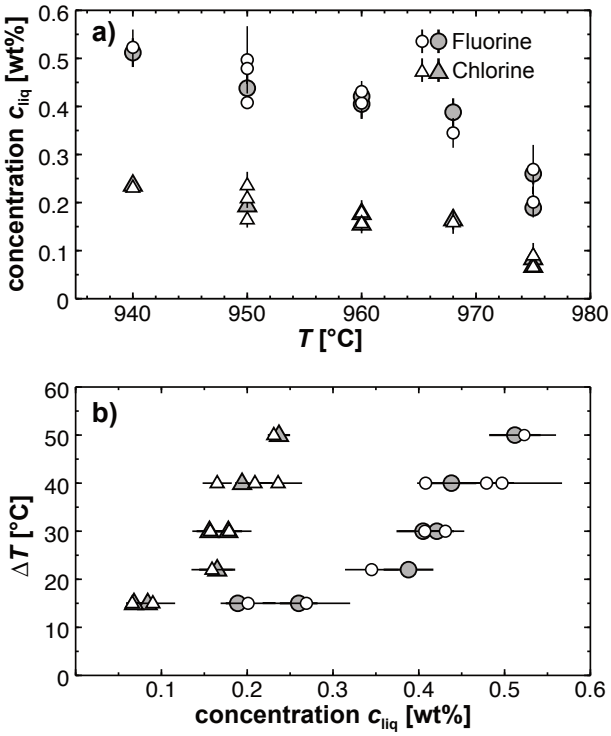

Figure 6.4: Diagrams of c_{liq} vs. temperature and ΔT, respectively. **a)** F and Cl concentration at the point of transition from crystal-bearing to crystal-free melt (c_{liq}) at the different experimental liquidus-temperatures. **b)** Depression of the liquidus relative to the different experimental liquidus concentrations. ΔT is calculated based on a halogen-free liquidus temperature of 990 °C. Small open symbols represent data averaged from the 4 points closest to the interface and larger solid symbols represent data from analysis along the dissolution front. Error bars on symbols illustrate the standard deviation of the values used to calculate the average concentration.

6.4 Discussion

6.4.1 Assessment of experimental approach

In this study, the influence of F and Cl on a near-liquidus silicic melt has been determined using a dynamic disequilibrium approach. The diffusion couple technique imposes a large concentration range of F and Cl in a single experiment and permits investigation of the whole range of compositions — from the extreme initial values to every intermediate concentration — at constant *P*-*T* conditions. This, of course, assumes that the diffusion of halogens at these conditions is slow enough to facilitate a response of the melt (e.g., crystal dissolution) on a local scale (tens of micrometers). Even though no equilibrium state can be reached during the short timescale of diffusion experiments, the melt does, however, react to the changing halogen concentrations in the form of crystal dissolution. The quenched glass can therefore be used as a series of chemical and textural "snapshots" of the systems' approach to equilibrium, including a robust record of varying halogen concentrations. The key to this approach is to bring the diffusion couple to a near-liquidus temperature (with respect to the halogen-poor melt). At these *T*-conditions, the halogen-rich melt is well above its liquidus. While the duration of equilibrium experiments is required to be sufficiently large to achieve equilibrium (e.g., Pichavant et al., 2007), our

experiments were deliberately quenched quickly enough so as to preserve the diffusion concentration profiles, which span the full range of F and Cl concentrations.

Diffusion profile fitting. The concentration profiles were fitted with the equation representing constant one-dimensional diffusion between two semi-infinite media in Cartesian coordinates (Crank, 1975):

$$C(x,t) = \frac{C_{high} + C_{low}}{2} + \frac{C_{high} - C_{low}}{2} \operatorname{erf}\left(\frac{x - x_0}{\sqrt{4\,D\,t}}\right) \tag{6.1}$$

where $C(x,t)$ is the concentration (wt.%) at distance x (m) after the experimental time t (s). C_{low} and C_{high} (wt.%) are the initial concentrations of each half-space, x_0 (m) the position of the diffusion interface, which is only used for fitting purposes (Zhang, 2010). D (m^2/s) is the diffusion coefficient. One example of a fitted concentration profile (15X) is shown in Figure 6.5. The good correlation between the concentration profile and the solution to the diffusion equation 6.1 shows that melt crystallization does not affect halogen diffusion, i.e., that the halogens are diffusing independently and are in turn affecting the crystallization of the melt.

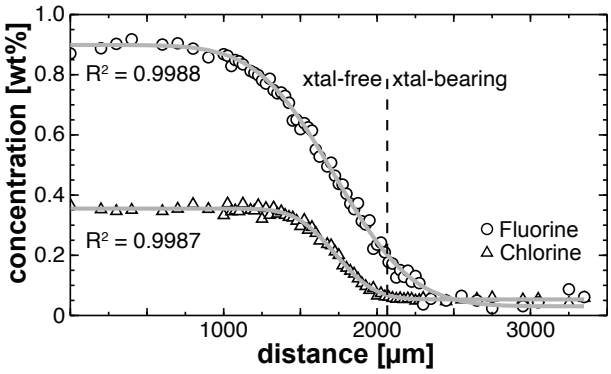

Figure 6.5: Fitted halogen concentration profiles of sample 15X. Gray lines show the fitted solution to diffusion equation 6.1.

Progression of crystal growth and dissolution. The zero-time experiment revealed that spherulitic clinopyroxene grew in the halogen-poor half within the heating phase of ~45 min (Fig. 6.1e), indicating that crystal growth was initiated before any substantial flux of halogen diffusion had occurred. A sharp transition developed from crystal-free to crystal-bearing glass, and crystals grew with the same spherulitic morphology as in the longer experiments. Given these observations, we infer that: (1) all diffusion couples began with a textural configuration of a crystal-free, halogen-rich melt juxtaposed against a crystal-free, halogen-poor melt; (2) crystal-free, halogen-poor melt experienced crystallization during the heating phase and thus in the absence of any substantial diffused halogen contribution to the melt, whereas the halogen contents of the halogen-rich melt inhibited such crystallization; and (3) diffusion of halogens into the crystal-bearing zone during the subsequent experimental run, causing crystal dissolution whose progress describes a planar dissolution front.

A glass transition temperature of ~350 °C was calculated based on the halogen-poor composition CC2 (Table 6.1) using the method of Giordano et al. (2008) and considering an average water concentration of 3.7 wt.%. The spherulites present here, comprising individual crystals that are not in direct contact with each other, could have formed by devitrification at relatively low degrees of undercooling and above T_g (Fenn, 1977; Lofgren, 1980; McArthur et al., 1998; Castro et al., 2008). The ensuing process of crystal dissolution during advancement of the halogen diffusion front at isothermal conditions rules out kinetic effects that may be introduced by heating or cooling. This ensures that no activation energy associated with crystal nucleation must be overcome, as would be the case in a crystallization scenario (e.g., Kirkpatrick, 1983; Burkhard, 2005). The latter would result in a "delayed" response of the melt to the changing halogen concen- trations leading to biased readings of c_{liq}. We, therefore, consider the measured halogen concentrations at the dissolution front to represent the halogen concentrations of the liquidus composition, which is defined by the halogen concentration necessary to keep the melt crystal free at the experimental *P-T* conditions. The significance of the measured liquidus composition is further confirmed by the two control experiments 33X and 34X, which developed similar textures like the diffusion couples and verified the liquidus depressing effect even over the longer run duration of ~30 h.

Br and I in the melt. As the initial halogen-bearing starting glass CC1 was also enriched in Br and I, their potential effect on crystal dissolution needs to be assessed. The diffusivity of Br was shown to be almost one order of magnitude slower than Cl in hydrous phonolitic melt (Balcone-Boissard et al., 2020) at 1250–1450 °C and in dry rhyodacitic melt (Feisel et al., 2021) at 850–1100 °C . However, our own unpublished data indicates Br diffusivity in the hydrous melt used in this study may be only slightly slower than Cl (<< 1 log unit). Even though the effect of Br on the phase equilibria cannot be completely ruled out, Br is not known to preferably bond with the major elements of clinopyroxene but has instead been demonstrated to form complexes with Na (Cochain et al., 2015; Webster et al., 2018). Therefore, we consider the effect of Br on clinopyroxene dissolution in our study to be negligible.

The diffusivity of I was found to be substantially slower than Br in dry rhyodacite and also in the hydrous trachytic melt used in the present study. We, therefore, conclude that on the timescales of the current experiments I mobility will be insignificant, and its concentration distribution will not deviate from the initial concentration geometry in the diffusion couple. Consequently, the crystal-dissolution front is not expected to correlate with I concentrations, and thus, we consider that I has no effect on melt crystallization or resorption.

Comparison to equilibrium experiments. Our experimental approach was further assessed by comparison to a phase-equilibrium study on a very similar melt composition. Castro et al. (2013) experimentally reproduced the mineral and glass compositions observed in the 2011 Cordón Caulle rhyolite magma to infer pre-eruptive magma storage and ascent conditions. They used natural

pumiceous samples of the Plinian phase of the eruption, with a major element composition almost identical to that of the obsidian lava used as a base material for the present experiments (Table 6.1). They applied a very similar experimental setup (NNO+1), and their starting material contained 0.14–0.2 wt.% Cl, which is comparable to the halogen-enriched starting composition of our study. No data on F concentration is available from their study; however, Schipper et al. (2019) report F concentrations around 0.1 wt.% in the matrix glass of pyroclasts of the same eruption.

Castro et al. (2013) found the liquidus temperature to be in the range of 940–950 °C, at a pressure of 100 MPa with ilmenite and magnetite being on the liquidus at these conditions. Clinopyroxene appeared in the phase assemblage about 40 °C lower. In our experiments, the liquidus temperature of halogen-enriched melt is similar to but at the lower end of this range (~950–900 °C) and is defined by the appearance of clinopyroxene. This offset is likely a consequence of slight compositional differences between the melts, particularly the enhanced Na and F contents transferred to the melt via sodium-salts during sample synthesis (Table 6.1). Additionally, while the experiments performed by Castro et al. (2013) were saturated in H_2O, those of this study were, by design, slightly undersaturated at 100 MPa (3.5–4 wt.% H_2O) to avoid the formation of gas bubbles. The correspondingly lower water activity in our experiments at equivalent confining pres- sure (100 MPa) explains some observed difference in liquidus relations between our study and the study of Castro et al. (2013) (e.g., see also Scaillet et al., 2016).

6.4.2 Effects of F and Cl on the melts liquidus temperature

The halogen concentrations necessary to suppress crystallization at a given temperature (c_{liq}) were quantified (Table 6.2). All experiments which resulted in a partially crystal-bearing sample can be viewed as experiments whose halogen concentrations at the dissolution front essentially define the liquidus composition at that temperature. The c_{liq} decreases linearly with increasing temperature (Fig. 6.4a), which shows that the depression of the liquidus temperature is proportional to the halogen contents. This trend is illustrated in Figure 6.4b, which shows the relation between the concentration of F and Cl and the liquidus depression (ΔT). The liquidus depression represents the difference between the liquidus temperature of the halogen-poor melt at ~990 °C (22X) and the run temperatures of each plotted experiment.

Figure 6.4b indicates that Cl is about twice as effective as F in depressing the liquidus. Indeed, considering their molar masses, Cl is almost four times more effective per atom than F. However, the concentrations of F and Cl measured at the dissolution front cannot be viewed as independent variables, as they each diffuse with a constant diffusivity over the same time period and at the same *P*-*T* conditions. Thus, the ratio of their concentrations will be dictated by their diffusivities and run time. In summary,

even though ΔT increases more strongly with increasing Cl than F, it is not possible to attribute the liquidus depressing effect to one of the halogens based on the values of c_{liq}.

Insights into the potential effects of the individual halogens may be elucidated by their typical bonding behavior. Previous studies have shown that F complexes with Al in aluminosilicate melts (Kohn et al., 1991; Schaller et al., 1992; Kiprianov and Karpukhina, 2006; Karpukhina et al., 2007), but may also form species with Na, Mg, or Ca (Zeng and Stebbins, 2000; Kiczenski et al., 2004; Mysen et al., 2004). Additionally, pronounced fluorine complexation of Mg over Fe was shown for a Mg-Fe rich basalt (Filiberto et al., 2014), and other studies found evidence for Si-F bonding in silicate melts (e.g., Liu and Nekvasil, 2002). In particular, the strong association of the network modifying cations Mg and Ca with F indicates that F has the potential to bond with two major components of clinopyroxene.

Cl was also shown to commonly bond with network modifying cations such as Ca and Mg, and especially Fe (e.g., Dingwell and Hess, 1998; Webster and De Vivo, 2002; Filiberto and Treiman, 2009; Dolejš and Zajacz, 2018). Along with the study of (Bell and Webster, 2015), who showed that the presence of Cl increases Fe solubility and affects the availability of Fe for magnetite crystallization in hydrous rhyodacitic melts, our results show a similar effect for clinopyroxene. According to Webster and De Vivo (2002) the solubility of Cl in a melt increases with the abundances of Mg ≈ Ca > Fe^{2+} >> Na > K. This indicates that dissolved Cl preferably bonds with the major components of clinopyroxene crystals Ca, Mg, and Fe. As both halogens likely have the potential to complex with some of the main components of clinopyroxene, namely F with Mg and Ca, and Cl with Mg, Ca, and Fe, we propose that crystal dissolution is a consequence of both halogens diffusing into the crystal-bearing melt. The presence of F and Cl enhances the solubility and reduces the activity of CaO, MgO, and FeO for clinopyroxene crystallization.

As no major element analyses of clinopyroxene are available, it is not possible to quantitatively compare crystals grown in halogen-bearing and halogen-depleted melt (e.g., 17X) to determine which of the constituents of clinopyroxene is the most affected by dissolved halogens. The weak depletion of CaO and MgO in the average bulk composition of the halogen-depleted melt (CC2; Table 6.1) indicates that the clinopyroxene may be composed of mainly these two components and only to a minor extent of FeO. This in turn argues that mainly Mg- or Ca-complexes should be formed by crystal dissolution, which can be attributed to both, F- and Cl-interaction.

Quantification of the liquidus depression. To quantify the liquidus depression as a function of halogen concentration, all F and Cl atoms are considered to be equally involved in the dissolution process. Even though this assumption is likely not representative of the actual experimental processes, it does, however, allow us to constrain a relation between halogen concentration and liquidus depression. The

concentrations of F and Cl were first recalculated to mol% and summed to plot the data relative to ΔT (Fig. 6.6). The data can be described using the following regression:

$$\Delta T = 1575\ (177)(K\ mol\%^{-1}) \times c\ (mol\%) - 8.9\ (\pm 9.8) \quad (6.2)$$

where c is the sum of the concentrations of F and Cl. The uncertainty of the linear regression represents the 95% confidence interval (2σ).

Equation 6.2 gives the minimum depression of the liquidus, assuming that both halogens are equally involved. If only one of the halogens was responsible for the crystal dissolution, the regression line would follow the respective data points of F or Cl and likewise increase in slope (Fig. 6.6). For example, if crystal dissolution was caused by Cl alone, the data points of F would not contribute to the regression and the slope would be 6902 ± 1763 (K mol%$^{-1}$ Cl), which means about a four times stronger effect than by combined halogens. This is the maximum liquidus depression that can be inferred from the present data. However, as discussed above, only the minimum depression of the liquidus (Eq. 6.2) is considered reliable due to the limitations of this data set in determining the individual effects of F and Cl.

The quantification of the liquidus depression (Eq. 6.2) is only valid at the H_2O concentrations and range of F- and Cl-concentrations investigated here. The concentration range is bracketed by the first appearance of crystals in the halogen-enriched melt (~0.87 wt.% F, ~0.36 wt.% Cl) to the point where no crystals are observed in the halogen-poor melt (~0.04 wt.% F, ~0.06 wt.% Cl). The relation may be valid for even lower temperatures, under the condition that halogen concentrations would be further enriched beyond the values studied in the investigated melts (e.g., Filiberto and Treiman, 2009).

As most recent studies on the liquidus depression effect of halogens were carried out on basaltic melt involving either F or Cl (e.g., Filiberto et al., 2012; Filiberto et al., 2014), a direct comparison to the present study is not straightforward. Nevertheless, the equations provided by Filiberto et al. (2012, 2014) and Farcy et al. (2016) were applied. The highest c_{liq} concentrations observed in the present study are 0.52 wt.% F and 0.23 wt.% Cl (940 °C; 26X), which together yield a total halogen content of 0.034 mol% in the melt (Table 6.2). Based on this total halogen content, equivalent concentrations of F and Cl were calculated, assuming that in each case the total halogen content (0.034 mol%) was given by either F or Cl only. Accordingly, the resultant equivalent F and Cl concentrations (~0.6 wt.% and ~1.2 wt.%, respectively) yield ΔT values of ~34 K for F-enrichment (Filiberto et al., 2012) and ~16 K for Cl-enrichment (Filiberto et al., 2014; Farcy et al., 2016) in basaltic melt. For the melt of the present study, the calculated ΔT is ~45 K, which is ~1.3 and ~2.8 times more effective than the effects observed for F and Cl in basalt, respectively.

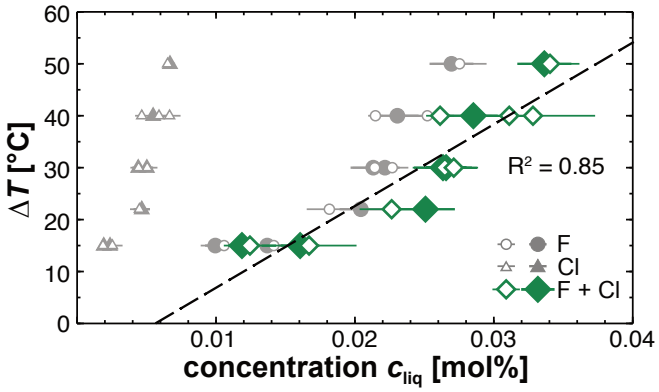

Figure 6.6: Relation between the observed drop in liquidus temperature based on the halogen-poor liquidus of 990 °C and the sum of c_{liq} of F and Cl (mol%). The dashed line indicates linear regression for the sum of F and Cl concentrations. The regression line involves all data of both approaches to determine c_{liq}. Small open symbols represent data averaged from the 4 points closest to the interface and larger solid symbols represent data from analysis along the dissolution front. Error bars on symbols illustrate the standard deviation of the values used to calculate the average concentration.

6.5 Implications

The liquidus-depressing effect of the halogens has implications for several magmatic scenarios and may also affect other alkaline earth elements and Fe-bearing crystals, as was shown in related studies for olivine and pyroxene in basalt, causing a liquidus depression of up to 50 °C (Filiberto et al., 2012; Filiberto et al., 2014). Increased abundance of F or Cl may promote enhanced magma production in addition to that controlled by dissolved H_2O only. Furthermore, we suggest that F and Cl may have the potential to hinder the crystallization of a near-liquidus degassing magma. The halogens could depress the liquidus beyond the temperature implied by H_2O alone and keep the magma crystal free even though H_2O may already have been degassed. Especially F, but also Cl, has been shown to remain dissolved in the melt until relatively shallow crustal levels (e.g., Spilliaert et al., 2006; Schipper et al., 2019) and could therefore promote crystal-free melt even after the loss of H_2O.

An example for a natural analog to the present experimental conditions (constant P, T, and H_2O content) would be a slowly cooling dome or lava flow such as the obsidian flow of the 2011 Cordón Caulle eruption. Schipper et al. (2019) studied the petrological and chemical properties of lavas and tephra of this eruption and found that natural lava samples with high amounts of microlites (>75%) have drastically lower matrix glass F and Cl concentrations than those with lower microlite-content (<75%). The halogen concentration in these lava samples was reported to be more similar to contents measured in plagioclase- or pyroxene-hosted melt inclusions (Schipper et al., 2019), representative of an earlier stage of magma differentiation. They concluded that crystallization caused halogens to leave the melt in a process analogous to second boiling. Our results indicate that the process of halogen diffusion and ensuing crystallization may appear reversed in nature, involving crystallization in response to halogen

devolatilization. This shows that halogens can have a large influence on melt crystallinity even at constant temperatures and at potentially various scenarios. Thus, halogen devolatilization may be one controlling factor for the bulk rheological characteristics of a magmatic body or a lava flow by enhancing microlite crystallization.

The disequilibrium technique used in this study can potentially be used to investigate the influence of minor yet influential chemical components on the phase equilibria by providing "snapshots" of the system approaching equilibrium. Diffusion couple experiments are well suited for this technique as they allow to track the influence of one or a few components, covering the full concentration range between the two starting compositions. This approach is, however, limited to systems where the crystal dissolution or crystallization occurs on a shorter timescale than the diffusion of the respective chemical components. We suggest this technique to be particularly suited to complement conventional *P-T-x* experiments, e.g., to investigate intermediate steps of *x* (e.g., H_2O, halogens, etc.) at fixed *P-T* conditions. Additionally, applying this technique as a standalone approach was shown to be useful in describing the response of a melt with a dynamically changing chemical composition, which is, for example, comparable to the process of devolatilization of a melt or lava.

The results of this study illustrate the influence of halogens on the stability of near-liquidus silicates in a temperature range applicable to silicic lava flows and domes. We demonstrate that even a small concentration enhancement of a few hundreds of parts per millions of halogens in a melt of otherwise fixed H_2O-content can affect the stability of Ca-Fe-Mg mineral phases. As crystal content is one of the most influential physical factors governing magma rheology (e.g., Maron and Pierce, 1956; Mueller et al., 2010; Klein et al., 2017), our results have implications for how magmas evolve physically and chemically during their ascent in the conduit and whether they erupt explosively or effusively.

6.6 Acknowledgements

We appreciate the help of B. Scheu, U. Kueppers, and K.-U. Hess with sample preparation and thank N. Groschopf, S. Buhre, and T. Haeger for their assistance with electron microprobe and Raman analyses. The authors thank J. Filiberto and two anonymous reviewers for their perceptive reviews and A. Cadoux for the editorial handling of this manuscript.

6.7 Funding

This research is part of the Ph.D. thesis of Y. Feisel and is supported by a fellowship of the Gutenberg Research College of the Johannes Gutenberg-University of Mainz to D.B. Dingwell. D.B. Dingwell acknowledges the support of ERC 2018 ADV Grant 834225 (EAVESDROP). Part of this research was

performed within the infrastructure established by the VAMOS research center of the Johannes Gutenberg-University, Mainz.

Supplementary Material

Supplementary Figures (Fig. S1–S4) can be found and downloaded online from *American Mineralogist*:

Deposit item AM-22-68120, Online Materials. Deposit items are free to all readers and found on the MSA website, via the specific issue's Table of Contents (go to http://www.minsocam.org/MSA/AmMin/TOC/2022/Jun2022_data/Jun2022_data.html).

Chapter 7
Conclusions and future scientific questions

The main aim of this thesis was to explore the diffusion characteristics of the halogens in natural silica-rich melt and to foster a detailed understanding of halogen behavior in magmatic processes. For this purpose, the experimental infrastructure at the Volcanology laboratories of the JGU Mainz was employed and developed further to enable the execution of specialized diffusion experiments. A total of 67 diffusion couple experiments were carried out using a range of experimental setups and evaluated by employing a variety of analytical methods. The results of many of these experiments that are presented in this thesis grant detailed insights into the diffusion characteristics of the halogens in silicate melts and highlight their importance on melt physical properties during volcanic processes. Moreover, the results presented herein include the first-ever published consistent diffusion dataset in silicate melt incorporating all four halogens.

7.1 Halogen diffusion in silica-rich melt

Halogen diffusivities in rhyodacitic to trachytic melts were determined experimentally over a typical natural temperature range and at anhydrous and hydrous conditions (chapters 4 and 5). The results are consistent among the different melt compositions in that F is always the fastest diffusing halogen and the subsequently larger halogens are progressively slower diffusers (F > Cl > Br > I). In anhydrous melt (chapters 4 and 5), a range of diffusivities of 3–4 orders of magnitude are covered among the halogens with F and I comprising diffusivities of 1×10^{-15} to $\sim7\times10^{-13}$ m^2 s^{-1} and 2×10^{-18} to 9×10^{-16} m^2 s^{-1}, respectively, over the investigated temperature range (750–1000 °C). In hydrous melt (1.5 wt.% H_2O; chapter 5) all diffusivities increase significantly. Moreover, the diffusivity increase correlates with the ionic radius *r*, meaning that I (largest *r*) diffusion is most strongly enhanced while F (smallest *r*) diffusion is only weakly enhanced over the anhydrous case. Here, F and I diffusivities span a range of 3×10^{-12} to 1×10^{-11} m^2 s^{-1} and 9×10^{-14} to 2×10^{-12} m^2 s^{-1}, respectively at 1000–1200 °C. This behavior leads to “compression” of the Arrhenius fits in the hydrous melt, yielding a diffusivity range of only 1–2 orders of magnitude across all halogen elements (Fig. 5.3 & 5.5).

The correlation of the ionic radii and the halogen diffusivity indicates the strong effect of melt structure on diffusion in the anhydrous silica-rich melts. The movement of all halogens in these polymerized melts is interpreted to be limited by the number and size of apertures in the melt structure that allow the halogens to “jump” from one site to another. Naturally, F, being the smallest halogen ion, can pass apertures of various sizes and is therefore only weakly limited by the melt structure. The larger halogens

instead rely on sufficiently large apertures for diffusive jumps and are therefore structurally limited. Upon depolymerization and concomitant increase in ionic porosity due to the addition of H_2O to the melt, the structural limitation on diffusion is weakened, leading to the observed increased diffusivities. In this case, while Cl, Br, and I are still affected by the melt structural environment, F diffusion is interpreted to be only weakly, if at all, limited by the melt structure and is mainly controlled by the breakage of bonds (i.e., "detachment") of its site before moving to another site.

Activation energies of diffusion, E_A, are relatively similar among all halogens, spanning ~200–290 kJ mol^{-1} in anhydrous melt. In hydrous melt E_A of Cl, Br and I are only weakly modified, however, E_A of F decreases to 131 kJ mol^{-1}, which is explained to be caused by the suppression of F from its (Al-) Si-F site by OH^-, making more F available for diffusion more easily.

The fundamental findings of the diffusion experiments are illustrated in Fig. 7.1–7.3, which show Arrhenius diagrams of all present halogen diffusion data including the results of this thesis. The data that these plots are based on can be found in Table 5.3. The Arrhenius fits for Fluorine (Fig. 7.1) in anhydrous silicic melt comprise a similar slope (i.e., activation energy) like those of basalt (Alletti et al., 2007) and K-rich phonolite (Balcone-Boissard et al., 2009). Indeed, when these fits are extrapolated to higher temperatures, the resulting F diffusivities are very similar to those determined in K-phonolite and only ~0.5 orders of magnitude lower than in basalt. This supports the idea that F diffusion is to a large extent limited by the detachment process — which is mainly temperature dependent in anhydrous melt — and only weakly limited by the melt structure and ionic porosity. At hydrous conditions, the diffusivities increase and are more similar to those determined for less polymerized, low-silica melts.

The Arrhenius fits of Cl diffusion (Fig. 7.2) in the anhydrous melt of this study comprise a similar slope to the fit of Cl diffusion in basalt (Alletti et al., 2007) and Na-phonolite (Balcone-Boissard et al., 2009). However, when extrapolating the fits to higher temperatures, Cl diffusion plots significantly below that in basalt and Na-phonolite indicating that Cl diffusion is more strongly dependent on the melt structure than F and is limited by the polymerized nature of the melt. The hydrous melt instead reveals enhanced Cl diffusivities that are similar to those in anhydrous basalt which agrees well with the lower degree of polymerization due to the enrichment of water.

The data of Br and I diffusion in the melts of this study are presented together with the literature data on Br diffusion in Figure 7.3. The activation energies of both halogens are very similar for each melt composition but are different between the different melts, which is attributed to the slight compositional differences, especially in Na_2O (~1 wt.% difference). Even at higher temperatures, Br and I in the CCX and HX melts are still significantly slower diffusers than Br in other, lower SiO_2-content melts. In hydrous melt, the diffusivities increase significantly and plot close to those of Br in Basalt and Na-

Phonolite, again confirming the strong control of the melt structure on the diffusion of larger halogen ions.

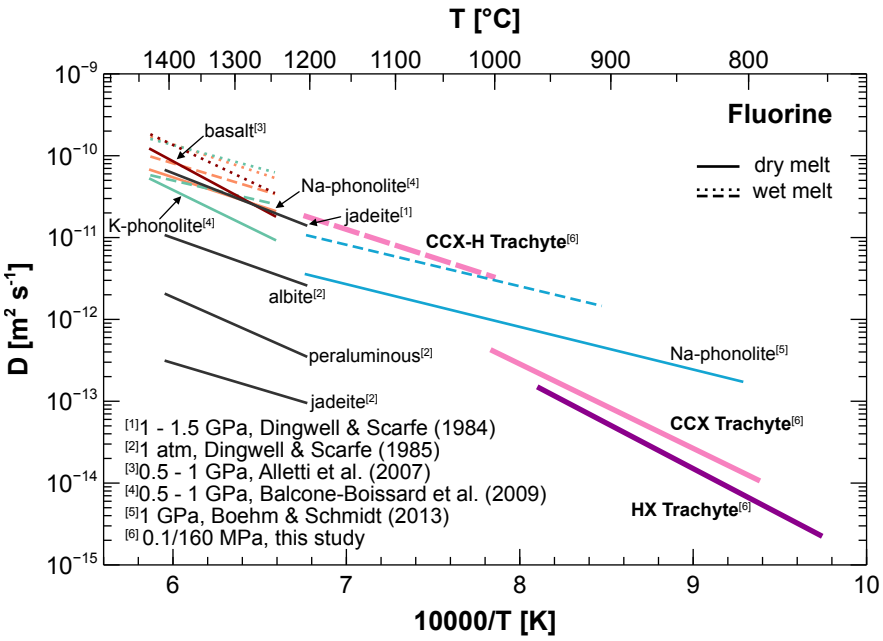

Figure 7.1: Arrhenius diagram illustrating fluorine diffusion data in silicate melt, including the new data collected during this study.

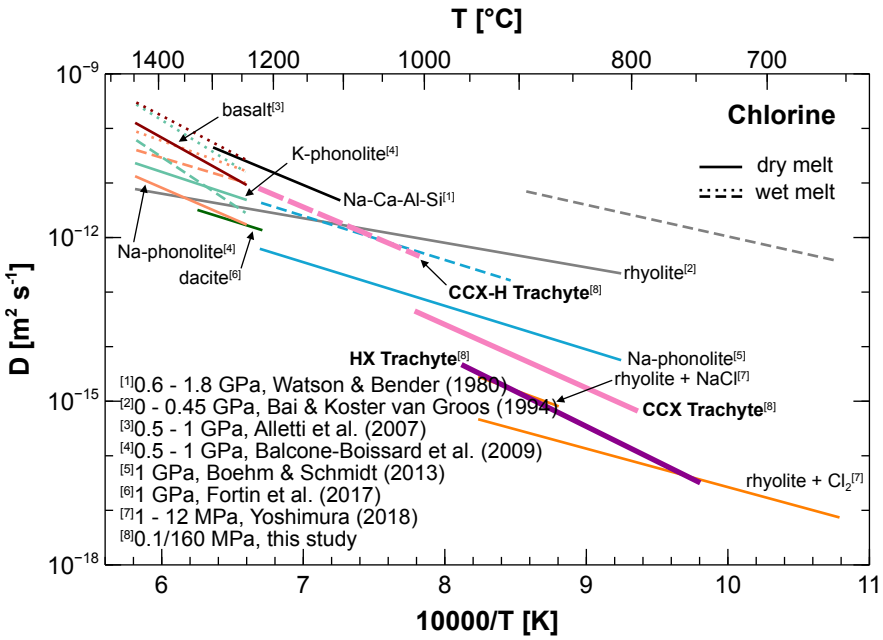

Figure 7.2: Arrhenius diagram illustrating chlorine diffusion data in silicate melt, including the new data collected during this study.

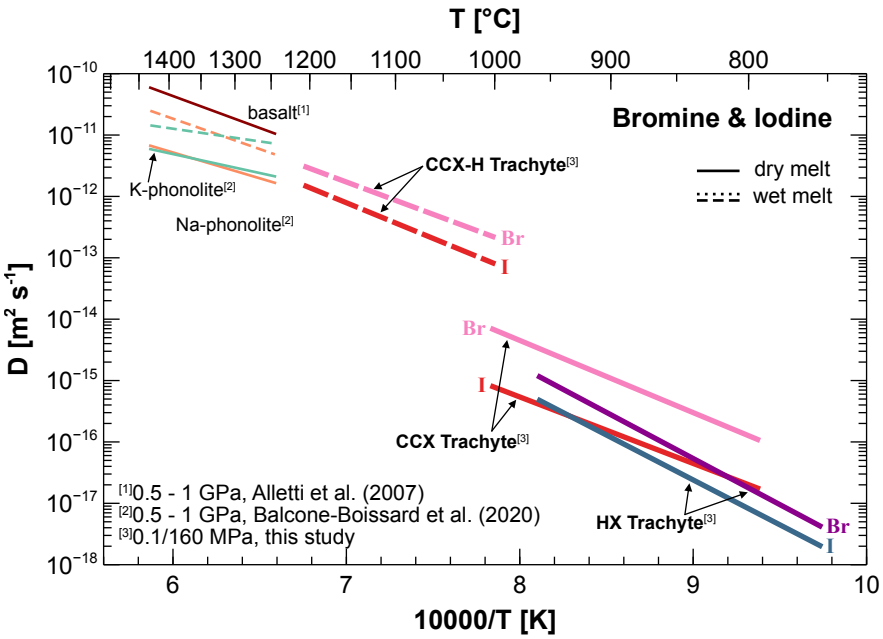

Figure 7.3: Arrhenius diagram illustrating bromine and iodine diffusion data in silicate melt, including the new data collected during this study.

7.1.1 Implications

These novel data are highly relevant for the better understanding of halogen mobility in magmatic processes and illustrate the strong dependence of halogen diffusion on the silicate melt composition. Highly different halogen diffusivities in silica-rich melts imply that diffusive fractionation could be important during crystal and bubble growth. It is expected that enrichment of faster diffusing species (e.g., F) and depletion of slower species (e.g., Cl, Br, and I) would occur around crystals (volatile expulsion) or within bubbles (via exsolution) relative to the equilibrium halogen content in the melt. Fractionation may be particularly pronounced under conditions of low H_2O content, which foster a large spread in halogen diffusivities. At typical magmatic water contents of ~3–6 wt.% in silica-rich melts (Wallace et al., 2015), the spread in diffusivities will be smaller, lowering the extent of diffusive fractionation. However, halogen saturation is typically associated with shallower crustal levels than those at which water saturation occurs (Spilliaert et al., 2006). Consequently, halogen degassing is likely to occur under low H_2O conditions after large amounts of water have already been degassed from the melt, increasing the potential for diffusive fractionation in natural volcanic scenarios. Halogen ratios in a plume of a passively degassing volcanic center may be monitored over time to determine steady-state halogen ratios. In the case of increased bubble growth rates or magma ascent, strong deviations from the steady-state halogen concentration ratios are expected which would foster the enrichment of F compared to the other halogens. Such deviations in a time-series of volcanic halogen ratio measurements could therefore indicate processes leading to volcanic unrest, which may ultimately enable volcanologists to apply halogen degassing measurements as a volcanic monitoring tool.

7.2 The effect of F and Cl on phase equilibria

The effect of F and Cl enrichment in hydrous trachytic melt was investigated experimentally by applying a novel disequilibrium approach involving diffusion couple experiments (chapter 6). The experiments revealed that clinopyroxene (cpx) crystallizes in the halogen-depleted melts within the short heating phase of 45–60 minutes. The subsequent diffusive enrichment of F and Cl in the cpx-bearing hydrous trachytic melt at near-liquidus temperatures (925–990 °C) induces dissolution of the mineral phases, thereby decreasing the liquidus temperature of the melt. In the diffusion couple samples, a cpx-dissolution front parallel to the initial diffusion interface followed the diffusion direction of F and Cl and progressed with the time of the experiments. The concentrations of F and Cl at the dissolution front (transition from pure to cpx-bearing glass), which are interpreted to represent the liquidus composition at the experimental temperature, were determined and used to formulate a general expression for the liquidus shift depending on the halogen content. The results yield a liquidus shift rate of ~1575 K mol.%$^{-1}$ of F and Cl in the melt. This value is a minimum estimate based on the assumption that both halogens equally drive dissolution and is valid for the temperature range and concentrations investigated (0.06–0.87 wt.% F; 0.06–0.36 wt.% Cl). However, this minimum estimate still yields a significantly more effective liquidus depression than the effects of F or Cl determined for basaltic melt (Filiberto et al., 2012; Filiberto et al., 2014; Farcy et al., 2016). Moreover, the assessment of the concentration profiles of F and Cl in all samples revealed that the presence of cpx crystals did not disturb halogen diffusion kinetics.

7.2.1 Implications

The pronounced effect of F and Cl on the near-liquidus melt of this study highlights the strong effect that the halogens may exert on the stability of Ca-Fe-Mg mineral phases, thereby modifying the melts crystal-content, which in turn is one of the most influential physical factors governing magma rheology (e.g., Klein et al., 2017). Increased abundances of F and Cl may foster enhanced magma production in addition to that implied by dissolved H_2O only, which further has the potential to keep a silicic magma crystal-free even after significant water-degassing. Since the halogens typically remain dissolved until shallow crustal levels, they may promote crystal-free melt during magma ascent and pre- or syn-eruptive processes, or may enhance crystallization, due to devolatilization at late stages of magma emplacement. Indeed, Schipper et al. (2019) showed that lava samples with high amounts of microlites in the obsidian lava flow of the 2011 Cordón Caulle, Chile eruption had significantly lower matrix glass F and Cl concentrations than microlite-poor glasses. They concluded that crystallization caused increased halogen degassing. Our results indicate that crystallization may have been additionally enhanced, involving increased microlite crystallization in response to halogen degassing.

The disequilibrium technique applied in this study was shown to be an effective alternative to conventional phase equilibria experiments (using fixed chemical compositions) by providing "snapshots" of the system approaching equilibrium. This technique is particularly suited to investigate the influence of minor chemical components on the phase equilibria. Using diffusion couple experiments enables to track the influence of one or few components over a broad concentration range, determined by the two starting compositions. However, such experiments need to be designed and built well, ensuring that the process of interest (e.g., crystal dissolution) occurs on short timescales relative to the timescales of diffusion. This technique is suggested to complement conventional phase equilibria experiments to investigate the influence of a chemical component (e.g., volatiles) at fixed *P-T* conditions, which is, for example, comparable to the process of magma or lava devolatilization.

7.3 Future scientific questions

7.3.1 Influence of water on diffusion

Additional water-bearing diffusion experiments similar to those described in chapter 5 were carried out using the CCX melt with higher water concentrations of ~3.5 wt.%. Only few of these experiments yielded homogeneous glassy samples that could be fitted well with equation 1.3, however, most experiments suffered from issues with the experimental approach resulting in severe water loss, the formation of bubbles or convection of the melt in the capsule. Consequently, this experimental series was discarded from further analysis and not presented in this thesis.

However, the few successful water-rich experiments were analyzed for halogen diffusion using both, EMPA and SIMS techniques. The results of these experiments showed that the general enhancement of diffusivities observed with the 1.5 wt.% H_2O experiments increased even more with the higher water content. While the halogen diffusivity at 1000 °C covers a range of ~1.6 orders of magnitude (F being the fastest, I being the slowest) in the melts containing 1.5 wt.%, the range is further reduced to only ~1.3 orders of magnitude in the same melt containing 3.5 wt.% H_2O (sample CCX-H-8). This trend is nicely illustrated in Figure 5.5, which shows a comparison of anhydrous and hydrous CCX melts, additionally including the results of a more water-rich experiment. Moreover, when plotting the diffusive range ($\Delta\log(D_{X\text{-}F}) = |\log(D_X)| - |\log(D_F)|$, where X : Cl, Br, or I) versus the H_2O content in the melt, it appears that the "compression" of the diffusivity range approaches a plateau for $\Delta D_{I\text{-}F}$ and $\Delta D_{Br\text{-}F}$ at a water content >3.5 wt. %. (Fig. 7.4). $\Delta D_{Cl\text{-}F}$ instead seems to follow a linear negative trend.

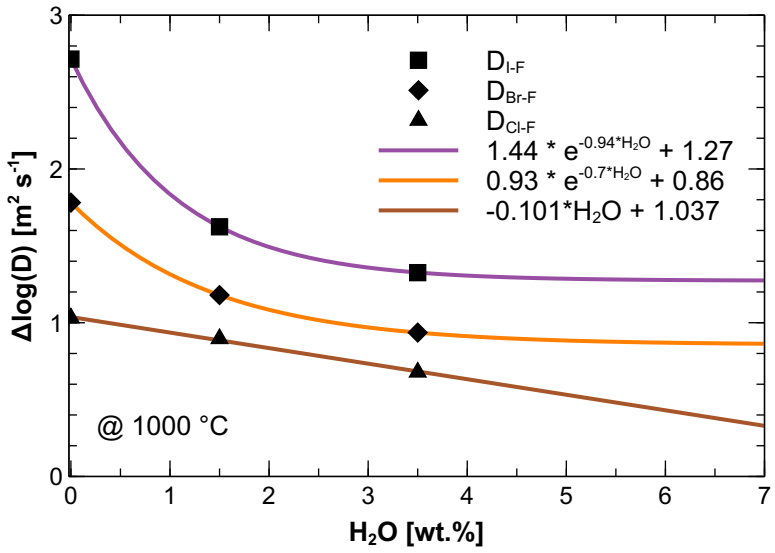

Figure 7.4: Plot of $\Delta\log(D_{X\text{-}F})$ (= $|\log(D_X)|$ - $|\log(D_F)|$) versus H_2O content in the melt. The general trend of decreasing diffusive range with added water is illustrated. This data is preliminary and only represents a proposed approach to discuss the influence of water on diffusion in the melt of this study.

Clearly, the fits in Figure 7.4 are idealized and each rely on three datapoints only. The curves will likely change significantly if more datapoints were determined and included and when the high-water content data is better constrained by conducting more experiments. It may be expected that the diffusivities all converge at very high water contents and resulting low degrees of polymerization, approaching $\Delta\log(D_{X\text{-}F}) \approx 0$. It may even be speculated that $\Delta\log(D_{X\text{-}F})$ approaches negative values when a melt is completely depolymerized due to high water enrichment and melt structural limits on diffusion disappear.

To gain improved insights on the influence of H_2O on the diffusion characteristics in silica-rich melt, additional experiments at both elevated and intermediate water contents should be performed. The resulting data may allow one to formulate equations that predict the change in diffusivity depending on the water content dissolved in the melt, and this in turn, may ultimately help better understand the melt structural effects of added water. Experiments at intermediate water contents (e.g., 0.8 wt.%) are furthermore highly relevant for natural volcanic processes in the crust.

However, to enable diffusion couple experiments of higher water contents, the experimental approach would have to be refined. A possible way to mitigate some of the encountered issues could be to run experiments at elevated pressures, i.e., above the saturation pressure of H_2O and the dissolved halogens at the experimental temperatures, to suppress the formation of bubbles. The problem of severe water-loss through the capsule walls could be tackled by: (i) employing a more complex setup, using an outer capsule around the experimental capsule, or (ii) by introducing a calibrated amount of CH_4 in the pressure gas to minimize H^+ concentration gradients between the sample and the gas atmosphere (e.g.,

Alex and Zajacz, 2020). Convection will likely be enhanced at high water contents. Proper diffusion couple geometry (perfectly horizontal interface) and minimal temperature gradients across the couple are therefore crucial for the success of such experiments.

7.3.2 Diffusion in melts of higher SiO_2 content

While halogen diffusion has been investigated in various kinds of silicate melts, with many studies focusing on silica-poor compositions (e.g., Alletti et al., 2007; Balcone-Boissard et al., 2020), few studies have examined silica-rich melt compositions such as rhyolites (Yoshimura, 2018). However, rhyolitic systems typically comprise the largest of volcanic eruptions. The experimental infrastructure developed during the PhD project was therefore applied to perform a pilot study on halogen diffusion in silica-rich melts synthesized from the 2008 Chaitén rhyolite (CHX series). The experiments were carried out in the scope of the Bachelors thesis of Caroline Scholl-Poensgen and employed the same experimental setup as used for the anhydrous experiments described in chapters 4 and 5. The following data and observations are presented to establish a concept of possible further investigations.

Diffusivities of F and Cl were determined over a temperature range of 800–1000 °C and at atmospheric pressure. Even though this melt has a significantly higher SiO_2 content (~72.5 wt.%), the resulting diffusivities are very similar to those determined in the anhydrous CCX melt (~68 wt.% SiO_2) of this thesis (Fig. 7.5a). The Arrhenius parameters were determined and yield pre-exponential factors of D_0(F) = 4.82×10^{-6} m^2 s^{-1} and D_0(Cl) = 1.02×10^{-4} m^2 s^{-1}. The activation energies are E_A(F) = 172 ± 20 kJ mol^{-1} and E_A(Cl) = 232 ± 21 kJ mol^{-1}. Many F diffusion profiles comprised increased F contents on the first half of the low concentration side of the profiles yielding positive deviations of the measured data from the fitted diffusion curve (Fig. 7.5b). Similar deviations were also recognized in few of the experiments of the CCX and HX series of this thesis. As this issue was observed with different samples, run at different experimental temperatures, it is expected that this behavior is not caused by physical processes during the experiment, e.g., the initial sintering of the glasses. The melts were also enriched in the other halogens Br and I and two of the samples were measured with a SIMS. Diffusion profiles of Br and I were very short which is why the derived diffusion coefficients are considered to carry significant uncertainty, especially in the low temperature sample CHX-5 (800 °C). Furthermore, many samples showed fluctuations in major element concentrations despite the initial homogenous compositions, causing uphill diffusion and oscillatory concentration profiles of the major elements CaO and SiO_2, commonly associated with multicomponent diffusion (Zhang, 2010).

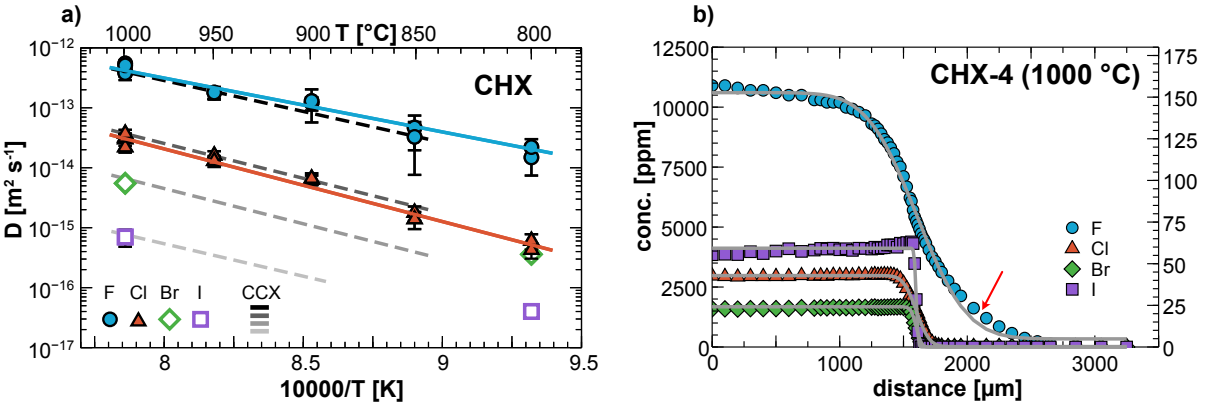

Figure 7.5: Arrhenius fits and diffusion profile examples of halogen diffusion in CHX melt. **a)** Arrhenius diagram of the CHX experimental series. Open symbols represent preliminary data of Br and I diffusion, determined by SIMS analysis. Solid symbols and corresponding Arrhenius fit lines are based on EMPA data of the Bachelor thesis of Scholl-Poensgen (2021). **b)** Diffusion profiles of all halogens in sample CHX-4 determined by SIMS analysis. The grey lines represent the fitted diffusion curves. The red arrow indicates the deviation of the fit curve from the measured data, present in almost all F concentration profiles of the CHX series.

The determined halogen diffusion data of the high-silica melt could highly benefit from further investigations, mainly focusing on Br and I by using longer experimental durations and potentially higher temperatures. Additionally, the unideal diffusion profiles of F (Fig. 7.5b) should be further assessed to try and find out if the initial F concentration enhancement on the low concentration side may be a characteristic feature of F behavior in silica-rich melt. The effects of halogen diffusion on the homogeneity of the major elements should be assessed in the light of multicomponent diffusion. However, ensuring perfect homogeneity of the starting material is the most crucial pre-requisite for addressing these issues.

7.3.3 Modelling of bubble growth and fluxes to the atmosphere

Halogens are an important constituent of volcanic volatiles and are known to exert strong effects on magma properties. Furthermore, after the release from the volcano, they may have severe effects on the atmospheric processes such as the destruction of atmospheric ozone by reactive Br-species. The novel dataset of halogen diffusivity in silicic melts can be readily included in existing models of bubble growth to simulate pre- and syn-eruptive processes of magma ascent and degassing (e.g., Gonnermann and Manga, 2012; Watson, 2017). The effectiveness of halogen loss from a magma or lava body and the concomitant flux to the atmosphere could be simulated by assessing the influence of different parameters such as bubble growth rate and coalescence, magma ascent rate, or H_2O-content of the magma. Such models could furthermore take advantage of the findings of chapter 6, by modelling the effect of halogen loss on the melt's crystallinity. Moreover, as already discussed in the light of volcanic processes, variable diffusivity among the halogens bears the potential to cause diffusive fractionation during bubble or crystal growth. With the new dataset, diffusive fractionation during degassing can be modelled and

predicted as a function of magma ascent speed, bubble growth rate, crystallization rate, etc. However, for the successful application of halogen diffusivities in modeling natural phase-transformation processes during magma ascent, also the (pressure-dependent) partition coefficients of the halogens in these melts also need to be known. Numerical models of the processes described above would therefore benefit from further experimental studies on halogen partitioning behavior in silicic melts.

7.4 Concluding remarks

This thesis presents the first consistent dataset of experimentally derived diffusion data of all stable halogens in silica-rich melts, under anhydrous and hydrous conditions and over a broad natural temperature range. Importantly, this study emphasizes that halogen diffusivity and the diffusion rate-limiting mechanism is highly dependent on the melt structure, resulting in a strong correlation of the ionic size and diffusivity in anhydrous polymerized melt. The effect of added water was shown to enhance diffusivities of all halogens and to strongly reduce rate-limiting effects on larger halogen ions. Moreover, this thesis highlights the pronounced impact of F and Cl enrichment on the mineral phase stability of a near-liquidus silica-rich melt, effectively depressing the melts isobaric liquidus temperature. These findings greatly contribute to an improved understanding of magmatic volatiles and highlight the relevance of halogens in magmatic systems.

References

Aiuppa A., Baker D. R. and Webster J. D. (2009) Halogens in volcanic systems. *Chem. Geol.* **263**, 1–18.

Aiuppa A., Bonfanti P., Brusca L., D'Alessandro W., Federico C. and Parello F. (2001) Evaluation of the environmental impact of volcanic emissions from the chemistry of rainwater: Mount Etna area (Sicily). *Appl. Geochemistry* **16**, 985–1000.

Alex A. and Zajacz Z. (2020) A new method to quantitatively control oxygen fugacity in externally heated pressure vessel experiments. *Eur. J. Mineral.* **32**, 219–234.

Alletti M., Baker D. R. and Freda C. (2007) Halogen diffusion in a basaltic melt. *Geochim. Cosmochim. Acta* **71**, 3570–3580.

Alloway B. V., Pearce N. J. G., Villarosa G., Outes V. and Moreno P. I. (2015) Multiple melt bodies fed the AD 2011 eruption of Puyehue-Cordón Caulle, Chile. *Sci. Rep.* **5**, 1–8.

von Aulock F. W., Kennedy B. M., Schipper C. I., Castro J. M., E. Martin D., Oze C., Watkins J. M., Wallace P. J., Puskar L., Bégué F., Nichols A. R. L. and Tuffen H. (2014) Advances in Fourier transform infrared spectroscopy of natural glasses: From sample preparation to data analysis. *Lithos* **206**–**207**, 52–64.

Baasner A., Schmidt B. C. and Webb S. L. (2013a) Compositional dependence of the rheology of halogen (F, Cl) bearing aluminosilicate melts. *Chem. Geol.* **346**, 172–183.

Baasner A., Schmidt B. C. and Webb S. L. (2013b) The effect of chlorine, fluorine and water on the viscosity of aluminosilicate melts. *Chem. Geol.* **357**, 134–149.

Bai T. B. and Koster van Groos A. F. (1994) Diffusion of chlorine in granitic melts. *Geochim. Cosmochim. Acta* **58**, 113–123.

Baker D. R. (1989) Tracer versus trace element diffusion: Diffusional decoupling of Sr concentration from Sr isotope composition. *Geochim. Cosmochim. Acta* **53**, 3015–3023.

Baker D. R. and Alletti M. (2012) Fluid saturation and volatile partitioning between melts and hydrous fluids in crustal magmatic systems: The contribution of experimental measurements and solubility models. *Earth-Science Rev.* **114**, 298–324.

Baker D. R. and Balcone-Boissard H. (2009) Halogen diffusion in magmatic systems: Our current state of knowledge. *Chem. Geol.* **263**, 82–88.

Baker D. R., Freda C., Brooker R. A. and Scarlato P. (2005) Volatile diffusion in silicate melts and its effects on melt inclusions. *Ann. Geophys.* **48**.

Balcone-Boissard H., Baker D. R., Villemant B. and Boudon G. (2009) F and Cl diffusion in phonolitic melts: Influence of the Na/K ratio. *Chem. Geol.* **263**, 89–98.

Balcone-Boissard H., Baker D. R., Villemant B., Cauzid J., Boudon G. and Deloule E. (2020) Br diffusion in phonolitic melts: Comparison with fluorine and chlorine diffusion. *Am. Mineral.* **105**,

1639–1646.

Balcone-Boissard H., Villemant B. and Boudon G. (2010) Behavior of halogens during the degassing of felsic magmas. *Geochemistry, Geophys. Geosystems* **11**.

Behrens H. and Zhang Y. (2009) H_2O diffusion in peralkaline to peraluminous rhyolitic melts. *Contrib. to Mineral. Petrol.* **157**, 765–780.

Behrens H., Zhang Y., Leschik M., Wiedenbeck M., Heide G. and Frischat G. H. (2007) Molecular H_2O as carrier for oxygen diffusion in hydrous silicate melts. *Earth Planet. Sci. Lett.* **254**, 69–76.

Behrens H., Zhang Y. and Xu Z. (2004) H_2O diffusion in dacitic and andesitic melts. *Geochim. Cosmochim. Acta* **68**, 5139–5150.

Bell A. S. and Simon A. (2011) Experimental evidence for the alteration of the $Fe^{3+}/\Sigma Fe$ of silicate melt caused by the degassing of chlorine-bearing aqueous volatiles. *Geology* **39**, 499–502.

Bell A. S. and Webster J. D. (2015) Dissolved Cl, oxygen fugacity, and their effects on Fe behavior in a hydrous rhyodacitic melt. *Am. Mineral.* **100**, 1595–1599.

Bobrowski N., von Glasow R., Aiuppa A., Inguaggiato S., Louban I., Ibrahim O. W. and Platt U. (2007) Reactive halogen chemistry in volcanic plumes. *J. Geophys. Res. Atmos.* **112**.

Bobrowski N., Hönninger G., Galle B. and Platt U. (2003) Detection of bromine monoxide in a volcanic plume. *Nature* **423**, 273–276.

Böhm A. and Schmidt B. C. (2013) Fluorine and chlorine diffusion in phonolitic melt. *Chem. Geol.* **346**, 162–171.

Boichu M., Oppenheimer C., Roberts T. J., Tsanev V. and Kyle P. R. (2011) On bromine, nitrogen oxides and ozone depletion in the tropospheric plume of Erebus volcano (Antarctica). *Atmos. Environ.* **45**, 3856–3866.

Botcharnikov R. E., Holtz F. and Behrens H. (2015) Solubility and fluid-melt partitioning of H_2O and Cl in andesitic magmas as a function of pressure between 50 and 500 MPa. *Chem. Geol.* **418**, 117–131.

Boudon G., Balcone-Boissard H., Villemant B. and Morgan D. J. (2015) What factors control superficial lava dome explosivity? *Sci. Rep.* **5**.

Brey G. P., Bulatov V. K. and Girnis A. V. (2009) Influence of water and fluorine on melting of carbonated peridotite at 6 and 10 GPa. *Lithos* **112**, 249–259.

Bureau H., Foy E., Raepsaet C., Somogyi A., Munsch P., Simon G. and Kubsky S. (2010) Bromine cycle in subduction zones through in situ Br monitoring in diamond anvil cells. *Geochim. Cosmochim. Acta* **74**, 3839–3850.

Bureau H., Keppler H. and Métrich N. (2000) Volcanic degassing of bromine and iodine: Experimental fluid/melt partitioning data and applications to stratospheric chemistry. *Earth Planet. Sci. Lett.* **183**, 51–60.

Bureau H. and Métrich N. (2003) An experimental study of bromine behaviour in water-saturated silicic

melts. *Geochim. Cosmochim. Acta* **67**, 1689–1697.

Burkhard D. J. M. (2005) Nucleation and growth rates of pyroxene, plagioclase, and Fe-Ti oxides in basalt under atmospheric conditions. *Eur. J. Mineral.* **17**, 675–686.

Cáceres F., Scheu B., Colombier M., Hess K. U., Feisel Y., Ruthensteiner B. and Dingwell D. B. (2022) The roles of microlites and phenocrysts during degassing of silicic magma. *Earth Planet. Sci. Lett.* **577**, 117264.

Cáceres F., Wadsworth F. B., Scheu B., Colombier M., Madonna C., Cimarelli C., Hess K. U., Kaliwoda M., Ruthensteiner B. and Dingwell D. B. (2020) Can nanolites enhance eruption explosivity? *Geology* **48**, 997–1001.

Carroll M. R. and Webster J. D. (1994) Solubilities of sulfur, noble gases, nitrogen, chlorine, and fluorine in magmas. In *Volatiles in Magmas* (eds. M. R. Carroll and J. R. Holloway). Rev. Mineral. Geochem., Mineralogical Society of America. pp. 231–279.

Cashman K. V. (2004) Volatile controls on magma ascent and eruption. *Geophys. Monogr. Ser.* **150**, 109–124.

Cashman K. V. and Sparks R. S. J. (2013) How volcanoes work: A 25 year perspective. *Bull. Geol. Soc. Am.* **125**, 664–690.

Cassidy M., Iveson A. A., Humphreys M. C. S., Mather T. A., Helo C., Castro J. M., Ruprecht P., Pyle D. M. and EIMF (*in press*) Experimentally-derived F, Cl, and Br fluid/melt partitioning of intermediate to silicic melts in shallow magmatic systems. *Am. Mineral.,* doi: 10.2138/am-2022-8109

Castro J. M., Beck P., Tuffen H., Nichols A. R. L., Dingwell D. B. and Martin M. C. (2008) Timescales of spherulite crystallization in obsidian inferred from water concentration profiles. *Am. Mineral.* **93**, 1816–1822.

Castro J. M., Cordonnier B., Schipper C. I., Tuffen H., Baumann T. S. and Feisel Y. (2016) Rapid laccolith intrusion driven by explosive volcanic eruption. *Nat. Commun.* **7**, 13585.

Castro J. M. and Feisel Y. (2022) Eruption of ultralow-viscosity basanite magma at Cumbre Vieja, La Palma, Canary Islands. *Nat. Commun.* **13**.

Castro J. M., Keller F., Feisel Y., Lanari P., Helo C., Mueller S. P., Ian Schipper C. and Thomas C. (2020) Lightning-induced weathering of Cascadian volcanic peaks. *Earth Planet. Sci. Lett.* **552**.

Castro J. M., Schipper C. I., Mueller S. P., Militzer A. S., Amigo A., Parejas C. S. and Jacob D. (2013) Storage and eruption of near-liquidus rhyolite magma at Cordón Caulle, Chile. *Bull. Volcanol.* **75**, 1–17.

Cherniak D. J., Hervig R., Koepke J., Zhang Y. and Zhao D. (2010) Analytical methods in diffusion studies. In *Diffusion in Minerals and Melts* (eds. Y. Zhang and D. J. Cherniak). Rev. Mineral. Geochem., Mineralogical Society of America. pp. 107–170.

Chevychelov V. Y., Botcharnikov R. E. and Holtz F. (2008) Partitioning of Cl and F between fluid and

hydrous phonolitic melt of Mt. Vesuvius at ~ 850-1000 °C and 200 MPa. *Chem. Geol.* **256**, 172–184.

Clarke D. B., Wunder B., Förster H.-J., Rhede D. and Hahn A. (2009) Experimental investigation of near-liquidus andalusite-topaz relations in synthetic peraluminous haplogranites at 200 MPa. *Mineral. Mag.* **73**, 997–1007.

Cochain B., Sanloup C., de Grouchy C., Crépisson C., Bureau H., Leroy C., Kantor I. and Irifune T. (2015) Bromine speciation in hydrous silicate melts at high pressure. *Chem. Geol.* **404**, 18–26.

Cole J. W. (1970) Structure and eruptive history of the tarawera volcanic complex. *New Zeal. J. Geol. Geophys.* **13**, 879–902.

Coombs M. L., Sisson T. W. and Kimura J. I. (2004) Ultra-high chlorine in submarine K̄ilauea glasses: Evidence for direct assimilation of brine by magma. *Earth Planet. Sci. Lett.* **217**, 297–313.

Cooper A. R. (1968) The use and limitations of the concept of an effective binary diffusion coefficient for multi-component diffusion. In *Mass Transport in Oxides* (eds. J. B. Wachman and A. D. Franklin). NBS Special Publication. pp. 79–84.

Crank J. (1975) *The Mathematics of Diffusion*., Clarendon-Oxford, London.

Cronin S. J., Neall V. E., Lecointre J. A., Hedley M. J. and Loganathan P. (2003) Environmental hazards of fluoride in volcanic ash: A case study from Ruapehu volcano, New Zealand. *J. Volcanol. Geotherm. Res.* **121**, 271–291.

Dingwell D. B. (1990) Effects of structural relaxation on cationic tracer diffusion in silicate melts. *Chem. Geol.* **82**, 209–216.

Dingwell D. B. (1987) Melt viscosities in the system $NaAlSi_3O_8$-H_2O-F_2O_{-1}. In *Magmatic Processes: Physicochemical Principles.* (ed. B. O. Mysen). The Geochemical Society Special Publication 1, pp. 423–431.

Dingwell D. B. and Hess K. U. (1998) Melt viscosities in the system Na-Fe-Si-O-F-Cl; contrasting effects of F and Cl in alkaline melts. *Am. Mineral.* **83**, 1016–1021.

Dingwell D. B. and Scarfe C. M. (1984) Chemical diffusion of fluorine in jadeite melt at high pressure. *Geochim. Cosmochim. Acta* **48**, 2517–2525.

Dingwell D. B. and Scarfe C. M. (1985) Chemical diffusion of fluorine in melts in the system $Na_2OAl_2O_3SiO_2$. *Earth Planet. Sci. Lett.* **73**, 377–384.

Dingwell D. B., Scarfe C. M. and Cronin D. J. (1985) The effect of fluorine on viscosities in the system Na_2O-Al_2O_3-SiO_2: implications for phonolites, trachytes and rhyolites. *Am. Mineral.* **70**, 80–87.

Dingwell D. B. and Webb S. L. (1990) Relaxation in silicate melts. *Eur. J. Mineral.* **2**, 427–449.

Dolejš D. and Baker D. R. (2007a) Liquidus equilibria in the system K_2O-Na_2O-$A1_2O_3$-SiO_2-F_2O_{-1}-H_2O to 100 MPa: I. Silicate-fluoride liquid immiscibility in anhydrous systems. *J. Petrol.* **48**, 785–806.

Dolejš D. and Baker D. R. (2007b) Liquidus equilibria in the system K_2O-Na_2O-Al_2O_3-SiO_2-F_2O_{-1}-H_2O to 100 MPa: II. Differentiation paths of fluorosilicic magmas in hydrous systems. *J. Petrol.* **48**,

807–828.

Dolejš D. and Zajacz Z. (2018) Halogens in Silicic Magmas and Their Hydrothermal Systems. In *The Role of Halogens in Terrestrial and Extraterrestrial Geochemical Processes* (eds. D. E. Harlov and L. Y. Aranovich). Springer-Verlag, Cham. pp. 431–543.

Edmonds M. and Wallace P. J. (2017) Volatiles and exsolved vapor in volcanic systems. *Elements* **13**, 29–34.

Evans K. A., Mavrogenes J. A., O'Neill H. S., Keller N. S. and Jang L. Y. (2008) A preliminary investigation of chlorine XANES in silicate glasses. *Geochemistry, Geophys. Geosystems* **9**, 1–15.

Farcy B. J., Gross J., Carpenter P., Hicks J. and Filiberto J. (2016) Effect of chlorine on near-liquidus crystallization of olivine-phyric shergottite NWA 6234 at 1 GPa: Implication for volatile-induced melting of the Martian mantle. *Meteorit. Planet. Sci.* **51**, 2011–2022.

Feisel Y., Castro J. M. and Dingwell D. B. (2019) Diffusion of F and Cl in dry rhyodacitic melt. *Am. Mineral.* **104**, 1689–1699.

Feisel Y., Castro J. M., Helo C. and Dingwell D. B. (2021) Halogen diffusion in silicic melts. In *EMPG - XVII 17th International Symposium on Experimental Mineralogy, Petrology and Geochemistry: Abstract Volume* Potsdam. p. 110.

Feisel Y., Castro J. M., Helo C. and Dingwell D. B. (2022) The effect of halogens (F, Cl) on the near-liquidus crystallinity of a hydrous trachyte melt. *Am. Mineral.* **107**, 1007–1017.

Fenn P. M. (1977) The nucleation and growth of alkali feldspars from hydrous melts. *Can. Mineral.* **15**, 135–161.

Filiberto J., Dasgupta R., Gross J. and Treiman A. H. (2014) Effect of chlorine on near-liquidus phase equilibria of an Fe-Mg-rich tholeiitic basalt. *Contrib. to Mineral. Petrol.* **168**, 1–13.

Filiberto J. and Treiman A. H. (2009) The effect of chlorine on the liquidus of basalt: First results and implications for basalt genesis on Mars and Earth. *Chem. Geol.* **263**, 60–68.

Filiberto J., Wood J., Dasgupta R., Shimizu N., Le L. and Treiman A. H. (2012) Effect of fluorine on near-liquidus phase equilibria of an Fe-Mg rich basalt. *Chem. Geol.* **312**–**313**, 118–126.

Flueck W. T. and Smith-Flueck J. A. M. (2013) Severe dental fluorosis in juvenile deer linked to a recent volcanic eruption in Patagonia. *J. Wildl. Dis.* **49**, 355–366.

Foley S. F., Taylor W. R. and Green D. H. (1986a) The effect of fluorine on phase relationships in the system $KAlSiO_4$-Mg_2SiO_4-SiO_2 at 28 kbar and the solution mechanism of fluorine in silicate melts. *Contrib. to Mineral. Petrol.* **93**, 46–55.

Foley S. F., Taylor W. R. and Green D. H. (1986b) The role of fluorine and oxygen fugacity in the genesis of the ultrapotassic rocks. *Contrib. to Mineral. Petrol.* **94**, 183–192.

Fortin M. A., Watson E. B. and Stern R. (2017) The isotope mass effect on chlorine diffusion in dacite melt, with implications for fractionation during bubble growth. *Earth Planet. Sci. Lett.* **480**, 15–24.

Gabitov R. I., Price J. D. and Watson E. B. (2005) Diffusion of Ca and F in haplogranitic melt from dissolving fluorite crystals at 900–1000°C and 100 MPa. *Geochemistry, Geophys. Geosystems* **6**, 1–7.

Geschwind C. H. and Rutherford M. J. (1995) Crystallization of microlites during magma ascent: the fluid mechanics of 1980-1986 eruptions at Mount St Helens. *Bull. Volcanol.* **57**, 356–370.

Giordano D. and Dingwell D. B. (2003) Non-Arrhenian multicomponent melt viscosity: A model. *Earth Planet. Sci. Lett.* **208**, 337–349.

Giordano D., Romano C., Dingwell D. B., Poe B. and Behrens H. (2004) The combined effects of water and fluorine on the viscosity of silicic magmas. *Geochim. Cosmochim. Acta* **68**, 5159–5168.

Giordano D., Russell J. K. and Dingwell D. B. (2008) Viscosity of magmatic liquids: A model. *Earth Planet. Sci. Lett.* **271**, 123–134.

von Glasow R., Bobrowski N. and Kern C. (2009) The effects of volcanic eruptions on atmospheric chemistry. *Chem. Geol.* **263**, 131–142.

Glasstone S., Laidler K. J. and Eyring H. (1941) *The Theory of Rate Processes*., McGraw-Hill, New York.

Goldstein J. I., Newbury D. E., Michael J. R., Ritchie N. W. M., Scott J. H. J. and Joy D. C. (2018) *Scanning electron microscopy and x-ray microanalysis*. 4th ed., Springer.

Gonnermann H. M. and Manga M. (2012) Dynamics of magma ascent in the volcanic conduit. In *Modeling Volcanic Processes: The Physics and Mathematics of Volcanism* (eds. S. A. Fagents, T. K. P. Gregg, and R. M. C. Lopes). Cambridge University Press. pp. 55–84.

Gonnermann H. M. and Manga M. (2007) The fluid mechanics inside a volcano. *Annu. Rev. Fluid Mech.* **39**, 321–356.

Hammer J. E., Rutherford M. J. and Hildreth W. (2002) Magma storage prior to the 1912 eruption at Novarupta, Alaska. *Contrib. to Mineral. Petrol.* **144**, 144–162.

Helo C., Castro J. M., Hess K. U. and Dingwell D. B. (2020) Determination of water speciation in hydrous haplogranitic glasses with partial Raman spectra. *Chem. Geol.* **553**, 119793.

Henderson P., Nolan J., Cunningham G. C. and Lowry R. K. (1985) Structural controls and mechanisms of diffusion in natural silicate melts. *Contrib. to Mineral. Petrol.* **89**, 263–272.

Hirayama C. and Camp E. (1969) The effect of fluorine and chlorine substitution on the viscosity and fining of soda-lime and potassium-barium silicate glass. *Glas. Technol.* **10**, 123.

Horwell C. J., Le Blond J. S., Michnowicz S. A. K. and Cressey G. (2010) Cristobalite in a rhyolitic lava dome: Evolution of ash hazard. *Bull. Volcanol.* **72**, 249–253.

Iacovino K. and Till C. B. (2019) DensityX: A program for calculating the densities of magmatic liquids up to 1,627 °C and 30 kbar. *Volcanica* **2**, 1–10.

Ihinger P. D., Hervig R. L. and McMillan P. F. (1994) Analytical methods for volatiles in glasses. In *Volatiles in Magmas* (eds. M. R. Carroll and J. R. Holloway). Rev. Mineral. Geochem.,

Mineralogical Society of America, Washington, D.C. pp. 67–121.

Ihinger P. D., Zhang Y. and Stolper E. M. (1999) The speciation of dissolved water in rhyolitic melt. *Geochim. Cosmochim. Acta* **63**, 3567–3578.

Jambon A. and Semet M. P. (1978) Lithium diffusion in silicate glasses of Albite, Orthoclase, and Obsidian composition: an ion-microprobe determination. *Earth Planet. Sci. Lett.* **37**, 445–450.

Johnson N. M. and Fegley B. (2003) Longevity of flourine-bearing tremolite on Venus. *Icarus* **165**, 340–348.

Karpukhina N. G., Werner-Zwanziger U., Zwanziger J. W. and Kiprianov A. A. (2007) Preferential binding of fluorine to aluminum in high peralkaline aluminosilicate glasses. *J. Phys. Chem. B* **111**, 10413–10420.

Keith H. D. and Padden F. J. (1963) A phenomenological theory of spherulite crystallization. *J. Appl. Phys.* **34**, 2409–2421.

Kiczenski T. J., Du L. S. and Stebbins J. F. (2004) F-19 NMR study of the ordering of high field strength cations at fluoride sites in silicate and aluminosilicate glasses. *J. Non. Cryst. Solids* **337**, 142–149.

Kiprianov A. A. and Karpukhina N. G. (2006) Oxyhalide silicate glasses. *Glas. Phys. Chem.* **32**, 1–27.

Kirkpatrick R. J. (1983) Theory of nucleation in silicate melts. *Am. Mineral.* **68**, 66–77.

Klein J., Mueller S. P. and Castro J. M. (2017) The influence of crystal size distributions on the rheology of magmas: New insights from analog experiments. *Geochemistry, Geophys. Geosystems* **18**, 4055–4073.

Kohn S. C., Dupree R., Mortuza M. G. and Henderson C. M. B. (1991) NMR evidence for five-and six-coordinated aluminum fluoride complexes in F-bearing aluminosilicate glasses. *Am. Mineral.* **76**, 309–312.

Koster van Groos A. F. and Wyllie P. J. (1969) Melting relationships in the system $NaAlSi_3O_8$-NaCl-H_2O at one kilobar pressure, with petrological applications. *J. Geol.* **77**, 581–605.

Koster van Groos A. F. and Wyllie P. J. (1968) Melting relationships in the system $NaAlSi_3O_8$-NaF-H_2O to 4 kilobars pressure. *J. Geol.* **76**, 50–70.

Lafuente B., Downs R. T., Yang H. and Stone N. (2015) The power of databases: The RRUFF project. In *Highlights in Mineralogical Crystallography* (eds. T. Armbruster and R. M. Danisi). De Gruyter, Berlin. pp. 1–29.

Larsen J. F. (2006) Rhyodacite magma storage conditions prior to the 3430 yBP caldera-forming eruption of Aniakchak volcano, Alaska. *Contrib. to Mineral. Petrol.* **152**, 523–540.

Lesher C. E. (2010) Self-diffusion in silicate melts: Theory, observations and applications to magmatic systems. *Rev. Mineral. Geochemistry* **72**, 269–309.

Liang Y., Richter F. M., Davis A. M. and Bruce Watson E. (1996) Diffusion in silicate melts: I. Self diffusion in CaO-Al_2O_3-SiO_2 at 1500° C and 1 GPa. *Geochim. Cosmochim. Acta* **60**, 4353–4367.

Liu Y. and Nekvasil H. (2002) Si-F bonding in aluminosilicate glasses: Inferences from ab initio NMR

calculations. *Am. Mineral.* **87**, 339–346.

Lofgren G. (1980) Experimental Studies on the Dynamic Crystallization of Silicate Melts. In *Physics of Magmatic Processes* (ed. R. B. Hargraves). Princeton University Press, Princeton, New Jersey. pp. 487–551.

Lofgren G. (1971) Spherulitic textures in glassy and crystalline rocks. *J. Geophys. Res.* **76**, 5635–5648.

Lowenstern J. B., Bleick H., Vazquez J. A., Castro J. M. and Larson P. B. (2012) Degassing of Cl, F, Li, and Be during extrusion and crystallization of the rhyolite dome at Volcán Chaitén, Chile during 2008 and 2009. *Bull. Volcanol.* **74**, 2303–2319.

Lowry R. K., Hender P. and Nolan J. (1982) Tracer Diffusion of Some Alkali, Alkaline-Earth and Transition Element Ions in a Basaltic and an Andesitic Melt, and the Implications Concerning Melt Structure. *Contrib. to Mineral. Petrol.* **80**, 254–261.

Lux G. (1987) The behavior of noble gases in silicate liquids: Solution, diffusion, bubbles and surface effects, with applications to natural samples. *Geochim. Cosmochim. Acta* **51**, 1549–1560.

Manga M., Castro J., Cashman K. V and Loewenberg M. (1998) Rheology of bubble-bearing magmas. *J. Volcanol. Geotherm. Res.* **87**, 15–28.

Manning D. A. C. (1981) The effect of fluorine on liquidus phase relationships in the system Qz-Ab-Or with excess water at 1 kB. *Contrib. to Mineral. Petrol.* **76**, 206–215.

Margaritz M. and Hofmann A. W. (1978) Diffusion of Sr, Ba and Na in obsidian. *Geochim. Cosmochim. Acta* **42**, 595–605.

Marks M. A. W., Kendrick M. A., Eby G. N., Zack T. and Wenzel T. (2017a) The F, Cl, Br and I Contents of Reference Glasses BHVO-2G, BIR-1G, BCR-2G, GSD-1G, GSE-1G, NIST SRM 610 and NIST SRM 612. *Geostand. Geoanalytical Res.* **41**, 107–122.

Marks M. A. W., Kendrick M. A., Wenzel T., Eby G. N. and Zack T. (2017b) Reply to 'Comment on The F, Cl, Br and I Contents of Reference Glasses BHVO-2G, BIR-1G, BCR-2G, GSD-1G, GSE-1G, NIST SRM 610 and NIST SRM 612.' *Geostand. Geoanalytical Res.* **41**, 475–478.

Maron S. H. and Pierce P. E. (1956) Application of Ree-Eyring generalized flow theory to suspension of spherical particles. *J. Colloid Sci.* **11**, 80–95.

Di Matteo V., Carroll M. R., Behrens H., Vetere F. and Brooker R. A. (2004) Water solubility in trachytic melts. *Chem. Geol.* **213**, 187–196.

Matthews W., Linnen R. L. and Guo Q. (2003) A filler-rod technique for controlling redox conditions in cold-seal pressure vessels. *Am. Mineral.* **88**, 701–707.

McArthur A. N., Cas R. A. F. and Orton G. J. (1998) Distribution and significance of crystalline, perlitic and vesicular textures in the Ordovician Garth Tuff (Wales). *Bull. Volcanol.* **60**, 260–285.

Mueller S., Llewellin E. W. and Mader H. M. (2010) The rheology of suspensions of solid particles. In *Proceedings of the Royal Society A* pp. 1201–1228.

Musselwhite D. S. and Drake M. J. (2000) Early Outgassing of Mars: Implications from Experimentally

Determined Solubility of Iodine in Silicate Magmas. *Icarus* **148**, 160–175.

Mysen B. O. (1988) *Structure and Properties of Silicate Melts*., Elsevier, Amsterdam.

Mysen B. O., Cody G. D. and Smith A. (2004) Solubility mechanisms of fluorine in peralkaline and meta-aluminous silicate glasses and in melts to magmatic temperatures. *Geochim. Cosmochim. Acta* **68**, 2745–2769.

Mysen B. O. and Virgo D. (1985) Interaction between fluorine and silica in quenched melts on the joins SiO_2-AlF_3 and SiO_2-NaF determined by raman spectroscopy. *Phys. Chem. Miner.* **12**, 77–85.

Mysen B. O., Virgo D., Harrison W. J. and Scarfe C. M. (1980) Solubility mechanisms of H_2O in silicate melts at high pressures and temperatures: a Raman spectroscopic study: discussion. *Am. Mineral.* **65**, 900–914.

Neuville D. R., de Ligny D. and Henderson G. S. (2014) Advances in Raman spectroscopy applied to earth and material sciences. In *Spectroscopic Methods in Mineralogy and Materials Sciences* (eds. G. S. Henderson, D. R. Neuville, and R. T. Downs). Rev. Mineral. Geochem., Mineralogical Society of America. pp. 509–541.

Ochs F. A. and Lange R. A. (1999) The density of hydrous magmatic liquids. *Science* **283**, 1314–1317.

Oishi Y., Terai R. and Ueda H. (1975) Oxygen Diffusion in Liquid Silicates and Relation to their Viscosity. In *Mass Transport Phenomena in Ceramics* pp. 297–310.

Pankhurst M. J., Scarrow J. H., Barbee O. A., Hickey J., Coldwell B. C., Rollinson G. K., Rodríguez-Losada J. A., Martín-Lorenzo A., Rodríguez F., Hernández W., Fernández D. C., Hernández P. A. and Pérez N. M. (2022) Rapid response petrology for the opening eruptive phase of the 2021 Cumbre Vieja eruption, La Palma, Canary Islands. *Volcanica* **5**, 1–10.

Papale P., Moretti R. and Barbato D. (2006) The compositional dependence of the saturation surface of H_2O + CO_2 fluids in silicate melts. *Chem. Geol.* **229**, 78–95.

Parejas C. S., Lara L. E., Bertin D., Amigo A. and Orozco G. (2012) The 2011-2012 eruption of Cordón Caulle volcano (Southern Andes): Evolution, crisis management and current hazards. *EGU Gen. Assem. Conf. Abstr.* **14**, 9382.

Pichavant M. (1987) The Macusani glasses, SE Peru: evidence of chemical fractionation in peraluminous magmas. *Magmat. Process. Physicochem. Princ.*, 359–373.

Pichavant M., Costa F., Burgisser A., Scaillet B., Martel C. and Poussineau S. (2007) Equilibration scales in silicic to intermediate magmas - Implications for experimental studies. *J. Petrol.* **48**, 1955–1972.

Roberts T. (2018) Ozone Depletion in Tropospheric Volcanic Plumes: From Halogen-Poor to Halogen-Rich Emissions. *Geosciences* **8**, 68.

Scaillet B., Holtz F. and Pichavant M. (2016) Experimental constraints on the formation of silicic magmas. *Elements* **12**, 109–114.

Schaller T., Dingwell D. B., Keppler H., Knöller W., Merwin L. and Sebald A. (1992) Fluorine in silicate

glasses: A multinuclear magnetic resonance study. *Geochim. Cosmochim. Acta* **56**, 701–707.

Schipper C. I., Castro J., Kennedy B., Christenson B., Aiuppa A., Alloway B., Forte P., Seropian G. and Tuffen H. (2019) Halogen (Cl, F) release during explosive, effusive, and intrusive phases of the 2011 rhyolitic eruption at Cordón Caulle volcano (Chile). *Volcanica* **2**, 73–90.

Schipper C. I., Castro J. M., Tuffen H., James M. R. and How P. (2013) Shallow vent architecture during hybrid explosive-effusive activity at Cordón Caulle (Chile, 2011-12): Evidence from direct observations and pyroclast textures. *J. Volcanol. Geotherm. Res.* **262**, 25–37.

Schipper C. I., Castro J. M., Tuffen H., Wadsworth F. B., Chappell D., Pantoja A. E., Simpson M. P. and Le Ru E. C. (2015) Cristobalite in the 2011–2012 Cordón Caulle eruption (Chile). *Bull. Volcanol.* **77**.

Schipper C. I., Rickard W. D. A., Reddy S. M., Saxey D. W., Castro J. M., Fougerouse D., Quadir Z., Conway C., Prior D. J. and Lilly K. (2020) Volcanic SiO_2-cristobalite: A natural product of chemical vapor deposition. *Am. Mineral.* **105**, 510–524.

Schipper I. C., Mandon C., Maksimenko A., Castro J. M., Conway C. E., Hauer P., Kirilova M. and Kilgour G. (2017) Vapor-phase cristobalite as a durable indicator of magmatic pore structure and halogen degassing: an example from White Island volcano (New Zealand). *Bull. Volcanol.* **79**, 74.

Schmidt B. C. and Behrens H. (2008) Water solubility in phonolite melts : Influence of melt composition and temperature. *Chem. Geol.* **256**, 259–268.

Scholl-Poensgen C. (2021) F and Cl diffusion in rhyolitic melt. Johannes Gutenberg-University, Mainz.

Shannon R. D. (1976) Revised effective ionic radii and systematic studies of interatomic distances in halides and chalcogenides. *Acta Crystallogr. Sect. A* **32**, 751–767.

Shea T. and Hammer J. E. (2013) Oxidation in CSPV experiments involving H_2O-bearing mafic magmas: Quantification and mitigation. *Am. Mineral.* **98**, 1285–1296.

Shimizu N. and Kushiro I. (1984) Diffusivity of oxygen in jadeite and diopside melts at high pressures. *Geochim. Cosmochim. Acta* **48**, 1295–1303.

Signorelli S. and Carroll M. R. (2002) Experimental study of Cl solubility in hydrous alkaline melts: Constraints on the theoretical maximum amount of Cl in trachytic and phonolitic melts. *Contrib. to Mineral. Petrol.* **143**, 209–218.

Silver L. A., Ihinger P. D. and Stolper E. (1990) The influence of bulk composition on the speciation of water in silicate glasses. *Contrib. to Mineral. Petrol.* **104**, 142–162.

Singer B. S., Jicha B. R., Harper M. A., Naranjo J. A., Lara L. E. and Moreno-Roa H. (2008) Eruptive history, geochronology, and magmatic evolution of the Puyehue-Cordón Caulle volcanic complex, Chile. *Bull. Geol. Soc. Am.* **120**, 599–618.

Sisson T. W. and Grove T. L. (1993) Experimental investigations of the role of H_2O in calc-alkaline differentiation and subduction zone magmatism. *Contrib. to Mineral. Petrol.* **113**, 143–166.

Sparks R. S. J., Barclay J., Jaupart C., Mader H. M. and Phillips J. C. (1994) Physical aspects of magma

degassing I.: Experimental and theoretical constraints on vesiculation. In *Volatiles in Magmas* (eds. M. R. Carroll and J. R. Holloway). Review in Mineralogy and Geochemistry, Mineralogical Society of America. pp. 413–445.

Spilliaert N., Métrich N. and Allard P. (2006) S-Cl-F degassing pattern of water-rich alkali basalt: Modelling and relationship with eruption styles on Mount Etna volcano. *Earth Planet. Sci. Lett.* **248**, 772–786.

Stein D. J. and Spera F. J. (1992) Rheology and microstructure of magmatic emulsions: theory and experiments. *J. Volcanol. Geotherm. Res.* **49**, 157–174.

Stolper E. (1982) Water in silicate glasses: An infrared spectroscopic study. *Contrib. to Mineral. Petrol.* **81**, 1–17.

Surl L., Donohoue D., Aiuppa A., Bobrowski N. and von Glasow R. (2015) Quantification of the depletion of ozone in the plume of Mount Etna. *Atmos. Chem. Phys.* **15**, 2613–2628.

Sverrisdottir G. (2007) Hybrid magma generation preceding Plinian silicic eruptions at Hekla, Iceland: Evidence from mineralogy and chemistry of two zoned deposits. *Geol. Mag.* **144**, 643–659.

Swanson S. E. and Fenn P. M. (1992) The effect of F and Cl on the kinetics of albite crystallization: a model for granitic pegmatites? *Can. Mineral.* **30**, 549–559.

Symonds R. B., Rose W. I., Bluth G. J. S. and Gerlach T. M. (1994) Volcanic-gas studies: methods, results, and applications. In *Volatiles in Magmas* (eds. M. R. Carroll and J. R. Holloway). Rev. Mineral. Geochem., Mineralogical Society of America. pp. 1–66.

Szramek L., Gardner J. E. and Larsen J. (2006) Degassing and microlite crystallization of basaltic andesite magma erupting at Arenal Volcano, Costa Rica. *J. Volcanol. Geotherm. Res.* **157**, 182–201.

Thomas R. W. and Wood B. J. (2021) The chemical behaviour of chlorine in silicate melts. *Geochim. Cosmochim. Acta* **294**, 28–42.

Thordarson T. and Larsen G. (2007) Volcanism in Iceland in historical time: Volcano types, eruption styles and eruptive history. *J. Geodyn.* **43**, 118–152.

Tribaudino M., Mantovani L., Bersani D. and Lottici P. P. (2012) Raman spectroscopy of (Ca,Mg)$MgSi_2O_6$ clinopyroxenes. *Am. Mineral.* **97**, 1339–1347.

Wallace P. J., Plank T., Edmonds M. and Hauri E. H. (2015) Volatiles in magmas. In *The Encyclopedia of Volcanoes* (ed. H. Sigurdsson). Academic Press. pp. 163–183.

Watson E. B. (1991) Diffusion of dissolved CO_2 and Cl in hydrous silicic to intermediate magmas. *Geochim. Cosmochim. Acta* **55**, 1897–1902.

Watson E. B. (2017) Diffusive fractionation of volatiles and their isotopes during bubble growth in magmas. *Contrib. to Mineral. Petrol.* **172**.

Watson E. B. and Bender J. F. (1980) Diffusion of cesium, samarium, strontium, and chlorine in molten silicate at high temperatures and pressures. *Geol. Soc. Am. Abstr. with Programs* **12**, 545.

Webb S. L., Murton B. J. and Wheeler A. J. (2014) Rheology and the Fe^{3+}-chlorine reaction in basaltic melts. *Chem. Geol.* **366**, 24–31.

Weber G. and Castro J. M. (2017) Phase petrology reveals shallow magma storage prior to large explosive silicic eruptions at Hekla volcano, Iceland. *Earth Planet. Sci. Lett.* **466**, 168–180.

Webster J. D., Baker D. R. and Aiuppa A. (2018) Halogens in Mafic and Intermediate-Silica Content Magmas. In *The Role of Halogens in Terrestrial and Extraterrestrial Geochemical Processes* (eds. D. E. Harlov and L. Y. Aranovich). Springer-Verlag. pp. 307–430.

Webster J. D. and Duffield W. A. (1994) Extreme Halogen Abundances in Tin-Rich Magma of the Taylor Creek Rhyolite, New Mexico. *Econ. Geol.* **89**, 849–850.

Webster J. D., Vetere F., Botcharnikov R. E., Goldoff B., McBirney A. and Doherty A. L. (2015) Experimental and modeled chlorine solubilities in aluminosilicate melts at 1 to 7000 bars and 700 to 1250 °C: Applications to magmas of Augustine Volcano, Alaska. *Am. Mineral.* **100**, 522–535.

Webster J. D. and De Vivo B. (2002) Experimental and modeled solubilities of chlorine in aluminosilicate melts, consequences of magma evolution, and implications for exsolution of hydrous chloride melt at Mt. Somma-Vesuvius. *Am. Miner.* **87**, 1046–1061.

Wiedenbeck M. (2017) Comment on: The F, Cl, Br and I Contents of Reference Glasses BHVO-2G, BIR-1G, BCR-2G, GSD-1G, GSE-1G, NIST SRM 610 and NIST SRM 612 by Marks et al. This Issue. *Geostand. Geoanalytical Res.* **41**, 147–152.

Wyllie P. J. and Tuttle O. F. (1961) Experimental investigation of silicate systems containing two volatile components; Part 2, the effects of NH_3 and HF, in addition to H_2O on the melting temperatures of albite and granite. *Am. J. Sci.* **259**, 128–143.

Wyllie P. J. and Tuttle O. F. (1964) Experimental investigation of silicate systems containing two volatile components. Part 3. The effects of SO_3, P_2O_5, HCl and Li_2O, in addition to water on the melting temperatures of albite and granite. *Am. J. Sci.* **262**, 930–939.

Yoshimura S. (2018) Chlorine diffusion in rhyolite under low-H_2O conditions. *Chem. Geol.* **483**, 619–630.

Yuen D. A., Scruggs M. A., Spera F. J., Zheng Y., Hu H., McNutt S. R., Thompson G., Mandli K., Keller B. R., Wei S. S., Peng Z., Zhou Z., Mulargia F. and Tanioka Y. (2022) Under the surface: Pressure-induced planetary-scale waves, volcanic lightning, and gaseous clouds caused by the submarine eruption of Hunga Tonga-Hunga Ha'apai volcano. *Earthq. Res. Adv.*, 100134.

Zeng Q. and Stebbins J. F. (2000) Fluoride sites in aluminosilicate glasses: High-resolution ^{19}F NMR results. *Am. Mineral.* **85**, 863–867.

Zhang Y. (2010) Diffusion in Minerals and Melts: Theoretical Background. In *Diffusion in Minerals and Melts* (eds. Y. Zhang and D. J. Cherniak). Rev. Mineral. Geochem., Mineralogical Society of America. pp. 5–59.

Zhang Y. and Ni H. (2010) Diffusion of H, C, and O components in silicate melts. In *Diffusion in*

Minerals and Melts (eds. Y. Zhang and D. J. Cherniak). Rev. Mineral. Geochem., Mineralogical Society of America. pp. 171–225.

Zhang Y., Ni H. and Chen Y. (2010) Diffusion data in silicate melts. In *Diffusion in Minerals and Melts* (eds. Y. Zhang and D. J. Cherniak). Rev. Mineral. Geochem., Mineralogical Society of America. pp. 311–408.

Zhang Y. and Stolper E. M. (1991) Water diffusion in a basaltic melt. *Nature* **351**, 306–309.

Zhang Y. and Xu Z. (2008) "Fizzics" of bubble growth in beer and champagne. *Elements* **4**, 47–49.

Zhang Y. and Xu Z. (2003) Kinetics of convective crystal dissolution and melting, with applications to methane hydrate dissolution and dissociation in seawater. *Earth Planet. Sci. Lett.* **213**, 133–148.

Zimova M. and Webb S. (2006) The effect of chlorine on the viscosity of Na_2O-Fe_2O_3-Al_2O_3-SiO_2 melts. *Am. Mineral.* **91**, 344–352.

Zimova M. and Webb S. L. (2007) The combined effects of chlorine and fluorine on the viscosity of aluminosilicate melts. *Geochim. Cosmochim. Acta* **71**, 1553–1562.

Appendix

A1 Supplementary Material of Chapter 5

The following figures and tables were submitted as supplementary material for the study presented in chapter 5 (Feisel et al., *under review*).

Contents:

Table S1: Compilation of the analytical conditions used during the different ion probe sessions.

Fig. S1a-e: Fitted concentration vs. distance profiles of the halogens and H_2O in the hydrous diffusion couple samples.

Fig. S2a-f: Fitted concentration vs. distance profiles of the halogens in samples of the HX series, acquired by SIMS.

Fig. S3a-h: Fitted concentration vs. distance profiles of the halogens in samples of the CCX series, acquired by SIMS and EMPA.

Fig. S4a-e: Fitted concentration vs. distance profiles of the halogens in samples of the CCX-H series, acquired by SIMS and EMPA.

Table S 1: Compilation of the analytical conditions used during the different ion probe sessions.

	Halogens Lausanne	**Halogens Heidelberg**	**H_2O Heidelberg**
Instrument	Cameca IMS1280-HR	Cameca IMS1280-HR	Cameca ims3f
Primary ions	$^{133}Cs^+$	$^{133}Cs^+$	$^{16}O^-$
Primary HV (kV)	10	10	12.5
Primary beam current (nA)	0.4	~0.7	10
Primary beam diameter (µm)	~4	~5	~20
Secondary HV (kV)	10	10	4.5
Secondary voltage offset (V)	–	60	75
Secondary energy window (eV)	50	40	40
'Max. Area' IMS1280-HR (µm)	80	40	–
Imaged field ims3f (µm)	–	–	25
Field aperture (µm)	5000	3000	200
Contrast aperture (µm)	400	400 (session 1), 150 (session 2)	150
Nominal mass resolving power M/DM	4000	4000	350
Pre sputter time (s)	90	30	120
Pre sputter raster size (µm)	15	4	0
Raster size during analysis	10	0	0
# of analysis cycles	15	5	6
Isotopes analysed	^{19}F, ^{28}Si, ^{30}Si, ^{35}Cl, ^{79}Br, ^{81}Br, ^{127}I	^{19}F, ^{28}Si, ^{35}Cl, ^{81}Br, ^{127}I	H, ^{30}Si
Integration times per cycle (s)	3, 2, 3, 2, 3, 3, 6	4, 1, 4, 8, 8	2, 4
Detection	Axial FC2 (^{19}F, ^{28}Si), Axial EM (^{30}Si, ^{35}Cl, ^{79}B, ^{81}B, 127I)	Axial EM	EM
Reference materials for calibration	Reference area in the enriched part to check instrument stability.	JV1 glass for F and Cl, GSE-1G for Br and I (semi-quantitative)	JV1 glass (0.46 wt.% H_2O)

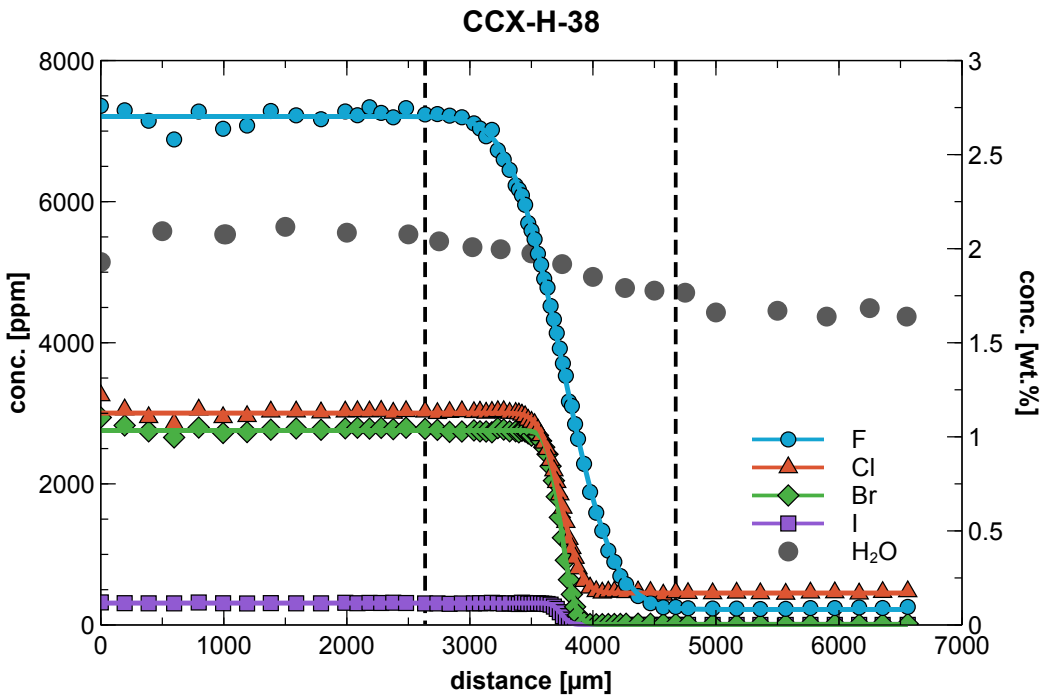

Fig. S1a: Concentration vs. distance profile of sample CCX-H-38 measured by SIMS and plotted together with the calculated fit curves. H_2O concentration data refers to the secondary y-axis. Dashed vertical lines bracket the region used for determining the average H_2O content in the relevant part of the sample.

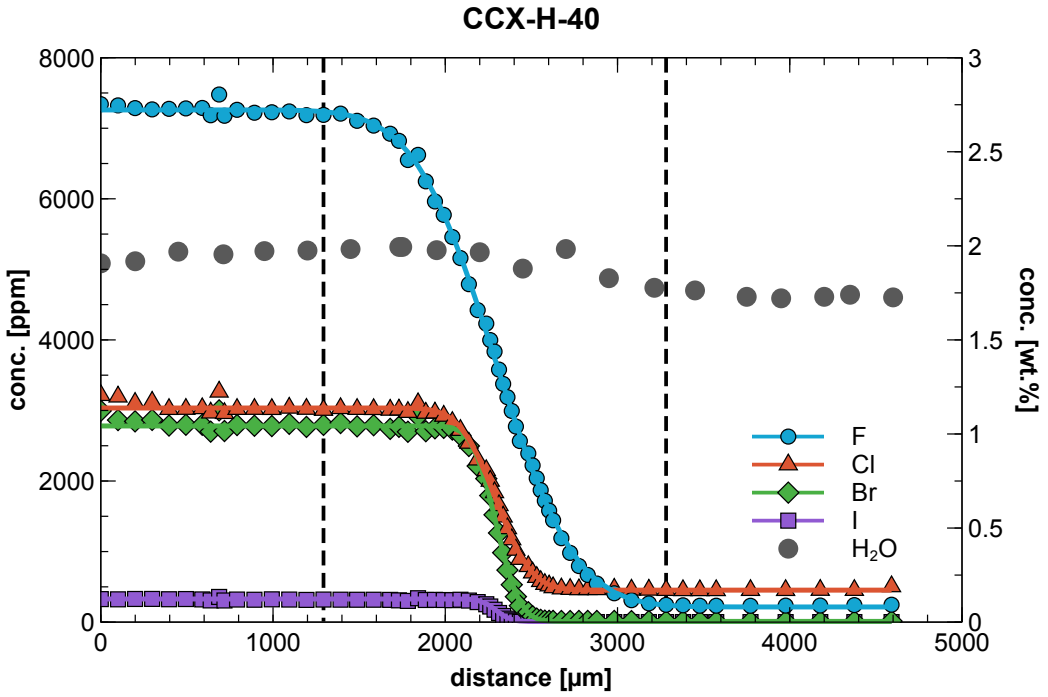

Fig. S1b: Concentration vs. distance profile of sample CCX-H-40 measured by SIMS and plotted together with the calculated fit curves. H_2O concentration data refers to the secondary y-axis. Dashed vertical lines bracket the region used for determining the average H_2O content in the relevant part of the sample.

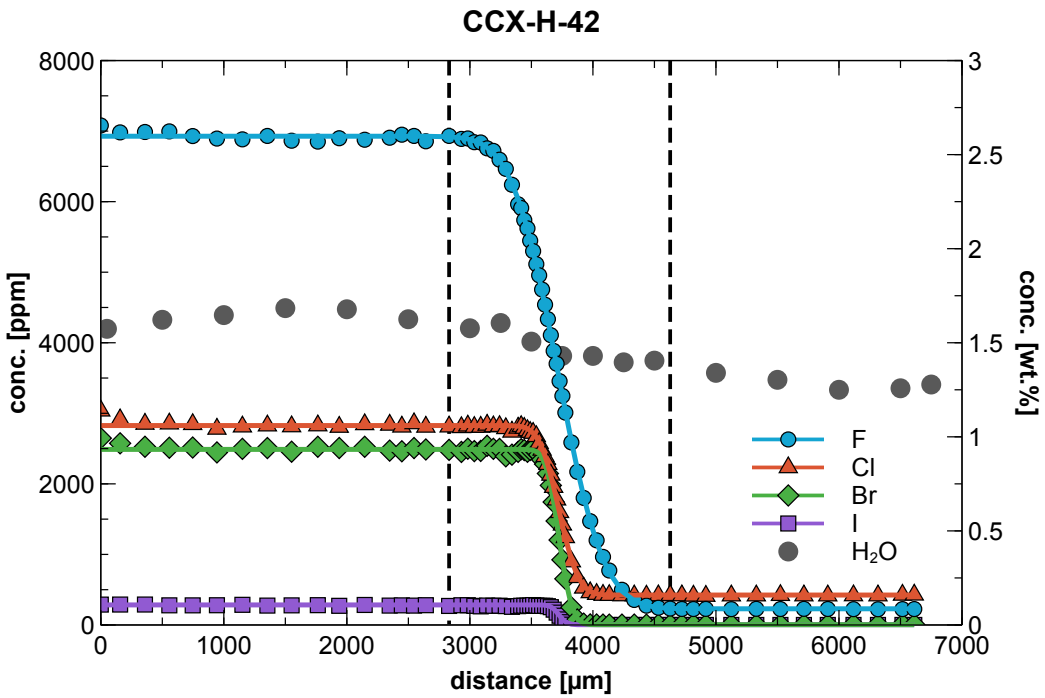

Fig. S1c: Concentration vs. distance profile of sample CCX-H-42 measured by SIMS and plotted together with the calculated fit curves. H_2O concentration data refers to the secondary y-axis. Dashed vertical lines bracket the region used for determining the average H_2O content in the relevant part of the sample.

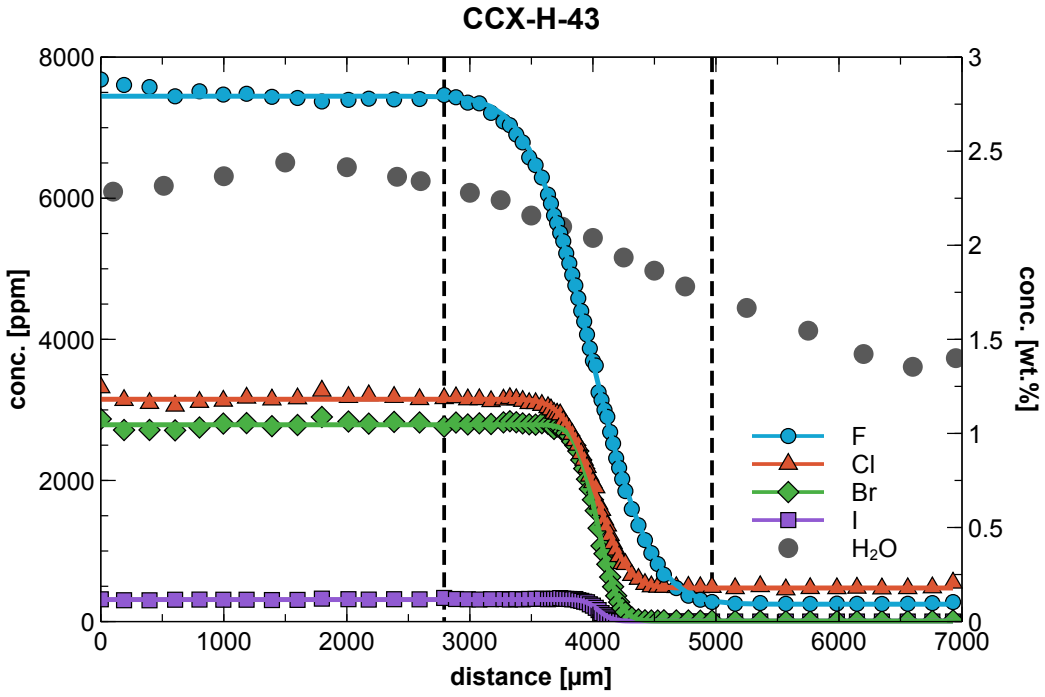

Fig. S1d: Concentration vs. distance profile of sample CCX-H-43 measured by SIMS and plotted together with the calculated fit curves. H_2O concentration data refers to the secondary y-axis. Dashed vertical lines bracket the region used for determining the average H_2O content in the relevant part of the sample.

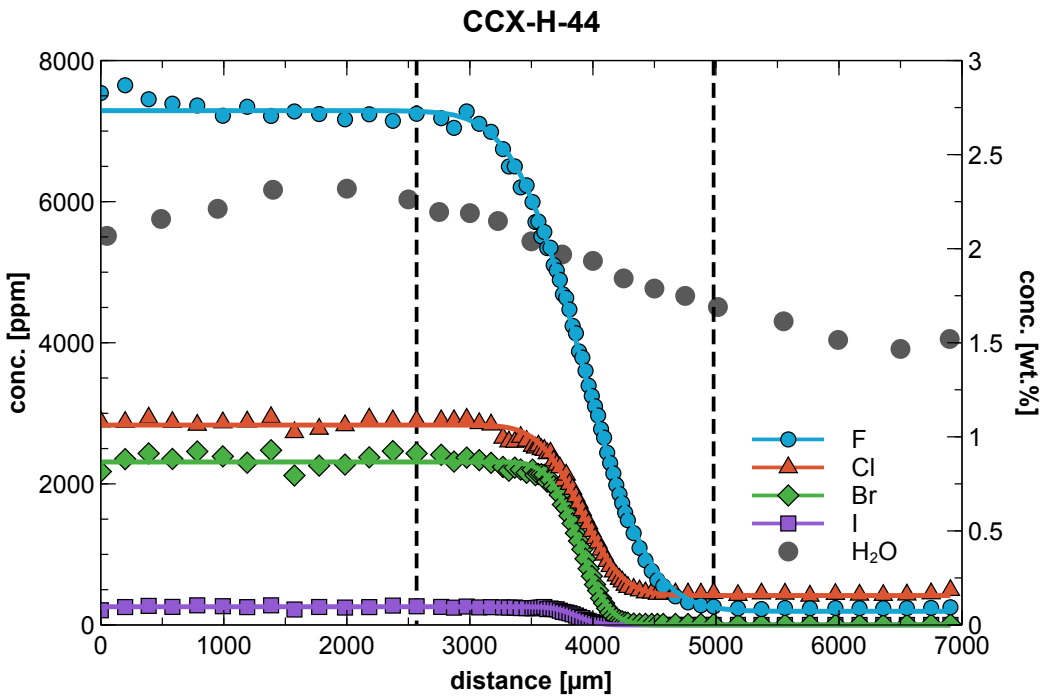

Fig. S1e: Concentration vs. distance profile of sample CCX-H-44 measured by SIMS and plotted together with the calculated fit curves. H_2O concentration data refers to the secondary y-axis. Dashed vertical lines bracket the region used for determining the average H_2O content in the relevant part of the sample.

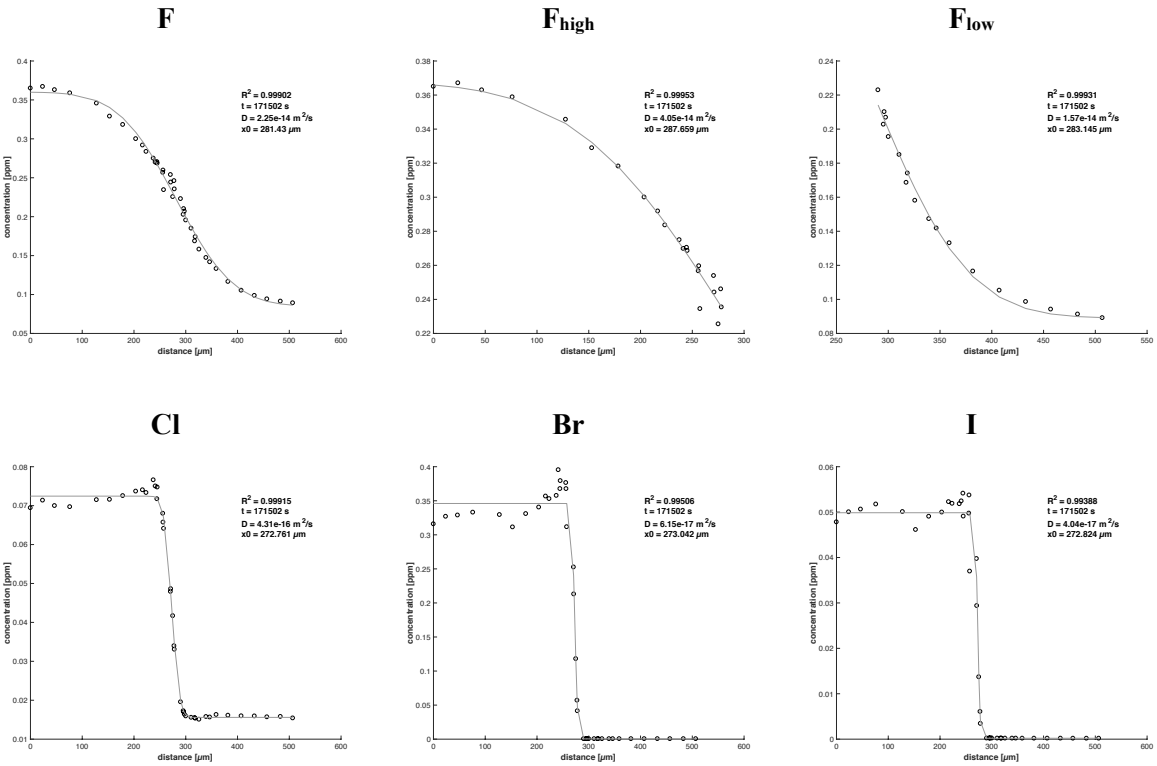

Fig. S2a: Fitted SIMS profiles of sample HX3 (850 °C).

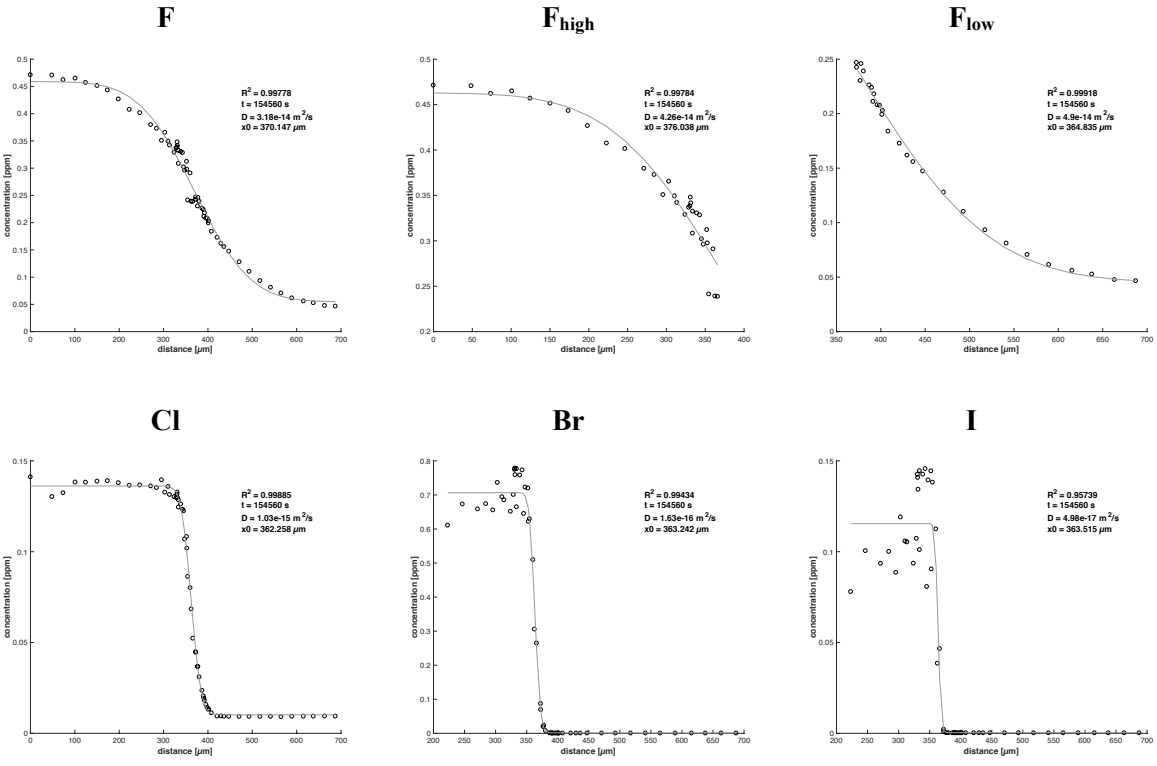

Fig. S2b: Fitted SIMS profiles of sample HX5 (900 °C).

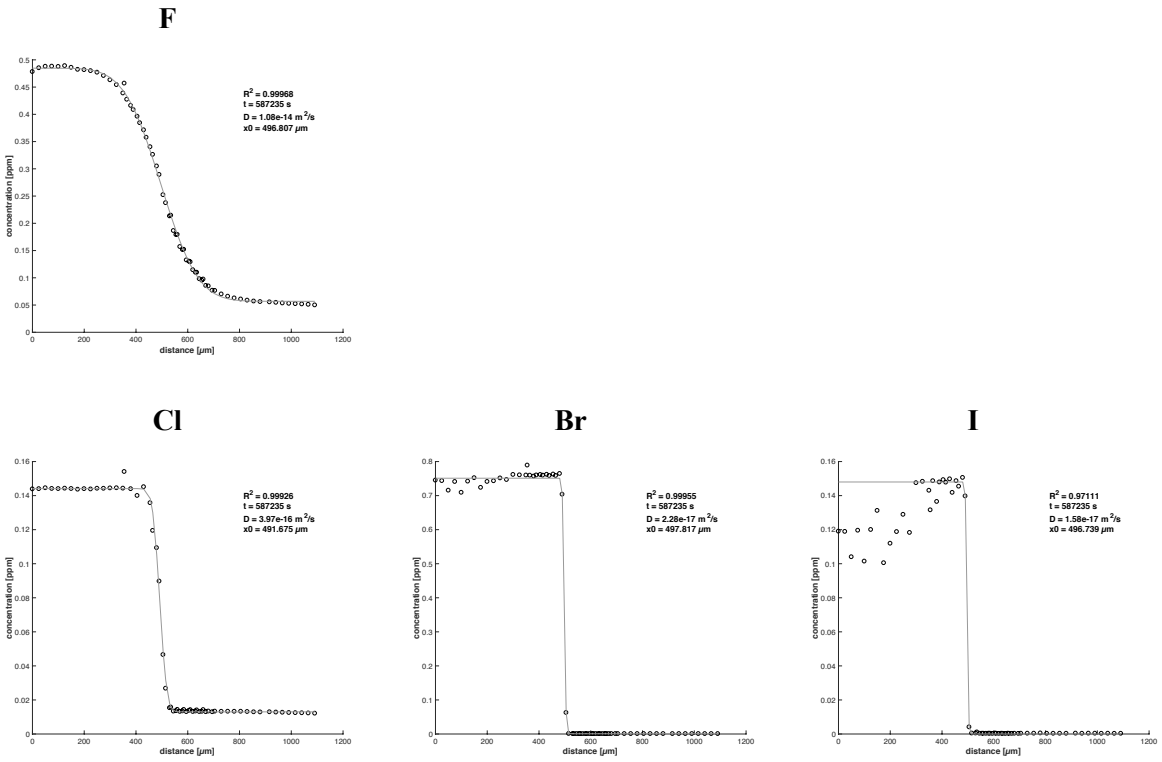

Fig. S2c: Fitted SIMS profiles of sample HX7 (800 °C).

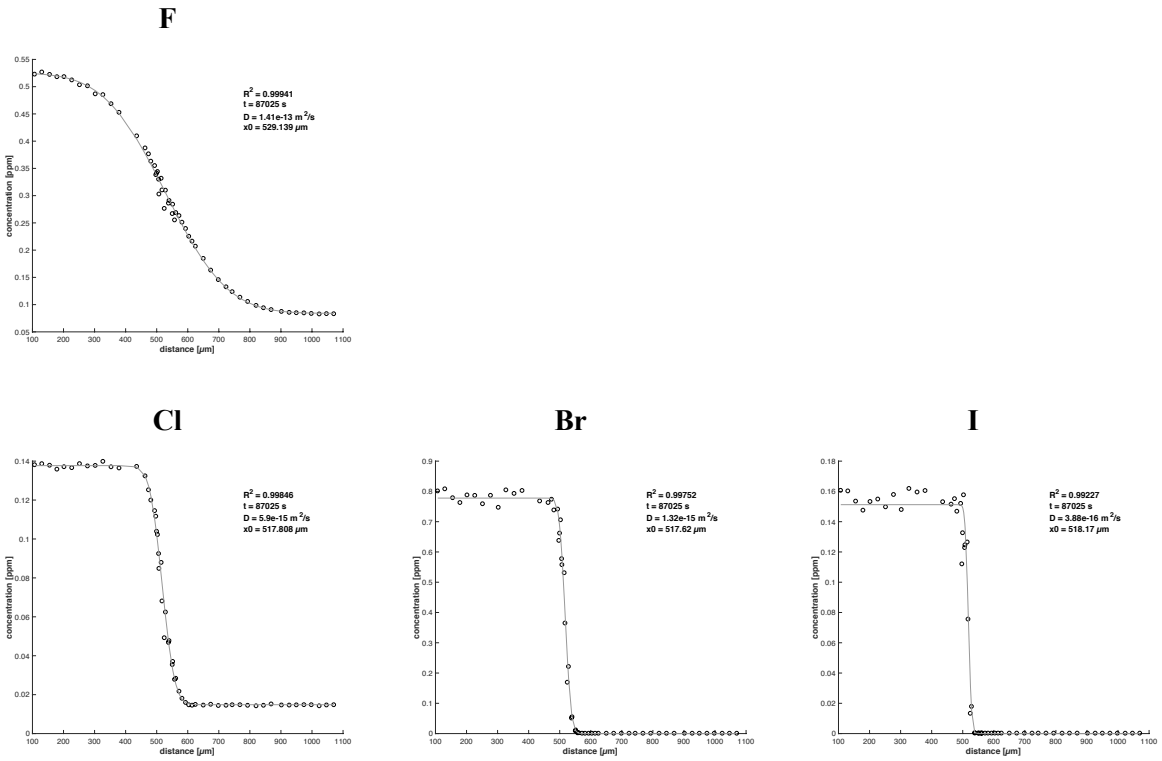

Fig. S2d: Fitted SIMS profiles of sample HX8 (950 °C).

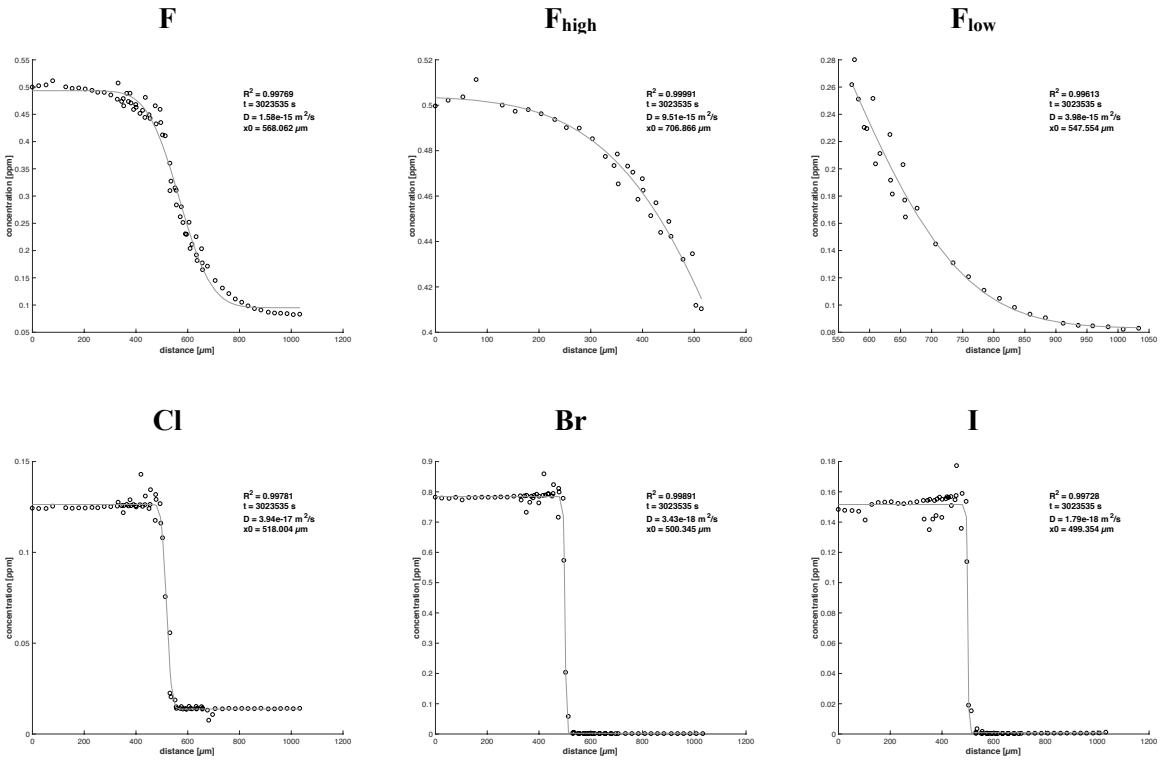

Fig. S2e: Fitted SIMS profiles of sample HX9 (750 °C).

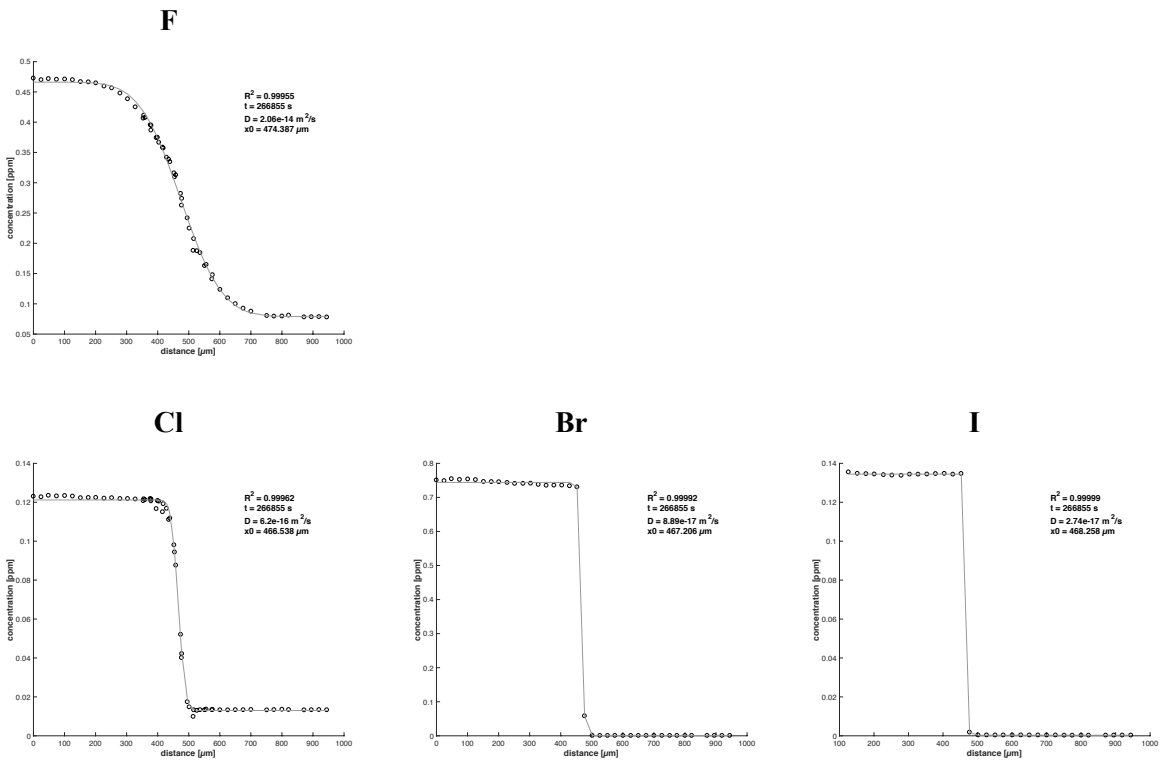

Fig. S2f: Fitted SIMS profiles of sample HX10 (850 °C).

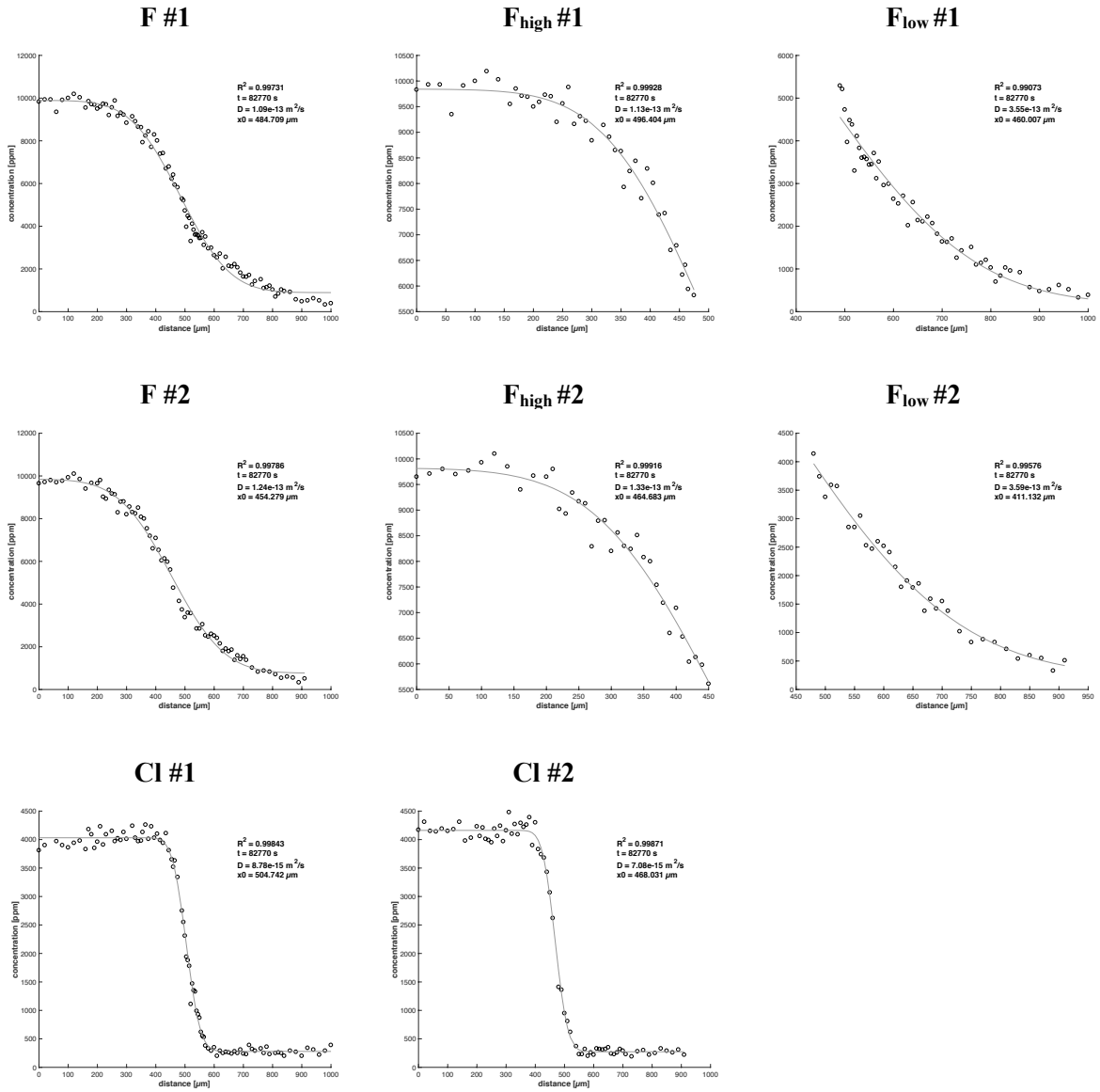

Fig. S3a: Fitted EMPA profiles of sample CCX1 (950 °C). The „#“ indicates the profiles number per sample.

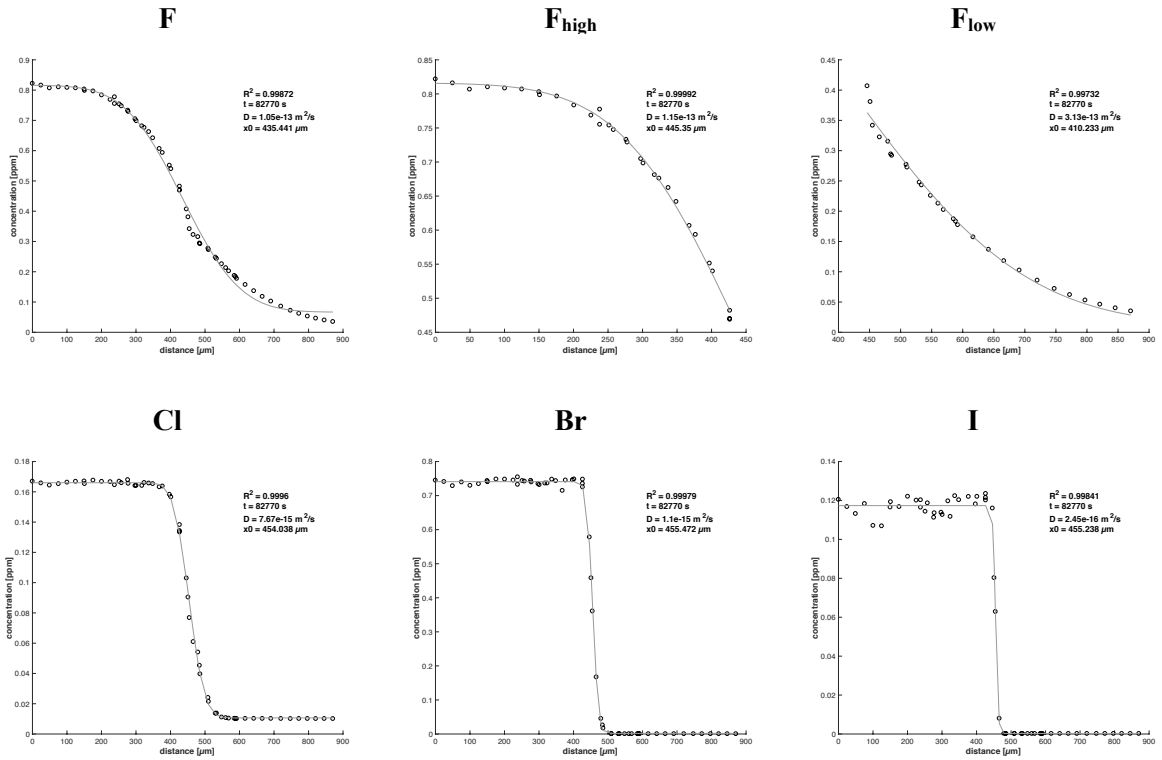

Fig. S3b: Fitted SIMS profiles of sample CCX1 (950 °C).

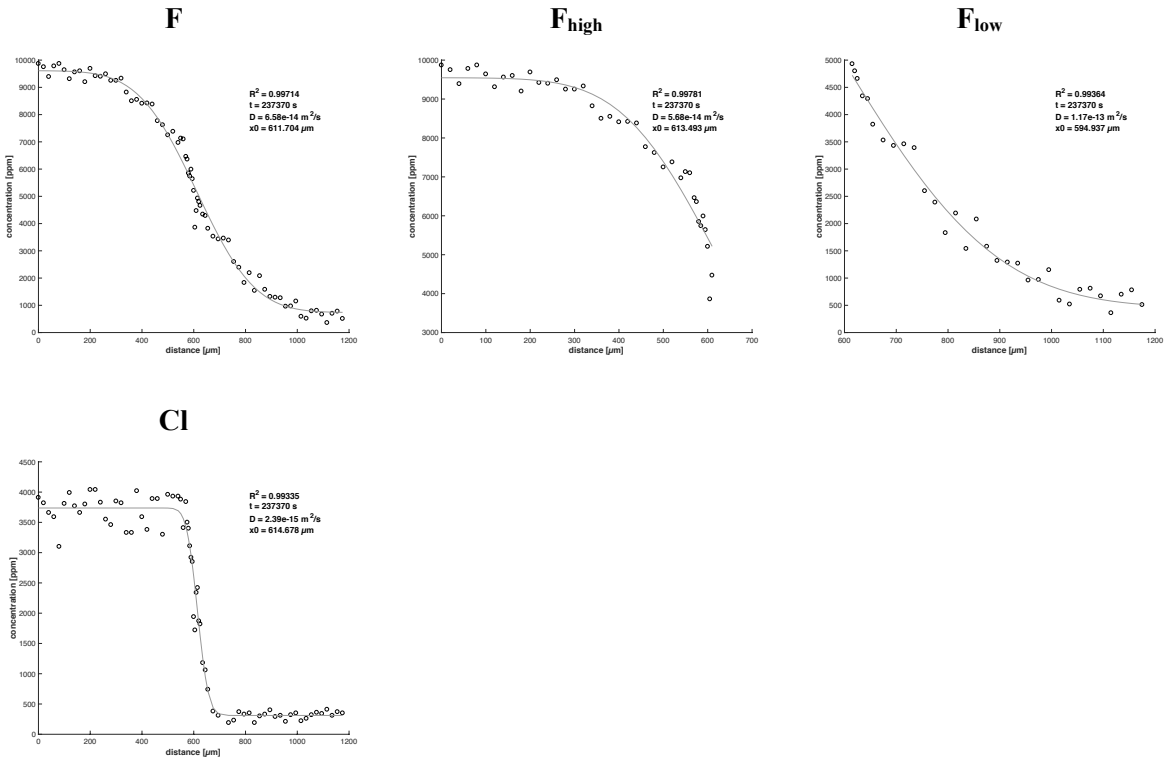

Fig. S3c: Fitted EMPA profiles of sample CCX3 (850 °C).

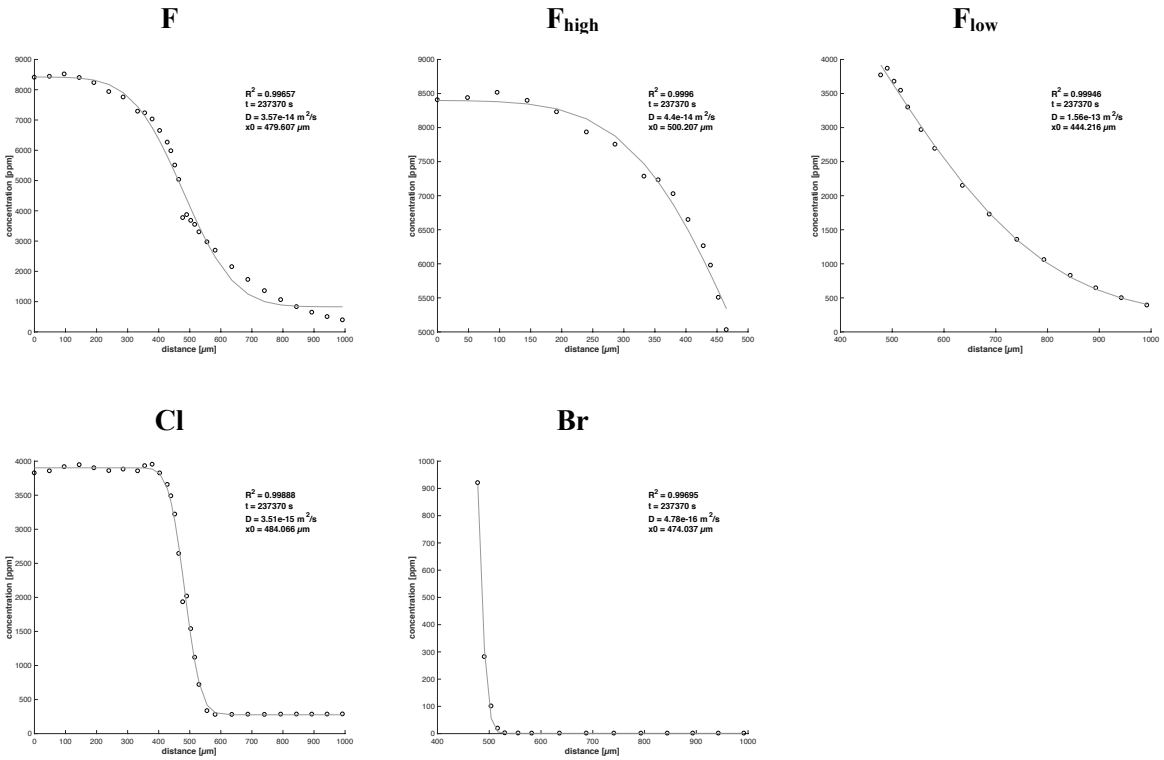

Fig. S3d: Fitted profiles of sample CCX3 (850 °C).

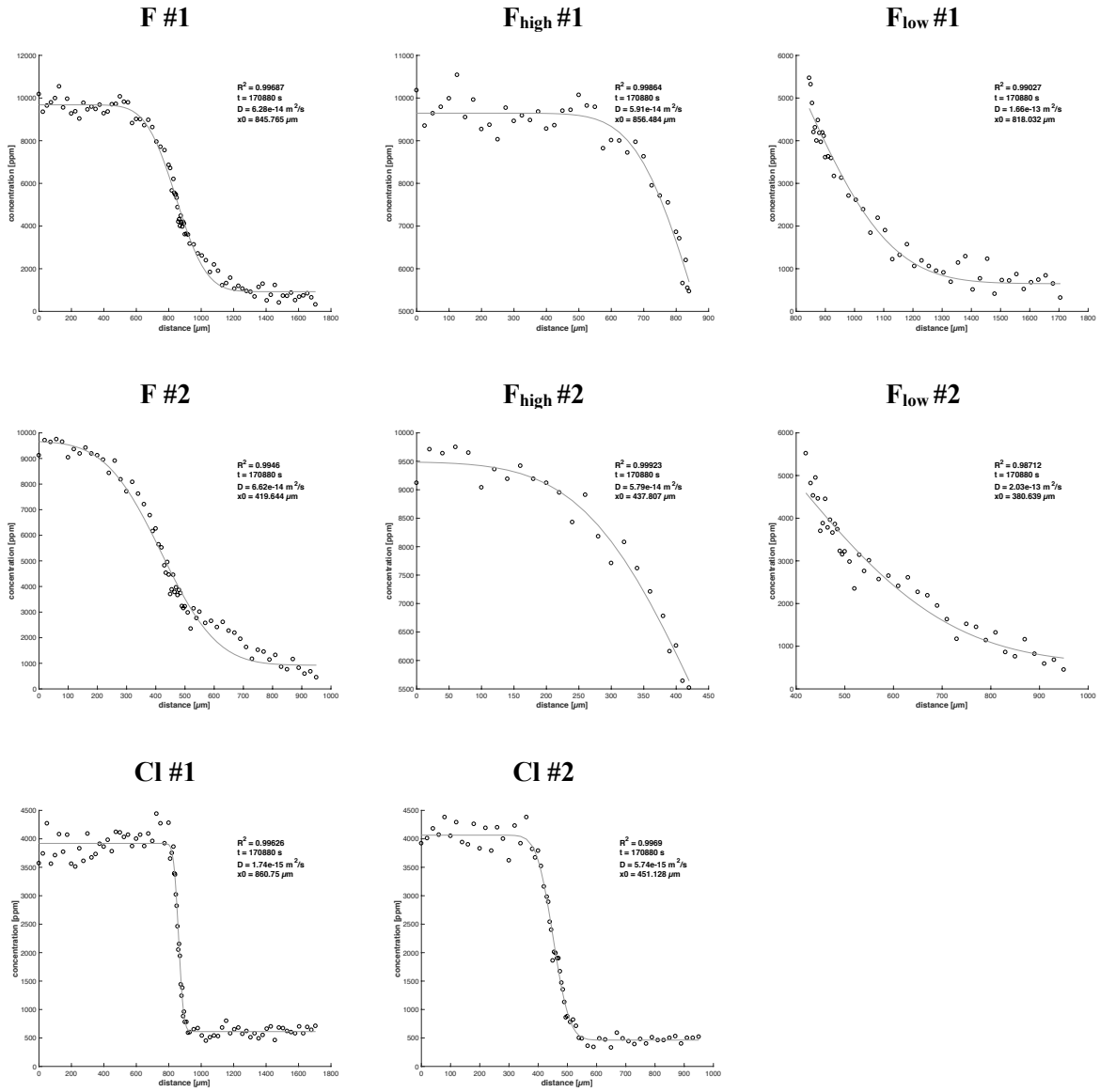

Fig. S3e: Fitted EMPA profiles of sample CCX4 (900 °C). The „#“ indicates the profile number per sample.

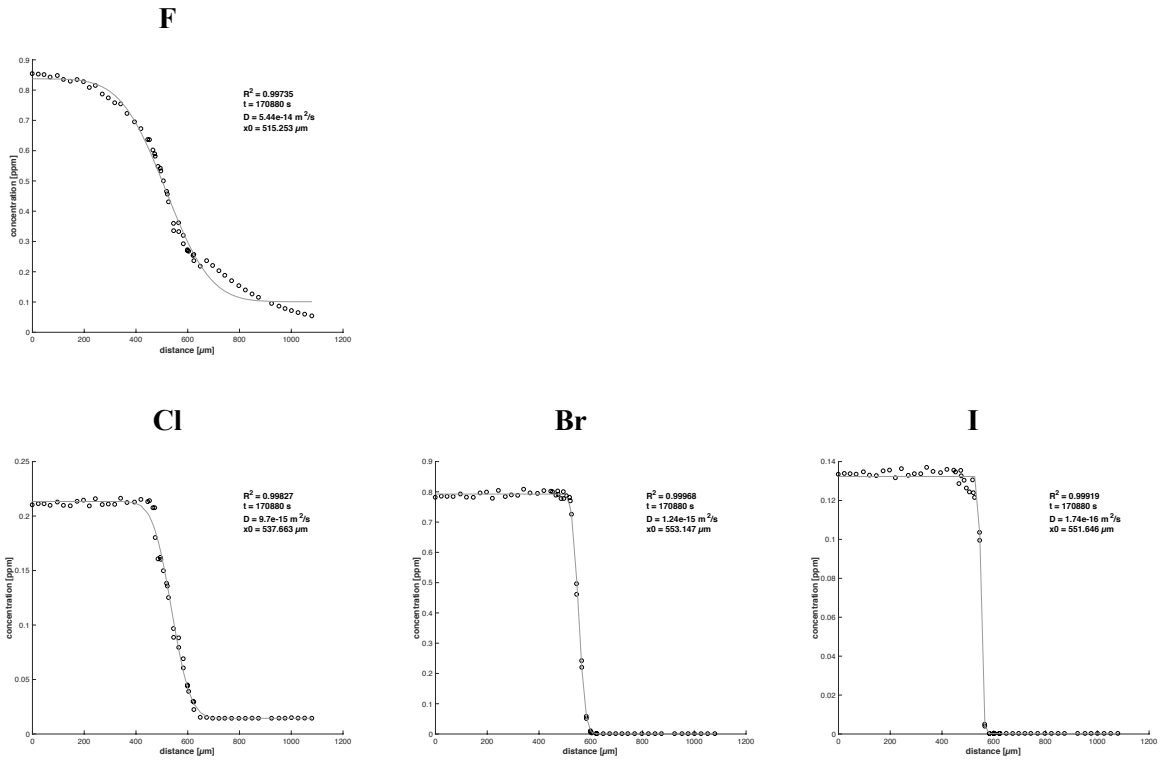

Fig. S3f: Fitted SIMS profiles of sample CCX 4 (900 °C).

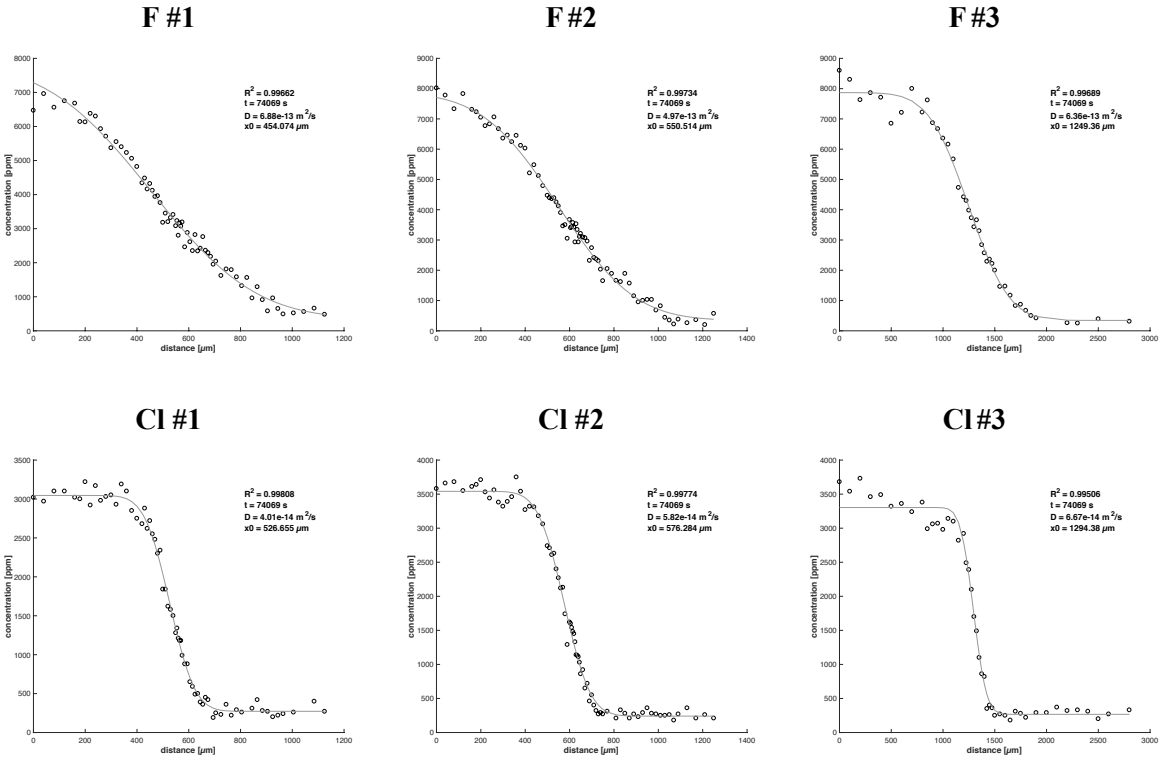

Fig. S3g: Fitted EMPA profiles of sample CCX 5 (1000 °C). The „#“ indicates the profile number per sample. C_{high} and C_{low} of F #1 and F #2 were fixed for fitting calculations by using the values of F #3.

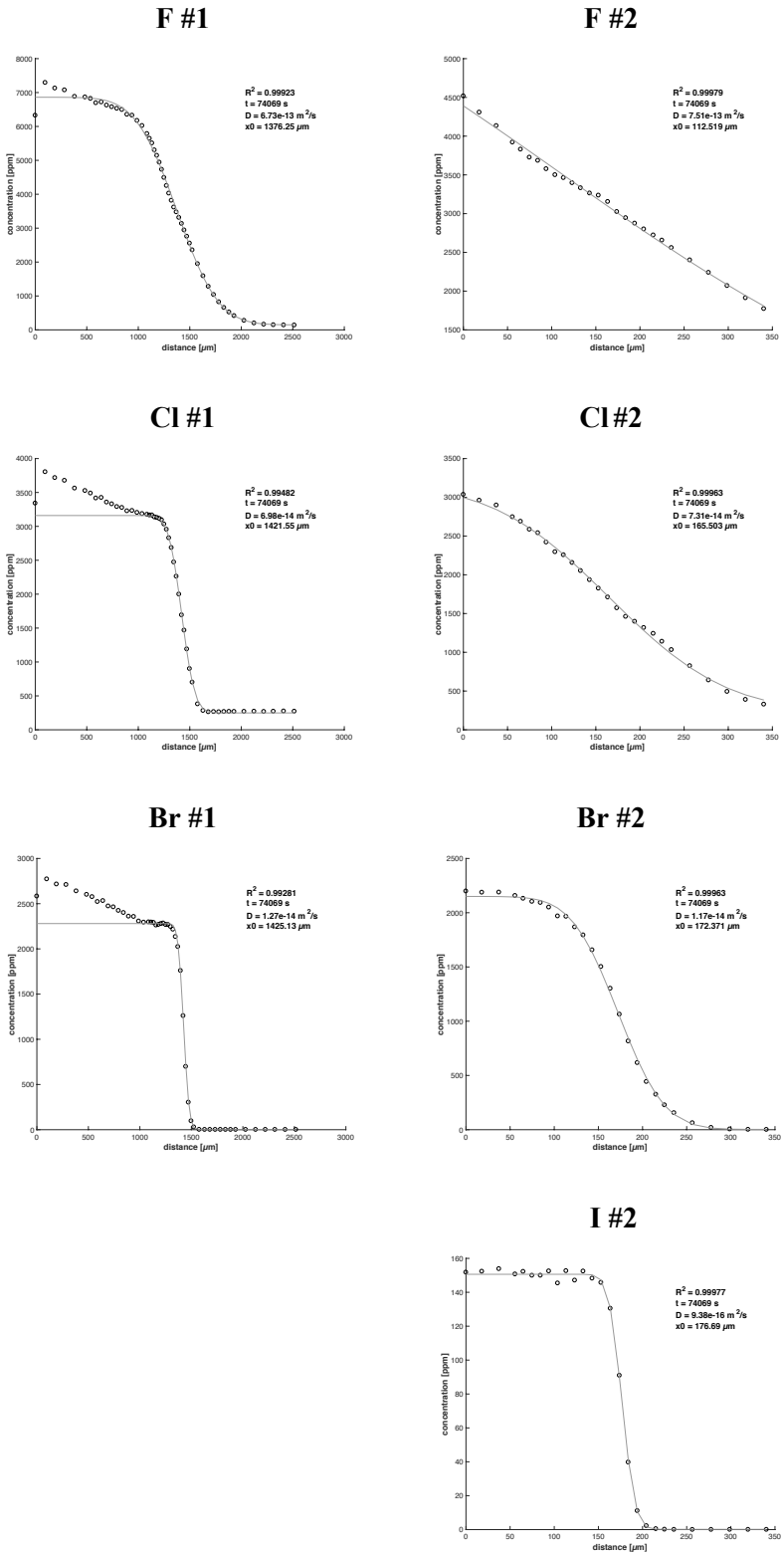

Fig. S3h: Fitted SIMS profiles of sample CCX-5 (1000 °C). The "#" indicates the profile number per sample. C_{high} and C_{low} of F #2 and Cl #2 were fixed for fitting calculations by using the values of their profile #1 counterparts.

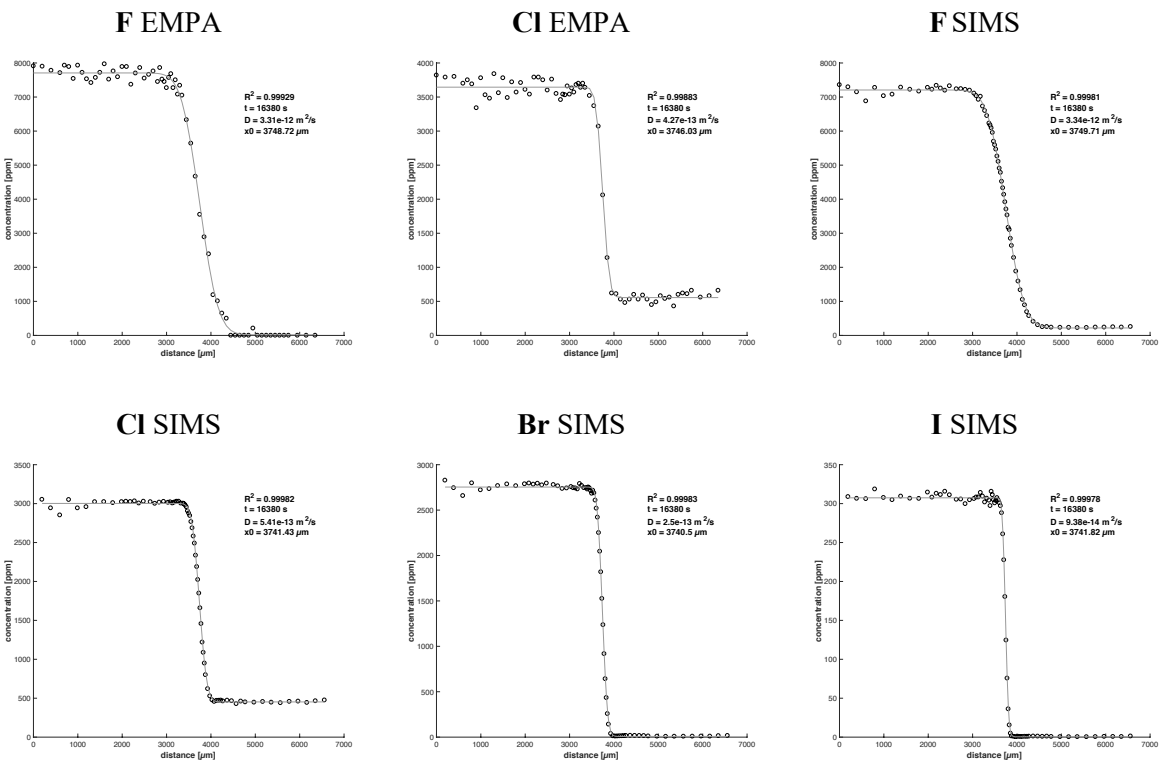

Fig. S4a: Fitted EMPA and SIMS profiles of sample CCX-H-38 (1000 °C).

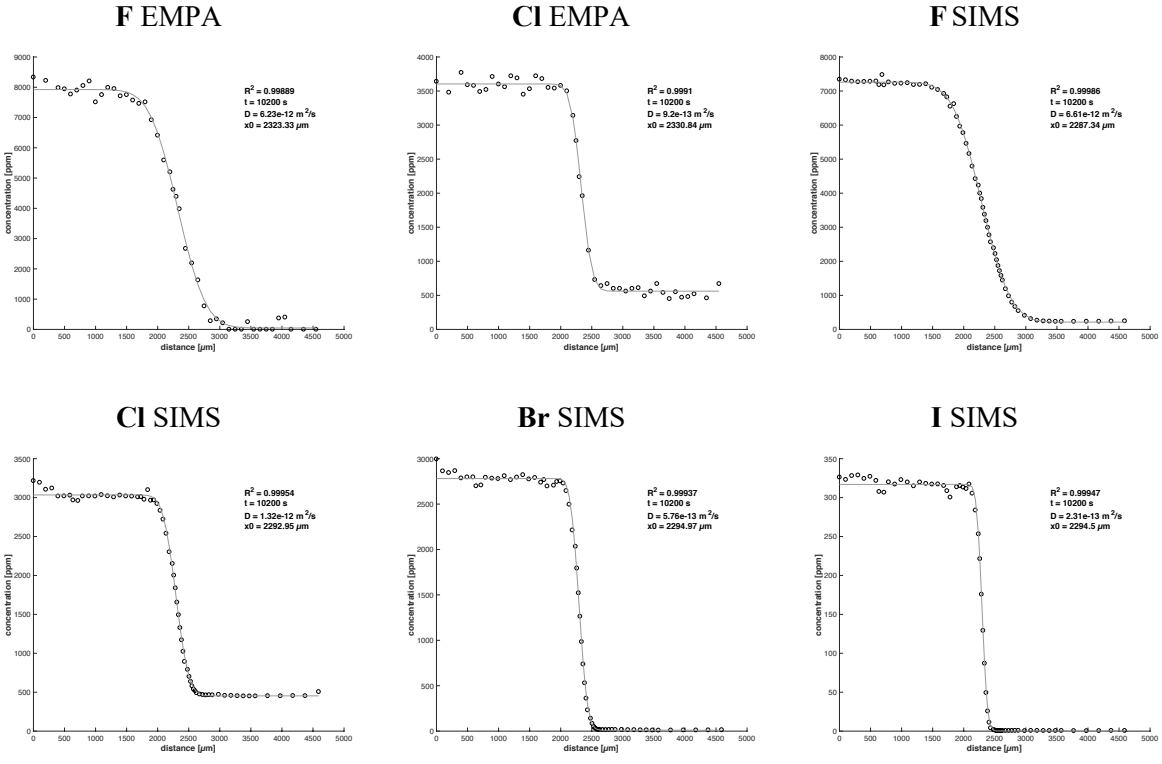

Fig. S4b: Fitted EMPA and SIMS profiles of sample CCX-H-40 (1050 °C).

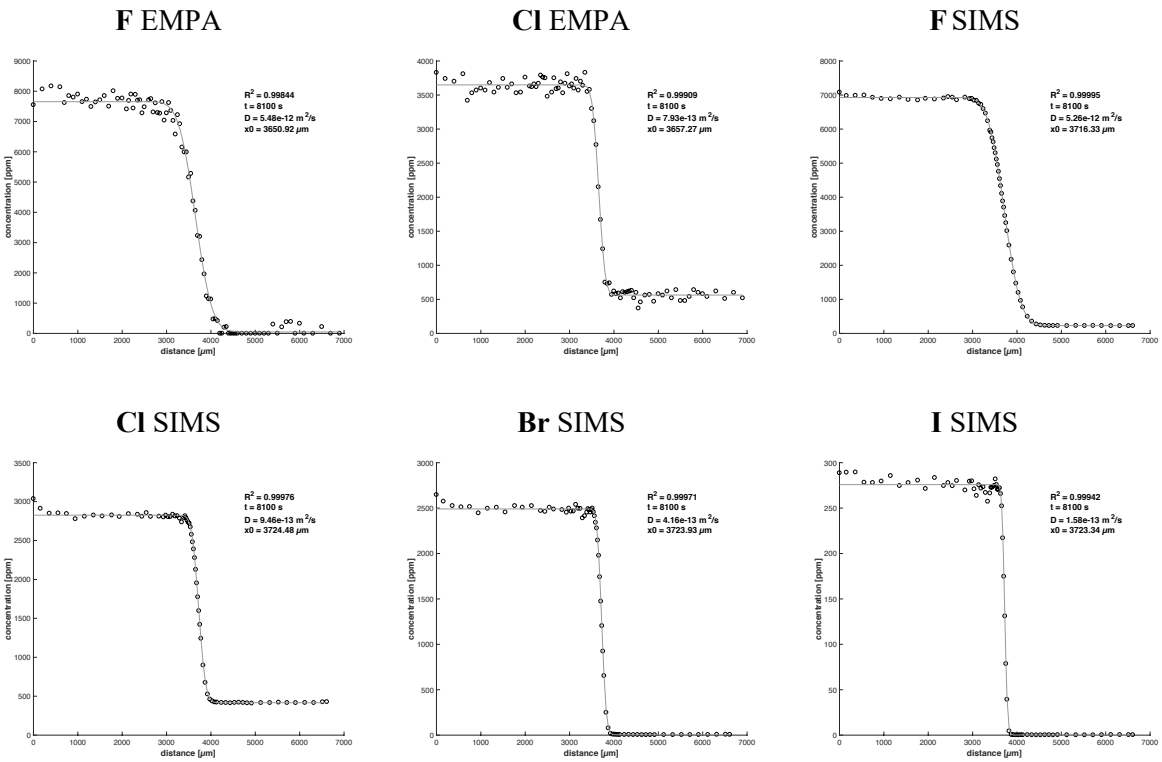

Fig. S4c: Fitted EMPA and SIMS profiles of sample CCX-H-42 (1100 °C).

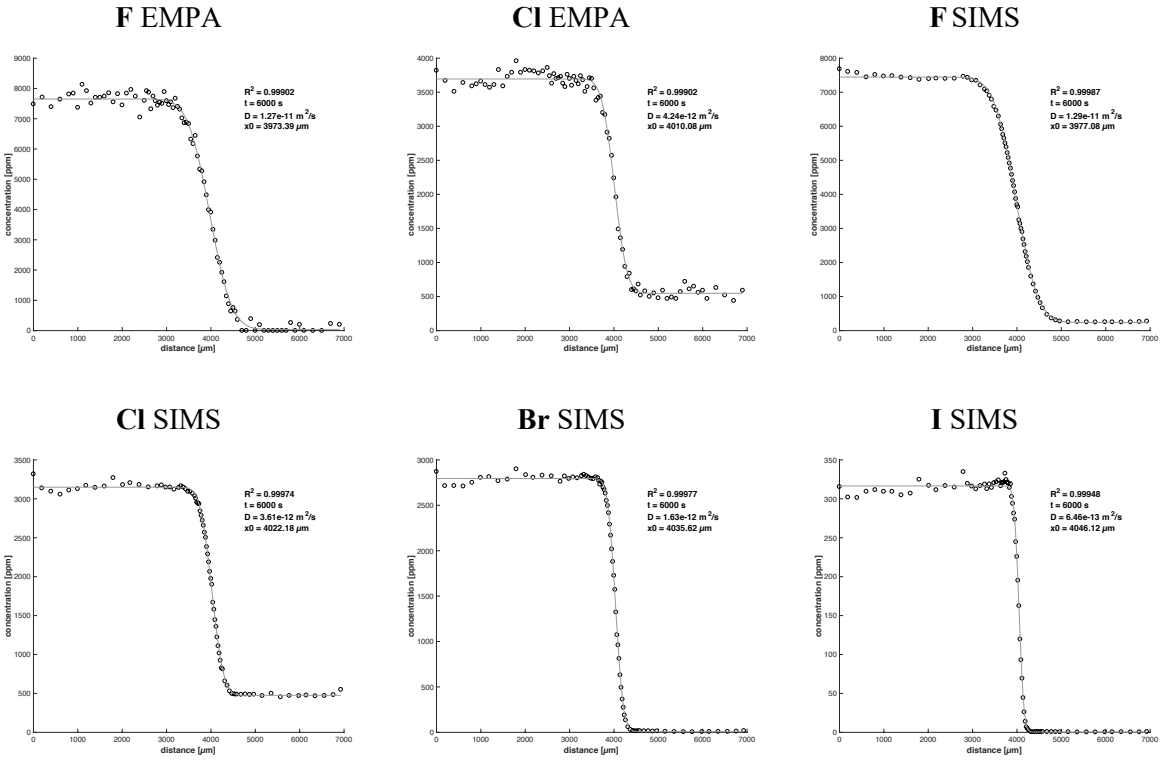

Fig. S4d: Fitted EMPA and SIMS profiles of sample CCX-H-43 (1150 °C).

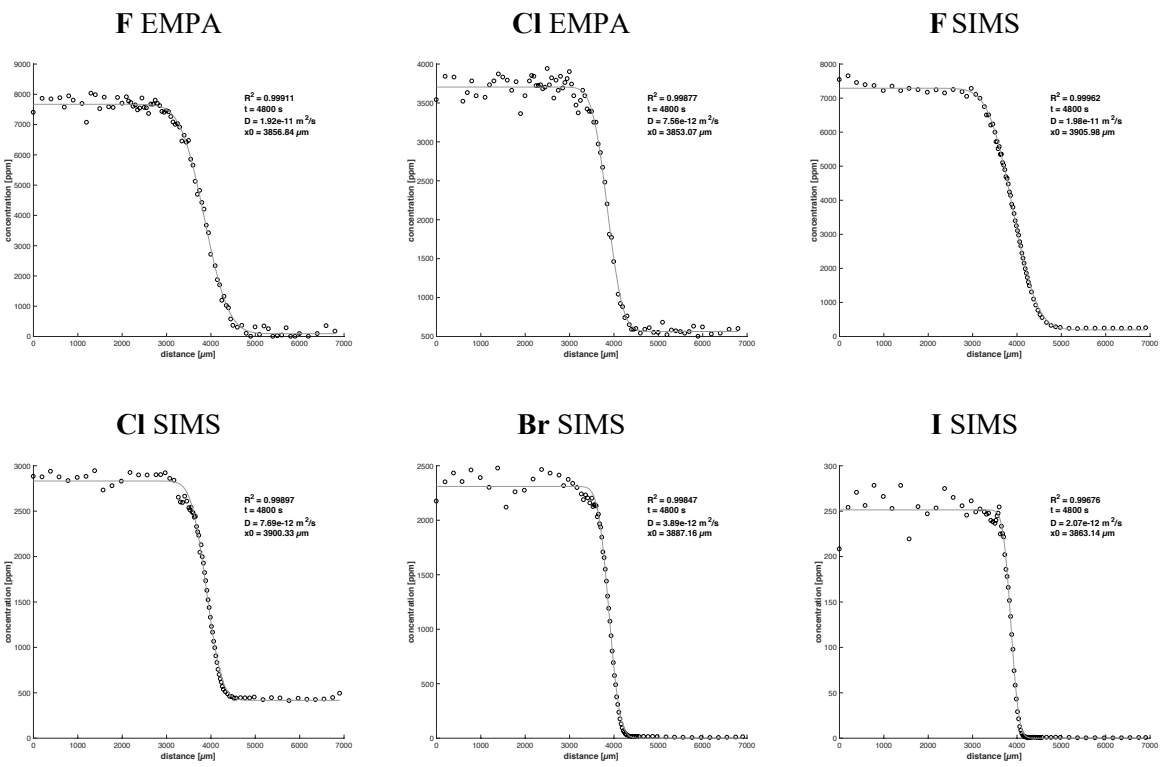

Fig. S4e: Fitted EMPA and SIMS profiles of sample CCX-H-44 (1200 °C).

Eidesstattliche Erklärung

Hiermit versichere ich, Yves Feisel, gemäß §10 Abs. 3d der Promotionsordnung des Fachbereichs 09 (Chemie, Pharmazie und Geowissenschaften) der Johannes Gutenberg-Universität Mainz vom 24.07.2007, die als Dissertation vorgelegte Arbeit selbstständig und nur unter Verwendung der in der Arbeit angegebenen Hilfsmittel verfasst zu haben. Die hier als Dissertation vorgelegte Arbeit habe ich nicht als Prüfungsarbeit für eine andere Prüfung eingereicht. Weder die jetzt als Dissertation vorgelegte Arbeit noch Teile davon habe ich bei einer anderen Fakultät bzw. einem anderen Fachbereich als Dissertation eingereicht.

_____

Datum, Unterschrift